

**Best  
Available  
Copy**

ADA278698

UNITED STATES AIR FORCE

SUMMER RESEARCH PROGRAM -- 1993

SUMMER RESEARCH PROGRAM FINAL REPORTS

VOLUME 8

PHILLIPS LABORATORY

RESEARCH & DEVELOPMENT LABORATORIES

5800 Uplander Way

Culver City, CA 90230-6608

Program Director, RDL  
Gary Moore

Program Manager, AFOSR  
Col. Hal Rhoades

Program Manager, RDL  
Scott Licoscas

Program Administrator, RDL  
Gwendolyn Smith

Program Administrator  
Johnetta Thompson

Submitted to:

AIR FORCE OFFICE OF SCIENTIFIC RESEARCH

Bolling Air Force Base

Washington, D.C.

December 1993

Accession For		1
NTIS	CRA&I	<input checked="" type="checkbox"/>
DTIC	TAB	<input type="checkbox"/>
Unannounced		<input type="checkbox"/>
Justification		
By <i>lts</i>		
Distribution /		
Availability Codes		
Dist	Avail and/or Special	
A-1		

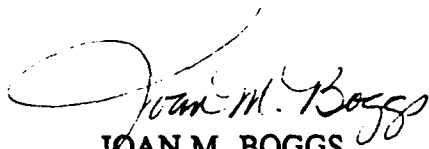
DTIC JOURNAL RELEASED 3

MEMORANDUM FOR DTIC (Acquisition)  
(Attn: Pat Mauby)

SUBJECT: Distribution of USAF (AFOSR Summer Research Program (Air Force Laboratories) and Universal Energy Systems, Inc., and the Research Initiation Program

FROM: AFOSR/XPT  
Joan M. Boggs  
110 Duncan Avenue, Suite B115  
Bolling AFB DC 20332-0001

1. All of the books forwarded to DTIC on the subjects above should be considered Approved for Public Release, distribution is unlimited (Distribution Statement A).
2. Thank you for processing the attached information.



JOAN M. BOGGS  
Chief, Technical Information Division

*1993 SRP Vol 1, 2, 3, 4, 5A, 5B, 6, 7, 8, 9  
(10 Books)*

## Master Index For Graduate Students

Ahmad, Imad  
BS  
Electrical Engineering  
Portland State University  
Portland, OR 97207-0000

Field: Electrical Engineering  
Laboratory: PL/WS

Vol-Page No: 8-19

Anselmo, Andrew  
MS  
Mechanical Engineering  
Columbia University  
New York, NY 10027-0000

Field: Mechanical Engineering  
Laboratory: RL/ER

Vol-Page No: 9- 3

Bapty, Theodore  
MS  
Box 1649 Station B  
Vanderbilt University  
Nashville, TN 37235-0000

Field: Electrical Engineering  
Laboratory: AEDC/

Vol-Page No: 11- 1

Barber, Brian  
BS  
Electrical Engineering  
Washington University  
St. Louis, MO 63130-0000

Field: Electrical Engineering  
Laboratory: RL/OC

Vol-Page No: 9-10

Bard, David  
MS  
Mechanical Engineering  
Columbia University  
New York, NY 10027-0000

Field: Applied Mechanics  
Laboratory: PL/SX

Vol-Page No: 8-14

Barnett, William  
BS  
CLOUD & Aerosol Science L  
University of Missouri  
Rolla, MO 65401-0000

Field: Chemistry  
Laboratory: PL/LI

Vol-Page No: 8- 6

Bartell, Craig  
BS  
Chemistry  
Wright State University  
Fairborn, OH 45435-0000

Field: Chemistry  
Laboratory: WL/PO

Vol-Page No: 10-26

Bartelt, Timothy  
MS  
Physics  
Clarkson University  
Potsdam, NY 13676-0000

Field: Physics  
Laboratory: RL/ER

Vol-Page No: 9- 4



## GSRP Participant Data

Brocklehurst, William  
BS  
Aerospace Engineering  
University of Cincinnati  
Cincinnati, OH 45221-0000

Field: Aerospace Engineering  
Laboratory: PL/RK

Vol-Page No: 8-10

Burns, Paul  
BS  
Electrical Engineering  
Auburn University  
Auburn, AL 36849-0000

Field: Electrical Engineering  
Laboratory: WL/MN

Vol-Page No: 10-21

Carlen, Edwin  
BS  
Electrical Engineering  
Oakland University  
Rochester, MI 48309-4401

Field: Electrical Engineering  
Laboratory: WL/AA

Vol-Page No: 10- 1

Carter, Charity  
MS  
Electrical Engineering  
Stevens Institute of Tech.  
Hoboken, NJ 7030-0000

Field: Interdisciplinary Engr.  
Laboratory: RL/IR

Vol-Page No: 9- 8

Caslin, Barry  
BS  
Computer Science/Engineer  
Wright State University  
Dayton, OH 45435-0000

Field: Computer Science  
Laboratory: WL/ML

Vol-Page No: 10-14

Charley, David  
BS  
Electrical Engineering  
University of Cincinnati  
Cincinnati, OH 45221-0030

Field: Computer Science  
Laboratory: WL/AA

Vol-Page No: 10- 2

Cisneros, John  
BS  
Psychology  
California State University  
Los Angeles, CA 90032-0000

Field: Psychology  
Laboratory: RL/XP

Vol-Page No: 7- 8

Craig, Ralph  
BS  
Mathematics  
North Carolina State Univ.  
Raleigh, NC 27695-8205

Field: Mathematics  
Laboratory: PL/VT

Vol-Page No: 8-15

## GSRP Participant Data

Curtis, Joseph  
MS  
Zoology  
University of California  
Davis, CA 95616-0000

Field: Biomedicine  
Laboratory: AL/OE

Vol-Page No: 7-25

Darnell, Julie  
BS  
Mechanical Engineering  
University of Tennessee  
Tullahoma, TN 37388-0000

Field: Mechanical Engineering  
Laboratory: AEDC/

Vol-Page No: 11- 2

Davis, Wyatt  
BS  
Mechanical Engineering  
Washington State University  
Pullman, WA 99164-2920

Field: Mechanical Engineering  
Laboratory: FJSRL/

Vol-Page No: 11-10

DeVilbiss, Alan  
BS  
Physics  
University of Colorado  
Colorado Springs, CO 80901-7150

Field: Physics  
Laboratory: FJSRL/

Vol-Page No: 11-11

Detwiler, Duane  
BS  
Aeronautical Engineering  
Ohio State University  
Columbus, OH 43235-0000

Field: Aerospace Engineering  
Laboratory: WL/FI

Vol-Page No: 10- 7

DiPietro, Jr., Anthony  
BS  
Aerospace Engineering  
Virginia Polytechnic Institute  
Blacksburg, VA 24060-0000

Field: Aerospace Engineering  
Laboratory: AEDC/

Vol-Page No: 11- 3

Dobransky, Mary  
MS  
Systems Science  
Binghamton University  
Binghamton, NY 13902-6000

Field: Advanced Technology  
Laboratory: RL/XP

Vol-Page No: 9-15

Doss, Ellen  
BS  
Biophysics  
University of Scranton  
Scranton, PA 18505-0898

Field: Biophysics  
Laboratory: AL/AO

Vol-Page No: 7- 1

## GSRP Participant Data

DuBois, Travis  
BS  
Mechanical Engineering  
Old Dominion University  
Norfolk, VA 23529-0247

Field: Mechanical Engineering  
Laboratory: FJSRL/

Vol-Page No: 11-12

Farquhar, John  
MS  
Instructional Technology  
University of Georgia  
Athens, GA 30602-0000

Field: Instructional Technology  
Laboratory: AL/HR

Vol-Page No: 7-17

Fischer, Verlyn  
BS  
Materials Science & Engr.  
University of Florida  
Gainesville, FL 32611-0000

Field: Physics  
Laboratory: WL/ML

Vol-Page No: 10-15

Foster, Robert  
BS  
Mechanical Engineering  
University of Iowa  
Iowa City, IA 52240-0000

Field: Mechanical Engineering  
Laboratory: WL/PO

Vol-Page No: 10-27

Frank, Jonathan  
MS  
Mechanical Engineering  
Yale University  
New Haven, CT 6520-0000

Field: Mechanical Engineering  
Laboratory: WL/PO

Vol-Page No: 10-28

Fuller, Joan  
BS  
Chemistry  
University of Alabama  
Tuscaloosa, AL - 0

Field: Chemistry  
Laboratory: FJSRL/

Vol-Page No: 11-13

Gavora, Mark  
MS  
Instructional Systems  
Florida State University  
Tallahassee, FL 32304-3551

Field: Instructional Systems  
Laboratory: AL/HR

Vol-Page No: 7-18

Geierman, Robert  
BS  
Mechanical Engineering  
University of Tennessee  
Tullahoma, TN 37388-0000

Field: Mechanical Engineering  
Laboratory: AEDC/

Vol-Page No: 11- 4

## GSRP Participant Data

Gluck, Kevin  
BS  
Psychology  
Trinity University  
San Antonio, TX 78212-0000

Field: Psychology  
Laboratory: AL/HR

Vol-Page No: 7-19

Gottlob, Lawrence  
MS  
Psychology  
Arizona State University  
Tempe, AZ 85287-0000

Field: Psychology  
Laboratory: AL/HR

Vol-Page No: 7-20

Griffin, Steven  
BS  
Engineering  
University of Texas  
San Antonio, TX 78249-0665

Field: Mechanical Engineering  
Laboratory: PL/VT

Vol-Page No: 8-16

Grosskopf, Kevin  
BS  
FAC 101  
University of Florida  
Gainesville, FL 32611-0000

Field: School of Bldg. Construct  
Laboratory: WL/FT

Vol-Page No: 10- 8

Harn, Patricia  
BS  
Technical Communication  
University of Washington  
Seattle, WA 98195-0000

Field: Communications  
Laboratory: AL/HR

Vol-Page No: 7-21

Hickman, Mary  
BS  
Physics and Astronomy  
University of Wyoming  
Laramie, WY 82071-0000

Field: Astrophysics  
Laboratory: PL/LI

Vol-Page No: 8- 7

Hovey III, Leland  
BS  
Computer Science  
SUNY Institute of Technology  
Utica, NY 13504-3050

Field: Mathematics  
Laboratory: RL/XP

Vol-Page No: 9-16

Jain, Sanjay  
BS

Field: Natural Sciences  
Laboratory: WHMC/

Northeastern Ohio University  
Rootstown, OH 44272-0000

Vol-Page No: 11-16

## GSRP Participant Data

Jefferson, Ellen  
BS  
Biology  
Trinity University  
San Antonio, TX 78212-0000

Field: Biology  
Laboratory: AL/OE

Vol-Page No: 7-26

Jenny, Jason  
BS  
Materials Science  
Carnegie-Mellon University  
Pittsburgh, PA 15213-0000

Field: Materials Science  
Laboratory: WL/ML

Vol-Page No: 10-16

Jolly, Mohanjit  
BS  
Aeronautics/Astronautics  
MIT  
Cambridge, MA 2139-0000

Field: Aeronautics/Astronautics  
Laboratory: PL/RK

Vol-Page No: 8-11

Jones, Claud  
BS  
Electrical & Computer Eng  
University of SW Louisiana  
Lafayette, LA 70504-3890

Field: Petroleum Engineering  
Laboratory: RL/C3

Vol-Page No: 9- 1

Kelly, John  
BS  
Electrical Engineering  
University of Florida  
Gainesville, FL 32601-0000

Field: Electrical Engineering  
Laboratory: PL/LI

Vol-Page No: 8- 8

Kimball, Lucia  
MS  
Mathematics  
Worcester Polytechnic Inst.  
Worcester, MA 1609-0000

Field: Applied Mathematics  
Laboratory: PL/GP

Vol-Page No: 8- 1

Kundich, Robert  
MS  
899 Madison Ave., Ste 801  
Univ. Tennessee-Memphis  
Memphis, TN 38163-0000

Field: Biomedical Engineering  
Laboratory: AL/CF

Vol-Page No: 7- 9

Kvasnak, William  
MS  
Mechanical Engineering  
Clarkson University  
Potsdam, NY 13699-5725

Field: Mechanical Engineering  
Laboratory: AEDC/

Vol-Page No: 11- 5

## GSRP Participant Data

Lair, John  
BS  
Civil Engineering  
University of New Orleans  
New Orleans, LA 70148-0000

Field: Industrial Design  
Laboratory: WL/FT

Vol-Page No: 10- 9

Lee, Daniel  
BS  
Electrical Engineering  
Southern Illinois University  
Carbondale, IL 62901-0000

Field: Electrical Engineering  
Laboratory: RL/ER

Vol-Page No: 9- 5

Leiweke, Robert  
BS  
Aeronautical Engineering  
Ohio State University  
Columbus, OH 43210-0000

Field: Aerospace Engineering  
Laboratory: PL/WS

Vol-Page No: 8-20

Litvin, Kerry  
MS  
Electrical Engineering  
Cornell University  
Ithaca, NY 14853-0000

Field: Electrical Engineering  
Laboratory: RL/OC

Vol-Page No: 9-11

Luker, Stephen  
MS  
Biological Science  
University of Alabama  
Tuscaloosa, AL 35487-0344

Field: Marine Science  
Laboratory: PL/GP

Vol-Page No: 8- 2

Masterson, Gina  
BS  
Industrial Engineering  
Auburn University  
Auburn, AL - 0

Field: Industrial Engineering  
Laboratory: AL/OE

Vol-Page No: 7-27

McMurtry, J.  
MS  
Mechanical Engineering  
Louisiana Tech University  
Ruston, LA 71272-0046

Field: Mechanical Engineering  
Laboratory: WL/MN

Vol-Page No: 10-22

Menendez-Barreto, Melani  
MS  
Physics  
University of Puerto Rico  
Mayaguez, PR 681-0000

Field: Physics  
Laboratory: PL/GP

Vol-Page No: 8- 3

## GSRP Participant Data

Messerschmitt, Jane  
MS  
Electrical Engineering  
Polytechnic University  
Farmingdale, NY 11735-0000

Field:  
Laboratory: PL/WS

Vol-Page No: 8-21

Mills, Jeffrey  
MS  
Chemistry  
Indiana University  
Bloomington, IN 47405-0000

Field: Chemistry  
Laboratory: PL/RK

Vol-Page No: 8-12

Monka, Gary  
BS  
Chemistry  
University of Scranton  
Scranton, PA 18510-0000

Field: Chemistry  
Laboratory: AL/OE

Vol-Page No: 7-28

Moore, Michael  
MS  
Electrical Engineering  
Vanderbilt University  
Nashville, TN 37235-0000

Field: Electrical Engineering  
Laboratory: AEDC/

Vol-Page No: 11- 6

Moriarty, Daniel  
MS  
Nuclear Engineering  
MIT  
Cambridge, MA 2139-0000

Field: Nuclear Engineering  
Laboratory: PL/GP

Vol-Page No: 8- 4

Nagaraja, Chandra  
BS  
Mechanical Engineering  
University of Dayton  
Dayton, OH 45469-0000

Field: Mechanical Engineering  
Laboratory: WL/PO

Vol-Page No: 10-29

Naghski, David  
MS  
Electrical Engineering  
University of Cincinnati  
Cincinnati, OH 45221-0000

Field: Electrical Engineering  
Laboratory: WL/ML

Vol-Page No: 10-17

Neaffer, Ronald  
BS  
Polymer Science  
University of Akron  
Akron, OH 44325-3909

Field: Physics  
Laboratory: WL/ML

Vol-Page No: 10-18

## GSRP Participant Data

Newell, Tim  
MS  
Physics  
University of North Texas  
Denton, TX 76203-0000

Field: Physics  
Laboratory: PL/LI

Vol-Page No: 8- 9

Nguyen, Sonny  
BS  
Electrical Engineering  
Wright University  
Dayton, OH 45401-0000

Field: Electrical Engineering  
Laboratory: WL/PO

Vol-Page No: 10-30

Nuteson, Todd  
BS  
Electrical Engineering  
Wright State University  
Dayton, OH 45435-0000

Field: Electrical Engineering  
Laboratory: WL/EL

Vol-Page No: 10- 4

Olson, Michael  
BS  
Electrical Engineering  
Florida State University  
Tallahassee, FL 32316-0000

Field: Electrical Engineering  
Laboratory: WL/MN

Vol-Page No: 10-23

Panek, Heather  
MS  
Biology  
University of Scranton  
Scranton, PA 18510-0000

Field: Biochemistry  
Laboratory: AL/AO

Vol-Page No: 7- 3

Petroziello, Joseph  
BS  
Biology  
University of Scranton  
Scranton, PA 18510-0000

Field: Biology  
Laboratory: AL/AO

Vol-Page No: 7- 4

Pobst, Jeffrey  
BS  
Aerospace Engineering  
University of Southern Calif.  
Los Angeles, CA 90089-1191

Field: Aerospace Engineering  
Laboratory: PL/RK

Vol-Page No: 8-13

Povich, Clinton  
BS  
Aerospace Engineering  
University of Kansas  
Lawrence, KS 66045-0000

Field: Aerospace Engineering  
Laboratory: FJSRL/

Vol-Page No: 11-14



## GSRP Participant Data

Radomsky, Leon  
MS  
Chemical Engineering  
Columbia University  
New York, NY 10027-0000

Field: Materials Science  
Laboratory: WL/EL

Vol-Page No: 10- 5

Reed, Jason  
BS  
Electrical Engineering  
Cornell University  
Ithaca, NY 14853-0000

Field: Physics  
Laboratory: RL/OC

Vol-Page No: 9-12

Reichmeyer, Francis  
MS  
Electrical Engineering  
Syracuse University  
Syracuse, NY 13244-1240

Field: Electrical Engineering  
Laboratory: RL/C3

Vol-Page No: 9- 2

Reiley, Daniel  
MS  
Physics  
University of Alabama  
Huntsville, AL 35899-0000

Field: Physics  
Laboratory: WL/MN

Vol-Page No: 10-24

Reister, Craig  
BS  
Electrical Engineering  
North Dakota State University  
Fargo, ND 58105-0000

Field: Electrical Engineering  
Laboratory: AL/AO

Vol-Page No: 7- 5

Reuster, Daniel  
MS  
Electrical Engineering  
University of Dayton  
Dayton, OH 45469-0000

Field: Electrical Engineering  
Laboratory: WL/AA

Vol-Page No: 10- 3

Riesinger, Joyce  
BS  
Ecology/Evolutionary Biol  
University of West Florida  
Pensacola, FL 32514-0000

Field: Marine Biology  
Laboratory: AL/EQ

Vol-Page No: 7-14

Ryan, Arthur  
BS  
Psychology  
Wright State University  
Dayton, OH 45435-0001

Field: Psychology  
Laboratory: AL/CF

Vol-Page No: 7-10

## GSRP Participant Data

Samad, Mohammed  
BS  
Mechanical Engineering  
University of New Orleans  
New Orleans, LA 70148-0000

Field: Mechanical Engineering  
Laboratory: WL/FI

Vol-Page No: 10-10

Schroeder, Mark  
BS  
Electrical Engineering  
North Dakota State University  
Fargo, ND 58105-0000

Field: Electrical Engineering  
Laboratory: AL/AO

Vol-Page No: 7- 6

Schwing, Ronald  
BS  
Mechanical Engineering  
University of Iowa  
Iowa City, IA 52242-0000

Field: Mechanical Engineering  
Laboratory: WL/PO

Vol-Page No: 10-31

Seifert, Jason  
BS  
Psychology  
University of Dayton  
Dayton, OH 45410-0000

Field: Psychology  
Laboratory: AL/HR

Vol-Page No: 7-22

Seydel III, Robert  
BS  
Aerospace Engineering  
University of Missouri  
Rolla, MO 65401-0000

Field: Aerospace Engineering  
Laboratory: WL/FI

Vol-Page No: 10-11

Shahidi, Anoosh  
MS  
Intelligent Systems Studi  
University of Pittsburgh  
Pittsburgh, PA 15260-0000

Field: Intelligent Systems  
Laboratory: AL/HR

Vol-Page No: 7-23

Shahrokhi, Kimball  
BS  
Mechanical Engineering  
Vanderbilt University  
Nashville, TN 37232-0000

Field: Mechanical Engineering  
Laboratory: AEDC/

Vol-Page No: 11- 7

Slater III, Robert  
MS  
Mechanical Engineering  
University of Cincinnati  
Cincinnati, OH 45221-0000

Field: Engineering  
Laboratory: WL/FI

Vol-Page No: 10-12

## GSRP Participant Data

Socci, Ed  
MS  
Materials Science & Engr  
University of Virginia  
Charlottesville, VA 22903-2442

Field:  
Laboratory: WL/ML

Vol-Page No: 10-19

Sodoy, Maureen  
BS  
Biology  
Trinity University  
San Antonio, TX 78212-0000

Field: Biology  
Laboratory: AL/OE

Vol-Page No: 7-29

Sorensen, Bryant  
MS  
Electrical Engineering  
University of Tennessee  
Tullahoma, TN 37388-0000

Field: Mathematics  
Laboratory: AEDC/

Vol-Page No: 11- 8

Spencer, Robert  
BS  
Electrical Engineering  
Cornell University  
Ithaca, NY 14853-0000

Field: Electrical Engineering  
Laboratory: RL/OC

Vol-Page No: 9-13

Stadler, Bethanie  
BS  
Materials Science  
Massachusetts Inst. of Tech.  
Cambridge, MA 2139-0000

Field: Materials Science  
Laboratory: RL/ER

Vol-Page No: 9- 6

Stansbery, Donald  
BS  
Aerospace Engineering  
University of Missouri  
Rolla, MO 65401-0000

Field: Aerospace  
Laboratory: WL/MN

Vol-Page No: 10-25

Starchville, Jr., Thomas  
MS  
Aerospace Engineering  
Pennsylvania State University  
University Park, PA 16802-0000

Field: Aerospace Engineering  
Laboratory: WL/FT

Vol-Page No: 10-13

Starks, Michael  
BS  
Electrical Engineering  
Boston University  
Boston, MA 2215-0000

Field: Electrical Engineering  
Laboratory: PL/GP

Vol-Page No: 8- 5

## GSRP Participant Data

Stauffer, Joseph  
MS  
Management  
University of Iowa  
Iowa City, IA 52242-1323

Field: Management  
Laboratory: AL/HR

Vol-Page No: 7-24

Stenger, Vincent  
BS  
Electrical Engineering  
University of Cincinnati  
Cincinnati, OH 45221-0030

Field: Electrical Engineering  
Laboratory: WL/EL

Vol-Page No: 10- 6

Stohs, Jonathan  
BS  
Physics  
University of New Mexico  
Albuquerque, NM 87131-0000

Field: Math  
Laboratory: PL/VT

Vol-Page No: 8-17

Stroman, Ronald  
BS  
Pharmacy  
University of South Carolina  
Columbia, SC 29208-0000

Field: Pharmacy  
Laboratory: AL/AO

Vol-Page No: 7- 7

Sullins, Tashia  
BS  
Chemistry  
University of Georgia  
Athens, GA 30605-0000

Field: Chemistry  
Laboratory: AL/EQ

Vol-Page No: 7-15

Sutcliffe, Ronald  
BS  
Chemistry  
Southwest Texas State  
San Marcos, TX 78666-0000

Field: Chemistry  
Laboratory: AL/OE

Vol-Page No: 7-30

Sweeney, Walter  
MS  
Electrical Engineering  
University of Maine  
Orono, ME 4469-0000

Field: Electrical Engineering  
Laboratory: RL/IR

Vol-Page No: 9- 9

Swindal, J.  
MS  
Applied Physics  
Yale University  
New Haven, CT 6520-0000

Field: Applied Physics  
Laboratory: WL/PO

Vol-Page No: 10-32

## GSRP Participant Data

Tascillo, Mark  
MS  
Electrical Engineering  
Binghamton University  
Binghamton, NY 13902-0000

Field: Electrical Engineering  
Laboratory: RL/OC

Vol-Page No: 9-14

Thomas, Stuart  
BS  
Chemical Engineering  
North Carolina State Univ.  
Raleigh, NC 27695-0000

Field: Chemical Engineering  
Laboratory: AL/EQ

Vol-Page No: 7-16

Tipton, Kevin  
MS  
Nutrition and Food Science  
Auburn University  
Auburn, AL 36849-5605

Field: Zoology  
Laboratory: AL/CF

Vol-Page No: 7-11

Tornow, Carina  
BS  
Quantitative Psychology  
Ohio State University  
Columbus, OH 43210-0000

Field: Psychology  
Laboratory: AL/CF

Vol-Page No: 7-12

Trick, Kimberly  
MS  
Chemical Engineering  
University of Dayton  
Dayton, OH 45401-0240

Field: Chemical Engineering  
Laboratory: WL/ML

Vol-Page No: 10-20

Weaver, Michael  
MS  
Aerospace Engineering  
Georgia Institute of Technology  
Atlanta, GA 30332-0150

Field: Aerospace Engineering  
Laboratory: AEDC/

Vol-Page No: 11- 9

Weitzman, Peter  
MS  
Thayer School of Engineering  
Dartmouth College  
Hanover, NH 3755-0000

Field: Electrical Engineering  
Laboratory: FJSRL/

Vol-Page No: 11-15

Whitmore, Christine  
BS  
Mechanical Engineering  
Washington University  
St. Louis, MO - 0

Field: Mechanical Engineering  
Laboratory: AL/CF

Vol-Page No: 7-13

## GSRP Participant Data

Widener, Charles  
MS

Electrical Engineering  
Syracuse University  
Syracuse, NY 13244-0000

Field: Electrical Engineering  
Laboratory: PL/VT

Vol-Page No: 8-18

Wierman, Mark  
MA

Systems Science  
Binghamton University  
Binghamton, NY 13902-6000

Field: Mathematics  
Laboratory: RL/XP

Vol-Page No: 9-17

Willemsen, Balam  
MS

Physics  
Northeastern University  
Boston, MA 2115-0000

Field: Physics  
Laboratory: RL/ER

Vol-Page No: 9- 7

Wolfe, Randall  
MS

Biopsychology  
University of Georgia  
Athens, GA 30612-0000

Field: General Psychology  
Laboratory: AL/OE

Vol-Page No: 7-31

Worthy, Mark  
BS

Environmental Engineering  
University of Alabama  
Huntsville, AL 35899-1750

Field: Electrical Engineering  
Laboratory: PL/WS

Vol-Page No: 8-22

CALCULATION OF ATMOSPHERIC COOLING RATES USING MODTRAN2

Lucia M. Kimball  
Graduate Student  
Mathematics Department

Worcester Polytechnic Institute  
100 Institute Road  
Worcester, MA. 01609

Final Report for:  
Graduate Student Research Program  
Phillips Laboratory

Sponsored by:  
Air Force Office of Scientific Research  
Bolling Air Force Base, Washington, D. C.

September 1993

## CALCULATION OF ATMOSPHERIC COOLING RATES USING MODTRAN2

Lucia M. Kimball  
Graduate Student  
Mathematics Department  
Worcester Polytechnic Institute

### Abstract

A technique for calculating atmospheric cooling rates has been developed based on infrared radiance calculations using MODTRAN2. Comparisons with benchmark line-by-line calculations show very good agreement. The technique provides significant computational time savings associated with band models vs. line-by-line calculations.



# CALCULATION OF ATMOSPHERIC COOLING RATES USING MODTRAN2

Lucia M. Kimball

## Introduction

Accurate calculations of the transfer of radiation through the atmosphere are necessary for many climate programs. Line-by-line models such as FASCODE perform detailed computations and are considered "exact" within the limitations of the current knowledge of molecular properties such as lineshape, line mixing and interaction with foreign gases. However, the amount of time required for most calculations is prohibitive. MODTRAN2, the most current version of MODTRAN, the Moderate Resolution Atmospheric Radiance and Transmittance Model, is a band model based code which has been extensively validated against FASCODE. For a 500  $\text{cm}^{-1}$  spectral interval with comparable vertical layering the time improvement is more than a factor of 100.

In this paper, we consider the use of MODTRAN2 to calculate clear sky, infrared cooling rates for several model atmospheres. The cooling rate results are compared to similar calculations performed with FASCODE as developed by Clough, et al., (1992). The

current method follows that of Clough as closely as possible so that differences in the results can be attributed primarily to the differences between the line-by-line and band models.

### Radiance Calculation

The radiant energy emitted at wavenumber  $\nu$  along a path with optical depth  $\tau_\nu$  and transmittance  $T_\nu$  is given by

$$I_\nu = \int_{T_\nu}^1 B_\nu(\theta(T'_\nu)) dT'_\nu,$$

$$I_\nu = \int_0^{\tau_\nu} B_\nu(\theta(\tau'_\nu)) e^{-\tau'_\nu} d\tau'_\nu.$$

where  $B_\nu$  is the Planck function at temperature  $\theta$ ,

$$B_\nu(\theta) = \frac{2h \nu^3}{c^2 e^{\frac{h\nu}{k\theta}} - 1}.$$

Here  $h$  is Planck's constant,  $c$  is the speed of light and  $k$  is Boltzmann's constant. In the present application, MODTRAN2, a moderate resolution transmittance code, has been used to first calculate the path transmittances and secondarily, the radiances.

The version of MODTRAN used to perform the necessary computations utilizes a one term Padé approximate for the effective Planck function of the form

$$B_\nu(\tau_\nu) = [\overline{B}_\nu + (a\tau_\nu) B_\nu(\theta_u)] (1 + a\tau_\nu)^{-1}$$

where  $\theta_u$  is the temperature at the nearest boundary of the layer (the upper boundary for downwelling radiance and the lower boundary for upwelling radiance),  $\overline{B}_v = B(\overline{\theta})$  where  $\overline{\theta}$  is the mean temperature for the layer  $\ell$ . The value chosen for  $a$  is 0.2 after Clough, et al., (1992). For a band model,  $\tau_v$  is an effective optical depth derived from the log ratios of the full path transmittances between adjacent layers

$$\tau_v = \ln \left( \frac{T_t}{T_{t+1}} \right) .$$

The radiance for a single layer is then given by

$$I_{v;t} = (T_{v,t} - T_{v,t+1}) B_v(\tau_v) .$$

The full path radiance for a path encompassing multiple layers is found recursively where the value at each layer depends on the contribution from the previous layer, see Clough, et al., (1981). Treating the ground as a black body, the boundary condition is given by

$$I_{v;0} = B_v(\theta_s)$$

#### Comparison of Radiance Calculations FASCODE vs. MODTRAN2

The most accurate technique for calculating atmospheric transmittance and radiances employs a line-by-line code such as FASCODE. Calculations are performed at small enough wavenumber intervals to adequately represent the location, strength and shape

of each spectral line within a layer, thus justifying Beer's law for calculating the optical depth. A more detailed description is available in Ellingson, et al., (1991). Due to the large number of spectral lines this is a slow and cumbersome process which is therefore impractical for most uses.

MODTRAN2 employs a two parameter band model to offer more efficient computations of the line contributions. Treatment of line tails and continua is similar for both models. The two parameters are an absorption coefficient ( $S/d$ ) and a line density parameter ( $1/d$ ) given by

$$(S/d) = \left( \frac{1}{\Delta\nu} \right) \sum S_i$$

where  $\Delta\nu = 1 \text{ cm}^{-1}$  and

$$(1/d) = \left( \frac{1}{\Delta\nu} \right) (\sum \sqrt{S_i})^2 / \sum S_i.$$

$S_i$  is the integrated line strength of line  $i$ , and the sum is over  $N$  lines whose centers are contained in a bin of width  $\Delta\nu$ . The transmittance,  $T$ , for the spectral bin  $\Delta\nu$  is given by

$$T = \left( \frac{2}{\Delta\nu} \int_0^{\Delta\nu/2} e^{-S u b(\nu)} d\nu \right)^n.$$

Here  $b(\nu)$  is the Voigt line shape function,  $u$  is the absorber amount,  $S$  and  $n$  are defined by the band model parameters as follows:

$$S = \frac{(S/d)}{(1/d)}$$

$$n = (1/d) \Delta v.$$

For a more detailed description see A. Berk, et al., (1987).

In one specific comparison, see L. Abreu, et al., (1993), MODTRAN2 was shown to be 100 times faster than a non-optimized version of FASCODE for a 500 cm<sup>-1</sup> spectral interval with comparable vertical layering. With proper vectorization and parallel processing, FASCODE's speed can be greatly enhanced. However, MODTRAN's structure is equally vectorizable, so the ratio of improvement should ultimately be maintained.

### Flux Calculation

The upwelling and downwelling fluxes of radiant energy at a given atmospheric level are calculated by integrating the radiance,  $I_v(\mu)$ , at wavenumber  $v$  over the appropriate hemisphere,

$$F_v^+ = \int_0^{2\pi} \int_0^1 I_v(\mu) \mu d\mu d\phi$$

$$F_v^- = \int_0^{2\pi} \int_{-1}^0 I_v(\mu) \mu d\mu d\phi$$

where  $\mu$  is the zenith direction cosine and  $\phi$  is the azimuthal angle. In our case, it is assumed the radiances are azimuthally independent; therefore the integrals become

$$F_v^\pm = \pm 2\pi \int_0^{\pm 1} I_v(\mu) \mu d\mu.$$

The required integration for determining the upwelling and downwelling fluxes was computed using a standard two point, first moment Gaussian quadrature. Comparison of two point vs. three point quadrature did not show sufficient improvement to justify the additional time involved in the computation. When simultaneously plotted, the 2 angle and 3 angle cooling rate curves were nearly coincident. The direction cosine values, associated angles and quadrature weights are given in the following table:

Direction Cosine	Angle	Weight
0.3550510257	69.2034283	0.1819586183
0.8449489743	32.3335307	0.3180413817

Table 1: Gaussian quadrature angles and weights

MODTRAN2 was used to calculate the radiance along a path to space corresponding to each of the given angles at each defined atmospheric level. The downwelling flux was then found by the first moment quadrature. The upwelling flux resulted from integrating the radiances along paths corresponding to the complement of each given angle.

The net flux at any level was then calculated as the difference between the upwelling and downwelling fluxes.

$$F_v = F_v^+ - F_v^-$$

## Cooling Rate Calculation

The divergence of the net flux at atmospheric level  $\ell$  represents the rate of energy loss per unit volume of atmosphere, or the cooling rate

$$Q_v = \Delta F_v.$$

The monochromatic cooling rate for the atmospheric layer bounded by levels  $\ell$  and  $\ell-1$  is computed in terms of change in temperature,  $\theta$ , with respect to time,  $t$ , by the finite difference formula

$$\frac{\partial \theta}{\partial t} \Big|_{v,t,t-1} = \frac{g(F_{v,t} - F_{v,t-1})}{C_p(P_t - P_{t-1})}$$

where  $g$  is gravitational acceleration,  $C_p$  is the specific heat of air at constant pressure, and  $P$  is pressure. A value of 8.422 (mbar K d<sup>-1</sup>) per (W m<sup>-2</sup>) is used for the ratio  $\frac{g}{C_p}$  as in Ridgway et al., (1991), independent of altitude.

## Comparison of Cooling Rate Results

All MODTRAN2 calculations were based on 60 atmospheric layers as defined by Clough, et al., (1992). Layers were spaced at increments of approximately 20 mb pressure from 0 mb to 1013 mb. Cooling rates were found to be sensitive to the chosen layering at both the top and bottom of the defined atmosphere.

Data for layer temperatures and water vapor densities were interpolated from the published ICRCCM data in *Ellingson, et al.*, (1991).

The cooling rate results as compared to the published FASCODE results were very good. Agreement was within the 2% documented FASCODE - MODTRAN agreement in most regions. Relative errors in the net fluxes, mid-latitude summer atmosphere, were all less than 1% with the exception of the net flux in the ground layer which had the maximum relative error of 3.7%.

A comparison of cooling rate results for mid-latitude summer, tropical, and sub-arctic winter atmospheres is given in figures 1-3. Plots represent spectrally integrated cooling rates.

A representation of spectrally dependent cooling rates corresponding to published FASCODE results (*Clough, et. al.*, (1992)) is given in figure 4.



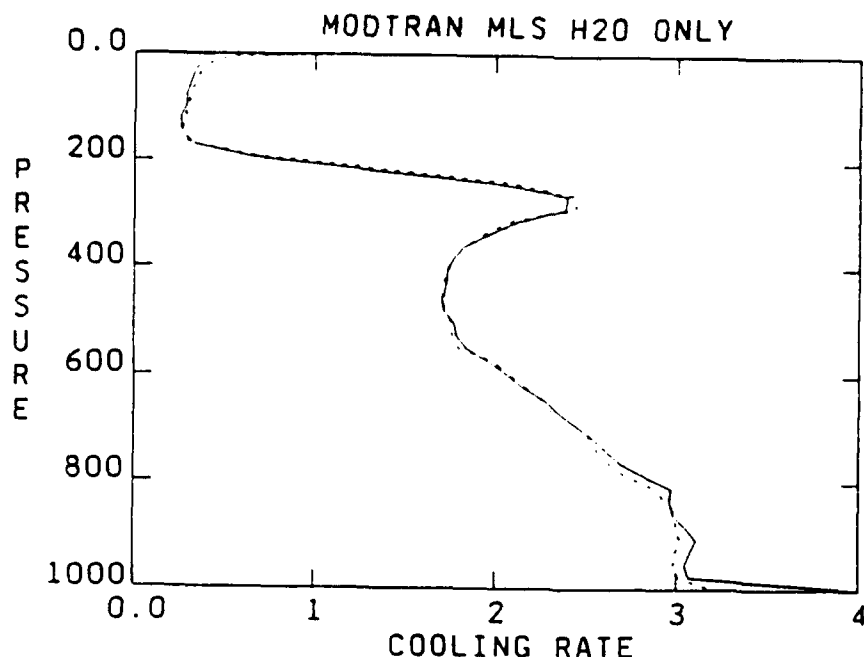


Figure 1: Comparison of spectrally integrated cooling rates: ICRCCM mid-latitude summer atmosphere, water vapor only. Solid line represents MODTRAN2 results and dashed line represents FASCODE results.

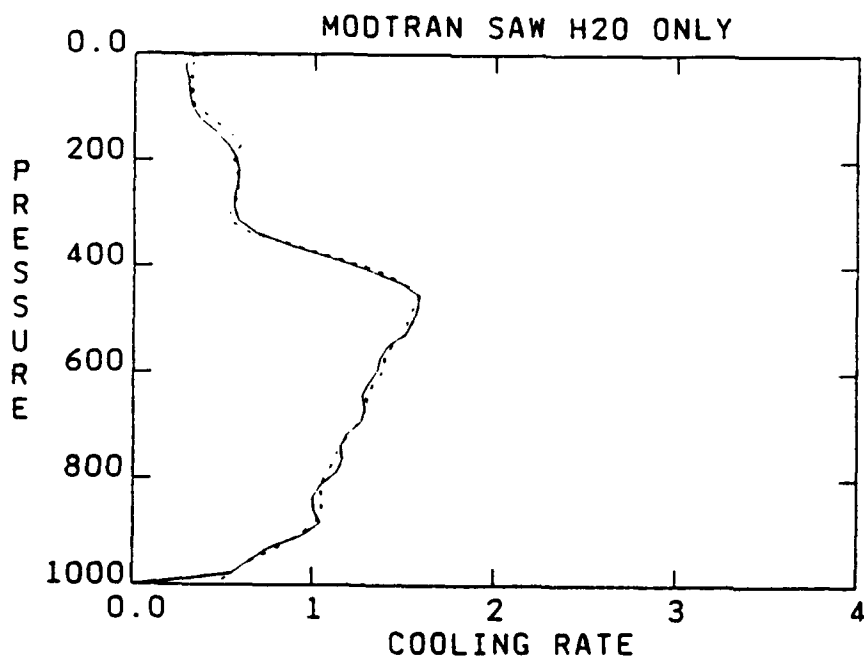


Figure 2: Comparison of spectrally integrated cooling rates: ICRCCM sub-arctic winter atmosphere, water vapor only. Solid line represents MODTRAN2 results and dashed line represents FASCODE results.

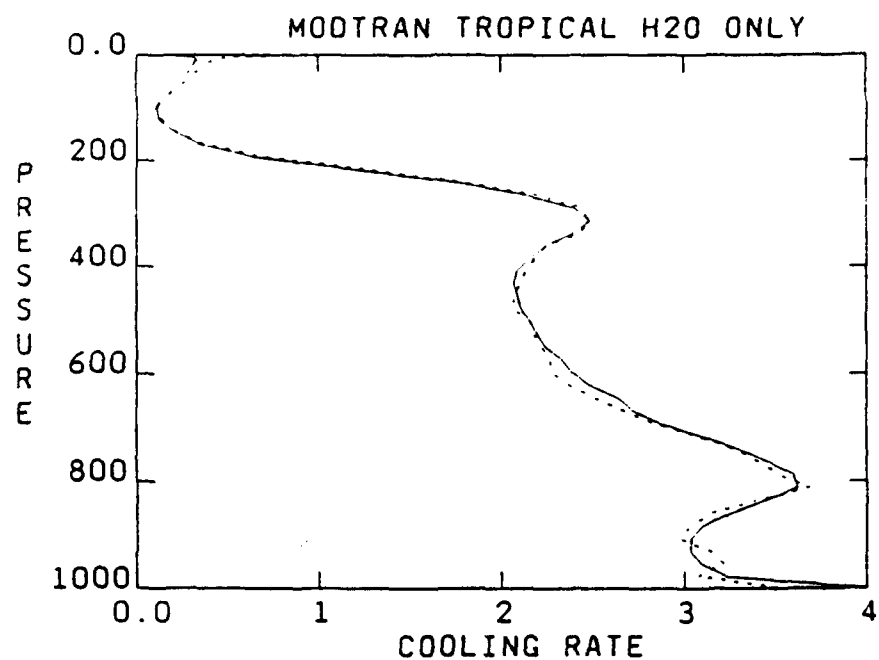
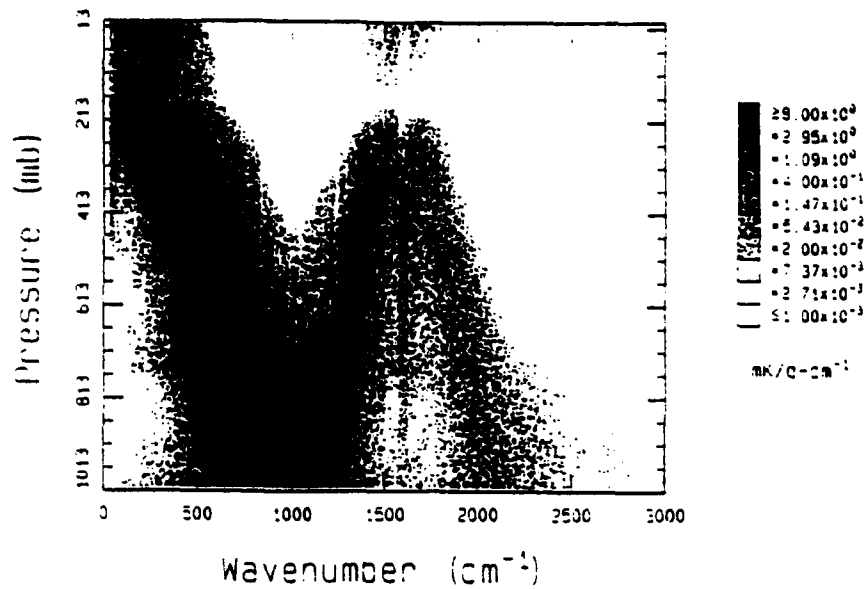


Figure 3: Comparison of spectrally integrated cooling rates: ICRCCM tropical atmosphere, water vapor only. Solid line represents MODTRAN2 results and dashed line represents FASCODE results.

# MODTRAN ICRCCM MLS H<sub>2</sub>O Only



# MODTRAN ICRCCM MLS H<sub>2</sub>O Only

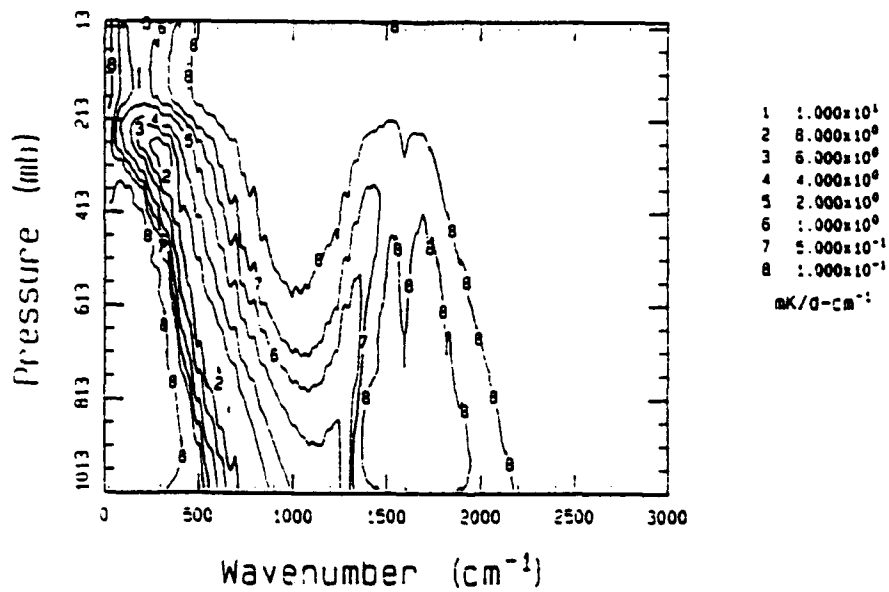


Figure 4: Spectral cooling rate profile for the ICRCCM mid-latitude summer atmosphere with water vapor only.

## REFERENCES

1. L. W. Abreu, P. Acharya, G. P. Anderson, A. Berk, J. H. Chetwynd, M. L. Hoke, F. X. Kneizys, D. C. Robertson, E. P. Shettle, J. M. Theriault, MODTRAN2 Suitability for Remote Sensing, *Proceedings of the Society of Photo-Optical Instrumentation Engineers*, Vol. 1968, 514-525, 1993.
2. A. Berk, L. S. Bernstein and D. C. Robertson, MODTRAN: A Moderate Resolution Model for LOWTRAN, Spectral Sciences, Inc. Rpt. No. SSI-TR-124, (08 July 1987). Prepared for Air Force Geophysics Laboratory (AFGL-TR-87-0220) under Contract No. F19628-86-C-0079.
3. S. A. Clough, M. E. Iacono, J. L. Moncet, Line-by-Line Calculations of Atmospheric Fluxes and Cooling Rates: Application to Water Vapor, *J. Geophysical Research*, 97, 15761-15785, 1992.
4. S. A. Clough, W. O. Gallery, F. X. Kneizys, L. S. Rothman, Atmospheric spectral transmittance and radiance: FASCOD1B, *SPIE*, 277, 152-166, 1981.
5. Ellingson, R. G., and Y. Fouquart, The Intercomparison of Radiation Codes Used in Climate Models: Longwave Results, *J. Geophysical Research*, 96, 8929 - 8953, 1991.
6. W. L. Ridgway, Harshvardhan, A. Arking, Computation of Atmospheric Cooling Rates by Exact and Approximate Methods, *J. Geophysical Research*, 96, 8969 - 8984, 1991.

**GIS SIMULATION OF TARGET BACKGROUNDS  
FOR ACT/EOS USING LANDSAT TM AND DTED**

**Stephen A. Luker  
Graduate Assistant  
Department of Biological Sciences**

**The University of Alabama  
Box 870344  
Tuscaloosa, AL 35487-0344**

**Final Report for:  
Graduate Student Research Program  
Phillips Laboratory, Hanscom AFB**

**Sponsored by:  
Air Force Office of Scientific Research  
Bolling Air Force Base, Washington D.C.**

**August 1993**

GIS SIMULATION OF TARGET BACKGROUNDS  
FOR ACT/EOS USING LANDSAT TM AND DTED

Stephen A. Luker  
Graduate Assistant  
Department of Biological Sciences  
The University of Alabama

Abstract

A methodology for deriving satellite based input parameters to satisfy the target contrast background model (TCM2) was developed using digital image processing and geographic information systems (GIS). Visible and thermal bands of Landsat TM data and digital terrain elevation data (DTED) were used to characterize growing condition and, to some extent, initial surface soil moisture for a 1-dimensional foliage model using an energy balance solution for solving the temperature of the composite background (foliage and ground). The raster-based GIS, Geographic Resources Analysis Support System (GRASS), served as a platform for the 3-dimensional analysis of thermal and visible bands of Landsat TM draped over a terrain model generated from DTED data. The resulting imagery will provide useful input for the infrared electro-optical tactical decision aid (IR EOTDA) models.

## Introduction

An Electro-Optical Tactical Decision Aid (EOTDA) is a software model that predicts the performance of air-to-ground weapon systems and direct view optics based on environmental and tactical information (Freni et al., 1978). Performance is expressed primarily in terms of maximum detection or lock-on range and results are displayed in alphanumeric and graphic formats. The EOTDA supports systems in three regions of the spectrum: infrared (8 - 12) ; visible (0.4 - 0.9  $\mu m$ ) ; and laser (1.06  $\mu m$ ).

Imaging IR sensors actually respond to the difference in radiance between target and background across the wavelength band. However, it is customary to specify sensor performances in terms of a temperature difference. This practice is made possible by converting the physical (actual) temperature of target and background to an equivalent blackbody temperature (EBBT). This conversion involves the IR inband emissivity of the body, which is taken to be constant across the 8-12  $\mu m$  range (Touart et al., 1993).

The thermal model used to compute target temperatures, TCM2 (Target Contrast Model #2), treats the target as a distinctive 3-dimensional network of nodes that exchange heat with one another and with their environment. There are many physical interactions that produce the thermal scene containing the target and its background. The following are the principal phenomena incorporated by the TCM2. Solar load is distributed by its components: direct, diffuse, and reflected. This allows the proper directionality, shadowing, and optical properties to be taken into account. Two spectral bands are treated. The total band represents the radiative contribution to heating. The sensor band treats reflected components in radiometric target and background temperatures. Mass and heat transfer effects of evaporation, condensation, sublimation, and precipitation are directly accommodated. Convective coupling to ambient air is based on the vector sum of wind speed and direction and the vehicle speed and bearing. All emissions and multiple reflections interact correctly in both the total band and the sensor band. The thermal analyzer provides conduction paths as well as internal heat sources. Fluid flow heating and cooling effects are incorporated in a mass-flow nodal/conductor network. Provisions are made for conductances, capacitances, and heating rates that depend on time or temperature.

The performance of electro-optical sensors are highly dependent on weather conditions and other environmental factors. For passive IR imaging sensors this sensitivity is derived from two sources. The inherent (zero-range) strength of target signature is strongly influenced by environmental parameters, and the degradation

of this signature as it propagates from target to sensor is determined by weather conditions. The TCM2 incorporates a model that attempts to characterize the affects of the existing background conditions on the IR signatures. The latest version of the TCM2 consists of six first principles background: vegetation, soil, snow, water, concrete, and asphalt. This study primarily focussed on the use of digital satellite imagery, digital elevation data, and GIS to provide necessary TCM2 input information describing these various backgrounds.

### Background Models

The background can be modeled with first principle techniques in three dimensions just as the targets are modeled. Two types of one dimensional background models are available in TCM2: empirical and first principle. When the background is based on one of these choices, a single background temperature representing the average background surface temperature is obtained. This temperature is obtained prior to solving the target temperature distribution so that it can influence the target temperatures. TCM2 will model several (up to 20) background textures simultaneously thus providing background temperatures and target-background contrasts for multiple comparisons. The remainder of this paper is only concerned with the first principles approach. Currently there are six background models within EOTDA. They include: vegetation, soils, water, snow, concrete, asphalt, and concrete. This paper is mainly concerned with the utilities of digital satellite imagery and GIS as a method for providing useful input parameters to these models. Consequently, the first principles relating to model development will not be addressed at depth.

The vegetation and soil models are both energy balance solutions derived from the Deardorff Model (Deardorff, 1989). The vegetation model is an efficient heat and mass transfer solution in which the foliage is parameterized by a single layer and the ground soil is divided into multiple (13) layers. The physical processes include convection with the air, foliage, and ground; radiation between foliage/sky, foliage/ground, and ground/sky; conduction through the soil layers; solar loading of foliage and ground; evapotranspiration within the foliage; evaporation within the ground; and precipitation to the foliage and ground. The soil model, also an efficient heat and mass transfer solution, solves for surface temperature for 7 different varieties of soil type under moisture conditions ranging from completely dry to saturated. The processes include convection between the air



and ground; radiation between the ground and sky; conduction through the soil layers; solar loading; evaporation/condensation; and precipitation.

The water model is an energy balance solution for solving the surface temperature as well as the temperature of internal layers for a lake/reservoir. The model is derived from the Kirk and Crain models (Kirk, 1988). It has an efficient one dimensional heat and mass transfer solution consisting of multiple layers with varying properties dependent on solar attenuation and atmospheric turbidity. The processes include convection between the air and surface; radiation between the surface and sky; conduction and convection through the water layers; solar loading; evaporation/condensation; and precipitation. The heat exchange between the surface layer and atmosphere includes radiant solar energy absorption; long-wave radiation onto the surface from the atmosphere; blackbody radiation emission; evaporative heat loss; sensible heat loss; eddy and molecular diffusivity; and precipitation. The heat exchange between internal layers includes radiant solar energy absorption; eddy diffusivity; and molecular diffusivity.

### Methodology

A Landsat thematic mapper (TM) scene dated September 16, 1987 was obtained for Hanscom Air Force Base located in eastern Massachusetts. The GIS Geographic Resources Analysis Support System (GRASS) was used to create a composite of visible TM bands 1 (0.45-0.52 $\mu m$ ), 2 (0.52-0.60 $\mu m$ ), and 3 (0.63-0.69 $\mu m$ ) as well as an image of the thermal channel, band 6 (10.4-12.5 $\mu m$ ). In addition, digital elevation data were extracted for the Hanscom area from digital terrain elevation data (DTED) available on CD-ROM. Linear contrast stretches were performed on both the visible composite image and the thermal image. Gray-scale images were then produced representing land cover contrasts in the visible and apparent heat contrasts in the thermal image. The DTED data were projected onto a Universal Transverse Mercator (UTM) coordinate system using the Clarke 1866 spheroid. Both the visible composite and thermal images were then "draped" over the DTED data and displayed in three dimensions using a 3-D visual analysis routine in GRASS.

In addition, the DTED data were used to generate slope and aspect models for the Hanscom site. These were accomplished in GRASS using a routine that calculates the slope or steepness of the terrain in degrees or percent and the aspect or azimuth direction the slope is facing.

## Results

Figure 1 illustrates the gray-scaled visible composite image representing TM bands 1, 2, and 3. The spatial resolution of these data are 30 meters. Although no formal classification was performed in this project, the darkest areas are water bodies, the brightest areas are urban (concrete, roads, parking lots, buildings), and the gray areas represent vegetation in the form of trees, shrubs, and grasses. The thermal image, with a spatial resolution of 100 meters (Figure 2), depicts apparent temperatures of the land surface. In this scene white represents "hot". Since this scene was taken during the daytime, urban areas are expected to be much warmer than the surrounding vegetation and water. Digital elevation for eastern Massachusetts is illustrated in Figure 3. Although this area is relatively flat, the white regions represent locations of higher altitude. Due to the homogeneous terrain of eastern Massachusetts, the aspect map did not prove to be visually suited for output. Therefore an aspect map for Boulder, Colorado, was created instead (Figure 4). The aspect map was generated only to demonstrate the utilities of a GIS for creating aspect and slope maps.

A 3-D image of the terrain (Figure 5) was then constructed, and the visible composite image (Figure 6) and thermal image (Figure 7) were then draped over the 3-D terrain. The flatness of the area prevents seeing any large topographic changes, however, the results are roughly true to scale and would probably represent a similar view coming from the thermal sensor's video monitor inside the pilot's cockpit.

## Discussion and Conclusions

Digital satellite data is often used for characterizing land use/land cover (Campbell, 1987; Jensen, 1986). Of the 3 variables within the vegetation model (growing state, coverage, and soil moisture), satellite data can be used, directly or indirectly, to determine each parameter. As described by the model, growing state can vary from dormant to fully growing. Temporal satellite data covering the same region can be used to determine the growth in biomass over time (Samson, 1993). The coverage factor can be directly estimated from the image using various measuring techniques (e.g. planimetry) common to most GIS systems or it can be obtained via leaf area indices (LEI). An LEI is the measure of total one-sided leaf area of the foliage relative to the ground area of the same

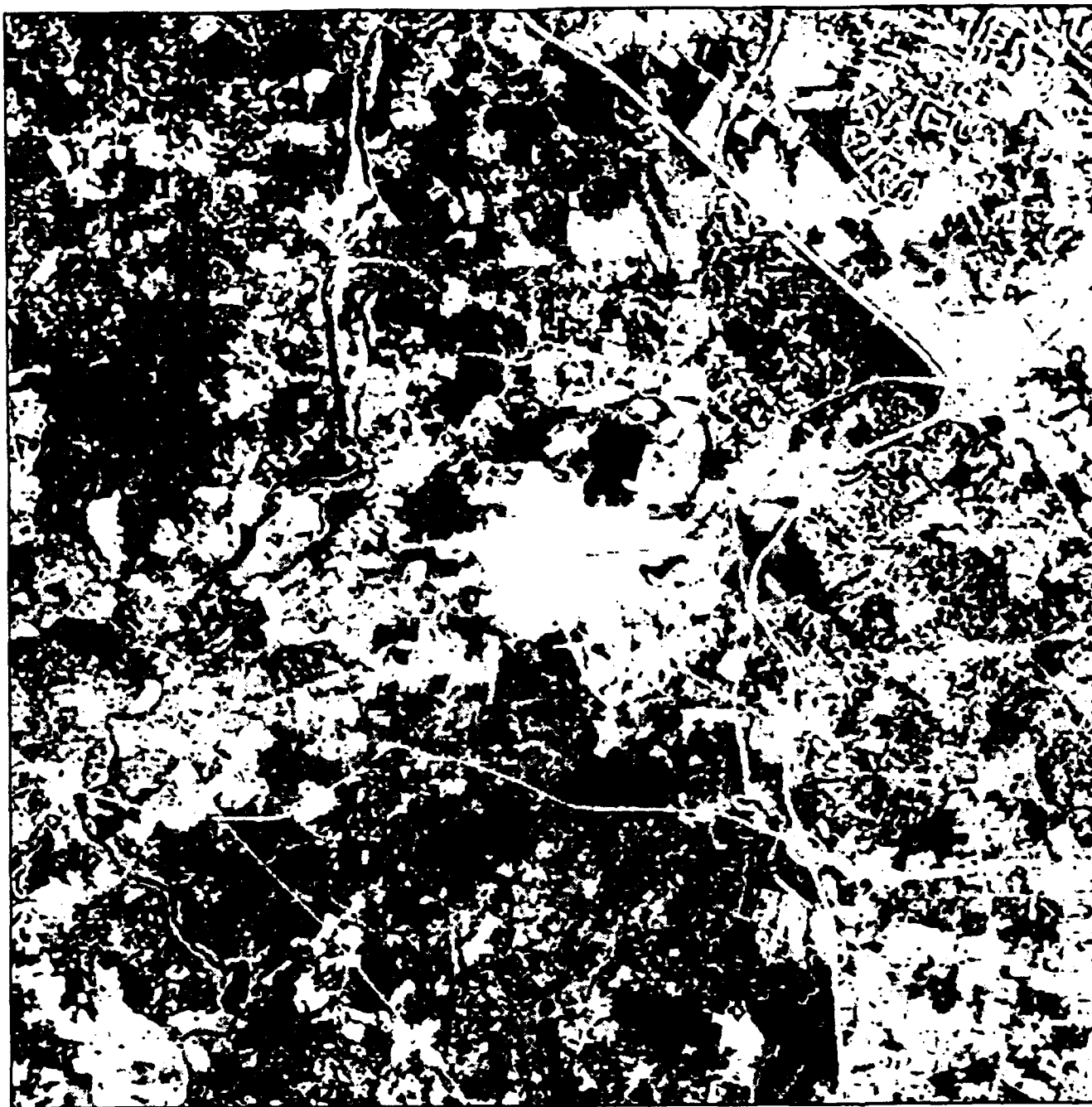


Figure 1. Landsat TM scene of Hanscom AFB area (bands 1, 2, and 3).

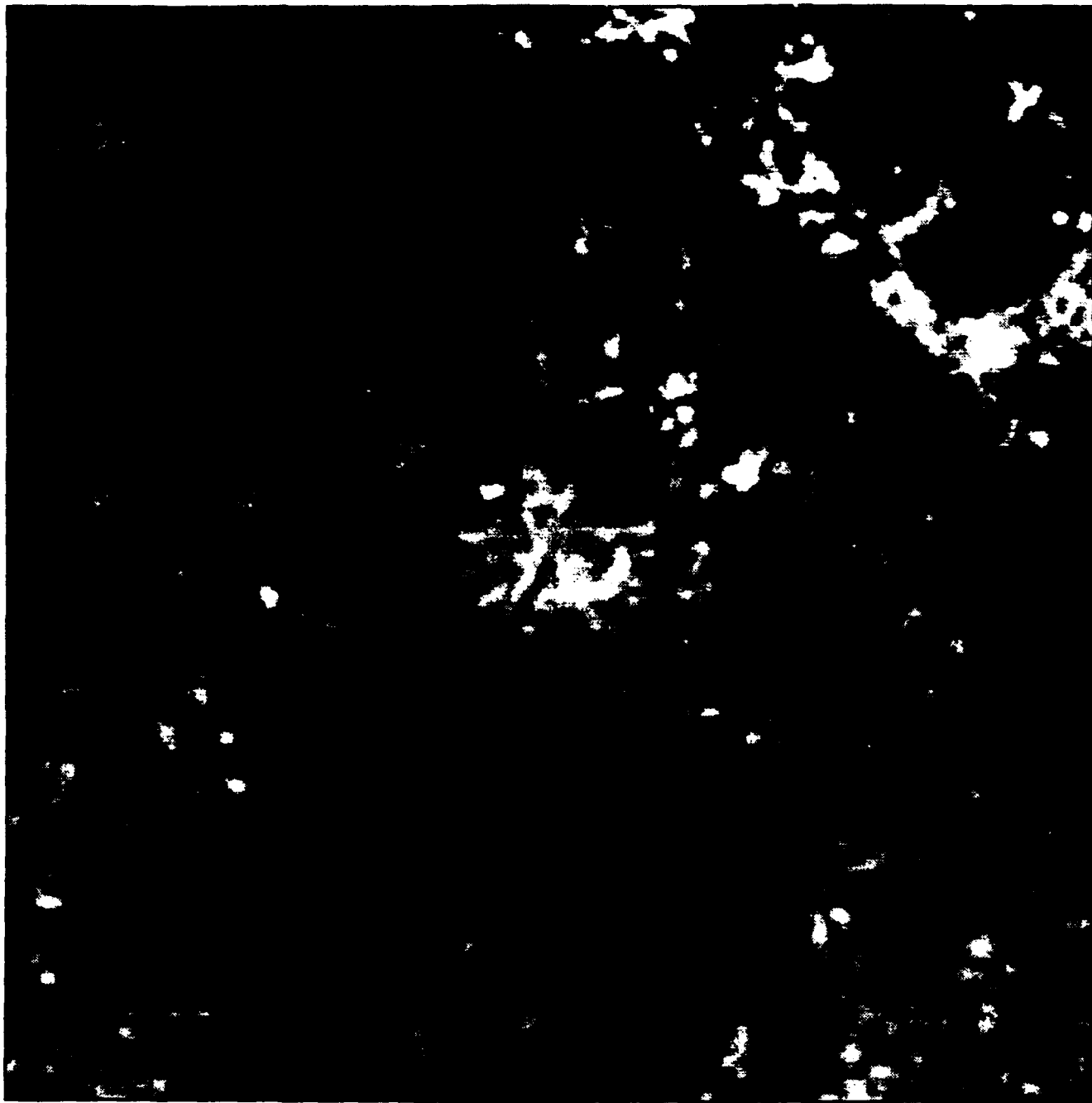


Figure 2. Landsat TM thermal image of Hanscom AFB area (band 6).

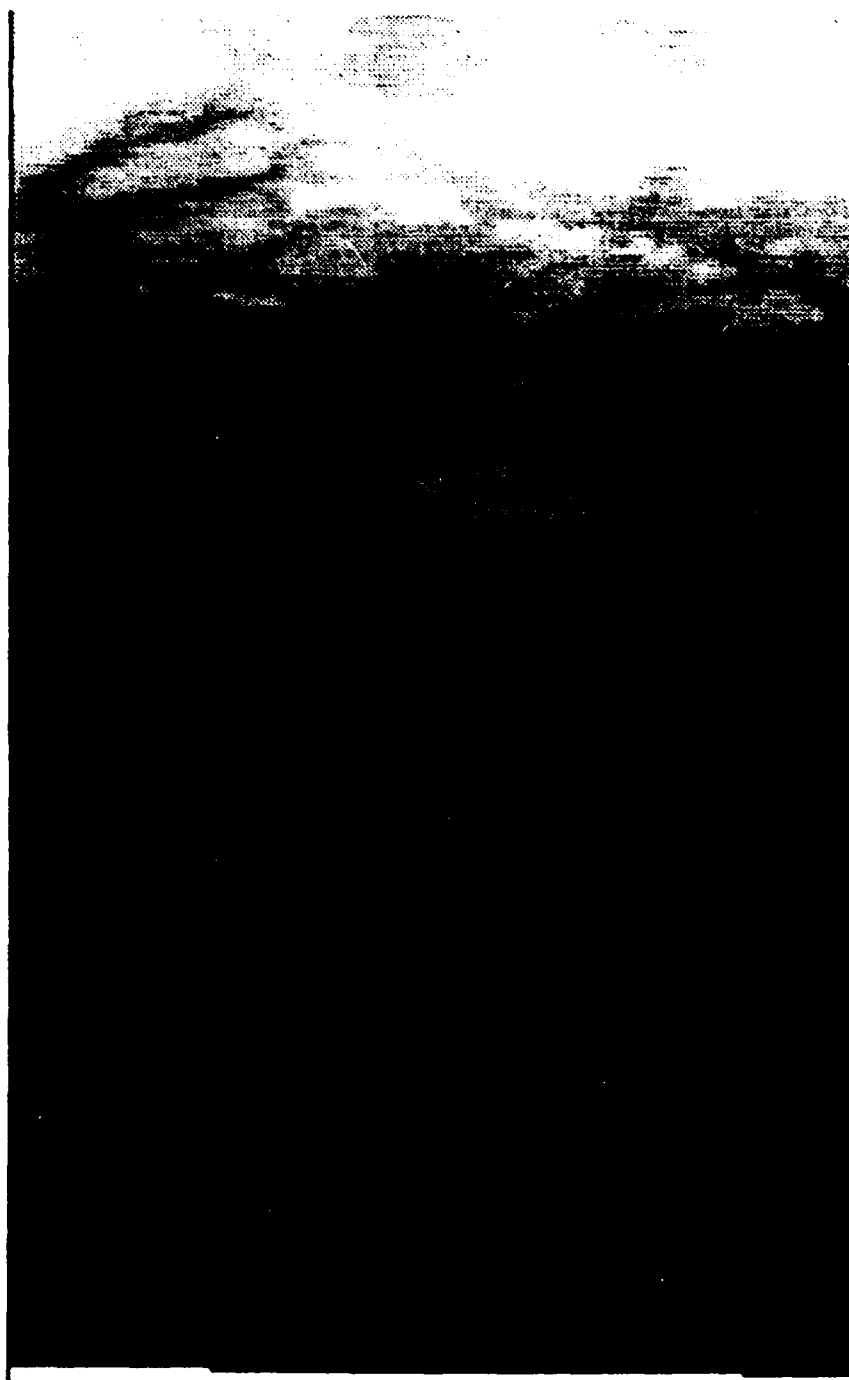


Figure 3. Digital Terrain Elevation Data (DTED) for eastern Massachusetts.



Figure 4. Aspect map generated from DTED data for Boulder, Co.

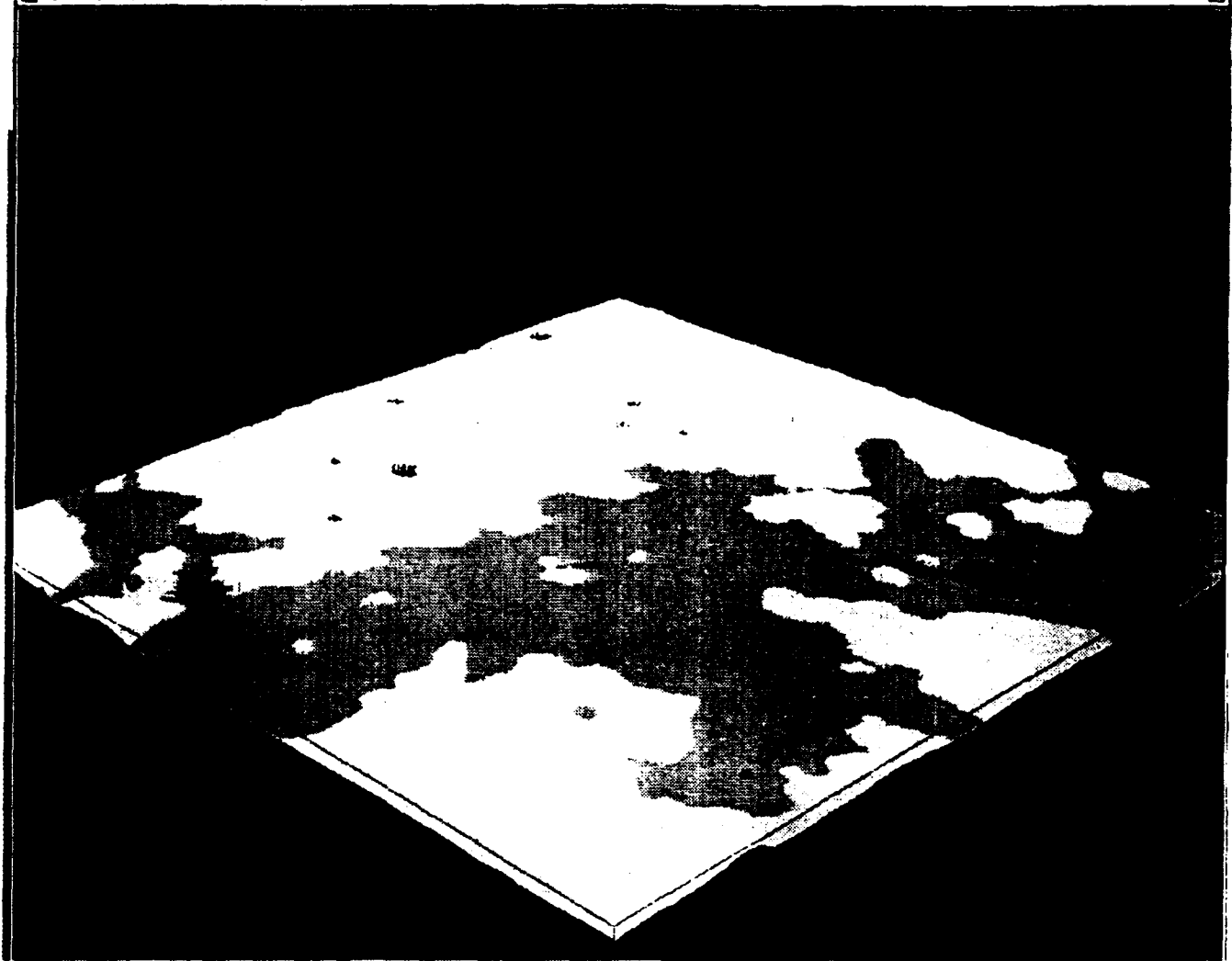


Figure 5. 3-D image using DTED data for Hanscom AFB area.

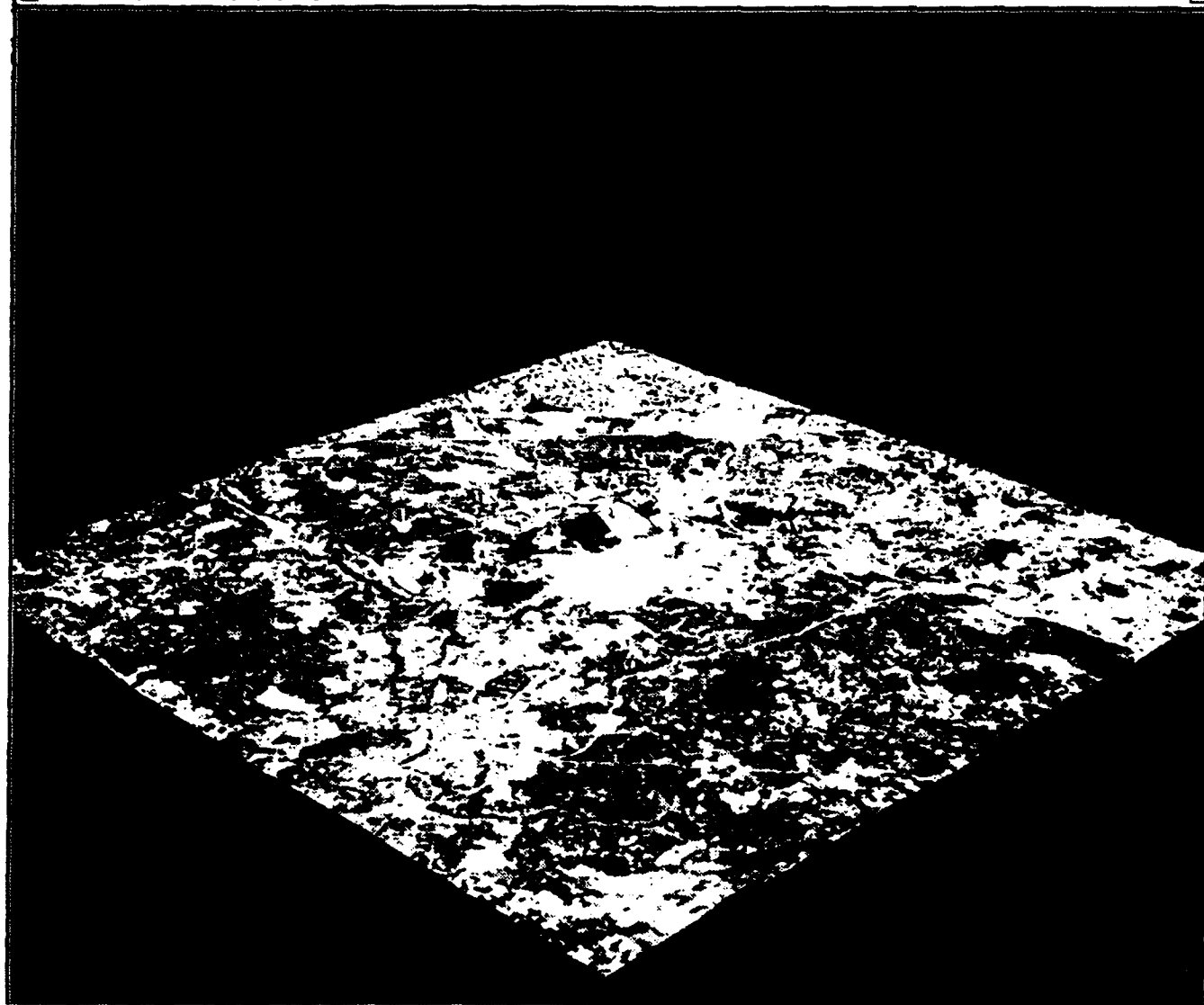


Figure 6. Landsat bands 1, 2, and 3 draped over 3-D terrain data for Hanscom AFB area.



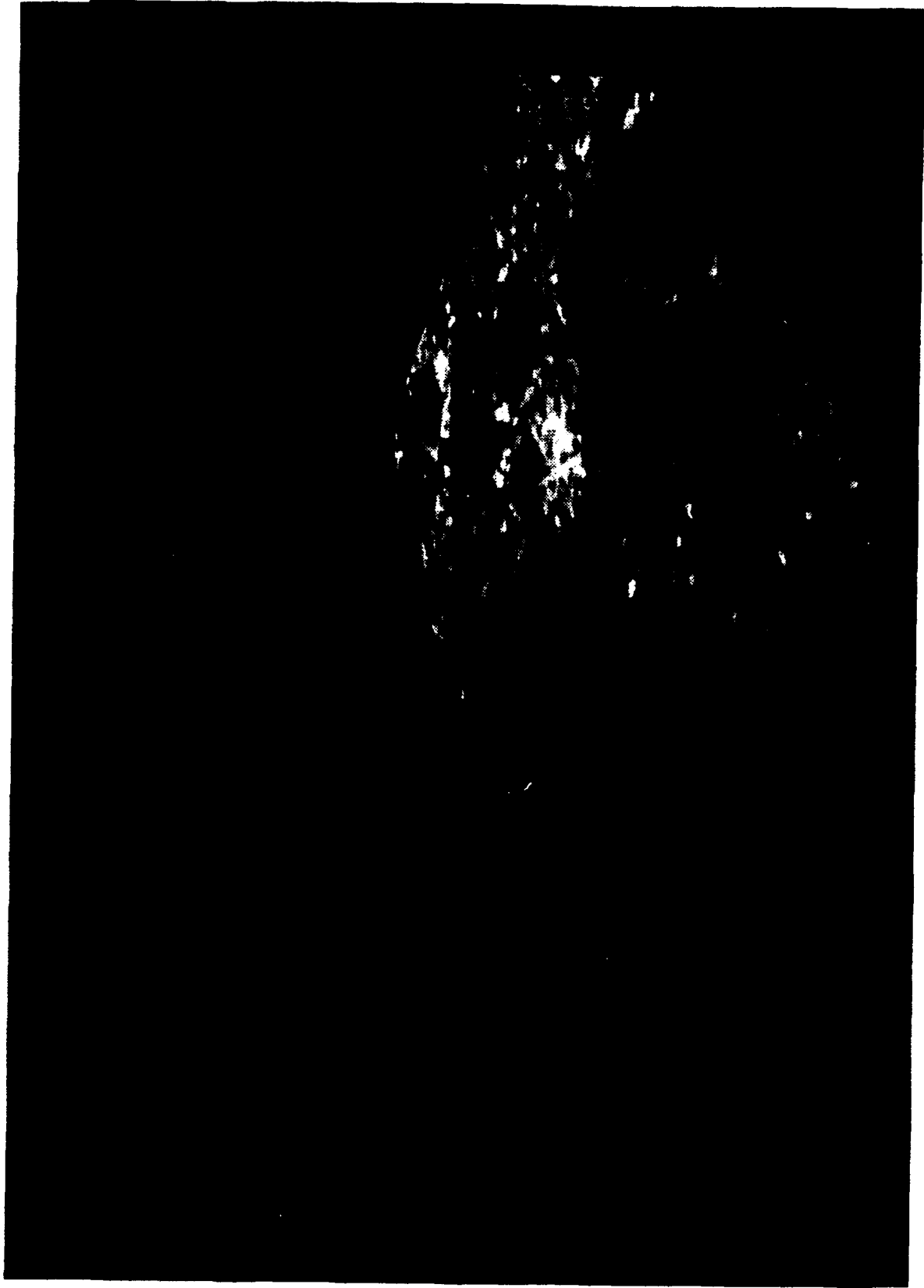


Figure 7. Landsat thermal image (band 6) draped over DTED data for Hanscom AFB.

region. Lookup tables exist depicting LEIs for different species of vegetation. Soil moisture inputs are explained in the following under the soil model.

The soil model requires soil type, surface moisture, and depth moisture as inputs. While soil type and surface moisture can be obtained, it is extremely difficult to obtain valid measures of soil moisture at depth because of the "masking" affect caused by the upper soil layers and any vegetation present. There are basically two methods of obtaining soil type with satellite data. First, the direct sensing of the soil properties is the most accurate measure of soil type, however, this can only be performed when bare soils are present. There can not be any vegetation obstructing the sensors measurements of the soil properties. As this condition is not often the case, the second method involves the use of proxies or substitutes such as topography, vegetation, and drainage patterns that serve as clues for the interpretation of soils. Surface soil moisture can be directly measured with longer wavelengths that penetrate through the vegetation and into the surface soils.

Spectral qualities of water bodies are determined by the interaction of several factors, including the radiation incident to the water surface, optical properties of the water, roughness of the surface, angles of observation and illumination, and in some instances, reflection of light from the bottom. The water model requires a depth as well as a clarity (clear or turbid) input parameter. Digital satellite data can be used to determine water depths of clear and in some cases turbid water bodies (Campbell, 1987). Multispectral bathymetry is based on the fact that the depth of penetration of solar energy is wavelength-dependent. If several spectral channels are available, then differences in brightness within the channels can be used to estimate water depth. Clarity can easily be determined visually as suspended particles reflect nearly all of the incident radiation. Determining depths in turbid water can prove difficult (although it has been done successfully in some regions). Fortunately, the water model only requires water depth when clear water exists. If attenuation coefficients can be estimated and certain assumptions regarding bottom reflectance can be made, it is feasible to make more refined estimates of water depth.

The images generated in this paper help to visualize in three dimensions natural terrain and land characterizations. It is thought that these images will enable EOTDA model programmers and analysts to better understand the actual views pilots may see through their video monitors inside the cockpit. With this additional

information at use, programmers can begin to modify existing models to increase the accuracy and precision of the TCMs and the overall EOTDA.

It is obvious that digital satellite data along with GIS can be utilized to provide necessary data inputs into the TCM2 of the EOTDA. In many, if not most, cases the availability of some of these required inputs can only be obtained remotely. Therefore, thematic information derived either directly or indirectly from satellites are essential to the success of the EOTDA. The TCM2 is extremely dependent on environmental factors which vary spatially as well as temporally. However, the use of satellite-based data can begin to capture and quantify changes in vegetative conditions, soil properties, land uses, and water qualities.

### Literature Cited

- Campbell, J.B. 1987. *Introduction to Remote Sensing*. New York: The Guilford Press, 404 pp.
- Deardorff, J.W. 1978. Efficient prediction of ground surface temperature and moisture, with inclusion of a layer of vegetation. *American Geophysical Union*, vol. 83, no. C4, pp. 1889-1903.
- Freni, J.M.L., M.J. Gouveia, D.A. DeBenedictis, I.M. Halberstam, D.J. Hamann, P.F. Hilton, D.B. Hodges, D.M. Hoppes, M.J. Oberlatz, M.S. Odle, C.N. Touart, and S-L Tung. 1993. Electro-optical tactical decision aid (EODTA) user's manual, version 3, PL-TR-93-2002. Scientific Report No. 48, vol. 1, Hughes STX Corporation, Lexington, MA.
- Jensen, J.R. 1986. *Introductory Digital Image Processing*. Englewood Cliffs, New Jersey: Prentice-Hall, 254 pp.
- Kirk, J. T. 1988. Solar heating of water bodies as influenced by their inherent optical properties. *Journal of Geophysical Research*, vol. 93, no. D9, pp. 10897-10908.
- Sam, S. A. 1993. Two indices to characterize temporal patterns in the spectral response of vegetation. *Photogrammetric Engineering & Remote Sensing*, vol. 59, no. 4, pp. 511-517.
- Touart, C.N. 1993. IR visibility, PL-TR-92-2170. Scientific Report No. 46, Hughes STX Corporation, Lexington, MA.

# ION-MOLECULE REACTIONS AT HIGH TEMPERATURES

Melani Menendez-Barreto  
Graduate Student  
Department of Physics and Astronomy  
University of Oklahoma  
Norman, OK 73019

Jeffrey Friedman  
Assistant Professor  
Department of Physics  
University of Puerto Rico at Mayaguez  
Mayaguez, P.R. 00680

Final Report for:  
Summer Research Program  
Phillips Laboratory, Geophysics Directorate

Sponsored by:  
Air Force Office of Scientific Research  
Bolling Air Force Base, Washington, DC

August 1993

# ION-MOLECULE REACTIONS AT HIGH TEMPERATURES

Melani Menendez -Barreto  
Graduate Student  
Department of Physics and Astronomy  
University of Oklahoma  
Norman, OK 73019

Jeffrey Friedman  
Assistant Professor  
Department of Physics  
University of Puerto Rico at Mayaguez  
Mayaguez, P.R. 00680

## Abstract

A High Temperature Flowing Afterglow was utilized in the study of ion-molecule reactions. Reaction rate coefficients were measured for the following reactions in the temperature range 300-1300 K:  $O^- + H_2$ ,  $D_2$ , and  $CH_4$ ;  $O_2^+ + CH_4$ .

The system performance was evaluated in terms of changes needed to effect a more durable and reliable instrument. The effects of the high temperatures and cycling to room temperature dictate further design modifications that will be the subject of another paper (in preparation)<sup>1</sup>.

# ION-MOLECULE REACTIONS AT HIGH TEMPERATURES

Jeffrey F. Friedman, and Melani Menendez-Barreto

## INTRODUCTION

Information on ion-molecule reactions is desirable for both scientific and practical reasons.<sup>2</sup> At high temperatures rotational and vibrational states are excited in both the ions and target molecule, making it possible for new reaction channels to open up. The controversial topic of "entropy-driven" reactions could more readily be investigated at high temperatures, as emphasized by Meot-Ner.<sup>3</sup>

Because of the need to understand and influence plasmas which occur naturally (e.g., auroras and the ionosphere) or man-made (e.g., around transonic aircraft, re-entry vehicles, or engine exhausts), the U.S. Air Force sponsors a great deal of research on low-energy interactions of electrons, ions, atoms, and molecules.

Laboratory studies of ion-molecule reactions are generally carried out within 200-300 Celsius degrees of room temperature. This represents a difficulty to the Air Force given many of the plasmas of their interest are at much higher temperatures (say, 1000-2000 K). Modelers are forced to make educated guesses as to the high temperature behavior of reaction rates and products.

Drift tube experiments have revealed the translational energy dependence of the reaction rate coefficients for some reactions, up to energies corresponding to thousands of degrees. However translational energy data are not directly applicable to high temperature plasmas because the target molecules are not at equivalently high

temperatures, and the projectile ions may or may not be excited by successive collisions with a buffer gas.

Only a few reaction rate coefficients had been measured as a function of temperature to prior our work on this high temperature flowing afterglow apparatus.<sup>4</sup> Those measurements typically extend into the 500-600 K range, limited by the materials and heaters used in the apparatus. There had only been one experiment that went beyond this conventional temperature limit before our last summer's experiments on the HTFA. In 1974, a group at NOAA modified the heaters in a flowing afterglow apparatus and measured reaction rate coefficients for several positive-ion reactions involving atmospheric species, up to 900 K.<sup>5</sup> Our experiments last year led to reaction rate coefficient measurements for a variety of both positive and negative reactions in the 300-1200 K range.

We have new measurements for some other ion-molecule systems of known importance in the ionospheric composition and have made a modest temperature advance to 1300K. We have studied  $O^-$  on  $H_2$ ,  $D_2$ , and  $CH_4$ , as well as  $O_2^+$  on  $CH_4$ .

### EXPERIMENTAL METHOD

We used a newly constructed and now extensively modified flowing afterglow apparatus at Hanscom AFB that was specially designed for high temperatures. The flowing afterglow technique was developed in the 1960s for the study of ion-molecule reactions by a group at NOAA laboratories (then part of the National Bureau of Standards). The flowing afterglow method is now a well-established technique used in 20-30 laboratories around the world.

The experimental method involves interacting a swarm of ions with a known number density ( $n$ ) of reactant molecules for a specific time ( $t$ ). Exponential attenuation of the primary ion signal ( $I$ , which is proportional to the primary ion density) will occur



if reactions take place which generate other species:

$$I = I_0 \exp(-knt),$$

where the signal at  $t=0$  is  $I_0$ . The ion-molecule reaction rate coefficient ( $k$ ) is given by:

$$k = -n^{-1} t^{-1} \ln(I/I_0).$$

The experiment was carried out in a flowing buffer gas to effectively transform the time measurement into one of distance.

The measurement procedure involved recording the primary ion count as the neutral reactant concentration was stepped from zero to an amount that affected no less than a factor of two attenuation in the primary ion signal. The (negative) logarithmic slope of the primary ion count rate versus reactant concentration is equal to  $-kt$ . The reaction time was readily determined from a measurement of the ion velocity and the known reaction distance.

The ionic products of the reaction under study were identified by the mass spectra. The lack of ionic products indicates electron attachment. Neutral products are now observable because of the addition of a residual gas analyzer (an ionizer in the lens region). We hope to make extensive use of this new feature in the future.

## **APPARATUS and PROCEDURES**

The ion swarm is created in the upstream end of the flow tube by electron impact on a suitable source gas ( $N_2O$  for  $O^-$  and  $O_2$  or  $CO_2$  for  $O_2^+$ ), and in the case of  $O_2^+$  from  $CO_2$  a rapid secondary reaction that must be essentially complete before the neutral reactant gases are added approximately 40 cm. downstream. The ions and neutrals can interact in a 63 cm. reaction region before sampling through a pinhole aperture to a mass spectrometer and detector. The time in the reaction region is determined by the gas flow. The ion velocity can be determined directly by applying an

electrical pulse to the internal thermocouples (each in turn) and timing the arrival of the ion attenuation minimum at the detector with a multichannel analyzer. The ion velocity is just the distance between the thermocouples divided by the arrival time difference. Velocities were generally in the range of 7000 to 35000 cm/s. Comparing this velocity with the neutral gas velocity determined by the temperature, pressure, and flow rate yields an almost constant ratio of  $V_{ion} / V_{neutrals}$  in the range of 1.6 to 1.9. The ratio has some dependence on the temperature and the pressure. The flows of the reactant and source gases can generally be ignored for this calculation compared to the He buffer, but this is not always the case as for slow rates when the reactant concentration could be a few percent. Occasionally high flows of source gas and Ar (to remove He metastables created in the electron beam) were also used. The total correction could run as high as 10% in some cases.

The concentration of neutral reactant in the flow tube was determined by comparing the flow rates of the He buffer gas and the reactant. Typical concentrations were .001 times the He buffer (except as noted above). The total gas pressure ranged from .3 to 1.2 torr.

The temperature of the flow tube is determined by averaging the readings from two thermocouples spaced about 30 cm. apart and roughly centered in the reaction region. Above ambient temperatures were achieved by 7 high temperature commercial heating tapes in four heating zones covering the flow tube from ion source to sampling port. For more information on special modifications made to the flow tube to allow operation at high temperatures see Menendez-Barreto, Friedman, and Miller<sup>6</sup> (and 1).

As a result of the heating-cooling cycle cracks developed at the downstream end of the flow tube where it is welded to the thin end flange. At first the resultant leaks could be sealed with conventional leak sealants, and generally disappeared at high temperature because of thermal expansion of the flow tube. This solution was deemed

expedient because a more permanent solution would require the removal of the flow tube, and the crystallized insulation on the heating tapes rendered this impracticable without the risk of destroying the tapes. However this proved only temporary as the cracks worsened. The use of the large vacuum box that surrounds the entire flow tube solved the problem, but is generally inconvenient, and we have undertaken a redesign of the end of the flow tube.<sup>1</sup>

In practice the lifetimes of the channel multipliers are very short at these elevated temperatures. It is not known if this is a purely temperature effect, which seems unlikely because of the low pressure in the detector region, or the result of highly reactive contaminants.

All of these issues will be addressed more fully in a paper in preparation for "Review of Scientific Instruments".<sup>1</sup>

## **RESULTS AND DISCUSSION**

In order to avoid thermal dissociation problems it was decided that only stable, but atmospherically important reactions would be studied. Figures 1-4 show reaction coefficient,  $k$ , versus temperature for the reactions  $O_2^+$  on  $CH_4$ ,  $O^-$  on  $CH_4$ ,  $O^-$  on  $H_2$  and  $O^-$  on  $D_2$  respectively. It is clearly obvious that the methane data are very different in nature than the hydrogen data. Presumably this reflects the opening of vibrational channels in methane at high temperature that are not yet available to the hydrogen and not seen in drift tube data at equivalent kinetic temperatures. The internal excitation of methane is the subject of a paper by Viggiano et al.<sup>7</sup> that will include these data and is currently in preparation. The minimum in the  $O_2^+$  curve is at the limit of the HTFA data, but is still consistent with them. You will notice a large amount of scatter in the molecular oxygen ion on methane plot, and this reflects the great difficulty in doing this experiment. However the trend of the data is clearly evident and represents results from

widely varying flow conditions in pressure and velocity as well as source and reactant concentrations and the presence or lack of Argon in the buffer. The data are also consistent with the VT-SIFT data with which they overlap (fig. 1). We are presently analyzing the ion-neutral chemistry in the flow tube and the possibility of new channels at elevated temperatures. There seems to be some, as yet unknown, mechanism for regenerating the molecular oxygen ion downstream, at least in the 600-800K range. The ratio of the ionic products is not constant in the data set as a function of temperature but it is not yet clear if this is a temperature effect, or the result of incomplete chemistry upstream of the reaction region because of different plasma velocities and/or changing reaction rates. The data are in fairly good agreement with the VT-SIFT data of Viggiano et al.<sup>7</sup> over the temperature range common to both. This is also true of the hydrogen data<sup>8</sup> and consistent with our 1992 data.<sup>6</sup> Comparison of the  $O^- + CH_4$  at high temperature with equivalent kinetic temperature SIFT drift tube data shows that they are not equivalent. Further collaboration is indicated to sort out the ion/neutral chemistry as a function of temperature, and the opening of new reaction channels.

## BIBLIOGRAPHY :

<sup>1</sup>Friedman, J.F., Miller, T.M., Menendez-Barreto, M., Paulson, J.F., Williamson, J., Dale, F., Viggiano, A.A., Morris, R.A., A Functioning 1300 K (1500K) Flowing Afterglow Apparatus, in preparation for *Review of Scientific Instruments*.

<sup>2</sup>*Gas Phase Ion Chemistry*, Vol. 2, Ed. Bowers, M.T. (Academic Press, New York, 1979)

<sup>3</sup>Moet-Ner, M., *J. Phys. Chem.* **95**, 6580, (1991).

<sup>4</sup>Ikezoe, Y., Matsuoka, S., Takebe, M., Viggiano, A.A., *Gas Phase Ion-Molecule Reaction Rate Constants Through 1986* (Maruzen Co. Ltd., Tokyo, 1987).

<sup>5</sup>Lindinger, W.L., Fehsenfeld, F.C., Schmeltekopf, A.L., and Ferguson, E.E., *J. Geophys. Res.* **79**, 4753 (1974).

<sup>6</sup>Menendez-Barreto, M., Friedman, J.F., Miller, T.M., *Final Reports AFOSR Summer Research Program*, Bolling AFB.

<sup>7</sup>Viggiano, A.A., Morris, R.A., Miller, T.M., Friedman, J.F., Menendez-Barreto, M., Paulson, J.F., Michels, H.H., and Montgomery Jr., J.A., in preparation for *J. Chem. Phys.*

<sup>8</sup>Viggiano, A.A., Morris, R.A., Deakyne, C.A., Dale, F., Paulson, J.F., *J. Phys. Chem.* **95**, 3644 (1991).

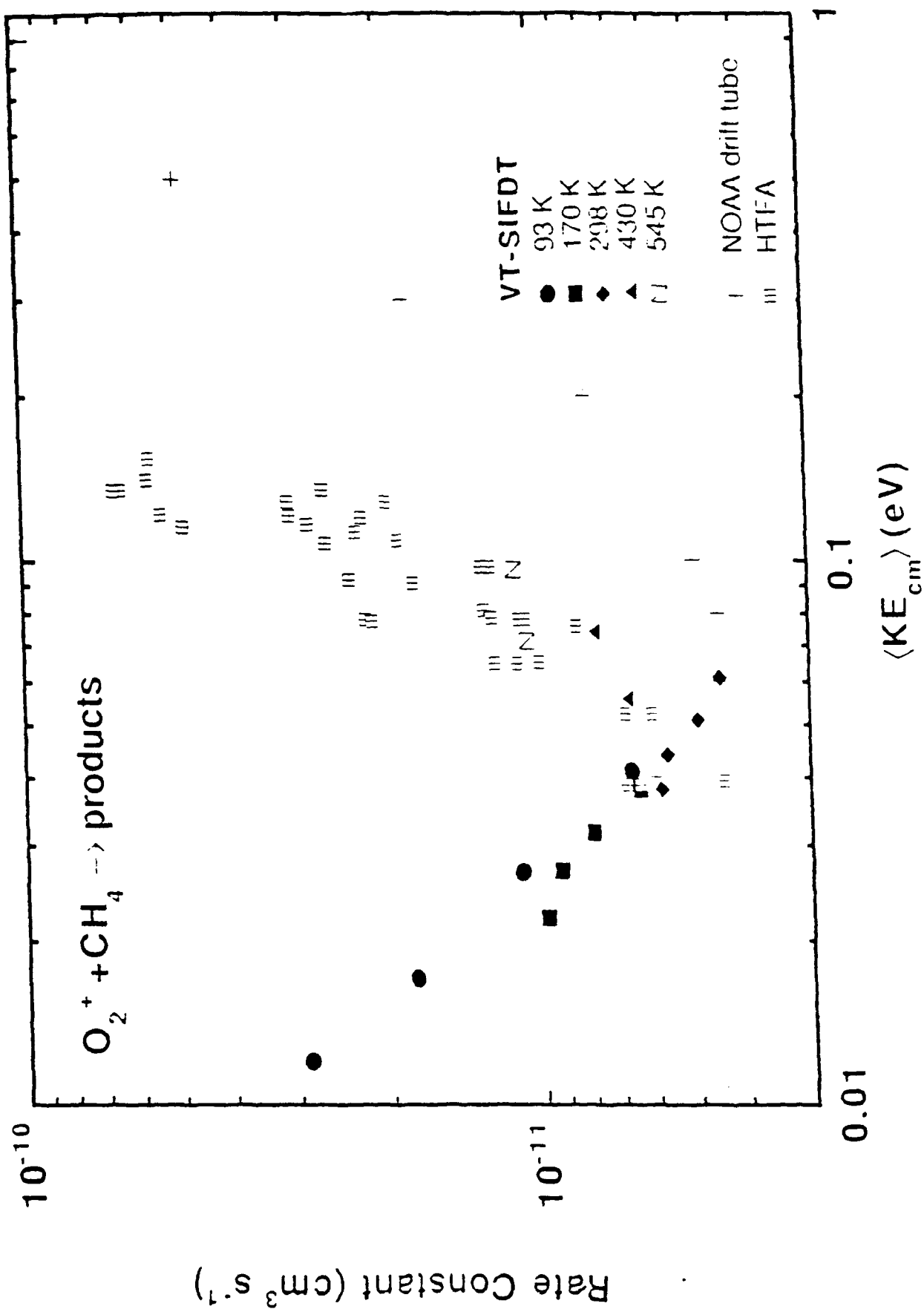


Figure 1

3-10



Rate Constant ( $\text{cm}^3 \text{s}^{-1}$ )

$10^{-10}$

100

1000

$10^4$

Kinetic Temperature (K)

- 93 K
- 173 K
- ◆ 298 K
- ▲ 568 K
- ||| k Hi T Machine

Figure 2

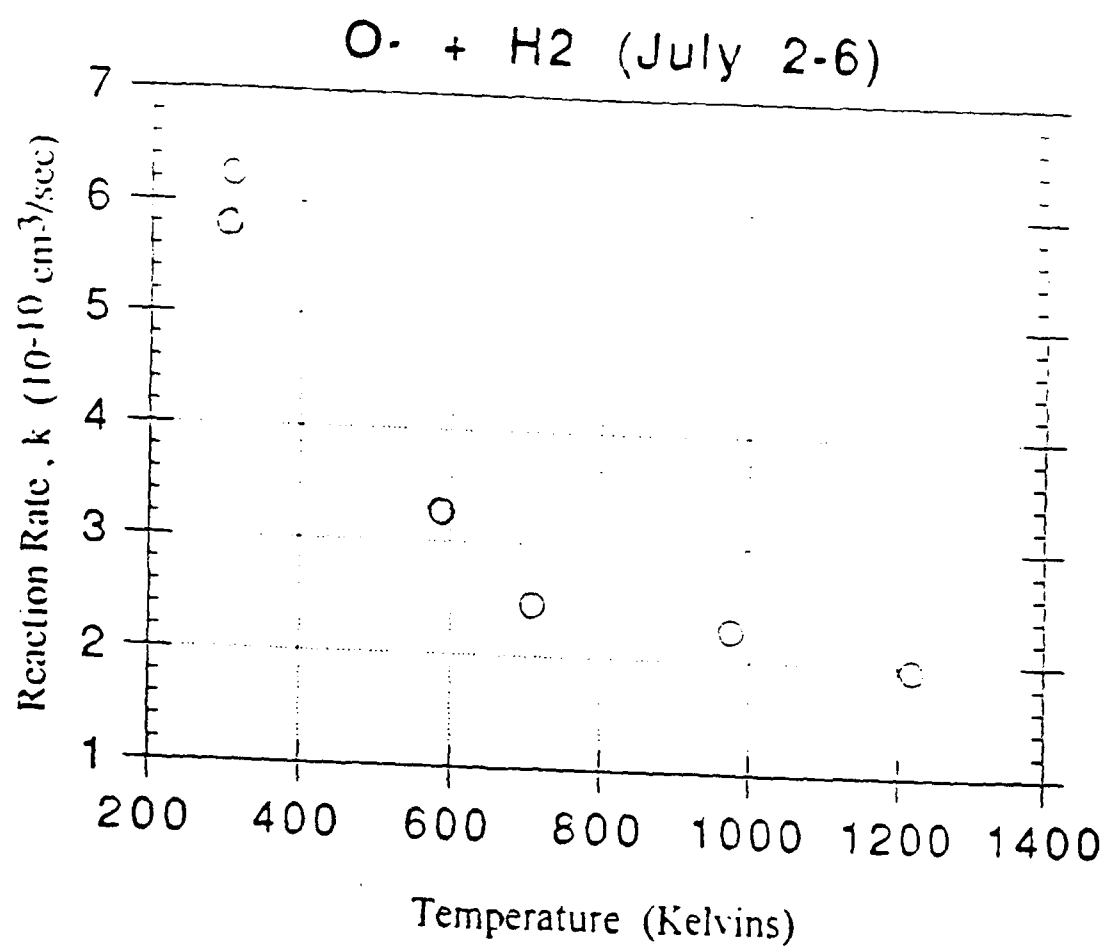


Figure 3



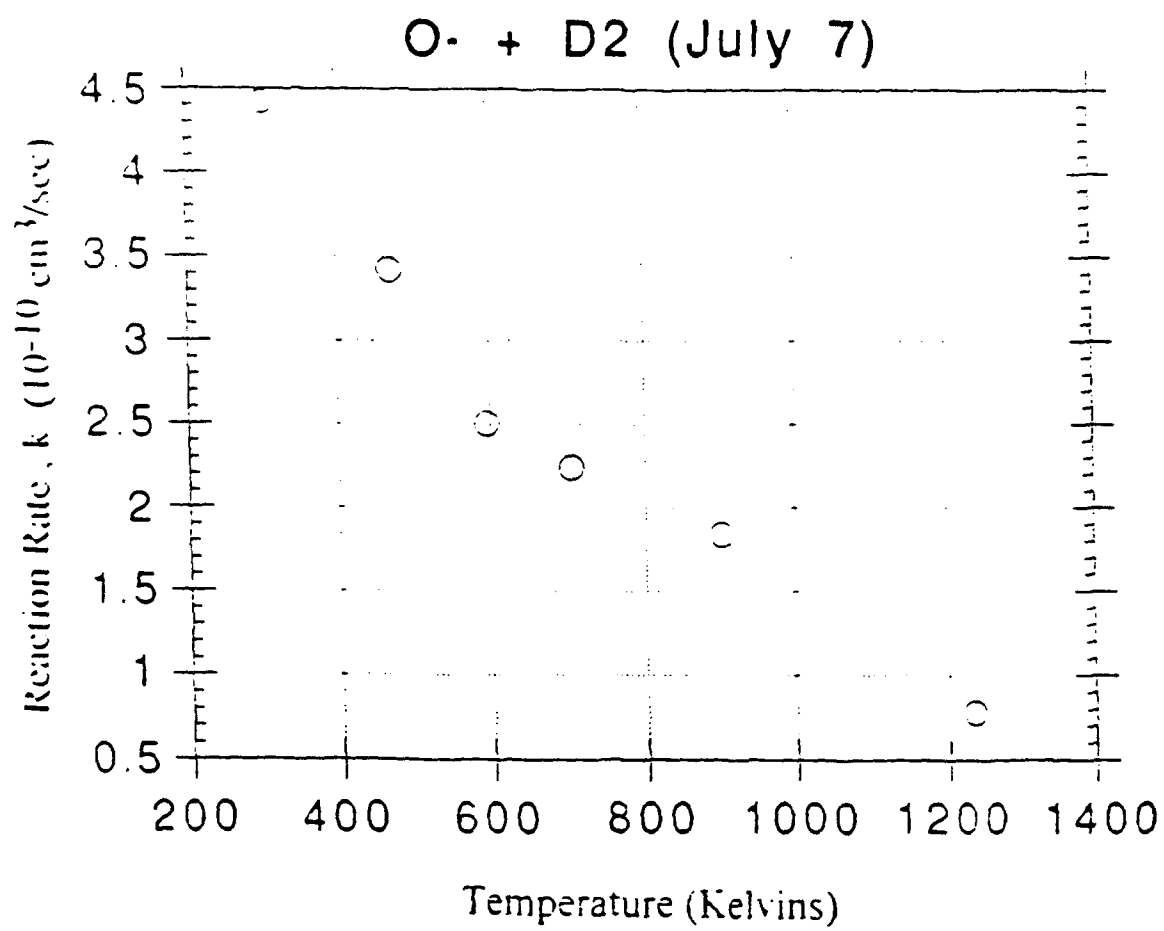


Figure 4

# **Whistler Waves and Ionospheric Particle Precipitation**

by

**Daniel Timothy Moriarty**

**S.B., Electrical Engineering, M.I.T. (1990)**

**S.M., Nuclear Engineering, M.I.T. (1992)**

**MIT PFC NW16-229**

**167 Albany St.**

**Cambridge, MA 02139**

**Submitted to the AFOSR  
as the summary report for the**

**Summer Research Program**

**at the**

**Phillips Laboratory**

**Sponsored by:**

**Air Force Office of Scientific Research  
Bolling Air Force Base. Washington, D.C.**

**September 1993**

# **Whistler Waves and Ionospheric Particle Precipitation**

by

Daniel Timothy Moriarty

Department of Nuclear Engineering

Massachusetts Institute of Technology

Submitted to the AFOSR  
on September 28, 1993, as the summary report of the  
Summer Research Program

## **Abstract**

A summary of the various phenomena leading up to ionospheric particle precipitation is presented. Lightning discharges emit VLF electro magnetic waves that propagate in all directions. The VLF waves are reflected at the ionosphere where a small fraction penetrate into the plasma beyond and are converted into whistler waves. The magnetized ionosphere guides the whistler waves into the radiation belts where they interact with high energy particles created by the solar wind. These particles are pitch angle scattered into the loss cone created by the Earth's dipole magnetic field and precipitate toward the Earth along the magnetic field lines that guided the VLF waves. Upon reaching the lower ionosphere - or upper atmosphere - they collide with neutral particles and create intense plasma patches.

Experiments performed at Arecibo regarding particle precipitation will then be presented. Analysis of data recovered from the Fall 1992 campaign will be discussed. Preliminary results indicate that modification of the ionosphere by HF heaters may enhance the particle precipitation events.

# Contents

<b>1</b>	<b>Introduction</b>	<b>5</b>
1.1	Overview . . . . .	6
1.2	Outline . . . . .	6
<b>2</b>	<b>Review of Phenomena and Theory</b>	<b>7</b>
2.1	Spherics as sources of VLF power . . . . .	7
2.2	Interactions at the atmosphere/ionosphere interface . . . . .	10
2.3	Electron cyclotron resonance and particle precipitation . . . . .	12
<b>3</b>	<b>Ionospheric Heating Experiments</b>	<b>15</b>

# List of Figures

2-1	Lightning as a source of VLF. From Liao 1989. . . . .	8
2-2	Frequency time plot indicating whistlers. From Kelley 1985. . . . .	9
2-3	Index of refraction surface for whistler waves indicating group and phase direction. From Farrell and Gurnett . . . . .	11
3-1	Experimental layout at Arecibo, Puerto Rico . . . . .	17
3-2	Typical ACF (above) and Power Spectra (below) . . . . .	18

# Chapter 1

## Introduction

Ionospheric Plasma Physics is by no means a new topic. Beginning the early part of this century radio scientists have been aware of the existence of the ionosphere and has used it to their advantage. By acting as the upper conductive boundary of the Earth-Ionosphere waveguide it allows radio operators to communicate around the globe without the otherwise necessary beacon satellites.

As communications technology grew so did our dependance on the information gathered courtesy of the ionosphere. However, due to the turbulent nature of the atmosphere below radio scientists quickly became aware of disturbances created by lightning generated electromagnetic noise. The existence of naturally occurring sources of noise and the subsequent error introduced into radar and other position sensing equipment has driven physicists to study the origins of such phenomena.

The particular phenomena discussed below begins with a lightning strike and ends with the occurrence of sporadic plasma patches. The continuing studies of such phenomena began decades ago and continues today. Because of this there exists a great number of publications that necessarily must be reviewed to understand the fundamentals of the various processes involved and to prevent the duplication of any of the fine experiments performed so far.

## 1.1 Overview

The present work reviews many fine articles discussing experiments and theories attempting to explain the causes of ionospheric particle precipitation events. The first half of this work reviews some relevant theory, whereas the second half describes a set of experiments performed at Arecibo, Puerto Rico in the Fall of 1992.

## 1.2 Outline

In Chapter 2 is discussed three main stages leading up to precipitation events: atmospheric disturbances or 'spherics' serving as natural sources of VLF EM noise; the conversion of the lightning emitted EM waves into whistler waves and the guidance of these whistler waves out to the radiation belts; and the wave particle interaction which scatters trapped particles down to the lower ionosphere and upper atmosphere.

Chapter 3 will introduce some ionospheric heating experiments performed in Arecibo to explore the causes of trimpi events.

## Chapter 2

# Review of Phenomena and Theory

This chapter is comprised of three main sections. The first section describes lightning as a source of VLF emission and some field experiments that have gathered data near intense storms. The next section concentrates on the penetration and guidance of VLF waves into and through the ionosphere. The last section reviews the wave-particle interaction which scatters particles down toward Earth.

### 2.1 Spherics as sources of VLF power

It is well known that lightning serves as an excellent source of VLF emission. In fact, lightning is common enough and powerful enough that it has become quite a nuisance to many types of communication and radar position sensing. Although the frequencies emitted by lightning are far too low to be directly picked up as noise by most radio systems. (This is not the case for most Naval transmitters as will be discussed later.) The secondary effects, e.g. plasma turbulence and patches created by lightning emission do, however, directly affect communications. A cartoon sketch of lightning generated whistler waves is shown in Figure 2-1.

A set of experiments performed recently [Kelley et. al. 1985] successfully made measurements of lightning emitted EM energy via two balloons named Thunder Hi and Thunder Lo. It was found that lightning typically has a rise time of 0.2 msec or so and lasts for



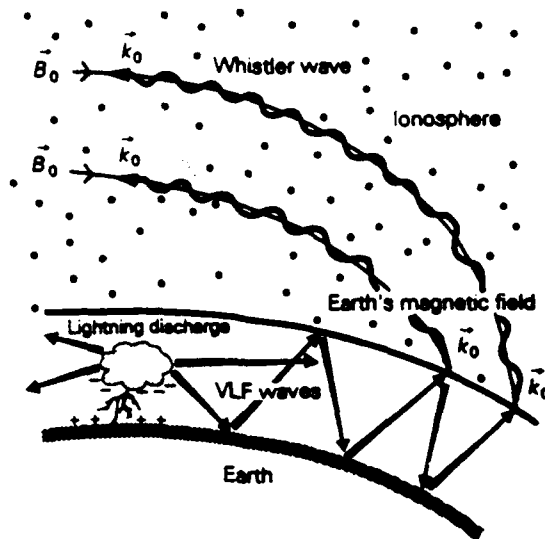


Figure 2-1: Lightning as a source of VLF. From Liao 1989.

approximately 10-20 msec. Hence the corresponding emission lies in the 1-10 kHz range. This range of frequencies corresponds to the whistler range of frequencies in the upper ionosphere. Frequency time plots clearly indicate a broadband spike occurring shortly after the lightning stroke followed by several and sometimes many downward sweeping tone bursts labelled as whistlers. See Figure 2-2. The mechanism creating multiple whistlers is well known. A packet of VLF waves is emitted by the lightning stroke. Some fraction penetrates the ionosphere and is guided along the Earth's dipole magnetic field toward the opposite pole. As the waves travel the dispersive nature of the plasma causes the higher frequencies to travel faster than the lower frequencies. After the packet reaches the other pole it is reflected at the ionosphere-atmosphere boundary and returns. The reflection from pole to pole may occur several times before the waves disperse or decay away.

The above mentioned experiments also revealed the amplitude of the first bounce whistler to be greater than the lightning emitted VLF packet. The single pass damping of whistler waves has been found to be typically 7dB [Helliwell 1965]. The measured peak amplitude near 4-6 kHz indicated an amplification of nearly 20 dB. This whistler wave amplification will be discussed in a later section.

Other experiments carried out have discovered events that are difficult to justify. Upward

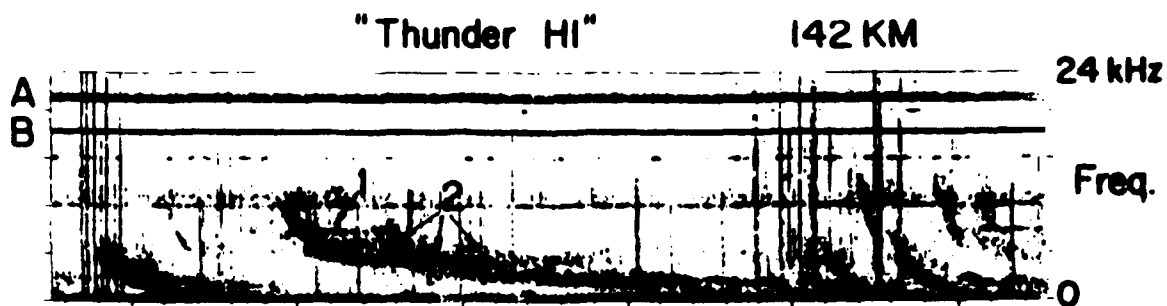


Figure 2-2: Frequency time plot indicating whistlers. From Kelley 1985.

streaming energetic electrons in the keV range have been found by both Kelley et. al. as well as others [Burke et. al. 1992]. Several mechanisms have been presented to account for these energetic electrons. Burke et. al. propose that the lightning generated radial electric field accelerates electrons freely along the earth's magnetic field until many runaway to the keV range. Recent experiments by Kelley have measured parallel electric fields that are far too great to be justified given the shielding effect of the ionosphere [Kelley et. al. 1990]. In addition it was found that the time delay from the lightning strike to the arrival of EM fields was too short to be explained. Attempts to explain the large parallel electric fields have incorporated non-linear three and four wave interactions. Parametric decays of whistler waves in the laboratory context have been described [Porkolab 1974] as well as in the ionospheric context [Lee and Kuo 1984]. Evidence supporting whistler decay has been observed [Liao, Freidberg and MC Lee 1989].

Considering the many and varied possibilities explaining the existence of inexplicably large electric fields the solution is by no means found. Thus is the justification for studying the wave interactions at the plasma-atmosphere interface.

## 2.2 Interactions at the atmosphere/ionosphere interface

The following section explores the physics that determine the fraction and direction of incident power that is transmitted through the plasma boundary. The above section describes some mechanisms for generating VLF waves. Given that some VLF power is incident on the ionospheric boundary it is a difficult task to calculate how much of the incoming linearly polarized power is converted to circularly polarized whistler waves. There are many factors affecting the final outcome. The density profile, angle of incidence, frequency range, and magnetic field strength are some. Qualitatively the problem is not so difficult. However, quantitatively the problem is nearly intractable.

The basic line of reasoning is as follows. Given a source of VLF waves, say a Naval transmitter, the power incident on the ionospheric boundary a distance  $r$  away is simply  $1/r^2$  times the transmitted power. Given the various plasma parameters a fraction,  $T$ , of this power gets through. The resulting whistler wave power is then guided along the earth's magnetic field.

Using Snell's law it is straightforward to determine the transmitted group velocity direction. As described in [Kong 1986] Snell's law can be written as:

$$N_1 \sin(\theta_1) = N_2 \sin(\theta_2) \quad (2.1)$$

where  $N_x$  is the refractive index in region  $x$ , and  $\theta_x$  is the incident(transmitted) angle in region  $x$ . Some difficulty is encountered initially since  $N_2$  is a function of  $\theta_2$ , however, for the case of interest, Snell's law is simplified. The index of refraction for whistler waves is typically quite large - approximately 40-70. Hence for almost all cases, the transmitted angle will be almost exactly at a right angle with respect to the interface, i.e. vertical. One must beware since this angle is the direction of phase velocity. For whistler waves the phase and group velocities are seldom aligned. The direction of group velocity is found to be normal to the polar plot of phase velocity [Farrel et. al. 1988].

For the case of interest the group velocity is nearly parallel to the magnetic field lines. This suggests that whatever power is transmitted into the ionosphere is effectively trapped

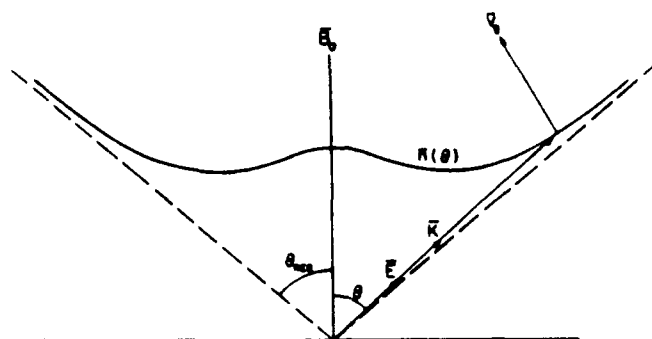


Fig. 1. The index of refraction surface for the whistler mode and the associated  $E$ ,  $k$ , and  $v_p$  vectors for propagation near the resonance cone ( $\theta \approx \theta_{res}$ ). For propagation near the resonance cone,  $k$  and  $E$  are parallel and nearly perpendicular to  $v_p$ . In this limit,  $E$  is linearly polarized and quasi-electrostatic.

Figure 2-3: Index of refraction surface for whistler waves indicating group and phase direction. From Farrell and Gurnett

onto the flux line and is confined to a banana shaped region created by the earth's dipole field and bounded at both ends by the boundary of the ionosphere.

The determination of transmitted power is a more difficult task. With a few simplifying assumptions the task is greatly reduced. The easiest approach is to assume a horizontally stratified plasma with a sharp boundary. From the equations for a plane wave it is straightforward to show the relationship:

$$T = \frac{2N_1}{N_1 + N_2} \quad (2.2)$$

where  $T$  is the fraction of transmitted electric field. For whistler waves with refractive indexes near 50, this simplified treatment clearly shows a small -  $1/2500$  - fraction of transmitted power. The transmitted power density is only  $1/50$  of the incident power density since by snell's law the angles of incidence are mapped onto a much smaller -  $1/50$  - region of transmitted angles. Nevertheless, the large majority of incident power remains below the ionosphere. This is not surprising considering this is exactly what radio engineers, particularly Navy radio engineers, have been relying on for decades. For further discussion of this analysis please refer to [Starks 1993].

This simplified approach breaks down under several realistic conditions. Firstly, the

assumption of a sharp ionospheric boundary does not consider the existence of the D or E region. For such low frequencies considered here even a tenuous plasma such as found in the D region can present significant conductivity. If this is the case then the initial  $1/r^2$  power drop will be much less, a.k.a. more power incident the boundary. Additional power may penetrate since the refractive indexes in the D region are much lower. Aside from the existence of the D or E region the gradual density profile of the E region may act as an impedance transformer. (Recent lab experiments performed by the author have shown that even an approximate impedance transformer, a horn attached to the end of a waveguide, can reduce reflections from 40% to less than 8%).

Still another model breakdown is revealed in the derivation of T and Snell's law. Both were derived using the linearly polarized plane wave (on both sides of the boundary) approximation. Our case meets the approximation only on one side. For applications where the transmitted wave is of a differing polarization, including electrostatic components, it is not clear how to approach the problem aside from solving the full wave equations. Will a Brewster angle come into play at any point?

Another approximation is in regards to the relative sizes of the incident wavelength and the size of the transmitted plasma region. Surely for the case of a quiescent ionosphere the short wavelength assumption is justified. For important cases to be described later the wavelength must be compared to the size of a heated region. Experiments have been performed using HF heaters to create plasma ducts that extend out into the magnetosphere. These ducts are believed to be on the order of a few kilometers. For the lower end of the whistler range of frequencies the wavelengths can be of the order 300 km. For this range of frequencies it is probably more reasonable to model the incoming wave and a current sheet at the mouth of a circular waveguide.

## **2.3 Electron cyclotron resonance and particle precipitation**

The list of plasma instabilities are many and varied. Some require no external disturbance to initiate a relaxation process. Others require a substantial input that must exceed some

threshold before the instability occurs. The following section describes an instability beginning with the injection of whistler waves into the ionosphere and ending with particle precipitation.

Above 300 km or so there exists a very tenuous plasma made up of fairly energetic - up to many keV - particles. These particles primarily come from the solar wind. As they near the Earth these particles become trapped in the geomagnetic field. Because of the dipole nature of the geomagnetic field, the energetic particles find themselves trapped within a magnetic mirror aligned North to South. This mirror trap system sets up a pitch angle anisotropy in the particles' velocity distribution. It is this anisotropy that provides the available free energy to drive electron cyclotron instabilities given the presence of whistler waves.

In the derivation of the cold plasma dielectric tensor it is easily shown that for waves travelling along the externally imposed magnetic field (or at small angles with respect to this field) a solution to the system is in the form of a right hand circularly polarized electromagnetic wave [Stix 1962]. If a temperature distribution is retained in the derivation it can be shown that a wave particle resonance can be set up if the following relation holds:

$$kV_R = \omega - N\Omega \quad (2.3)$$

where  $k$  is the wave number,  $V_R$  is the resonant particle's parallel velocity,  $\omega$  is the wave frequency, and  $\Omega$  is the particle's gyrofrequency. This resonance condition occurs when a particles velocity relative to a travelling wave doppler shifts the frequency to match the particles gyrofrequency. Right handed waves below the local electron gyrofrequency will resonate with electrons if the particles are streaming toward the approaching wave. If there are more resonant particles with higher energies than lower energies the wave grows. This is precisely the case for upgoing whistler waves and downcoming electrons.

For the case of the magnetosphere the earth's dipole magnetic field sets up a flat particle distribution i.e. mostly perpendicular to the earth's field. Any particles that manage to be pitch angle scattered into the loss cone quickly precipitate down to earth. However, particles do not necessarily need to collide with another particle to pitch angle scatter.

If a whistler wave passing through the magnetosphere becomes resonant with a group of particles they will lose their energy to the wave and diffuse toward the loss cone until being lost [Kennel and Petschek 1966]. For the steady state magnetosphere interacting with naturally occurring VLF hiss there tends to be a steady 'drizzle' of particle precipitation. If a whistler wave becomes resonant its amplitude will grow. Kennel and Petschek have shown that the diffusion rate of particles is a strong function of whistler wave amplitude. This relation further accelerates the instability until most particles are quickly lost and rain down as a large 'splash' of energetic particles. After the release of a splash, the velocity distribution is left in such a way that the instability is no longer supported. Thus the particle precipitation can be described as a steady 'drizzle' interrupted from time to time by large 'splashes' whenever a lightning strikes or something sources a large VLF signal.

## Chapter 3

# Ionospheric Heating Experiments

Because of the existence of natural sources of VLF hiss, and because of the ability of lightning to create precipitation at both ends of a flux tube, the occurrences of particle precipitation are frequent. These frequent trimpi events can cause intense, sporadic plasma patches that can disturb communications. Subsequently, physicists and radio engineers alike have attempted to understand and possible control or at least account for such sources of noise.

Field experiments studying particle precipitation have been ongoing for decades yet the need for more study still exists. Many experiments of the past have utilized nearby Naval transmitters to act as sources of VLF [Kelley 1985]. Although the power output of a Naval transmitter is less than 1/100th of that of a lightning discharge, the power density per frequency is comparable to that of lightning thus making these transmitters very suitable for controlled studies. VLF may also be artificially created by the beating of two HF waves [Koh 1993].

In the Fall of 1992 a series of experiments were performed at Arecibo, Puerto Rico by the MIT Ionospheric Group led by Prof. Min Chang Lee. These experiments, in addition to studying other phenomena, studied the effects of heating the atmosphere on the frequency of trimpi events. See Figure 3-1 for a cartoon sketch of the experimental setup. Data is generated from the 440 MHz backscatter radar. The use of auto-correlation functions and



FFT's greatly aid in distinguishing meteors, spread F, or particle precipitation. By taking the FFT of the auto-correlation function, the resulting power spectrum provides a wealth of information [Blackman and Tukey 1958]. See Figure 3-2 for typical ACF and power spectra.

The existing Arecibo radar data is under review. A brief overview of the data has suggested the use of different data acquisition parameters. Certain information was found to be missing due to bandwidth and resolution limitations of the Arecibo data system. In future studies the data system parameters may be tailored specifically for precipitation studies thus maximizing bandwidth and resolution. Pending the conclusion of the data analysis, further experiments will be conducted.

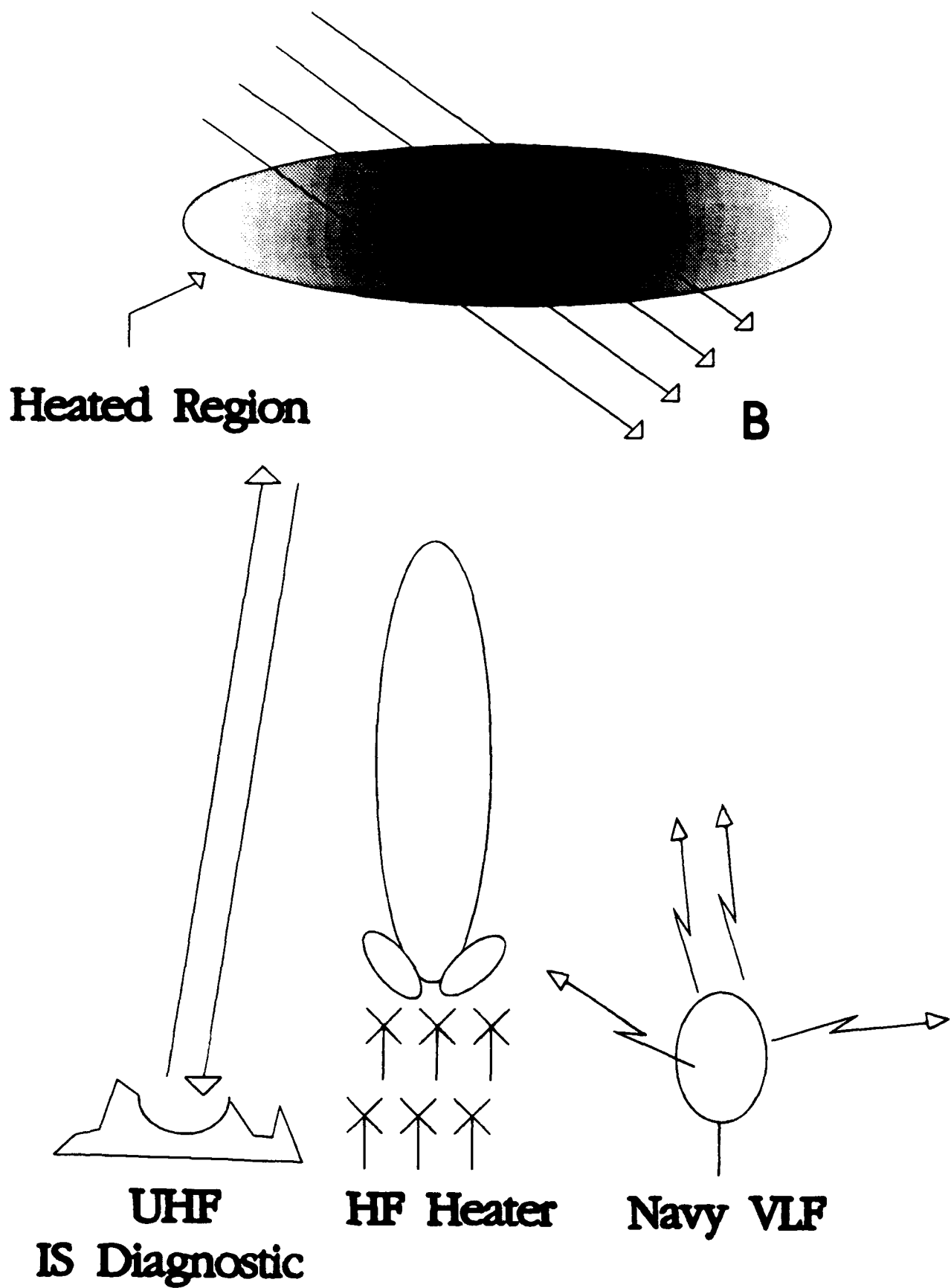


Figure 3-1: Experimental layout at Arecibo, Puerto Rico

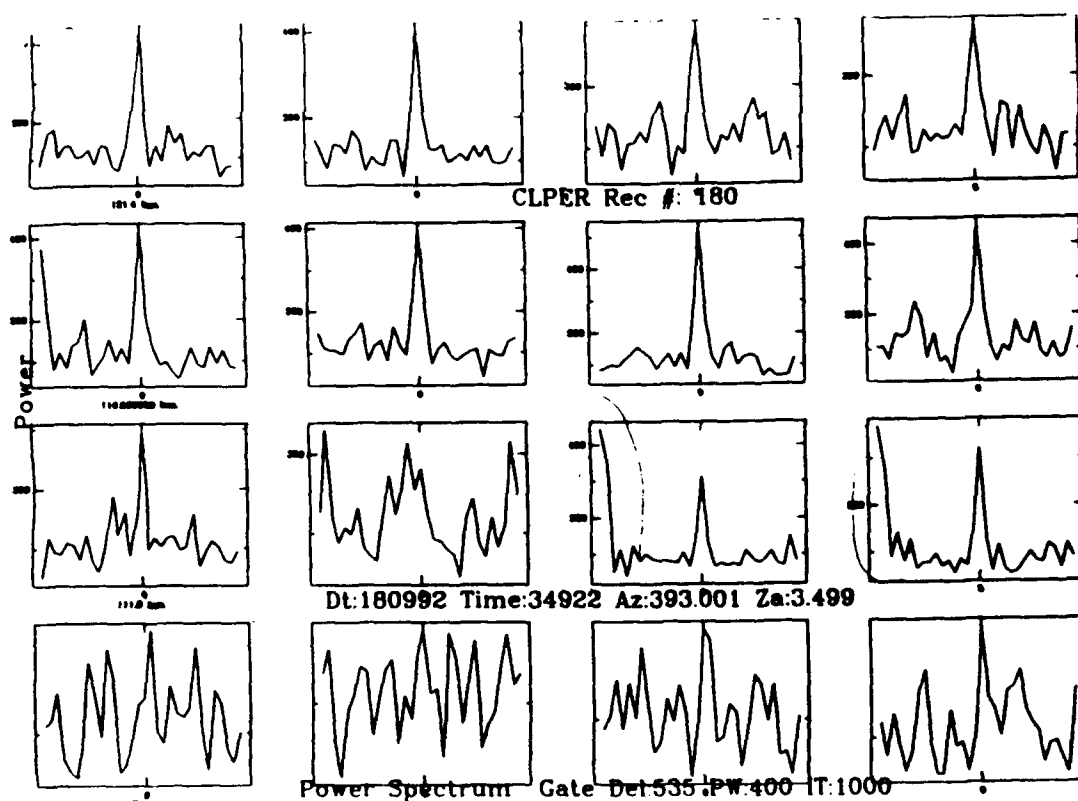
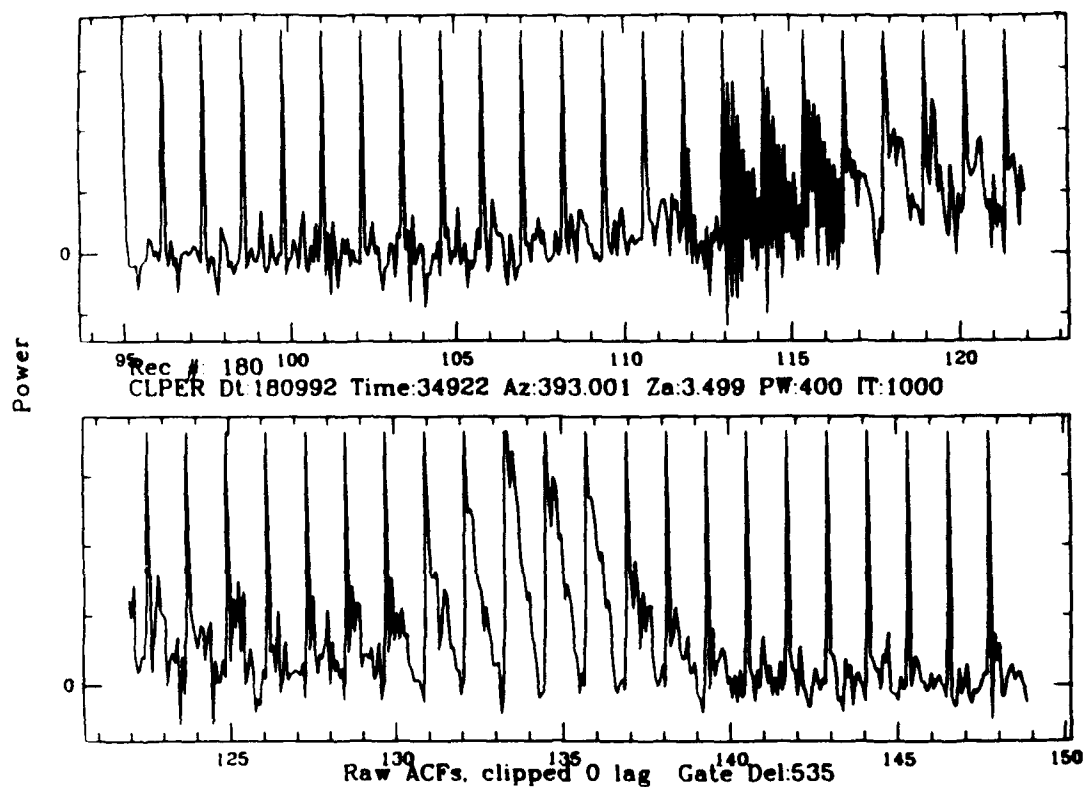


Figure 3-2: Typical ACF (above) and Power Spectra (below)

# Bibliography

- [1] Blackman, R.B., and J.W. Tukey, *The Measurement of Power Spectra* Dover Publications Inc., New York, 1958.
- [2] Burke, W.B., et. al., Effects of a Lightning Discharge Detected by the DE 2 Satellite Over Hurricane Debbie, *Journal of Geophysical Research*, 97(A5), 6359-6367, 1992.
- [3] Farrell, W.M., et. al., An Analysis of Whistler Mode Radiation From the Spacelab 2 Electron Beam, *Journal of Geophysical Research*, 93(A1), 153-161, 1988.
- [4] Helliwell, R.H., *Whistlers and Related Ionospheric Phenomena*, Stanford U. Press, Stanford, CA, 1965.
- [5] James, H.G., VLF Saucers, *Journal of Geophysical Research*, 81(4), 501-514, 1976.
- [6] Kelley, M.C., et. al., Electrical Measurements in the Atmosphere and the Ionosphere Over an Active Thunderstorm, *Journal of Geophysical Research*, 90(A10), 9815-9823, 1985.
- [7] Kelley, M.C., et. al., Intense Ionospheric Electric and Magnetic Field Pulses Generated by Lightning, *Geophysical Research Letters*, 17(12), 2221-2224, 1990.
- [8] Kennel, C.F., and H.e. Petschek, Limit on Stably Trapped Particle Fluxes, *Journal of Geophysical Research*, 71(1), 1966.
- [9] Koh, K., *Stimulation of Ionospheric Plasmas Using the Arecibo Radar Systems*, Master's Thesis submitted to MIT EECS, 1991.

- [10] Kong, J.A., *Electromagnetic Wave Theory* Wiley & Sons, New York, 1986.
- [11] Lee, M.C., and S.P. Kuo, Production of Lower Hybrid Waves and Field-Aligned Plasma Density Striations by Whistlers, *Journal of Geophysical Research*, 89, 10873-10880, 1984.
- [12] Liao, C.P., J.P. Freidberg, and M.C. Lee, Explosive Spread F Caused By Lightning-Induced Electromagnetic Effects, *Journal of Atmospheric and Terrestrial Physics*, 51(9/10), 751-758, 1989.
- [13] Porkolab, M., Theory of parametric instability near the lower hybrid frequency, *Physics of Fluids*, 17, 1974.
- [14] Starks, M., *Transmission of VLF Waves Into Ionospheric Ducts at Arecibo, Puerto Rico*, Summary Report to AFOSR Summer Research Program, 1993.
- [15] Stix, T.H., *The Theory of Plasma Waves*, McGraw-HillBook Co., New York, 1962.

**Transmission of VLF Waves into  
Ionospheric Ducts at Arecibo, Puerto Rico**

Michael J. Starks  
Graduate Fellow  
Electrical, Computer, and Systems Engineering

Boston University  
44 Cummington Street  
Boston, MA 02215

Final Report for:  
Graduate Student Research Program  
Phillips Laboratory GPSG  
Hanscom AFB, Bedford, MA.

Sponsored by:  
Air Force Office of Scientific Research  
Bolling Air Force Base, Washington, D.C.

September 1993

# **Transmission of VLF Waves into Ionospheric Ducts at Arecibo, Puerto Rico**

Michael J. Starks  
Graduate Fellow  
Electrical, Computer, and Systems Engineering  
Boston University

## **Abstract**

The coupling of monochromatic VLF waves into the ionosphere is discussed. The specific problem of 28.5 kHz transmissions from NAU, the Navy communications transmitter in Puerto Rico, entering artificially-induced ducts over Arecibo is studied. Detailed consideration is given to index of refraction, transmission coefficients, group velocity, and energy flow. Computations are performed for the case at hand as a rough approximation of the coupled power.

# **Transmission of VLF Waves into Ionospheric Ducts at Arecibo, Puerto Rico**

Michael J. Starks

## **Introduction**

It has long been understood that both natural and man-made VLF emissions propagating in the earth-ionosphere waveguide may be coupled into the ionosphere. These transmitted signals propagate in the ionosphere and magnetosphere as whistler waves. Ducted whistlers may travel back and forth along the magnetic field line many times and be amplified by wave-particle interactions at the equator. Such waves may also disturb the orbits of electrons trapped in the radiation belts and, through pitch angle scattering, promote the precipitation of energetic electrons into the lower ionosphere. Ongoing research has shown that these precipitation events may then be visible on backscatter radar returns as sporadic ionization through a significant altitude range.

The theoretical dynamics of this complex effect are generally understood, but detailed consideration and calculation of each step in the process have mostly been limited to quick and rough approximation or to cases of propagation along a vertical magnetic field. In an attempt to better understand the coupling and ducting of whistlers and the subsequent wave-particle interactions, detailed research and calculation were undertaken for each component of the problem. This document considers the first step: the coupling of VLF transmissions into ionospheric ducts. Rough calculations for the Navy transmitter at Aguada, Puerto Rico, are also included.

The consideration of VLF coupling is approached from a geometric optics point of view. There is evidence to support that geometric optics yield results close to those of full-wave solutions for frequencies above about 10 kHz at 100 km altitude. We therefore consider our monochromatic transmitter to operate above this frequency, as is the case for NAU.

Detailed examination is given to the index of refraction of the ionospheric plasma, the derivation of transmission coefficients valid for all angles of incidence, power transmission from a linear dipole antenna, and the concept of group velocity and energy flow. While some simplifications are performed for the specific case in Puerto Rico, the entire analytical process is applicable to most other locations.

## **Index of Refraction**

One of the important characteristics of a medium is the index of refraction, denoted by  $n$ . The index of refraction of a medium, also termed refractive index, is the ratio of the speed of light



in free space to the speed of light in that medium, hence:

$$n = \frac{c}{v_\phi} \quad (5-1)$$

where  $v_\phi$  is the phase velocity of a wave in the medium and  $c$  is the velocity in free space.

The ionosphere is anisotropic due to the earth's static magnetic field, and the index of refraction varies widely depending on parameters such as the plasma frequency, the wave frequency, and the direction of propagation relative to the field. Assuming a homogeneous medium, where parameters vary slowly in the space of one wavelength, and a propagating wave with wave normal in the positive  $y$ -direction, the square of the index of refraction is given by Appleton's equation:

$$n^2 = 1 - \frac{X}{1 - iZ - \frac{\frac{1}{2}Y_T^2}{1 - X - iZ} \pm \frac{1}{1 - X - iZ} \left[ \frac{1}{4}Y_T^4 + Y_L^2(1 - X - iZ)^2 \right]^{1/2}} \quad (5-2)$$

where:

$n$  = complex refractive index =  $\mu - i\chi$

$\mu$  = refractive index (real part of  $n$ )

$\chi = \kappa c / \omega$  = absorption index (negative imaginary part of  $n$ )

$\kappa$  = absorption coefficient (nepers/meter)

$c$  = velocity of light in free space

$X = \omega_{pe}^2 / \omega^2$

$Y_T = \omega_T / \omega$

$Y_L = \omega_L / \omega$

$Z = \nu / \omega$

$\omega_{pe} = \sqrt{\frac{Ne^2}{\epsilon_0 m_e}}$  electron plasma frequency

$\omega_{ce} = \frac{|B_0|e}{m_e}$  electron gyro frequency

$\omega_L = \omega_{ce} \cos \theta$

$\omega_T = \omega_{ce} \sin \theta$

$\omega$  = wave frequency

$e$  = charge on an electron

$\nu$  = electron collision frequency

$\epsilon_0$  = dielectric constant of free space

$N$  = number density of electrons

$m_e$  = electron mass

$B_0$  = imposed magnetic field

$\theta$  = angle between  $B_0$  and  $y$ -direction

## Quasi-Longitudinal and Low Frequency Approximations

The somewhat cumbersome Appleton equation for refractive index can be substantially simplified by the use of several approximations. We make the quasi-longitudinal (QL) approximation when the direction of propagation is close enough to the direction of the earth's magnetic field. This allows us to drop the terms in (5-2) that contain  $Y_T$ . The condition for this approximation to be valid is:

$$\frac{Y^2 \sin^4 \theta}{4 \cos^2 \theta} \ll |(1 - X - iZ)^2| \quad (5-3)$$

This condition can be simplified at very low frequencies. For whistler waves,  $X$  is usually quite large compared to  $I$ , allowing us to neglect  $I$  with respect to it. Further, since  $v$  is sufficiently less than  $\omega$ , we may eliminate terms containing  $v$  as well. These approximations reduce the condition in (5-3) to:

$$\frac{\sin^2 \theta}{\cos \theta} < \frac{2}{3} \frac{\omega_{pe}^2}{\omega \omega_{ce}} \quad (5-4)$$

The range of angles over which the QL and low-frequency approximations are valid can be computed for the case at hand. Assuming the following parameters:

$$\begin{aligned} \omega &= 2\pi \times 28.5 \times 10^3 \\ \omega_{pe} &= 2\pi \times 3 \times 10^6 \end{aligned} \quad \omega_{ce} = 2\pi \times 1.2 \times 10^6 \quad (5-5)$$

we find that the limiting angle  $\theta \cong 90^\circ$ , ensuring that the approximations are valid over all propagation angles.

Selecting the minus sign in (5-2) for a propagating whistler wave, we obtain:

$$n^2 = \mu^2 = 1 + \frac{X}{|Y_L| - 1} \quad (5-6)$$

Replacing the quantities  $X$  and  $Y_L$  with appropriate expressions and regrouping yields:

$$n^2 = \frac{A^2}{B(\cos \theta - B)} \quad (5-7)$$

where the  $I$  has been neglected as being significantly smaller than the  $A^2$  quantity and:

$$A = \frac{\omega_{pe}}{\omega_{ce}} \quad B = \frac{\omega}{\omega_{ce}}$$

Equation (5-7) will henceforth be used to describe the index of refraction.

## Resonance Cone

The refractive index of equation (5-7) may be used to find an angle  $\theta$  at which the propagating wave encounters a resonance and  $n$  approaches infinity. As shown in *figure 5-1*, as  $\theta$  increases and a wave propagates with  $k$  less and less parallel to  $B_0$ , the  $\cos \theta$  term in the denominator of (5-7) approaches zero. When  $\cos \theta = B$ , the refractive index becomes infinite and the wavelength approaches zero. The wave is generally absorbed at the resonance which, for whistler waves, is the electron cyclotron resonance.

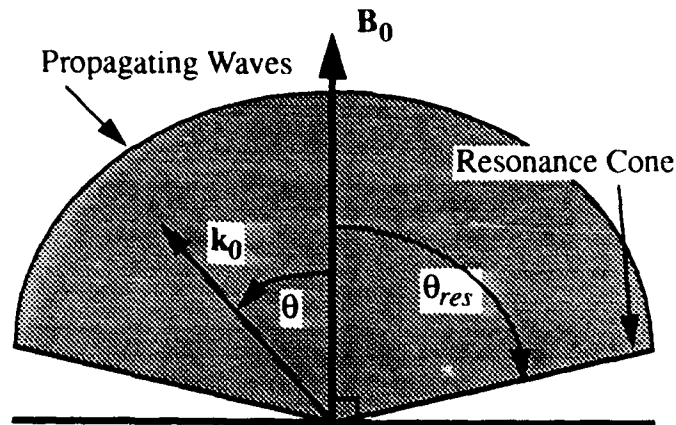


Figure 5-1: Schematic of the Resonance Cone

For the case at hand, we solve  $\cos \theta_{res} = B$  for the parameters given in (5-5). The half-angle width of the resonance cone can easily be calculated as  $\theta_{res} = 88^\circ$ . This indicates that whistlers may propagate at nearly any angle to the magnetic field as they enter the duct. The direction of power transmission in the duct, however, may not be the same. This will be demonstrated later.

## Snell's Law and Approximating $n$

From the derived equation for the index of refraction, we may estimate the value of  $n$  in the direction of propagation using the geometry shown in *figure 5-2*. Assuming the magnetic dip angle of Arecibo, Puerto Rico, as  $D = 50^\circ$  yields a mean transmission angle with respect to  $B_0$  of  $\theta = 40^\circ$  and we find, from equation (5-7),  $n \approx 18.9$ . This high index of refraction indicates that waves impinging on the boundary from a broad range of angles in the free space below will be focused into a narrow cone of transmission in the plasma above.

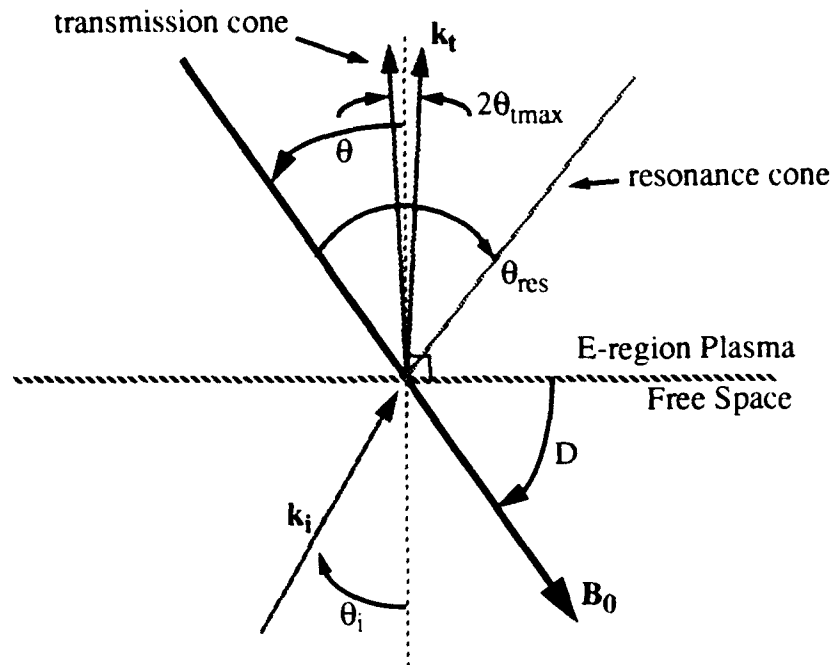


Figure 5-2: Geometry of Transmission Cone

From Snell's law of refraction we have:

$$\frac{\sin \theta_t}{\sin \theta_i} = \frac{n_i}{n_t} \quad (5-8)$$

where  $\theta_i$  is the angle of incidence with respect to the normal to the boundary between the two media,  $\theta_t$  is the angle of transmission with respect to the normal, and  $n_i$  and  $n_t$  are the refractive indices of the incident and transmitted media, respectively. Substituting  $n_i = 1$ ,  $n_t = 18.9$  and  $\theta_{imax} = 90^\circ$ , the limiting angle of incidence, yields:  $\theta_{tmax} = 3.0^\circ$ . This indicates a cone of transmission  $6^\circ$  wide, centered on the normal to the boundary. Note that the resulting maximum angle from the magnetic field,  $43^\circ$ , is still well within the resonance cone of  $88^\circ$  found previously.

In making this calculation, we have assumed that  $n$  varies slowly enough with  $\theta$  that three degrees has a negligible effect on the value obtained for  $\theta_t$ . Indeed, it can be shown that:

$$\frac{dn}{d\theta} \cong 0.3 (\text{degree})^{-1} \quad (5-9)$$

which introduces an error of 5% in the calculation of  $\theta_t$ . Thus the approximation is valid and we may make the further approximation that all transmitted waves travel with  $\theta = 40^\circ$  from  $B_0$ .

## Transmission Coefficients

Having found an approximate value for the refractive index of the plasma for all incident angles, we now derive expressions accounting for the impedance mismatch between the free space below the boundary and the plasma above. Assuming a linearly polarized TEM plane wave incident on an abrupt boundary, we make use of the geometry shown in *figure 5-3* below. The axis names are assigned arbitrarily, and they have no bearing on the final result.

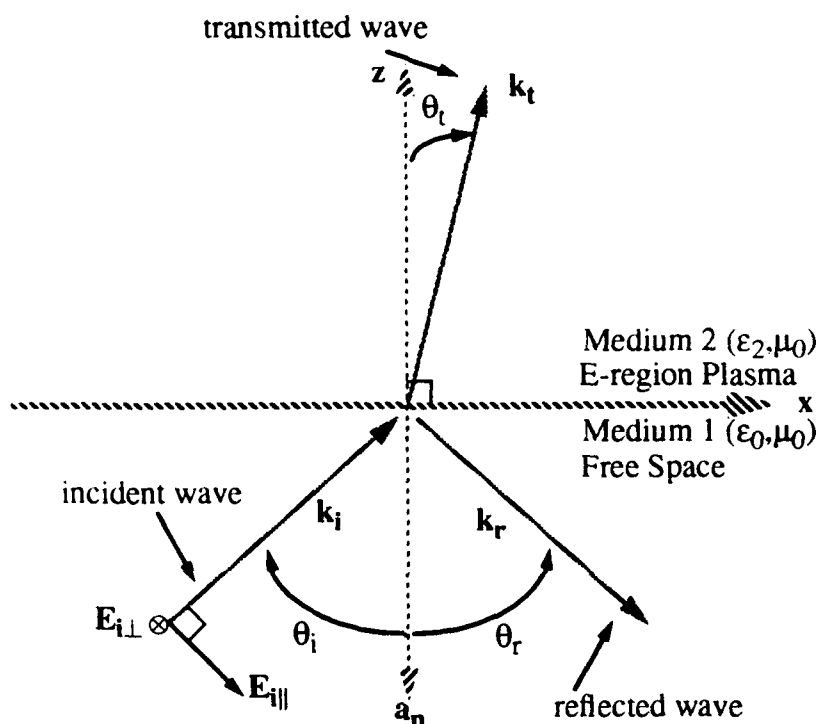


**Figure 5-3: Geometry of Transmission Coefficients**

*Perpendicular Polarization.* The normal to the boundary,  $\mathbf{a}_n$ , and the incident wave normal,  $\mathbf{k}_i$ , define the plane of incidence. For the case of perpendicular polarization, where  $\mathbf{E}$  of the incident wave is normal to the plane of incidence, we write the following expressions for the incident, reflected, and transmitted waves:

$$\begin{aligned}\vec{E}_i(x, z) &= \hat{y} E_{i0} e^{-jk_1(x \sin \theta_i + z \cos \theta_i)} \\ \vec{H}_i(x, z) &= \frac{E_{i0}}{\eta_0} (-\hat{x} \cos \theta_i + \hat{z} \sin \theta_i) e^{-jk_1(x \sin \theta_i + z \cos \theta_i)} \\ \vec{E}_r(x, z) &= \hat{y} E_{r0} e^{-jk_1(x \sin \theta_r - z \cos \theta_r)}\end{aligned}\tag{5-10}$$

$$\vec{H}_r(x, z) = \frac{E_{r0}}{\eta_0} (\hat{x} \cos \theta_r + \hat{z} \sin \theta_r) e^{-jk_1(x \sin \theta_r - z \cos \theta_r)}$$

$$\vec{E}_t(x, z) = \hat{y} E_{t0} e^{-jk_2(x \sin \theta_t + z \cos \theta_t)}$$

$$\vec{H}_t(x, z) = \frac{E_{t0}}{\eta_2} (-\hat{x} \cos \theta_t + \hat{z} \sin \theta_t) e^{-jk_2(x \sin \theta_t + z \cos \theta_t)}$$

where  $\eta = \sqrt{\mu/\epsilon}$  is the intrinsic impedance of the medium. Boundary conditions require that the tangential components of  $\mathbf{E}$  and  $\mathbf{H}$  be continuous across the boundary at  $z = 0$ , leading to the constraints:

$$\begin{aligned} E_{iy}(x, 0) + E_{ry}(x, 0) &= E_{ty}(x, 0) \\ H_{ix}(x, 0) + H_{rx}(x, 0) &= H_{tx}(x, 0) \end{aligned} \quad (5-11)$$

Substituting from (5-10) yields:

$$\begin{aligned} E_{i0} e^{-jk_1 x \sin \theta_i} + E_{r0} e^{-jk_1 x \sin \theta_r} &= E_{t0} e^{-jk_2 x \sin \theta_t} \\ \frac{1}{\eta_0} (-E_{i0} \cos \theta_i e^{-jk_1 x \sin \theta_i} + E_{r0} \cos \theta_r e^{-jk_1 x \sin \theta_r}) &= -\frac{E_{t0}}{\eta_2} \cos \theta_t e^{-jk_2 x \sin \theta_t} \end{aligned} \quad (5-12)$$

Since the expressions in (5-12) must hold for all  $x$ , the exponential factors must be equal in  $x$  as follows:

$$k_1 x \sin \theta_i = k_1 x \sin \theta_r = k_2 x \sin \theta_t$$

This form yields  $\theta_i = \theta_r$ , known as Snell's law of reflection, and two simplified constraints:

$$\begin{aligned} E_{i0} + E_{r0} &= E_{t0} \\ \frac{1}{\eta_0} (E_{i0} - E_{r0}) \cos \theta_i &= \frac{E_{t0}}{\eta_2} \cos \theta_t \end{aligned}$$

These last expressions are then combined and rearranged to define the transmission coefficient for perpendicular polarization, denoted  $\tau_{\perp}$ :

$$\tau_{\perp} = \frac{E_{t0}}{E_{i0}} = \frac{2\eta_2 \cos \theta_i}{\eta_2 \cos \theta_i + \eta_0 \cos \theta_t} \quad (5-13)$$

**Parallel Polarization.** We next consider the case where  $\mathbf{E}_i$  lies within the plane of incidence defined above. As before, we write the equations for the three waves in question:

$$\begin{aligned}
\vec{E}_i(x, z) &= E_{i0} (\hat{x} \cos \theta_i - \hat{z} \sin \theta_i) e^{-jk_1 (x \sin \theta_i + z \cos \theta_i)} \\
\vec{H}_i(x, z) &= \hat{y} \frac{E_{i0}}{\eta_0} e^{-jk_1 (x \sin \theta_i + z \cos \theta_i)} \\
\vec{E}_r(x, z) &= E_{r0} (\hat{x} \cos \theta_r + \hat{z} \sin \theta_r) e^{-jk_1 (x \sin \theta_r - z \cos \theta_r)} \\
\vec{H}_r(x, z) &= -\hat{y} \frac{E_{r0}}{\eta_0} e^{-jk_1 (x \sin \theta_r - z \cos \theta_r)} \\
\vec{E}_t(x, z) &= E_{t0} (\hat{x} \cos \theta_t - \hat{z} \sin \theta_t) e^{-jk_2 (x \sin \theta_t + z \cos \theta_t)} \\
\vec{H}_t(x, z) &= \hat{y} \frac{E_{t0}}{\eta_2} e^{-jk_2 (x \sin \theta_t + z \cos \theta_t)}
\end{aligned} \tag{5-14}$$

Similarly, applying boundary conditions yields Snell's law and the following constraints:

$$\begin{aligned}
(E_{i0} + E_{r0}) \cos \theta_i &= E_{t0} \cos \theta_t \\
\frac{1}{\eta_0} (E_{i0} - E_{r0}) &= \frac{1}{\eta_2} E_{t0}
\end{aligned}$$

Combining and rearranging these expressions, we obtain the transmission coefficient for parallel polarization, denoted  $\tau_{\parallel}$ :

$$\tau_{\parallel} = \frac{E_{t0}}{E_{i0}} = \frac{2\eta_2 \cos \theta_i}{\eta_2 \cos \theta_i + \eta_0 \cos \theta_t} \tag{5-15}$$

The derived transmission coefficients in (5-13) and (5-15) depend on the angle  $\theta_i$  in a complex manner since, in general,  $\eta_0$  and  $\eta_2$  may themselves be functions of  $\theta_i$  and  $\theta_t$ , and  $\theta_t$  is a function of  $\eta_2$ ,  $\eta_0$  and  $\theta_i$ . This loop of dependencies rapidly leads to a numerical approach to obtaining values for the coefficients unless some simplification can be performed.

For the case under study here, we found previously that  $\theta_{tmax} \cong 3^\circ$ , so we may assume that  $\cos \theta_t \cong 1$ . By converting impedances  $\eta$  to indices of refraction  $n$  using the formula  $n = \mu c / \eta$  and recognizing that  $n_0 = 1$  for free space, the transmission coefficients become:

$$\tau_{\perp} = \frac{2 \cos \theta_i}{\cos \theta_i + n_2} \quad \tau_{\parallel} = \frac{2 \cos \theta_i}{1 + n_2 \cos \theta_i} \tag{5-16}$$

These equations are easily plotted for varying angles of incidence by approximating  $n_2 = 18.9$  as before. The graphs are shown below. As expected, for  $\theta = 0^\circ$  normal incidence  $\tau_{\perp} = \tau_{\parallel}$ . It is clear from the plots that parallel-polarized waves are more readily transmitted into the ionosphere than perpendicular-polarized waves.

The transmission coefficients found here figure prominently in estimating the power coupled into the ionosphere by the Navy transmitter. This calculation will be performed next.

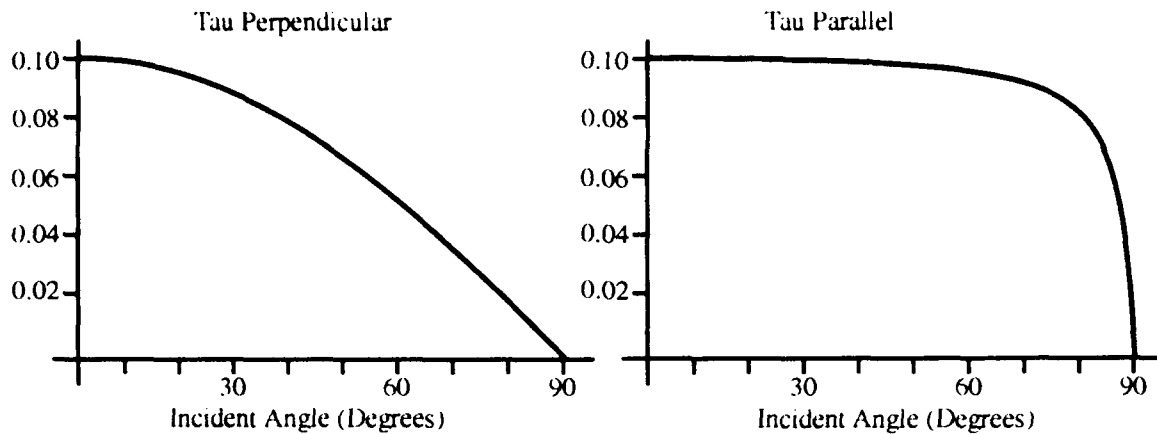


Figure 5-4: Plots of Transmission Coefficients

## Modelling the Transmitter and Power Transmission

**Transmitter Model.** The Navy submarine communications transmitter at Aguada, Puerto Rico, consists of an array of antennae spread across the ground and radiating 100 kW of transmitted power at 28.5 kHz. For the purposes of analysis, this antenna array may be modelled as a single half-wavelength center-fed dipole antenna. The cardinal orientation of the dipole is of no consequence as previous analysis has shown the normals of the waves transmitted into the ionosphere to be normal to the media boundary and thus at a constant inclination to  $\mathbf{B}_0$  for all orientations of the incident plane.

In general, the discussion of antenna radiation is divided into two regions known as the *near-zone* and the *far-zone* in order to simplify field expressions. The requirement for far-zone analysis is:

$$R \gg \frac{\lambda}{2\pi}$$

where  $R$  is the distance from the antenna. As we are interested in radiation fields in the free space below the duct opening, we calculate  $\lambda$  using  $\lambda = c / f$ . For a 28.5 kHz transmission,  $\lambda \cong 10.5 \text{ km}$ . Since we assume the coupling between free space and the ionosphere to occur at  $\sim 100 \text{ km}$  altitude, the problem is one of far fields.

The derivation of radiation fields for antennae is well beyond the scope of this work and the far-zone electric field expression for a half-wavelength center-fed dipole oriented in the  $\mathbf{z}$ -



direction is given without proof:

$$E_{\theta} = j \frac{60 I_M}{R} e^{-jk_1 R} \frac{\cos\left(\frac{\pi}{2} \cos\theta_k\right)}{\sin\theta_k} \quad (5-17)$$

where  $I_M$  is the maximum current in the dipole given by:

$$I_M = \sqrt{\frac{P_r}{36.54}} \quad (5-18)$$

and  $P_r$  is the radiated power. The magnitude of  $E_{\theta}$  is given by:

$$|E_{\theta}| = \frac{60 I_M}{R} \left( \frac{\cos\left(\frac{\pi}{2} \cos\theta_k\right)}{\sin\theta_k} \right) \quad (5-19)$$

The normalized magnitude of  $E_{\theta}$  is plotted in spherical coordinates in *figure 5-5*. The view is somewhat canted to provide perspective. Note that the antenna lies along the  $z$ -axis and  $y$  points in the vertical direction. Note also the very deep nulls at the ends of the antenna. The plot terminates at the ground plane.

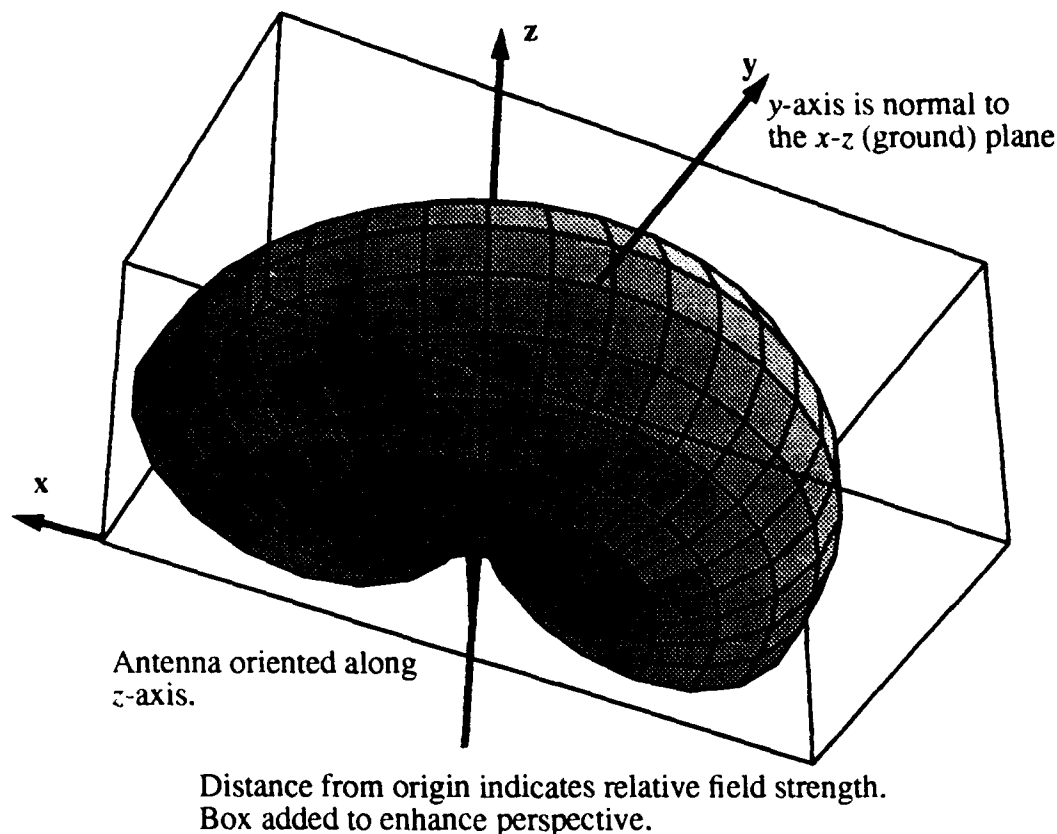


**Figure 5-5: Plot of Normalized Far-Zone  $|E_{\theta}|$  for a Half-Wave Dipole**

*E-Field in the Duct.* Obtaining the equation for the electric field inside the duct requires knowledge of the incident angle and incident field strength in order to properly apply the transmission coefficients of (5-16). An incident electric field can in general be decomposed into components parallel and perpendicular to the plane of incidence. It is to these components that the appropriate transmission coefficients are then applied. To perform such a decomposition requires knowledge of the angle between  $\mathbf{E}_\theta$  and the normal to the plane of incidence. A little geometry eventually shows that this angle is  $\phi_k$ . A rigorous proof using unit vectors follows.

In spherical coordinates,  $(r, \theta, \phi)$ , the wave normal unit vector is:

$$\hat{k} = (1, \theta_k, \phi_k) \quad (5-20)$$

The unit vector in the  $\theta$ -direction for a given  $\mathbf{k}$  can be found to be:

$$\hat{E}_\theta = (1, \theta_k + \frac{\pi}{2}, \phi_k) \quad (5-21)$$

(This will be shown below to be correct vector.) For ease of calculation, these unit vectors are converted into Cartesian,  $(x, y, z)$ , coordinates using:

$$x = r \sin \theta \cos \phi \quad y = r \sin \theta \sin \phi \quad z = r \cos \theta$$

Hence, (5-20) and (5-21) become:

$$\hat{k} = \sin \theta_k \cos \phi_k \hat{x} + \sin \theta_k \sin \phi_k \hat{y} + \cos \theta_k \hat{z} \quad (5-22)$$

$$\hat{E}_\theta = \sin (\theta_k + \frac{\pi}{2}) \cos \phi_k \hat{x} + \sin (\theta_k + \frac{\pi}{2}) \sin \phi_k \hat{y} + \cos (\theta_k + \frac{\pi}{2}) \hat{z}$$

Then, using  $\sin (\frac{\pi}{2} \pm \theta) = \cos \theta$  and  $\cos (\frac{\pi}{2} + \theta) = -\sin \theta$ :

$$\hat{E}_\theta = \cos \theta_k \cos \phi_k \hat{x} + \cos \theta_k \sin \phi_k \hat{y} - \sin \theta_k \hat{z} \quad (5-23)$$

It is trivial to show that  $\mathbf{k}$  is indeed orthogonal to  $\mathbf{E}_\theta$ :

$$\hat{k} \cdot \hat{E}_\theta = \sin \theta_k \cos \theta_k \cos^2 \phi_k + \sin \theta_k \cos \theta_k \sin^2 \phi_k - \sin \theta_k \cos \theta_k = 0$$

Using  $\hat{k} \times \hat{E}_\theta$  we can also find  $\hat{E}_\phi = -\sin \phi_k \hat{x} + \cos \phi_k \hat{y}$ . As this vector does not depend on  $\theta_k$ , it is clear that the  $\theta$ -vector was correctly identified above.

The normal to the boundary between free space and the plasma above, in Cartesian coordinates, is simply:

$$\hat{a}_n = (0, -1, 0) \quad (5-24)$$

$\mathbf{a}_n$  and  $\mathbf{k}$  then define the plane of incidence, and the normal to that plane is given by  $\hat{k} \times \hat{a}_n$ . The angle between  $\mathbf{E}_\theta$  and the normal is then calculated from the dot product:

$$\begin{aligned} \cos \theta_{Ea} &= \hat{E}_\theta \cdot (\hat{k} \times \hat{a}_n) = \hat{E}_\theta \cdot (\cos \theta_k \hat{x} - \sin \theta_k \cos \phi_k \hat{z}) = \cos \phi_k \\ \therefore \theta_{Ea} &= \phi_k \end{aligned} \quad (5-25)$$

We then apply the transmission coefficients as follows:

$$E_{\theta_t}(r, \theta_k, \phi_k) = (\tau_{\parallel} \sin \phi_k + \tau_{\perp} \cos \phi_k) E_{\theta_i}(r, \theta_k, \phi_k) \quad (5-26)$$

However, the value of  $\theta_i$  has yet to be related to  $\theta_k$  and  $\phi_k$ .  $\theta_i$  is of course the angle between  $\mathbf{k}$  and  $\mathbf{a}_n$ , which is given by:

$$\cos \theta_{ka} = \hat{k} \cdot \hat{a}_n = \sin \theta_k \sin \phi_k = \cos \theta_i \quad (5-27)$$

Using (5-26) and (5-27) together with the equations for  $E_\theta$ ,  $\tau_{\parallel}$  and  $\tau_{\perp}$ , one can now find  $\mathbf{E}$  in the plasma given a position at the boundary  $(r, \theta_k, \phi_k)$  relative to the antenna.

*Power Transmission.* The electric field found above can be used to calculate the power transmitted into the duct. The magnitude of the time-average Poynting vector is defined as:

$$\bar{P} = \frac{1}{2} \frac{|n|}{\mu c} (E)^2 \quad (5-28)$$

We have, for the incident wave:

$$\bar{P}_i = \frac{1}{2} \frac{n_0}{\mu_0 c} (E_{\theta_i})^2 \quad (5-29)$$

And, for the transmitted wave:

$$\bar{P}_t = \frac{1}{2} \frac{n_2}{\mu_0 c} (\tau_{\parallel} \sin \phi_k + \tau_{\perp} \cos \phi_k)^2 (E_{\theta_i})^2 \quad (5-30)$$

Then, the ratio of transmitted power to incident power is:

$$\frac{\bar{P}_t}{\bar{P}_i} = \frac{n_2}{n_0} (\tau_{\parallel} \sin \phi_k + \tau_{\perp} \cos \phi_k)^2 \quad (5-31)$$

This derivation is based on the transmitted electric field  $E_{\theta_t}$  found above. This transmitted field is, however, linearly polarized. Since we are interested in whistler waves, which are right-hand circularly polarized, we know that left-hand circularly polarized waves will be rejected. That is, at the frequencies of interest,  $n$  of equation (5-2) becomes purely imaginary for the + sign. The linearly

polarized  $E_{\theta_i}$  can be decomposed into left- and right-hand circularly polarized waves. The transmitted power is then half that obtained above. Further, we can substitute  $n_2 \cong 18.9$  and  $n_0 = 1$  in (5-31). The ratio of transmitted power to incident power for a given duct location relative to the antenna is given by:

$$K_{PT} = \frac{\bar{P}_t}{\bar{P}_i} = 9.45 (\tau_{\parallel} \sin \phi_k + \tau_{\perp} \cos \phi_k)^2 \quad (5-32)$$

where  $\tau_{\parallel}$  and  $\tau_{\perp}$  are given by (5-16) and  $\cos \theta_i$  is given by (5-27). Equation (5-32) is the constant of transmitted power and represents the end product of this work.

*Sample Calculation: Maximum Transmitted Power.* It can be shown from (5-32) that the maximum transmitted power occurs when  $\theta_k = \pi/2$ . A plot of  $K_{PT}$  for values of  $\phi_k$  is shown in figure 5-6 below. It is then apparent that maximum power transmission into the duct occurs when  $\theta_k = \pi/2$  and  $\phi_k \cong \pi/3$ . The value of  $K_{PT}$  is about 0.16, indicating a maximum of 16% transmitted power.

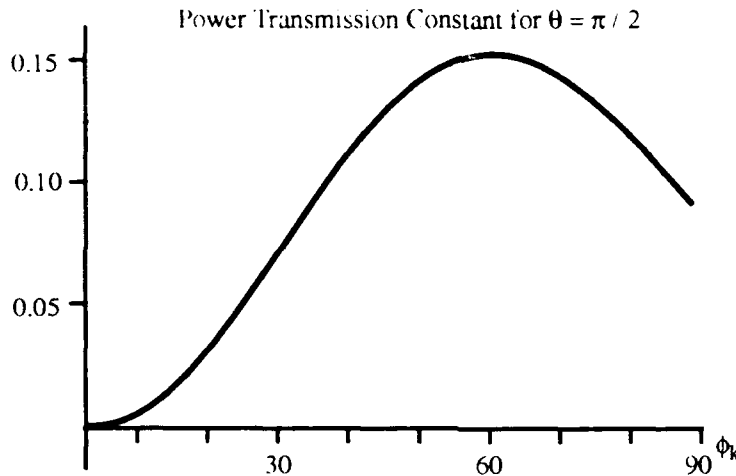


Figure 5-6: Plot of  $K_{PT}$  for  $\theta = \pi/2$

*Sample Calculation: Arecibo Scenario.* For the situation upon which this work is based, ducts are formed at Arecibo, Puerto Rico, while the antenna of the Navy transmitter is located at Aguada, Puerto Rico, approximately 80 km to the north. Assuming duct entrances at 100 km altitude, we examine two cases: east-west and north-south antenna orientation. For east-west orientation,  $\theta_k = \pi/2$  and  $\phi_k = \tan^{-1}(100/80) \cong 0.90$ . Then  $K_{PT} = 0.153$  and roughly 15% of the power is coupled. For north-south orientation,  $\theta_k \cong 0.90$  and  $\phi_k = \pi/2$ . Then  $K_{PT} = 0.093$  and roughly 9% of the power is coupled. Both results represent a large amount of power being lost into the upper atmosphere.

## Group Velocity and Energy Flow

The concept of group velocity applies to the velocity at which a wave packet travels through space. This wave packet may be represented as the beat frequency generated by the interference of two monochromatic waves of the same frequency traveling in slightly different directions, as shown in *figure 5-7*.

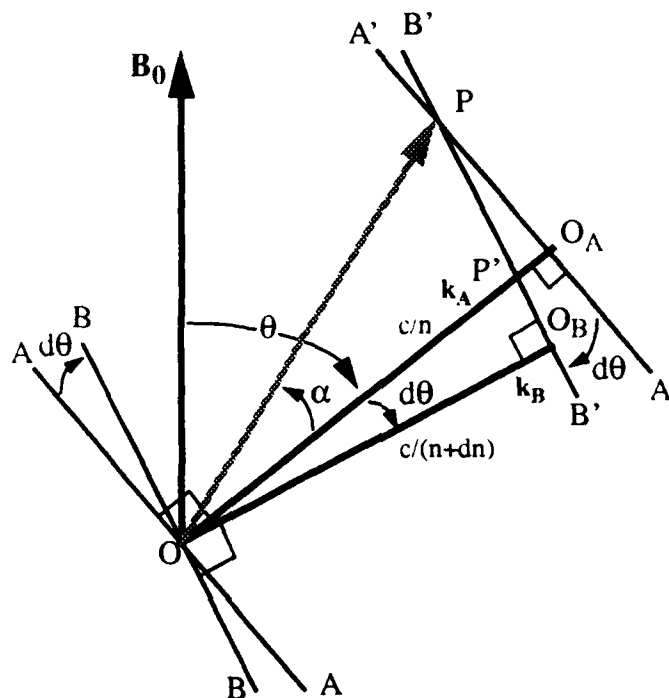


Figure 5-7: Geometry of Energy Flow

Wave A has wave normal  $k_A$  directed at an angle  $\theta$  from the ambient magnetic field  $B_0$ . Wave B has wave normal  $k_B$  directed at an angle  $\theta + d\theta$  from the field. The waves begin at point  $O$ , and wave fronts (equiphase lines) are drawn as  $AA$  and  $BB$  for the respective waves. After a unit time has elapsed, the two waves have traveled a distance equal to the speed of light divided by the refractive index in the direction of propagation. The two wave fronts then arrive at  $A'A'$  and  $B'B'$  after the unit time. The intersection of the two wave fronts, and therefore the location of the peak energy concentration, begins at point  $O$  but moves to point  $P$  as the waves propagate. The path between  $O$  and  $P$  is the path of peak energy flow and the direction of the group velocity.

In an isotropic medium, where  $dn=0$ , the two waves travel at the same speed. The path of peak energy flow and group velocity direction then correspond to the wave normal direction. However, in an anisotropic medium, such as the magnetized cold plasma considered here,  $n$  varies with  $\theta$ . The peak energy flow path then is generally not in the direction of the wave normal.

It is simple to relate the angle  $\alpha$  (between the energy flow direction and the wave normal) to  $n$  and its derivative with  $\theta$ . First, we examine the triangle  $PP'O_A$ . Note that:

$$P'O_A = OO_A - OP'$$

and that:

$$OP' = \frac{OO_B}{\cos d\theta} \cong OO_B \text{ since } \cos d\theta \cong 1$$

Then:

$$P'O_A = OO_A - OO_B$$

Further:

$$PO_A = P'O_A \times \frac{1}{\tan d\theta} \cong (OO_A - OO_B) \times \frac{1}{d\theta}$$

Now, examining triangle  $OPO_A$ , it is clear that:

$$\tan \alpha = \frac{PO_A}{OO_A} = \frac{OO_A - OO_B}{OO_A} \times \frac{1}{d\theta} = \frac{\frac{c}{n} - \frac{c}{n + dn}}{\frac{c}{n}} \times \frac{1}{d\theta} \quad (5-33)$$

Simplifying, we have:

$$\tan \alpha = \frac{1}{n} \frac{dn}{d\theta} \quad (5-34)$$

indicating that the angle  $\alpha$  depends on the magnitude of  $n$  and the change of  $n$  with  $\theta$ . For an isotropic medium, where  $dn/d\theta = 0$ ,  $\tan \alpha = 0$  and the energy flow follows the wave normal as expected.

## The Refractive Index Surface and Group Velocity

To relate the group velocity vector to the refractive index  $n$ , we make use of the  $n$ -surface. The refractive index vector is drawn from the origin in the direction of the wave normal with a length proportional to the value of  $n$  in that direction. As  $\theta$  is varied, the vectors trace a curve. Since the refractive index of a fixed point in the ionosphere varies only with the angle between  $\mathbf{B}_0$  and  $\mathbf{k}$ , the index of refraction surface is a figure of revolution obtained by rotating the curve described above about the  $B_0$  axis.

Consider first the refractive index curve shown in *figure 5-8*. Here the refractive index vector  $\mathbf{n}$  intersects the refractive index curve at point  $P$ . The tangent to the  $n$ -surface makes an angle  $\phi$  with the normal to  $\mathbf{n}$ . Following the same geometrical arguments given above for *figure 5-7*, it is easily shown that:

$$\tan \phi = \frac{1}{n} \frac{dn}{d\theta} \quad (5-35)$$

This is the same expression obtained for  $\alpha$  in (5-34), so  $\phi = \alpha$ . Simple geometry shows that  $\hat{v}_g$  is then perpendicular to the  $n$ -surface.

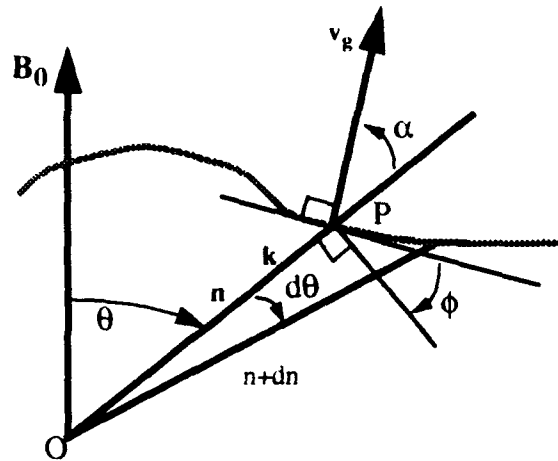


Figure 5-8: Geometry of Refractive Index Curve

A formula relating  $\alpha$  and  $\theta$  is easily derived. We begin with equation (5-7) for the index of refraction. Taking the square root of both sides yields:

$$n = \frac{A}{\sqrt{B(\cos\theta - B)}} \quad (5-36)$$

Substituting into (5-34) and simplifying, we obtain:

$$\tan\alpha = \frac{1}{n} \frac{dn}{d\theta} = \frac{\sin\theta}{2(\cos\theta - B)} \quad (5-37)$$

*Sample Calculation: Arecibo Scenario.* We take as an example the propagation of radio waves into ducts formed over Arecibo, Puerto Rico. As shown previously, the waves travel as whistler waves in the plasma approximately normal to the lower boundary, giving an angle between the ambient magnetic field and the wave normal of  $\theta = 40^\circ$ . Using the parameters described in (5-5), we find that  $\alpha \cong 17^\circ$ . Thus the direction of energy flow is at  $23^\circ$  to the magnetic field.

## Conclusion

This detailed analysis represents only a first-order attempt at estimating power transmission into ionospheric ducts for all incident angles. While by no means a complete model of the

process, it provides some insight into the interactions of ground-based VLF transmitters with the boundary between the ionosphere and the lower atmosphere. Further analysis of the problem will extend to ducted whistler modes, wave-particle interactions, and pitch-angle scattering and subsequent electron precipitation.

Refinements to the geometric optics model of power transmission include collisional damping and the analysis of more complex antenna arrays. This work will be carried out in the future.



## References

- [1] Aksinov, V.I., The Passage of Electromagnetic Waves of Super Low Frequency through Ionospheric Plasma, *Radiotekhnika i Elektronika* (English translation), *11*, 1030, 1966.
- [2] Chen, F. F., *Introduction to Plasma Physics and Controlled Fusion: Volume 1*. New York: Plenum, 1990.
- [3] Cheng, D. K., *Field and Wave Electromagnetics*, Second Edition. New York: Addison-Wesley, 1990.
- [4] Helliwell, R. A., *Whistlers and Related Ionospheric Phenomena*. Stanford: Stanford University Press, 1965.
- [5] Kelley, M.C., *The Earth's Ionosphere*. New York: Academic Press, 1989.
- [6] Kelley, M.C., et. al., Electrical Measurements in the Atmosphere and the Ionosphere over an Active Thunderstorm: 1. Campaign Overview and Initial Results, *J. Geophys. Res.*, *90*, 9815, 1985.
- [7] Maynard, N.C., T.L. Aggson, J.P. Heppner, Electric Field Observations of Ionospheric Whistlers, *Radio Science*, *5*, 1049, 1970.
- [8] Wolfram, S., *Mathematica™: A System for Doing Mathematics by Computer*. New York: Addison-Wesley, 1988.

THE IMPACT OF CONDENSING WATER VAPOR IN  
CHEMICAL OXYGEN IODINE LASERS.

Philip D. Whitefield  
Research Associate Professor  
Departments of Physics and Chemistry  
and  
W. Mark Barnett  
Graduate Student  
Department of Chemistry

Cloud and Aerosol Sciences Laboratory  
University of Missouri - Rolla  
Norwood Hall G11  
Rolla, MO 65401

*Final Report for:*  
Summer Faculty Research Program  
Phillips Laboratory (PL/LIDB)

Sponsored by:  
Air Force Office of Scientific Research  
Bolling Air Force Base, Washington, D.C.

and

University of Missouri - Rolla

September 1993

THE IMPACT OF CONDENSING WATER VAPOR IN  
CHEMICAL OXYGEN IODINE LASERS.

Philip D. Whitefield  
Research Associate Professor  
Departments of Physics and Chemistry  
and  
W. Mark Barnett  
(Graduate Student - Chemistry)  
Cloud and Aerosol Sciences Laboratory  
University of Missouri - Rolla

Abstract

This final report describes the results and interpretation of a joint research project sponsored by (i) AFOSR through its SRE, SFR and GSR programs and (ii) the University of Missouri - Rolla, to investigate the impact of condensing water vapor in the reacting flow regimes of chemical oxygen iodine lasers (COIL's). The "condensation shock phenomenon" first reported in 1991 has been successfully simulated and recreated under non-reacting flow conditions in two independent COIL devices. The two-phase singlet oxygen generator has been identified as the major source of particulates (condensation nuclei), especially those upon which heterogeneous nucleation can take place. These particulates have been characterized in terms of size distribution, total concentration, hydration and dependence on typical generator operating parameters such as chlorine flow rate, disc rotation rate, basic hydrogen peroxide concentration and temperature. Based on the heterogeneous nucleation characterization and known heat released into the laser supersonic flow during the "condensation shock" it is reasonable to conclude that both homogeneous and heterogeneous nucleation are responsible for water vapor condensation in the COIL devices, however, homogeneous nucleation is the dominant step in "condensation shock". Furthermore, the onset of the shock is readily observed at very low BHP temperatures.

# THE IMPACT OF CONDENSING WATER VAPOR IN CHEMICAL OXYGEN IODINE LASERS.

Philip D. Whitefield and Wm. Mark Barnett

## INTRODUCTION

Water vapor, when supersaturated, will spontaneously condense both heterogeneously and homogeneously, growing water droplets or aerosols provided the appropriate supersaturation is sustained. Heterogeneous nucleation requires the presence of condensation nuclei (CN) in the flow. The soluble mass fraction of the CN will determine its critical supersaturation spectrum which in turn determines the specific water vapor supersaturation for a given CN to grow without bound. Heterogeneous nucleation occurs at low supersaturations of water vapor typically  $< 5\%$ . At very high water vapor supersaturations homogeneous nucleation will occur. In this case it is thermodynamically favorable for molecules of water vapor to spontaneously cluster to form aerosols. In both cases the concomitant heat of condensation will be released into the gas flow. The criteria for both types of nucleation exist in supersonic COIL's and a massive heat release has been reported immediately following the supersonic expansion in several devices, especially where the water vapor pressure in the gas flow was thought to be high (typically 5 mole%).[1] Any increase in temperature in the cavity will manifest itself as a ramp in the laser cavity pressure profile, and will diminish the gain of the laser and reduce the optimum laser performance.[2] The relative importance of either type of nucleation channel must be determined for COILs if the impact of condensing water on the devices is to be characterized.

This report describes how the UMR Mobile Aerosol Sampling System (MASS) is being used in conjunction with a small scale supersonic COIL device (SSSC) to continue a study, initiated in 1992,[3,4] investigating the impact of condensing water vapor on the performance of COIL devices. The conclusions and recommendations from the 1992 study were as follows[3,4]:

- o Heterogeneously nucleated aerosols are present in COILs.
- o They are mechanically produced in the generator and their production rate and

size are governed by generator operating parameters.

- o The relationship between these parameters and aerosol production should be explored in detail.
- o The limits of detectability of aerosols using the UMR-MASS in its current state of the art configuration may have led to an underestimate of the total concentration of aerosols produced in the generator. As a result of the studies to date, design upgrades should be made to the sampling probe system and counting system to customize the UMR-MASS to this COIL investigation
- o The inability to simulate the pressure ramp in the supersonic nozzle flow system indicates that the pressure ramp is not a simple gas dynamic effect arising from the enthalpy of condensation associated with a homogeneous nucleation event.
- o The calculations upon which the homogeneous nucleation rational are based should be re-examined.
- o The principles of operation and performance of the spray generator concepts, as singlet oxygen generators for COIL's, should be examined to determine whether submicron aerosol formation will occur in these devices and whether it will affect their predicted performance.

The investigative approach in the preliminary study relied upon the UMR MASS to characterize any heterogeneous nucleation. In this very limited study although heterogeneous nucleation was observed it was not possible to correlate nucleus formation to generator operating parameters, or to quantify total nucleus production concentrations. As a result, it was impossible to determine what proportion of the heat release driving the pressure ramp in the cavity was due to heat of heterogeneous condensation. Using the experience gained from the preliminary studies a methodology was rationalized, to complete the characterization of the heterogeneous processes. The methodology and results of these experiments are described below.

Attempts were also made, in the preliminary study, to simulate or recreate the cavity pressure profile ramp downstream of a particle free supersonic expansion of a water laden gas flow, the rationale being that the cavity pressure profile ramp was a physical indication of a

purely gas dynamic "condensation shock"[5]. These experiments were not successful. Once again, based on the experience gained in the preliminary study a methodology was rationalized and a series of experiments were carried out to test the negative results of the preliminary study. This approach has led, in 1993, to several successful demonstrations of the condensation shock phenomena. The methodology and results of these experiments are, also described below.

## METHODOLOGY

The basic methodology behind the condensation shock phenomenon experiments has been described previously [3,4] and will not be repeated here. A novel approach in the 1993 studies involved the use of a pitot tube pressure sensor to define the boundary layers in the various COIL's examined in this study. The pitot tube methodology is described below. The heterogenous nucleation experiment methodologies are those of the UMR MASS and have been described in detail elsewhere [6-8] and therefore only a brief summary will be given here. The setup and operation of the laser device and supersonic nozzle facility is not described in this report. Detailed descriptions of this activity can be found elsewhere [9,10].

*The Pitot Tube - design and principles of operation:* In order to better understand the nature of the boundary layers in the nozzle and cavity flow regimes of the various COIL devices at our disposal during this study, a pitot tube was designed and constructed to measure the total pressure profile as a function of the vertical displacement of the pitot tube at various positions along the flow axis of the cavity, but in particular close to the expansion nozzles. Flow velocity can be interpreted in terms of "static" and "dynamic" pressure at any point in a flow regime. "static" pressure is measured at the cavity walls perpendicular to the supersonic flow direction. It is assumed to be fairly constant throughout a given cross-section. The "dynamic" pressure is extracted from pressure measurements made with the pitot tube. The pitot tube measures the total pressure of the supersonic flow by sampling parallel with and into the

supersonic flow direction. The thrust or "dynamic" pressure attributed to the supersonic flow is the difference between the total and "static" pressures, measured at any point in the flow. A schematic diagram of the "static" and total pressure measurement approach is given in figure (1). The orifice of the pitot tube has a diameter is  $8.1 \times 10^{-5} \text{m}$  and all pressure measurements were made using MKS Baratron pressure transducers calibrated against an NIST standard.

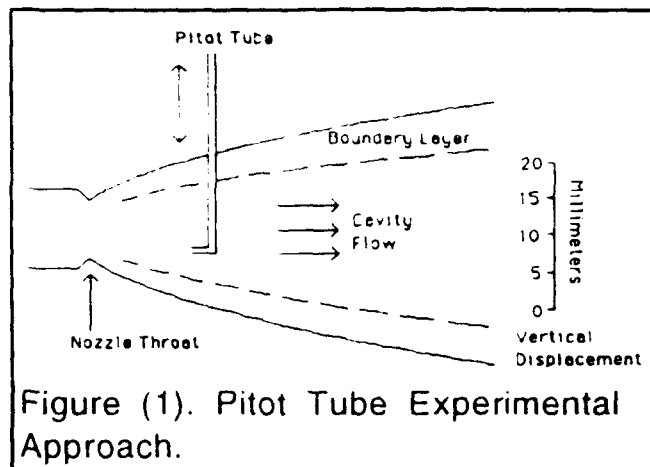


Figure (1). Pitot Tube Experimental Approach.

For the purposes of this experiment the boundary layer is defined in terms of the pitot tube measurements as that region of the vertical cross section "dynamic" pressure profile where the difference between the "dynamic" pressure and the "static" pressures approaches zero.

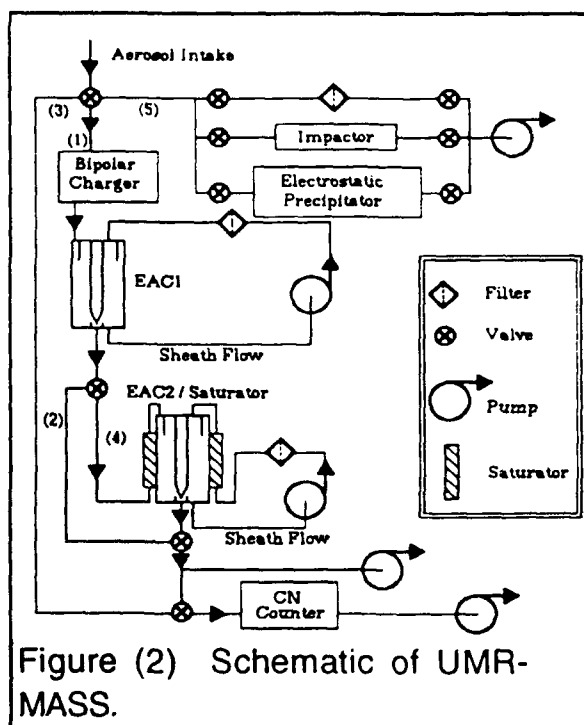


Figure (2) Schematic of UMR-MASS.

*Heterogeneous Nucleation Characterization Using the UMR/MASS:* The Mobile Aerosol Sampling System (UMR-MASS), figure (2) was employed to characterize aerosols in the gas flow of a COIL in terms of their total number density, size distribution and/or hydration properties. The MASS was operated in its rapid sample acquisition/storage mode, with off line sample analysis. This mode is employed under test conditions where it is not possible to characterize aerosol in real-time because the aerosol generation system (in this case the COIL) cannot be run continuously with fixed operating parameters for the time periods required to perform the characterization tests in

real time. Typical minimum continuous operation times of 3 minutes are required. The experimental sequence of events is as follows:

(a) Particulate Concentration Size Distributions - The particulate stream emanating from the sampling probe and dilution facility is sent through, initially, an alcohol counter to examine the total size range of aerosols sampled and determine the total concentration. For a size distribution the aerosol is charged with a bipolar charger and is then sized via its electric mobility using an electric aerosol classifier (EAC). The EAC passes only particles contained in a narrow size range (typically 10% of mean size). A specific particle size is set by the EAC voltage. This voltage and hence the selected particle size is variable. The resulting monodisperse particle stream is then passed through the alcohol counter where it is exposed to a fixed supersaturation of alcohol of sufficient magnitude to condense alcohol on the particle, thus forming aerosols large enough to be detected by the optical particle counter, OPC, sub system of the counter. The enlarged aerosols are passed through the OPC where individual aerosols are counted and the aerosol concentration is determined.

(b) Hydration Properties - For particulate hydration property measurements, specifically the critical supersaturation spectrum (i.e. the minimum supersaturation of water that will cause condensation of water onto a particle to produce a continuously growing droplet presented as a function of particle diameter) is measured. The particulate stream is first passed through an EAC to select a specific size element of the sample distribution. The resulting monodisperse element is then passed through a saturation chamber holding water vapor at 100% relative humidity. As the aerosols pass through the chamber they deliquesce and increase in diameter. This growth is monitored by passing the droplets, after they exit the saturator, through a second EAC, the output of which can be monitored by the alcohol counter. Should a particulate prove difficult to hydrate ( i.e. require significant supersaturation (>1%) of water a continuous flow diffusion chamber (CFD) is employed. (For a more detailed description of the overall UMR approach to particulate measurements, see references 11-14).[11-14]



## RESULTS

### Simulation of "Condensation Shock" in COILs operated under cold flow conditions.

*The Small Scale Supersonic Device (Preliminary Results):* In the preliminary study, [3,4] of the condensation shock phenomenon an SSSC was used to attempt the simulation. A schematic diagram of this device indicating the various components, flow regimes and sampling ports is given in figure (3). During the 1992 experimental campaign this device was considered to be identical to the COIL device in which the pressure ramp had originally been detected[1] and similar results were expected from the SSSC. As reported initially [3,4] no pressure ramp could be detected. This was later explained by an over-simplification of the gas mixtures employed in those initial simulation studies where just nitrogen and water vapor were employed. The actual laser mixture

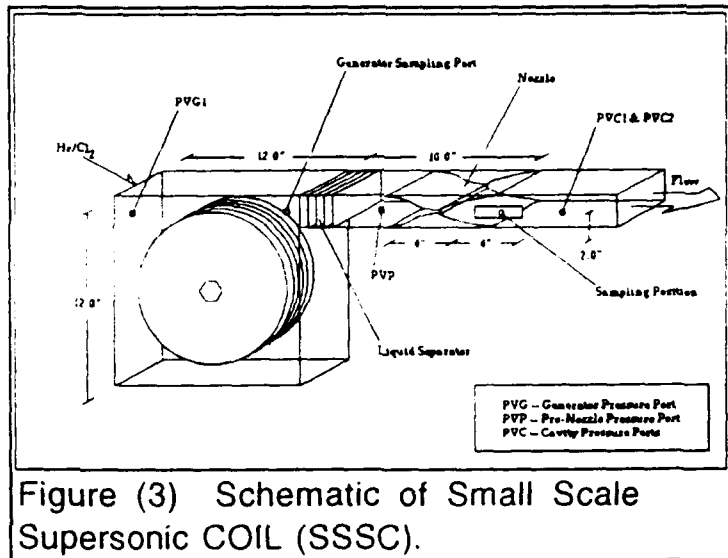


Figure (3) Schematic of Small Scale Supersonic COIL (SSSC).

constituents are helium, oxygen and water vapor, with helium as the bath gas constituting the major part of the flow (75%)[10]. In retrospect, it was reasonable to substitute oxygen with nitrogen but not helium with nitrogen. The significant difference in their heat capacities forfeits such a substitution ( $C_{(\text{Nitrogen})} = 29.124 \text{ J/}[\text{mole}\cdot\text{K}]$  ,  $C_{(\text{Helium})} = 20.786 \text{ J/}[\text{mole}\cdot\text{K}]$ ).[15]

Further simulation experiments were performed after the submission date of the 1992 report [3] using helium, nitrogen, water vapor mixtures. They were successful in detecting pressure ramps in the cavity, however, the increases in pressure were small compared to the original experimental results. These data have subsequently been published elsewhere[16]. A typical maximum pressure increase was found to be on the order of 10-20% significantly smaller than the originally reported 40% [1]. The assumption that the devices could be considered identical was re-examined. There was some indication that the supersonic expansion nozzle configurations were different. If this were so it would be reasonable to assume that the boundary layers, created in the nozzle region during the supersonic expansion, in each of these devices could be different. Dissimilar boundary layers would explain the difference in the

pressure ramps since these boundary layers define the supersonic flow cross-section and the effective gas volume into which any heat of condensation could be released. For example a thick boundary layer will reduce the effective supersonic flow volume which in turn will result in a diminished pressure ramp.

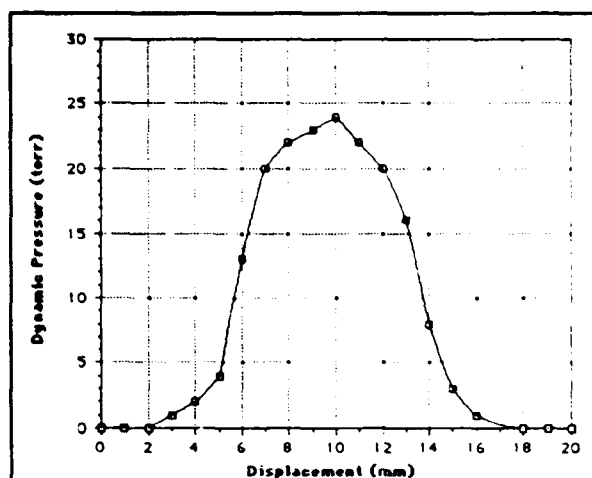


Figure (4) Boundary Layer of SSSC Cavity Downstream of Throat.

*Boundary Layer Definition:* Before proceeding further with the simulation experiments it was decided that the boundary layer issue should be resolved. The pitot tube pressure sensor, described above, was used to measure the "dynamic" pressure, as a function of the vertical displacement in the cavity close to the supersonic nozzle exit plane in the small scale

device. These data are presented in figure (4), where the flow parameters were, for the primary flow: He -  $110 \times 10^{-3} \text{ mole.s}^{-1}$ ,  $\text{N}_2$  -  $35 \times 10^{-3} \text{ mole.s}^{-1}$  and the secondary flow: He -  $60 \times 10^{-3} \text{ mole.s}^{-1}$  with the pitot tube port located 2.5 inches (0.06 meters) downstream of the nozzle throat. These data clearly reveal a massive boundary layer occupying as much as 50% of the cavity flow volume in the region of the vertical displacement of the pitot tube. The rounded appearance of the pressure profile indicates that the boundary layers converge. The profile was only measured at one position in the cavity however successive measurements demonstrated excellent reproducibility.

It was not possible to define the actual boundary layer conditions of the device in which the original shock observations were made.[1] However, another COIL device (RADICL) [9, 10], was available, although, much larger than the SSSC device that had been

used to date. The boundary layer for this device was characterized using the pitot tube method

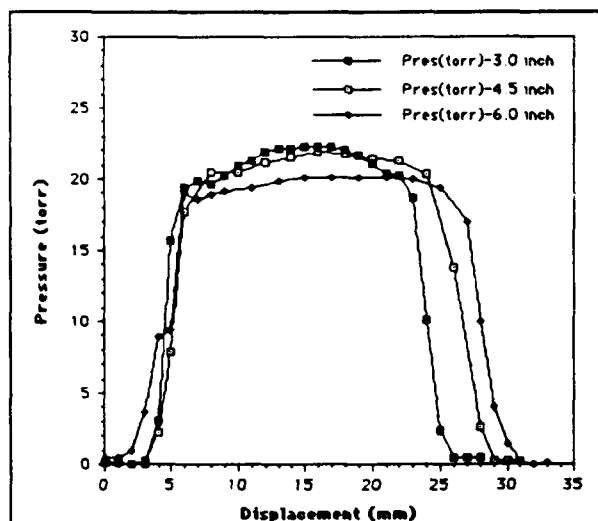


Figure (5) Boundary Layer for RADICL Downstream of Throat.

described above. The data from these experiments is given in figure (5). In the case of the RADICL measurements, profiles were obtained at four discrete locations along the flow axis in the cavity. Even though the geometry of the RADICL cavity differs slightly from that of the SSSC device, it is clear that the boundary layer in RADICL is much smaller. Also, in the region of high total pressure (typically 85% of the flow volume) the profiles are flat indicating the supersonic core is broad and uncompromised.

*Condensation Shock Simulation with RADICL:* The boundary layer results for RADICL indicated that a measurable shock would be more likely to be observed in RADICL than in the SSSC device, therefore, shock simulation studies were transferred to RADICL. Unlike the small scale device RADICL cannot be run by one or two individuals with a few minutes notice. Instead all experiments have to be scheduled in advance or have to be "piggybacked" on previously scheduled tests. Nevertheless, data were obtained. The shock indicator, as described previously, is a change in magnitude of the ratio of the "static" pressure in the supersonic cavity to that in the subsonic generator region ( $P_{cav} : P_{gen}$ ). In the absence of a condensation shock, a condition that can be achieved by

eliminating all water vapor from the flow, this ratio remains constant for a fixed set of run conditions. A typical plot of the constant pressure ratio profile as a function of time is given by the solid line in figure (6a). When water vapor is added to the flow, if the condensation shock model is correct, at an appropriate water vapor concentration, to be determined, the threshold supersaturation of water vapor in the cavity will exceed that required for homogeneous nucleation. Nucleation occurs instantaneously under these conditions and is accompanied by a rapid release

of heat (heat of condensation), this is the so called shock. This heat is released into the supersonic gas flow and manifests itself as a localized pressure increase in the cavity.

A thermally controlled 30% aqueous solution of potassium hydroxide, initially cooled to 243K, was used as a variable water vapor concentration source. The cold solution was placed in

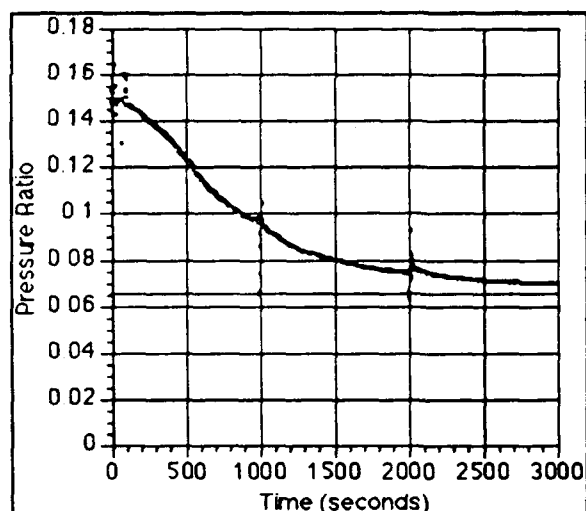
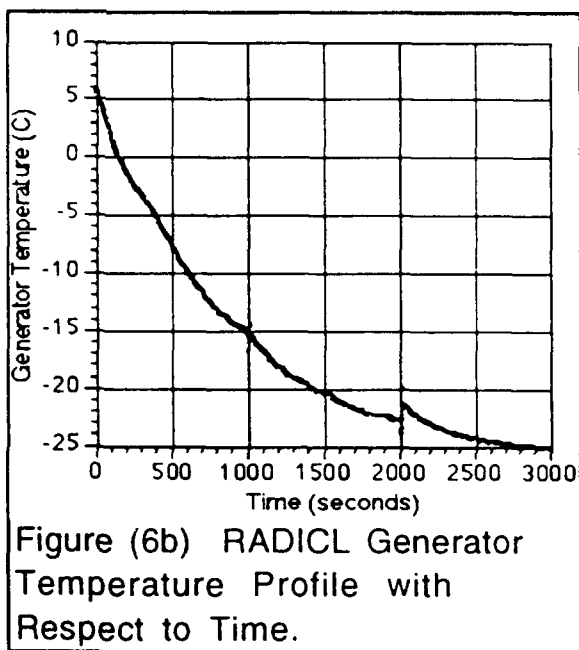


Figure (6a) RADICL Pressure Ratio Profile with Respect to Time.

the RADICL generator, a helium nitrogen (3:1) mixture was passed at subsonic speeds through the generator and duct, where it entrained water vapor, the concentration of which was controlled by the bulk solution temperature. In the absence of any active cooling of the KOH solution, the solution temperature steadily increased with time as it sought to come to thermal equilibrium with its surroundings. During this period the KOH solution temperature, and the pressure ratio of the cavity to the duct were monitored. The pressure ratio profile is plotted in figure (6a) and the temperature profile is plotted in figure (6b).



#### Characterization of Heterogeneous Nucleation:

Based on the findings of the preliminary study of heterogeneous nucleation [3, 4] the measurements in the current study were confined to samples taken in the subsonic, post-generator, pre-cavity regions of the SSSC device (see figure (3)). Since it was clear from the preliminary study, that the particulate production rate was not coupled to either, the bulk temperature in the generator, or the presence of iodine in the flow these parameters were not re-investigated in the current study. As previously reported the largest particulate production rates occurred in

the immediate vicinity of the rotating disc generator during the passage of chlorine gas over the BHP wetted disc walls. In the current study, therefore, the parameters: disc rotation rate, BHP concentration as a function of the age of BHP mixture, neutralization salt concentration, also as a function of the age of the BHP mixture and chlorine flow rate were examined for any correlation to particulate production rate.

**Disc Rotation Rate:** Disk rotation rates were varied within the range 0-45 rpm (where 45rpm is considered the optimum disc rotation rate for singlet oxygen production). The discs were rotated in a BHP solution but in the absence of a chlorine flow. The particle number densities increased with increasing rotation rate, however, at 45rpm the maximum particle number densities recorded did not exceed  $5 \text{ cm}^{-3}$

**BHP Concentration:** During the course of a days testing on a single batch of BHP, periodic samples of BHP were drawn from the generator and titrated for the hydroperoxide anion [17]. These titrations repeatedly showed the concentration of the hydroperoxide ion to be relatively constant during the lifetime of the mixture during which time the BHP was being exhausted. For example a typical batch had a 9.5M hydroperoxide ion concentration, initially, and a 9.1M concentration at the end of the test, with a 9.3M mid-test value.

**Neutralization Salt Concentration:** As a batch of BHP solution is exhausted, during the course of a days testing, large concentrations of potassium chloride (KCl) build up in solution and eventually start to precipitate as the BHP solution approaches saturation with respect to KCl (~2% mass solubility in BHP). Observations of the particulate number densities present in the generator measured, between chlorine flow periods, but with a disc rotation rate of 45rpm in an aging BHP mixture demonstrated a reproducible increase in particulate number density with KCl build-up. For example a fresh BHP solution would yield typically  $5 \text{ cm}^{-3}$  at 45rpm and after 5 chlorine runs this number would increase to  $60 \text{ cm}^{-3}$ .

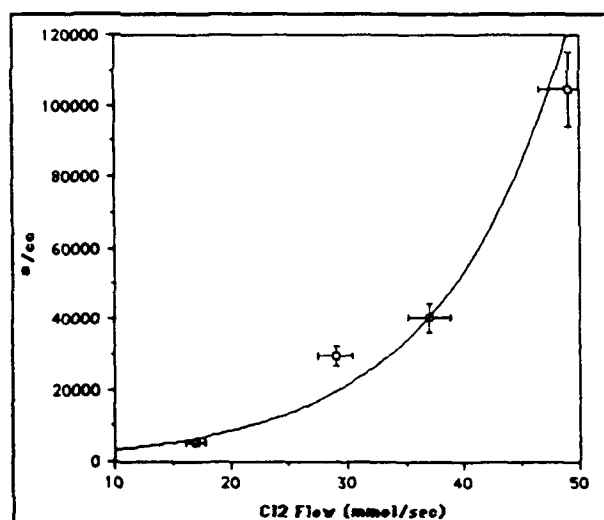


Figure (7) Particulate Concentration as a Function of Chlorine Flow Rate.

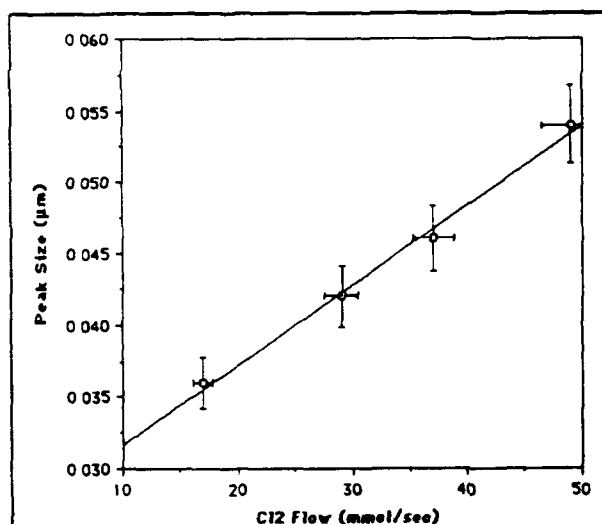


Figure (8) Peak Particle Diameter as a Function of Chlorine Flow Rate.

**Chlorine Flow rate:** At a typical chlorine flowrate of  $37 \times 10^{-3} \text{ moles.s}^{-1}$  and total generator pressure of 56 torr the mean particulate concentration is  $1.45 \times 10^4 \text{ cm}^{-3}$ . This is three orders of magnitude greater than the concentrations generated by any other process. The total concentration of particles is determined either by integrating the size distribution function

over a specific size range or by monitoring the total concentration of particulates with a CNC counter. Both methods were employed in this study and good agreement was obtained between them. Figure (7) is a plot of the total concentration as a function of chlorine flow rate. The particulate yield correlates exponentially with the chlorine flowrate over the flow range studied (i.e.  $0 - 50 \times 10^{-3} \text{ moles.s}^{-1}$ , yielding a maximum particulate concentration in excess of  $1 \times 10^6 \text{ cm}^{-3}$ . These data are a clear indication that chlorine flow rate is the primary generator operating parameter controlling particulate production. The peak size of the particulates demonstrates a linear correlation with the chlorine flow rate, indicating a shift in the size distributions to larger mean particulates at higher chlorine flows. Typical data are presented in figure (8).

## DISCUSSION

### Condensation Shock Simulation

These data represent the first detailed investigation of the potential for, and characteristics of "condensation shock" in COIL devices. The simulation experiments described here, when combined with the findings of the heterogeneous nucleation studies, also described here, lead to the following inferences.

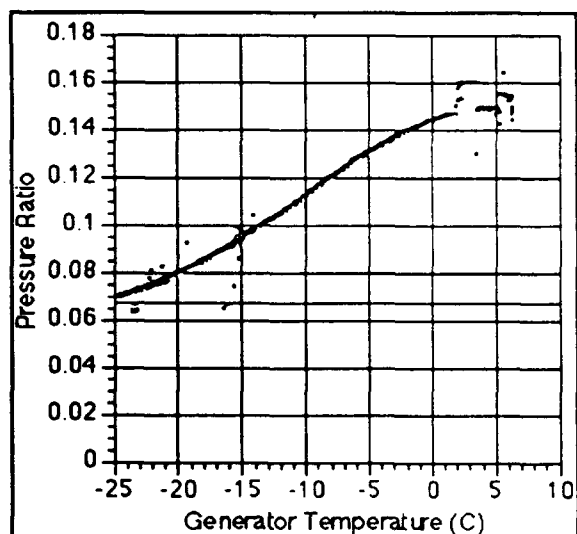


Figure (9) RADICL Pressure Ratio as a Function of Generator Temperature.

A gas dynamic condensation shock can be induced in COIL devices in the absence of any condensation nuclei. Figure (9) is a plot of pressure ratio versus temperature for RADICL derived from the data in figures (6a) and (6b). The dry system pressure ratio line is included for comparison. The  $P(\text{ratio})$  versus  $T$  plot can be seen to diverge from the "dry line" as  $T$  increases. The rate of divergence increases from 253K to 268K. It, then, slows and approaches zero at  $T = 278\text{K}$ . This divergence is direct evidence of the onset of condensation shock and can be entirely attributed to the heat released during the "shock". Calculations using the 3-D MINT code by Plummer

and coworkers at RDA-Logicon [18] successfully model these results and explain the asymptotic behavior as the onset of choked flow in the cavity due to the heat of condensation released into the flow during the shock.

The concentrations of aerosols emanating from the generator, ( $\sim 10^6 \text{ cm}^{-3}$ ), are not large enough to contribute significantly to the total heat released into the flow through condensation. It is reasonable to assume, however, that heterogeneous and homogeneous condensations are taking place simultaneously in COILS. Furthermore, in the case of RADICL, evidence of the shock (in the P ratio vs T plot) at very low temperatures (i.e. low partial pressures of water) is clearly observed. It is not possible to determine the total water concentration with the current experimental configuration. An upper limit for this concentration could be taken as the equilibrium vapor pressure of water above the KOH solution. A sensitive absolute water vapor concentration diagnostic is being constructed currently. It will be used to profile the massive change in the water vapor concentration in the laser cavity at the onset of the shock. The latter will be monitored by the pressure versus temperature profile as in figure (9). Such data will unequivocally validate the theory of condensation shock as it affects COIL devices. These experiments are planned for this fall when the state of the art water vapor diagnostic is to be delivered. It is hoped that these results will then be incorporated into the AIAA paper planned for publication of this work and the SREP contract report due in December 1993.

#### Heterogeneous Nucleation

The results of this study and the preceding preliminary study clearly demonstrate that heterogenous nucleation is not necessary to create a condensation shock in COIL devices. They further demonstrate, that the maximum concentration of particulates generated under typical COIL operating conditions, although large, is orders of magnitude too small to account for the heat release detected via the pressure ratio divergence data as seen in figure (9). These nucleation data, however, are important. A production mechanism was suggested in the preliminary study: " These results indicate that heterogeneously nucleated aerosols are mechanically generated during the explosion of gas bubbles on the basic hydrogen peroxide (BHP)/chlorine interface and that certain generator operating parameters such as disc velocity and degree of neutralization of the BHP can strongly influence the aerosol production rate." [3,4]. The data from the current study support this mechanism but take our understanding of the process further. The particulate production rate and size distributions depend primarily on the chlorine flow rate. The data acquired to date indicates the dependence to be exponential for total concentration and linear with respect to the shift in the peak size of the size distribution. The sampling techniques and dilutions employed in this study eliminate the potential for agglomeration of particulates, that might skew the data in such a manner [19].

## CONCLUSIONS

The following conclusions can be drawn from this study:

- Condensation shock occurs in COIL devices even at extremely low water vapor concentrations.
- The onset of the shock will directly impact the gain of the device in which it occurs.
- Heterogeneous nucleation is controlled primarily by the chlorine flow rate into the generator.
- Nuclei production rates grow exponentially with increasing chlorine flow rate.
- Nuclei diameters increase with increasing chlorine flow rate (0.033-0.055  $\mu\text{m}$  for the chlorine flow range investigated in this work).
- The onset of foaming in the generator is indicative of massive sub-micron nuclei production rates.
- The next generation of COILs may employ spray generators. These generators should be examined to define their characteristics with respect to condensation shock and heterogeneous nucleation if their performance is to be accurately compared to current wetted-wall type generators as are found in the SSSC and RADICL.

## REFERENCES

- ( 1) Private Communication, D. Plummer RDA, 19 July 1991.
- ( 2) RDA Memo 87-A/K-3-02-752 Particulates/Aerosols in Oxygen/Iodine Lasers, P.G. Crowell, January 1989.
- ( 3) Whitefield, P.D., AFOSR-SFRP Final Report September 1992.
- ( 4) Whitefield, P.D., AFOSR-SREP Final Report December 1992.
- ( 5) Fundamentals of Gas Dynamics, Editor H.W. Emmons, Princeton University Press, 1958.
- ( 6) Hagen, D.E., M.B. Trueblood, and J. Podzimek, "Combustion Aerosol Scavenging", Atmos. Env. 25A, 2581 (1991).
- ( 7) Hagen, D.E., Whitefield P.D., and M.B. Trueblood, "A field Sampling of Jet Exhaust Aerosols." Particulate Science and Technology, 10, 53, 1992.
- ( 8) Whitefield, P.D., M.B. Trueblood and D.E. Hagen, "Size and Hydration Characteristics of Laboratory Simulated Jet Engine Combustion Aerosols," Particulate Science and Technology, 11, 25, 1993.
- ( 9) Review of Modern Physics vol. 59, No.3 paper II, July 1987 pp 541-546
- ( 10) Oxygen Iodine Supersonic Technology Program, Part III - Management and Technical



Proposal, MDRL/MDAC Report No. D9299-953003, June 1982.

- ( 11 ) Alofs, D.J., "Performance of a dual-range cloud nucleus counter", J. Appl. Meteor. 17, 1286-1297 (1978).
- ( 12 ) Alofs, D.J., M.B. Trueblood, D.R. White, and V.L. Behr, "Nucleation experiments with monodisperse NaCl aerosols", J. Appl. Meteor. 18, 1106-1117 (1979).
- ( 13 ) Hagen, D.E., and D.J. Alofs, "A Linear Inversion Method to Obtain Aerosol Size Distributions from Measurements with a Differential Mobility Analyzer", Aerosol Sci. and Tech. 2, 465-475 (1983).
- ( 14 ) Alofs, D.J. and M.B. Trueblood, "UMR Dual Mode CCN Counter (Modes:CFD plus Haze)," J. Rech. Atmos. 15, n° 3-4, 219-223 (1981)
- ( 15 ) CRC Handbook of Physics and Chemistry 73rd Edition, 1992.
- ( 16 ) Whitefield, P.D., D.E. Hagen, M.B. Trueblood, W.M. Barnett and C. Helms, SPIE vol 1871 Intense Laser Beams and Applications (1993) pp 277-288.
- ( 17 ) Richardson, R.J., Wiswall, C.E., Carr, P.A.G., Hovis, F.E., and Lilienfeld, H.V., "An Efficient Singlet Oxygen Generator For Chemically Pumped Iodine Lasers", J. Appl. Phys. 52, 4962-4969, (1981).
- ( 18 ) RADICL Data presented at a briefing on the condensation shock phenomena by D. Plummer RDA, August 1992.
- ( 19 ) Whitefield, P.D., D. E. Hagen and H.V. Lilienfeld Geophysica Acta (submitted September 1993)

IMPLEMENTATION OF A NEAR-INFRARED ARRAY CAMERA  
FOR SPECKLE IMAGING

Mary Ann Hickman  
Graduate Student  
Department of Physics and Astronomy

University of Wyoming  
Laramie, WY 82071

Final Report for:  
Graduate Student Research Program  
Phillips Laboratory

Sponsored by:  
Air Force Office of Scientific Research  
Bolling Air Force Base, Washington, D.C.

August 1993

IMPLEMENTATION OF A NEAR-INFRARED ARRAY CAMERA  
FOR SPECKLE IMAGING

Mary Ann Hickman  
Graduate Student  
Department of Physics and Astronomy  
University of Wyoming

Abstract

The near-infrared camera from Infrared Laboratories was acquired for use on the 1.5 meter telescope at Starfire Optical Range. Ultimately, the camera will be used for speckle imaging of satellites. Normally, detectors using the 1.5-meter are located in a coud'e room or in the imaging lab. For infrared detection, however, the camera must be on or near the telescope since the many mirrors and lenses required to pipe light into a neighboring building allow very little infrared radiation to be transmitted. Due to the size of the camera dewar, a mount was constructed for the camera on the telescope. Testing of the camera and electronics proved successful. It is clear that all mirror optics must be used in the future for optimal transmission. Methods for reducing the data once it is acquired still need to be perfected.

## Contents

- 1 Introduction
- 2 The IR Labs Camera
  - 2.1 Detector
  - 2.2 Computer Control
  - 2.3 Filters
- 3 Data Flow
- 4 Software Support
- 5 Camera Mounting
  - 5.1 Mechanics
  - 5.2 Optics
- 6 Testing
  - 6.1 Observing Program
  - 6.2 Calibration
  - 6.3 Focusing
- 7 Future Improvements
  - 7.1 Tracker
  - 7.2 Mirror Optics
  - 7.3 Cryogenics

# IMPLEMENTATION OF A NEAR-INFRARED ARRAY CAMERA FOR SPECKLE IMAGING

Mary Ann Hickman

## 1 Introduction

Advances in the technology of infrared detectors made possible the development of imaging arrays for infrared wavelengths similar to the charge-coupled device now the standard for optical imaging. Previously, infrared detectors were single-element devices which gave only information about object intensity. No spatial information was available. Now, imaging at infrared wavelengths is possible. One result of this advance is the ability to perform speckle imaging of objects in the infrared. With both intensity and spatial information available, high-resolution images can now be obtained.

Why is infrared imaging of value? Other than simply allowing us to learn the nature of an object's appearance at non-visual wavelengths, infrared imaging makes possible detection of objects which may not be luminous enough at visual wavelengths to image well but are much more luminous at longer, and hence cooler, wavelengths. Also, daytime acquisition is possible with infrared detectors. In the infrared, the sky is equally luminous both day and night. The only limit on daytime imaging (other than avoiding objects near the sun) is the pointing and tracking accuracy of the telescope, since one cannot rely on optical tracking cameras to center an object in the infrared camera during the day.

## 2 Camera System

### 2.1 Detector

The detector for the infrared camera is a NICMOS 3 HgCdTe array. Actually, the detector consists of four 128 X 128 pixel arrays which are configured to simulate a 256 X 256 array. One of the four arrays is dead. Currently, only one of the three operational arrays is in use.

The NICMOS variety of detectors differ from CCD detectors in that the NICMOS array may be read without resetting. This produces the problem of the part of the chip integrating while another part is being read, leading to uneven exposure of the chip. To avoid this problem, a shutter was placed in front of the camera window to allow an even exposure of the array. The shutter had a

reflective coating so that when the shutter was closed, the detector saw the cool interior of the dewar.

## 2.2 Computer Control

All camera functions are controlled by a 286 computer. Commands are executed in the PROCOMM environment. To enter PROCOMM, execute the following series of commands:

```
C:\> D:
```

```
D:\> CD\PROCOMM
```

```
D:\PROCOMM> PROCOMM
```

Once in PROCOMM, load the default camera commands by:

```
<ALT>M      (to select Macro menu)
```

```
L           (to load a Macro)
```

```
setup       (loads camera commands)
```

```
<ESC>       (returns to main program)
```

When ready to begin camera operation, execute commands <ALT>1 through <ALT>6.

To stop the camera, type <ALT>7. To reset the camera, type <ALT>10.

Currently, the default mode of operation is reset-read-integrate-read.

## 2.3 Filters

The filters which are provided with the camera are standard J, H, and K broadband filters. The K filter is of particular interest because one begins

FILTER	EFF. WAVELENGTH (microns)	BANDPASS (microns)
J	1.25	1.1 - 1.4
H	1.65	1.5 - 1.8
K	2.20	2.0 - 2.4

to see thermal features at 2.2  $\mu$ m, yet the thermal background is still relatively low. Also, gas and dust which are opaque at visual wavelengths become transparent at 2.2  $\mu$ m. This allows imaging of dust-obscured objects such as

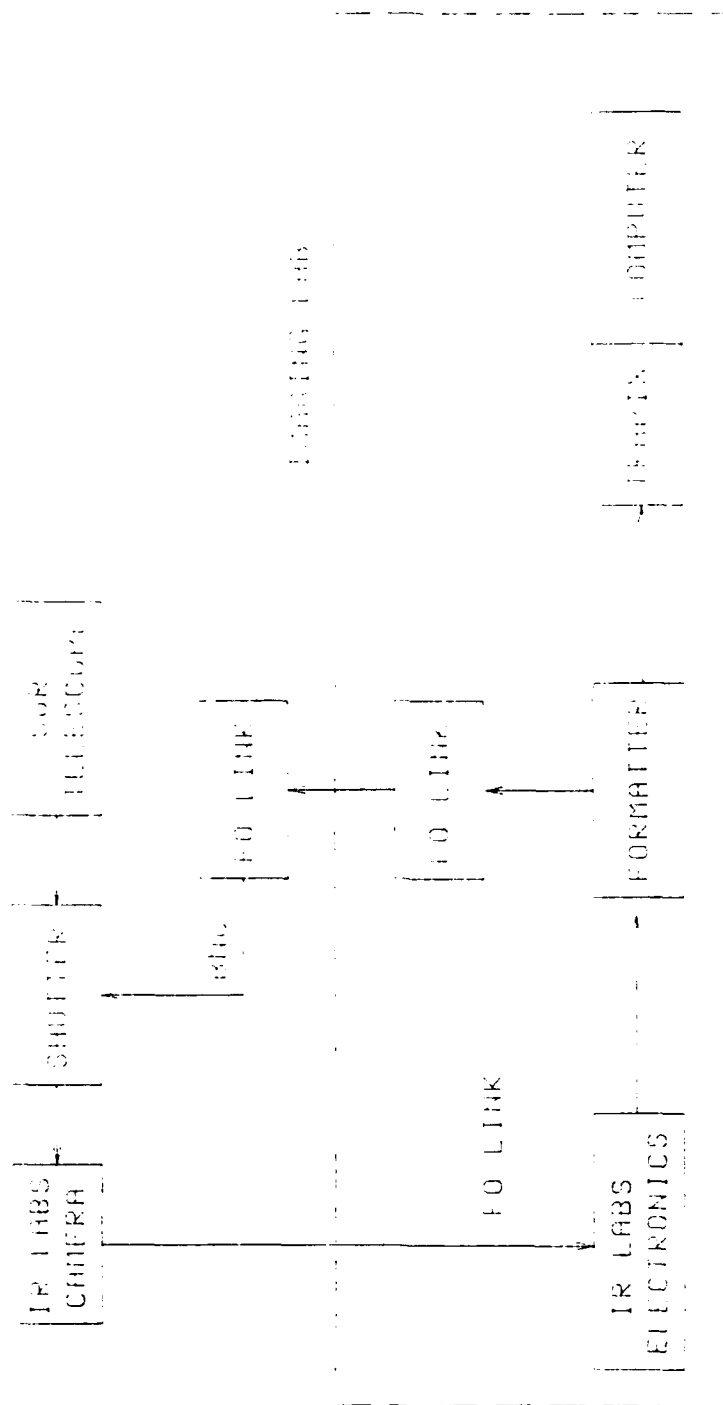
star-formation regions.

The filters and dark slide are on a wheel which may be turned manually by the dome operator or remotely via the camera control computer. Details of the commands may be found in the camera manual.

### 3 Data Flow

A primary concern of this experiment was getting the data from the camera to the acquisition computer in the imaging lab. Infrared Laboratories designed the camera system to use a fiber optic link for two-way communication between the electronics on the telescope and the electronics in the imaging lab. The shutter and eventually a tracker must also be linked to the imaging lab electronics to coordinate them with the camera operation. A fiber optic link between the shutter and the formatter was chosen. The fiber optic link boxes used to convert signal from a regular BNC cable to optical fiber and back were borrowed from the ADONIS experiment. When a tracker is added to the system, the same boxes will support it, as well.

Figure 1. Data Flow of the Infrared Camera System.





#### 4 Software Support

A Microvax computer with the Trapix data acquisition system was already installed in the imaging lab at SOR. Existing software for acquiring data with the Trapix was modified to suit the purposes of the IR camera experiment by Bob Pierson of Applied Technology Associates. Calibration software written for the FLOODBEAM experiment was also modified for use with the IR camera.

#### 5 Mounting and Optics

##### 5.1 Mechanics

Since the telescope optics are optimized for visual, not infrared, wavelengths, one must be concerned with the infrared transmission of elements in the optical path. Thus, the infrared camera must be as close to the telescope as possible. Ideally, it would be mounted at the cassegrain or even the prime focus of the telescope. Since this is not possible on the 1.5-meter SOR telescope, the M5 focus (analogous to the nasmyth focus) was chosen. With five mirrors and a lens in the light path, transmission at  $2.2\text{ }\mu\text{m}$  is estimated to be only 57%. Additional optics to direct the light into the camera reduce transmission even more.

The dewar which contains the detector and filters is rather large; much too large to mount on the test plate at M5. Originally, plans called for constructing a shelf which would attach to the plates protecting the M5 mirror. However, the combined mass of the dewar, the electronics, and the shelf itself would be too much to place on one side of the telescope. The alternative plan called for mounting the camera and electronics on the front of the telescope on a shelf which would take the place of a removable plate. This is the design which was approved, with the agreement that any equipment which sat on the telescope yoke would be removed at the end of each evening's observations.

##### 5.2 Optics

The light from the M5 lens was directed to the camera by a flat mirror. The beam then passed through a lens which provided the detector an approximately 10 arcsecond ( $48\text{ }\mu\text{R}$ ) field of view. Next, there was a beamsplitter which transmitted the infrared light to the camera while reflecting the visual light

back to a CCD camera on the M5 test plate. The CCD image was used by the telescope operator to center the object on the IR camera. Finally, a mechanical shutter was placed directly in front of the camera window.

The flat mirror was on a kinematic mount on the test plate. The beamsplitter, reimaging lens, and shutter were supported by a piece of aluminum channel which ran between the camera mount and the M5 test plate (please see Figure 4). Both the beamsplitter and lens were mounted on translation stages to facilitate alignment and focusing. The beamsplitter (serial number: 93048) has an Infrasil substrate and a dichroic coating which transmits wavelengths longer than  $1.2\text{ }\mu\text{m}$  while reflecting wavelengths from  $.60\text{ }\mu\text{m}$  to  $1.2\text{ }\mu\text{m}$ . The reimaging lens (serial number: 93068) is a cemented achromat made for the ADONIS project. It has a focal length of 120 mm and a  $150\text{ }\mu\text{R}$  field of view. Of course, since this lens was designed to be achromatic at visual wavelengths, it is not completely achromatic at the infrared wavelengths with which this experiment was concerned.

Figure 2. Mounting Plate for Camera Support.

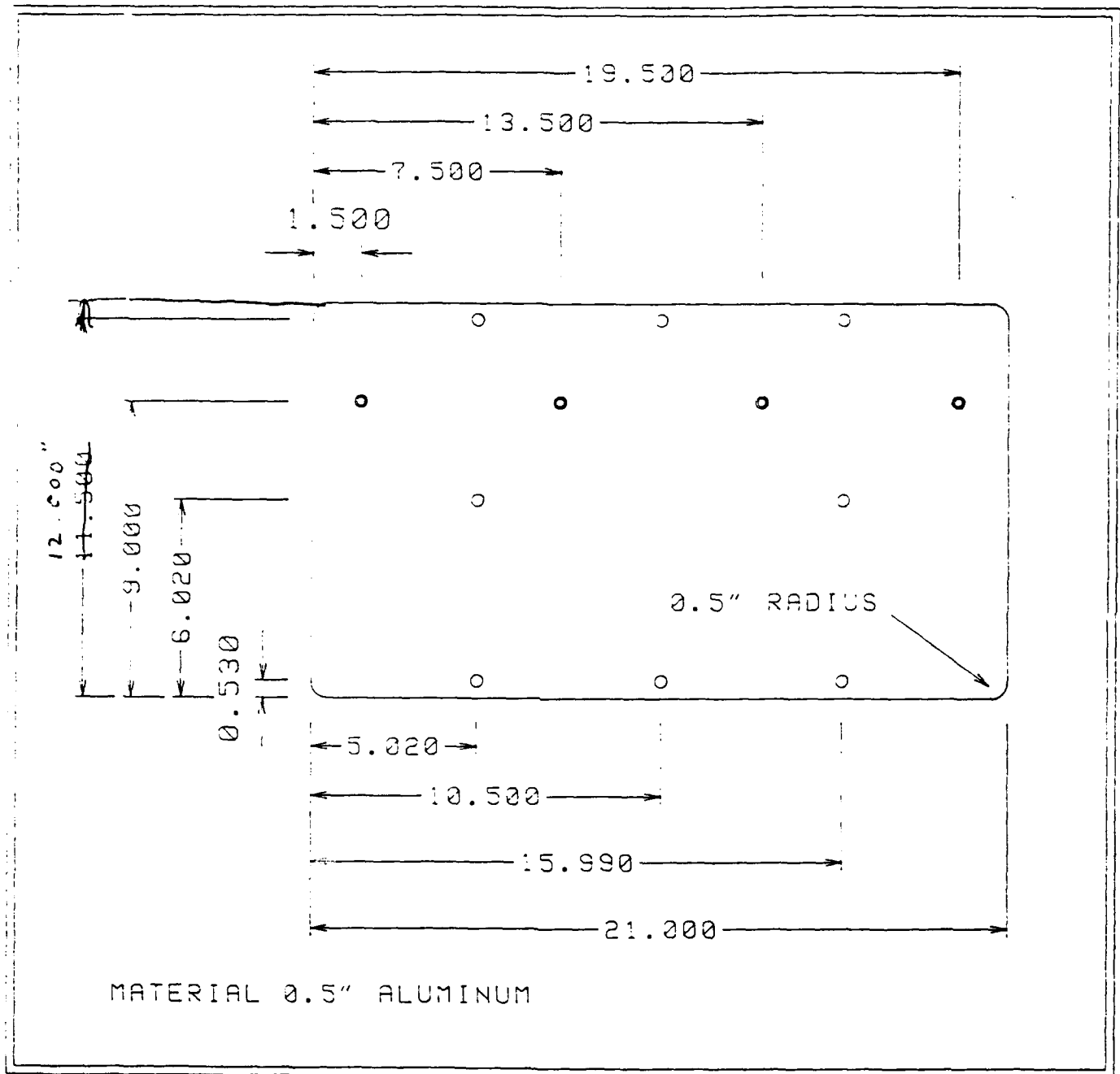


Figure 3. Shelf of Camera Support.

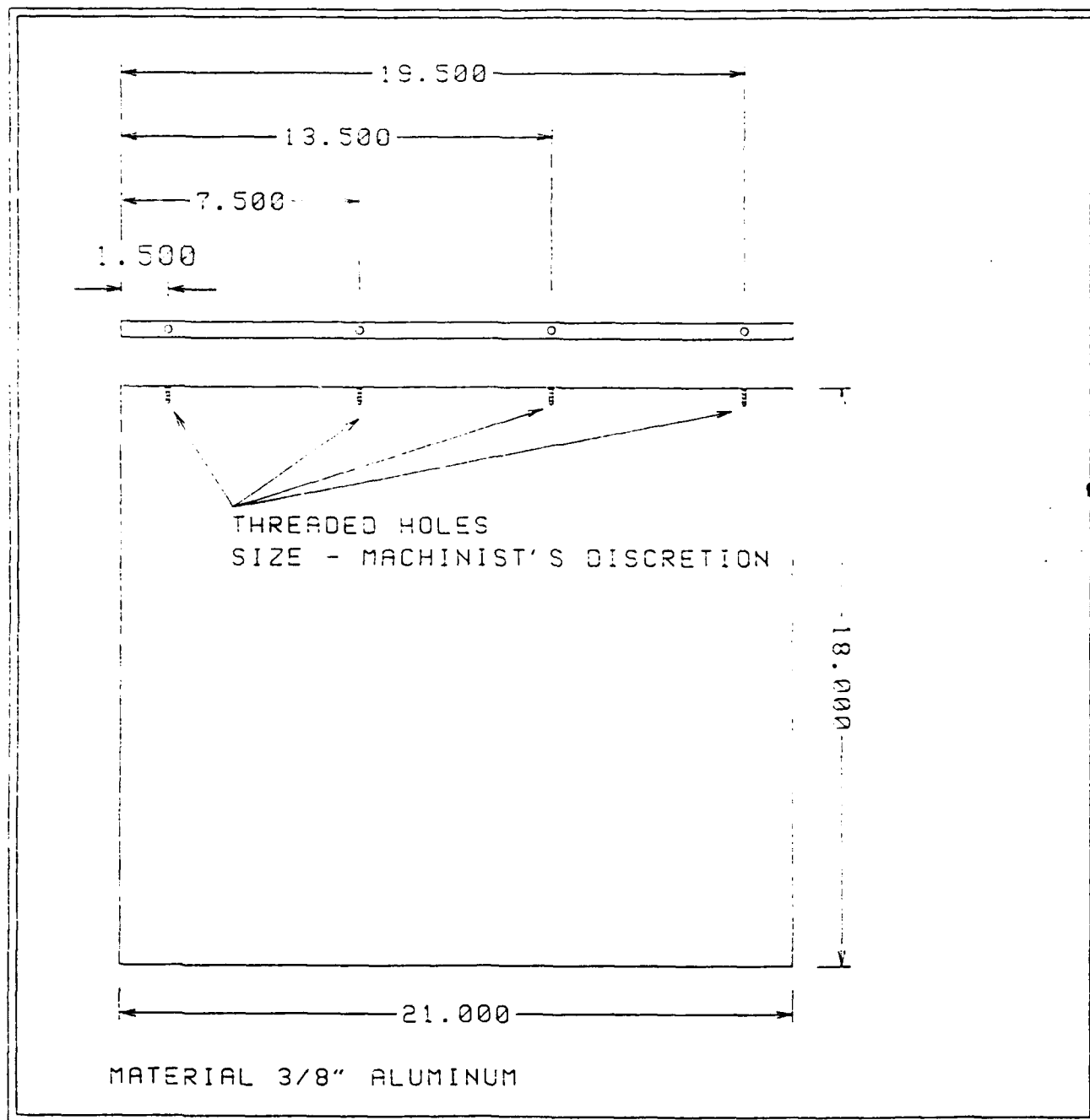
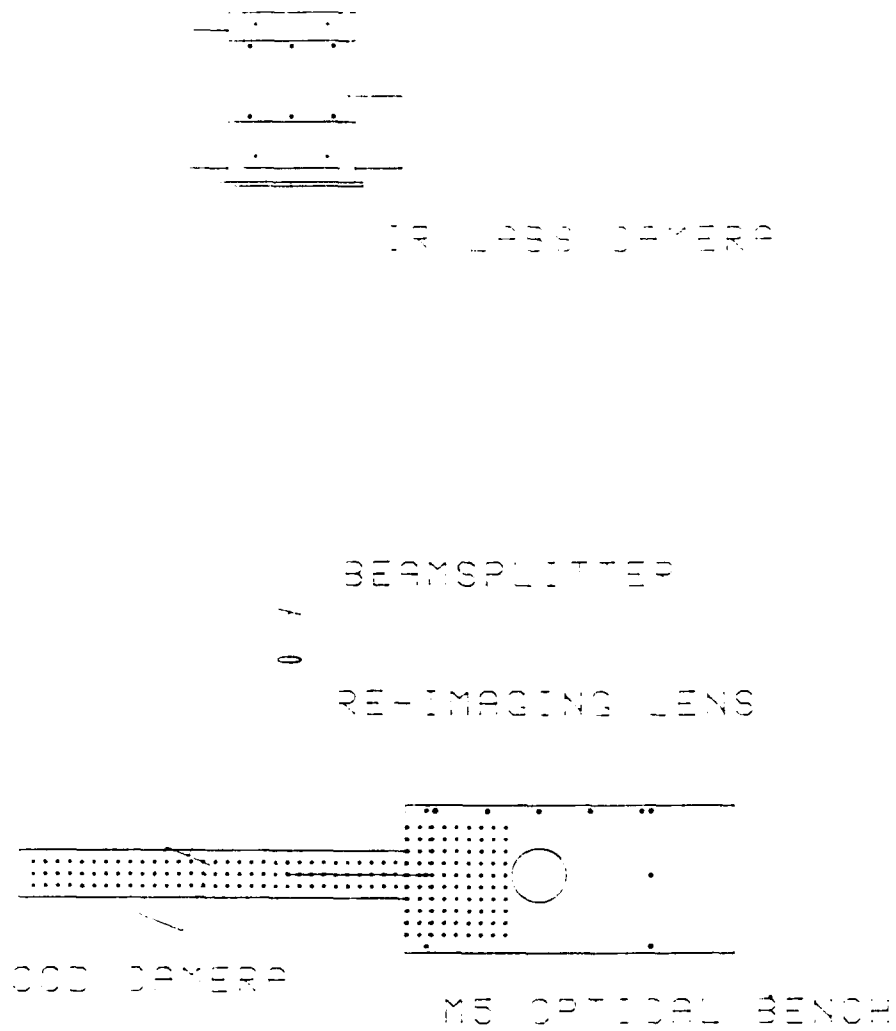


Figure 4. Light Path From M5 Lens to Camera.



## 6 Testing

### 6.1 Observing Program

To test the camera system, associated optics, and software in a "real-life" application, I chose to observe astronomical objects which promised to yield interesting results from speckle imaging. While this camera will be used to observe satellites in the future, stars are a good choice for test observations since they are observable for several hours at a time.

I chose to focus on cool supergiant stars with dust shells. Supergiants are very massive (10 - 100+ solar mass) stars with low density photospheres (the outer atmosphere of the star which we see). They are generally old stars, coming to this stage of their evolution after spending most of their life as stars much like the Sun (these are known as main-sequence stars). Many cool supergiants are characterized by rapid mass loss through their stellar winds. For a number of these stars, the material expelled from the star forms a shell of dust and gas around the star. The dust and gas in a shell absorb short wavelength radiation from the central star and re-emit the energy at much longer infrared wavelengths. For reasons unknown, some supergiants have much higher mass loss rates than others. The rate at which a supergiant loses mass appears to affect the evolutionary path it will take after the supergiant stage (Jura and Kleinmann 1990). The structure and size of circumstellar shells tell us about the central star's mass loss rate and thus the nature of its evolution.

With the exception of a very few stars such as Vega, resolution of circumstellar shells by direct imaging is not possible. Some success in resolving dust shells has been made using speckle interferometry (e.g., Benson, et al. 1989; Dyck and Benson 1992). These studies have used one-dimensional interferometry (i.e. a one-element detector) with very narrow bandpasses. With the IR Labs camera, it is possible to acquire a two-dimensional image of each source.

When developing this observing program, I anticipated having observing time in the early morning hours. Therefore, all but three of my program objects are observable only after 2:30 A.M. in late July. Unfortunately, the allotted time

for this experiment was for the evening until about 1:00 A.M.

#### PROGRAM OBJECTS

Name	RA(2000)	Dec(2000)	V*	J	K*	Time**
BI Cyg	20 <sup>h</sup> 21 <sup>m</sup> 21 <sup>s</sup>	36°55'54"	9.33	-	0.60	21:00-04:30
mu Cep	21 <sup>h</sup> 43 <sup>m</sup> 31 <sup>s</sup>	58°46'48"	4.02	-0.52	-1.71	22:10-06:05
PZ Cas	23 <sup>h</sup> 44 <sup>m</sup> 05 <sup>s</sup>	61°47'42"	8.60	2.42	1.02	00:15-08:00
T Per	02 <sup>h</sup> 19 <sup>m</sup> 22 <sup>s</sup>	58°57'40"	8.64	3.91	2.66	02:45-10:40
FZ Per	02 <sup>h</sup> 21 <sup>m</sup> 00 <sup>s</sup>	57°09'30"	7.96	3.75	2.55	02:45-10:40
SU Per	02 <sup>h</sup> 22 <sup>m</sup> 07 <sup>s</sup>	56°36'15"	7.73	2.76	1.49	02:30-10:25
RS Per	02 <sup>h</sup> 22 <sup>m</sup> 24 <sup>s</sup>	57°06'34"	8.57	3.03	1.63	02:45-10:45
GP Cas	02 <sup>h</sup> 39 <sup>m</sup> 51 <sup>s</sup>	59°35'51"	9.54	3.53	1.95	03:05-11:00
W Per	02 <sup>h</sup> 50 <sup>m</sup> 38 <sup>s</sup>	56°59'00"	8.39	3.45	2.00	03:15-11:10

\* From Stencel, et al. (1989).

\*\* Period objects are above 45°. Calculated for 31 July/1 August, MDT.

#### References

- Benson, J.A., Turner, N.H., and Dyck, H.M. (1989). *Astron. J.*, **97**, 1763.  
 Dyck, H.M. and Benson, J.A. (1992). *Astron. J.*, **104**, 307.  
 Johnson, H.L. (1966). *Ann. Rev. of Astron. and Astrophys.*, **4**, 1993.  
 Jura, M. and Kleinmann, S.G. (1990). *Astrophys. J. Suppl.*, **73**, 769.  
 Stencel, R.E., Pesce, J.E., and Bauer, W.H. (1989). *Astron. J.*, **97**, 1120.

#### 6.2 Calibration

Camera calibration was done by illuminating the detector with a uniform light source. Initially, the calibration was expected to be independent of filter. However, when the calibration was tested by using it on a uniformly illuminated image, the resulting frame had a speckled interference pattern. With further experimentation, it was discovered that the interference was due to a dependence on the light's angle of incidence on the detector. At this time, this phenomenon is not understood. Before meaningful data reduction can be done, some way of compensating for this speckle effect must be found.

Calibrations were made for J, H, and K in both dim and bright light, in

addition to a dark frame calibration. The calibrations for the K filter are of doubtful value since the thermal background of the room was quite substantial. Use of the J calibration seemed to improve the visibility of dim objects at K, however. Once the speckle interference is understood, perhaps only one calibration will be needed.

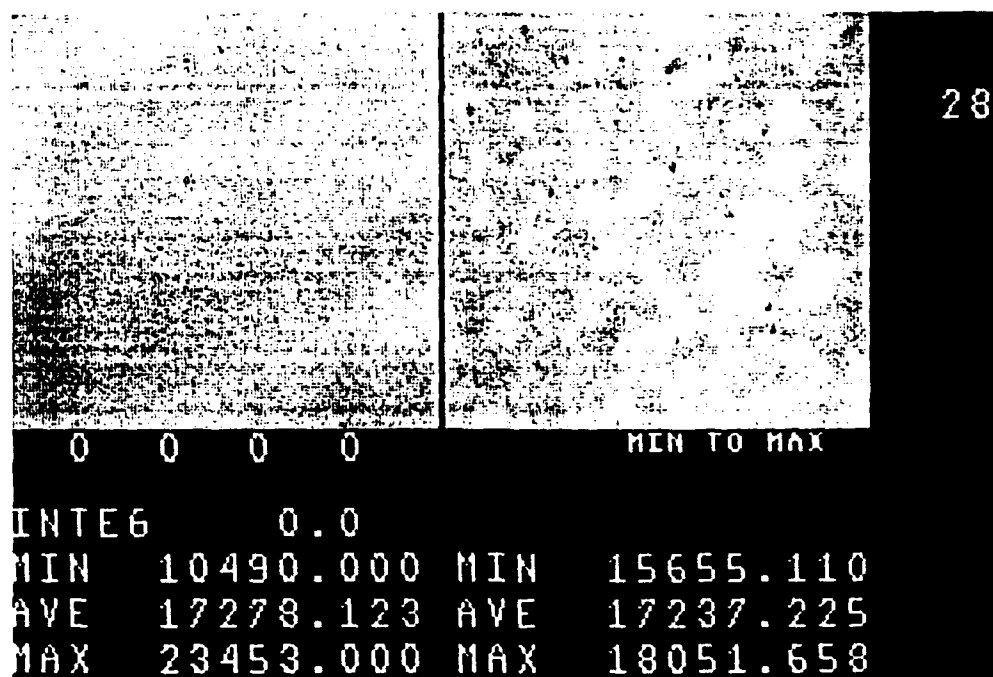
### 6.3 Focusing

Due to the use of lenses which were non-achromatic at infrared wavelengths, the focus of a source on the detector varied between the filters. The difference was so substantial that the range of focus of the telescope itself was not enough to make the corrections. Therefore the beamsplitter and reimaging lens were on translation stages so that focusing might be done there.

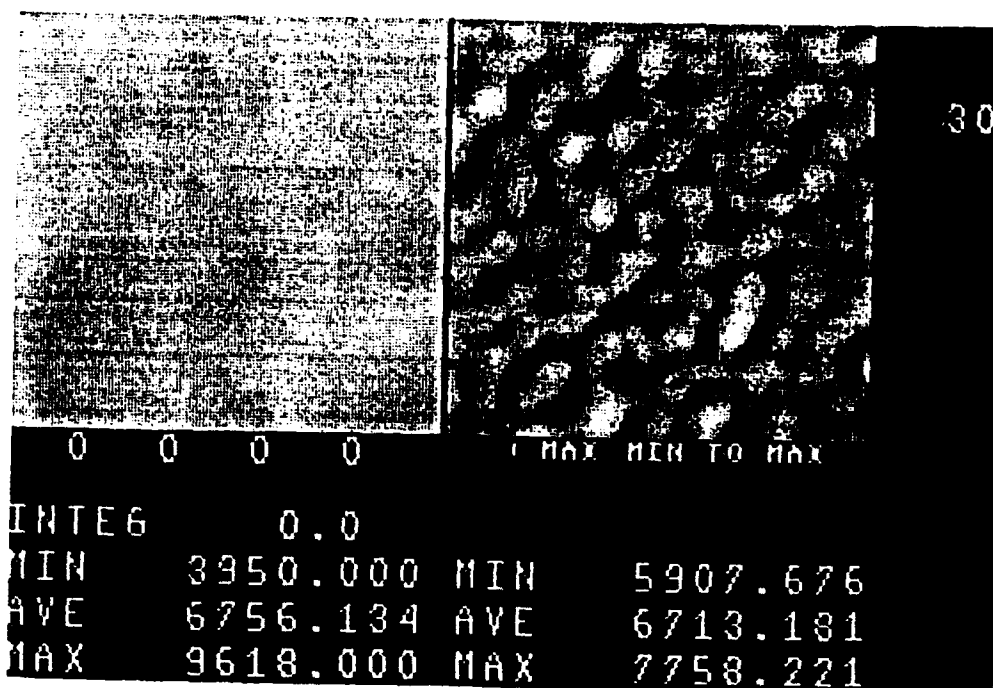
One goal of the testing was to make note of focus positions for the three filters. Unfortunately, poor weather prevented the completion of these tests. Obviously, manual adjustment of the focus between filters is not ideal. It is too time-consuming. The only alternatives I see are either purchasing specially-made infrared achromatic lenses or eliminating all lenses in favor of mirrors.



Figure 5. Interference Effect From J and H Calibration.



a) J Filter (bright light)



b) H Filter (dim light)

## 7. Future Improvements

### 7.1 Tracker

Initial plans called for using a tracker in the tests. The system would use the ADONIS experiment's tracking software with some modifications. For example, the tracker would have to be programmed to read a 128 X 128 array rather than a 64 X 64. Alterations were made to the software, but time limitations prevented full debugging of the system. Since satellites were not being observed, the tracker was not indispensable. The telescope tracks astronomical objects quite well. For the future, however, the tracking system does need to be perfected.

### 7.2 Optical Path

As mentioned before, lenses in the light path cause problems with transmission and with chromatic aberration. In the future, all mirror optics should be considered. This involves not only replacing the reimaging lens, but also involves removing the lens at the M5 position of the telescope. Since this lens is part of the telescope itself, there is likely to be a great deal of administrative resistance to its removal.

Testing was done without any sort of baffle about the light path. Surprisingly, ambient radiation did not seem to make a large contribution to the background. Of course, in the future, a baffle will be a good addition since the detector window is some distance from the telescope.

### 7.3 Cryogenics

The dewar in which the detector and filters are encased can contain enough liquid nitrogen to cool the camera for up to eighteen hours. Also, the dewar will hold the cryogen when it is either in an upright or a horizontal orientation. While these features of the dewar are good, they also make the dewar large and heavy. If a smaller, lighter cryogenic system can be used to cool the camera, there will be more flexibility in positioning the camera on the telescope. If the system is small enough, perhaps the camera can even be mounted directly at the M5 focus. Inquiries about a closed-cycle cooler have been made.

Figure 6. Proposed Data Flow for Infrared Camera With Tracker.

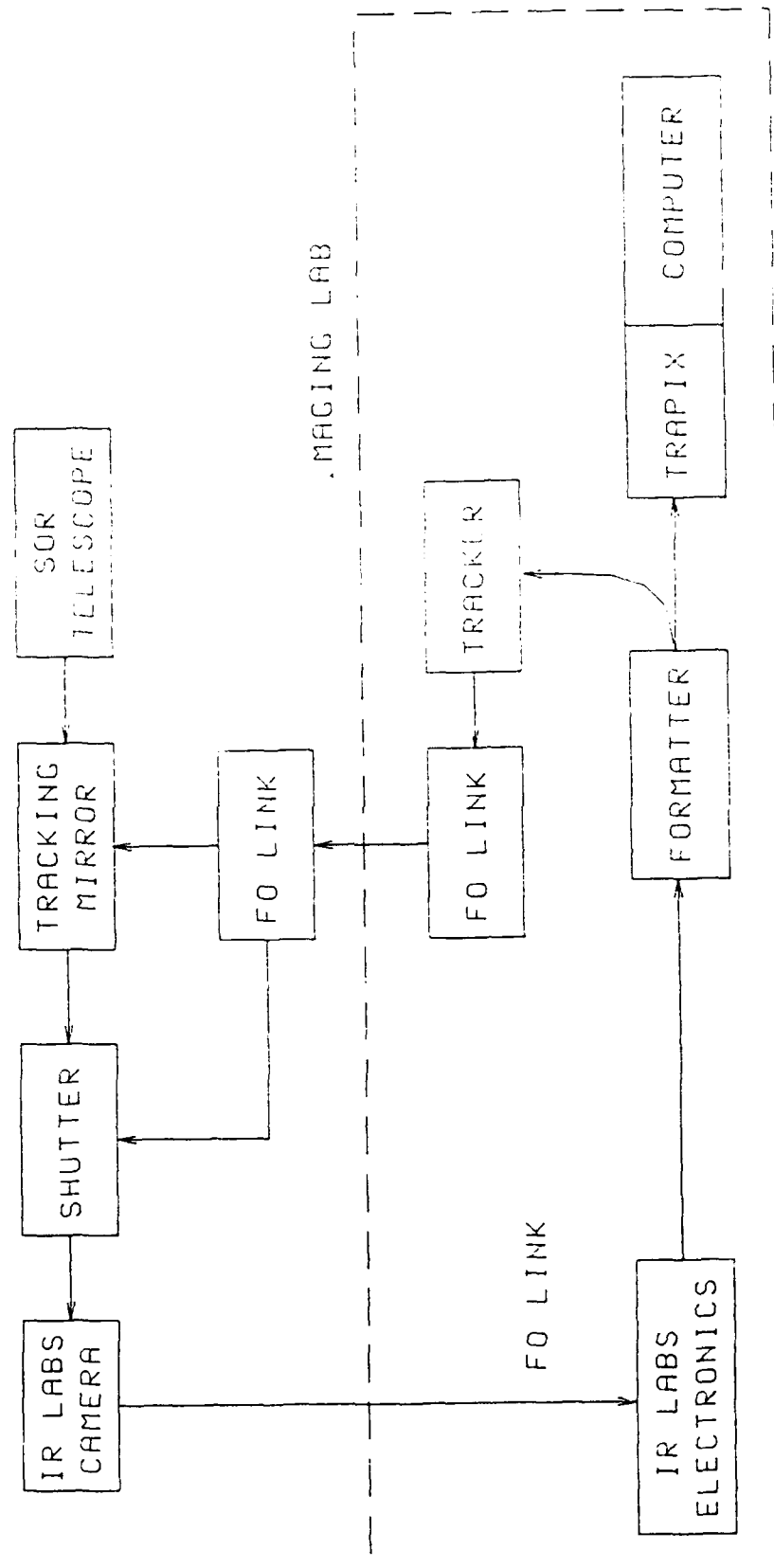
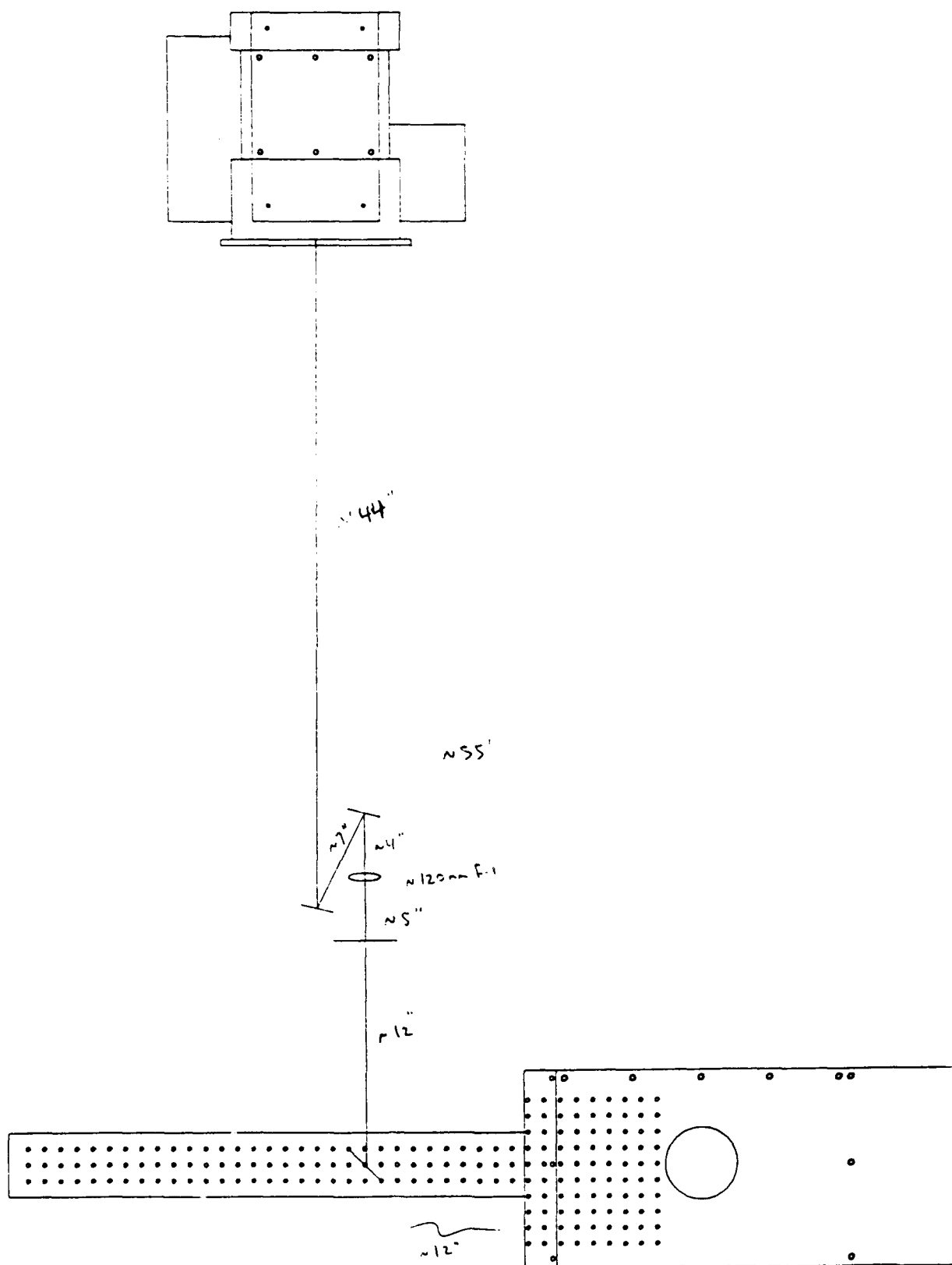


Figure 7. Light Path From M5 Lens With Tracking Mirror in Place.



### Acknowledgements

I would like to thank Mr. Roy Tucker and Mr. Lyle Finkner for their help with hardware and optics, Mr. Bob Pierson for his assistance with the data acquisition software, and Dr. Marsha Fox, Capt. Mark Von Bokern, and SSgt. Michael Schubach for serving as escorts at SOR. All schematics were provided by Roy Tucker.

John Kelly's report unavailable at time of publication.

**Synchronization of Chaos Using Proportional Feedback:  
The Case of the Diode Resonator**

Timothy C. Newell

Department of Physics  
University of North Texas  
North Texas Station, Denton, TX 76203

Final Report for:

Graduate Student Research Program  
Nonlinear Dynamics Laboratory  
Nonlinear Optics Center  
Phillips Laboratory

Sponsored by:  
Air Force Office of Scientific Research  
Bolling Air force Base, Washington, D.C.

July 1993

# Synchronization of Chaos Using Proportional Feedback: The Case of a Diode Resonator

T. C. Newell

*Department of Physics, University of North Texas*

*North Texas Station, Denton, TX 76203*

(July 20, 1993)

## Abstract

We have demonstrated experimentally a proportional feedback algorithm for the synchronization of chaotic time signals generated from a pair of independent diode resonator circuits. Synchronization was easily obtained and occurred for relative feedback levels between three and eight percent of the driving voltage. Once established, the synchronization persisted throughout the whole range of the resonator bifurcation diagram without varying the gain of the feedback.



## I. INTRODUCTION

Upon first consideration, the likelihood of synchronizing chaotic signals appears a dismal prospect at best. Chaos is characterized by a dynamical system's sensitive dependence to initial conditions. Small initial deviations between two chaotic signals lead to exponential divergences of the trajectories in a time on the order of the inverse Lyapunov exponent characterizing the orbit. With the inclusion of either internally or externally generated noise, the prospect of synchronizing two chaotic signals seems to pale even further. Despite this naive pessimism, it has been shown that chaotic synchronization of signals can be realized [1]. Demonstrations have been performed in numerical simulations of evanescently coupled laser arrays [2] and experimentally in chaotic circuits [1,3,4]. Recently, methods based on the OGY scheme for controlling unstable periodic orbits [5] have been adapted [6] and extended [7] to handle the stabilization of one chaotic trajectory of one system about a chaotic trajectory of another system.

In practice, the methods to date for synchronizing two chaotic signals have relied extensively on some knowledge of the system. In the earlier work of Carroll and Pecora [1,3] this meant knowledge of the governing dynamical equations so that the system could be divided into subsystems characterized by Lyapunov exponents of the same sign. The subsystem containing the largest positive Lyapunov exponent can be used to drive the other subsystem (containing only negative Lyapunov exponents) into synchronization with a duplicate subsystem. The work of Mehta and Henderson [6] relied on knowledge of the systems equations in order to construct an artificial dynamical system in which errors between the system's output and the desired aperiodic orbit could be evolved. By using OGY based parameter perturbations when the artificial system was near a fixed point, synchronization of the original system to a target chaotic trajectory could be achieved. Lai and Grebogi [7] use a more direct OGY extension in which the parameter perturbations are applied directly to the original dynamical system. Although their OGY based method intrinsically precludes *a priori* knowledge of the dynamical equations for the system, they still require

local knowledge of the Poincaré map in order to calculate the necessary parameter perturbation. While this can in principle be done numerically for a straight forward application of the OGY method to controlling a unstable periodic orbit, it is more problematic in the case of synchronizing to an arbitrary chaotic trajectory.

In this report we present a new approach for synchronization of chaotic time signals which is also easy to implement experimentally. In the spirit of the occasional proportional feedback method developed by Hunt and implemented by him in a diode resonator [8] and with Roy *et al.* [9] in a multimode solid-state laser system, we propose a synchronization scheme based feeding back a proportional amount of the difference between two chaotic signals. We demonstrate this scheme experimentally in a driven diode resonator of the type well studied in the literature [10]. We present an explanation for the success of this method and discuss its applicability to other chaotic dynamical systems. The outline of this paper is as follows: in the section II we discuss the theoretical basis for this method, in section III we present the experimental setup and in section IV we discuss the experimental results. In section V we summarize our main results and conclude.

## II. SYNCHRONIZATION OF CHAOTIC TRAJECTORIES

Before discussing the use of proportional feedback applied to synchronizing chaotic orbits, let us first recall its normal use in the context of controlling unstable periodic orbits. In the now standard OGY method for controlling an unstable periodic orbit of a chaotic dynamical system, the parameter perturbation necessary to achieve control is given by

$$\delta p_n = \frac{\lambda_u}{\lambda_u - 1} \frac{\mathbf{f}_u \cdot [\mathbf{x}_n - \mathbf{x}_F(p_0)]}{\mathbf{f}_u \cdot \partial \mathbf{x}_F / \partial p}. \quad (2.1)$$

Here  $\mathbf{f}_u$  is the contravariant eigenvector, with eigenvalue  $\lambda_u$ , of the unstable direction of the jacobian  $\mathbf{J} = D_{\mathbf{x}}\mathbf{F}(\mathbf{x}, p_0)|_{\mathbf{x}=\mathbf{x}_F, p}$  of a Poincaré surface of section  $\mathbf{x}_{n+1} = \mathbf{F}(\mathbf{x}_n, p_0)$ , where  $p_0$  is the nominal value of some control parameter  $p$ . The quantity  $\partial \mathbf{x}_F / \partial p = D_p \mathbf{F}(\mathbf{x}, p)|_{\mathbf{x}=\mathbf{x}_F, p=p_0}$  is the change in the fixed point with respect the control parameter evaluated at the fixed point  $\mathbf{x}_F$ , of the map.

The essence of the occasional proportional feedback scheme [8.9] for controlling unstable periodic orbits with one local positive Lyapunov exponent, is to replace the structural prefactors of Eq. (2.1) with an empirically chosen constant,  $\alpha$ . This constant then multiplies the difference of the signal  $V$  from some reference value,  $V_{ref}$ . The control algorithm is then simplified to a form which is much easier to implement experimentally

$$\delta p_n = \alpha (V_n - V_{ref}) \quad (2.2)$$

At least for unstable orbits with one local positive Lyapunov exponent, this scheme is reasonable since it is essentially Eq. (2.1). The reference signal  $V_{ref}$ , selects out the fixed points of the system and remaining structural factors which have been lumped into the constant  $\alpha$  can be found experimentally by *turning the  $\alpha$  knob* until control has been achieved. Equation (2.2) is not precisely the OGY formula since the former has been used in practice to control other than unstable period one orbits [11]. In addition, the OGY formula implicitly assumes that the parameter perturbation is applied for the entire duration between successive crossings of the Poincaré surface of section. In practice, Eq. (2.2) is typically applied for only a fraction of a characteristic period of the system. This period is essentially the mean value between successive crossings of the Poincaré surface of section. There is precedence for this type of control via proportional feedback called adaptive control [12]. It was implemented as a re-stabilizing algorithm for systems in which sudden parameter changes created chaotic oscillations, and not as a method to control unstable periodic orbits.

A straight forward extension of Eq. (2.2) for synchronizing two chaotic signals would be

$$\delta p_n = \alpha [V^M(t) - V^S(t)]. \quad (2.3)$$

Here  $V^S(t)$  is some chaotic slave signal which we wish to synchronize to some other chaotic master signal,  $V^M(t)$ . Equation (2.3) could be understood as utilizing a feedback signal derived from the difference between the proportional feedback signals for the master and the slave; i.e.  $\delta p_n = \alpha (V^M(t) - V_{ref}) - \alpha (V^S(t) - V_{ref})$ .

Further support for this synchronizing algorithm can be inferred from the recently proposed synchronizing scheme of Lai and Grebogi [7]. In there paper the authors propose the

synchronization of a slave signal  $y_n$  to a master signal  $x_n$  via the proportional difference

$$\delta p_n = \frac{[D_y F(y, p) \cdot \{y_n - x_n(p_0)\} \cdot f_{u(n+1)}]}{D_p F(y, p) \cdot f_{u(n+1)}} \Big|_{y=x, p=p_0} \quad (2.4)$$

This formula is derived by expanding the chaotic slave orbit  $y_n$  locally about the chaotic master orbit  $x_n$  and requiring that the next iteration of  $y_n$ , after falling into a small neighborhood around  $x_n$ , lie on the stable direction of  $x_{n+1}(p_0)$ , i.e.  $[y_n - x_{n+1}(p_0)] \cdot f_{u(n+1)} = 0$ . Hence this perturbation formula is proportional to the instantaneous difference between the master and slave signals.

Experimental implementation this algorithm is non-trivial, especially in real time. For chaotic orbits, one needs to calculate the unstable contravariant eigenvector one step forward in time, i.e.  $f_{u(n+1)}$ . This requires some knowledge of the mapping so that a small circle of points can be propagated forward in time in order to estimate this unstable direction (see [7,13] for details). In addition, the Jacobian of the map and the derivative of the map with respect to the parameter are iterate dependent since they depend on the current value  $x_n$ , of the master orbit. This structural knowledge of the system would be needed at each instant along the chaotic trajectory in order to maintain synchronization.

Lai and Grebogi demonstrate numerically that the synchronization is tolerant to a small degree of externally generated noise. This is reminiscent of the robustness of the standard OGY algorithm Eq. (2.1), to noise. In their original paper, OGY defined a region about the unstable fixed point about which control could be achieved. If the magnitude of the noise exceeded the radius of this region, control was lost. A similar, although less well defined region exists for Eq. (2.4) as well, outside which synchronization will be lost.

We can capitalize on the robustness of the OGY synchronization scheme in the following way. Typically, once synchronization is achieved, the parameter perturbations necessary to maintain the locking become very small, usually less than one percent of the nominal value  $p_0$ . This is true in the case of controlling unstable periodic orbits, using Eq. (2.1) or variations thereof, as well [14]. By adjusting the control parameter by an amount proportional to the instantaneous difference between the master and slave signals, synchronization should be

able to be achieved in which iterate dependent structural constants of Eq. (2.4) could be treated as noise about some mean perturbation. In other words, Eq. (2.4) could be written formally as  $\delta p_n = \alpha_n (V_n^M - V_n^S)$  where  $\alpha_n$  encapsulates the iterate dependent structural constants. Equation (2.3) approximates  $\alpha_n$  by an empirically determined constant  $\alpha$  and relies on the intrinsic robustness of the OGY scheme to treat the difference  $\alpha_n - \alpha$  as tolerable noise.

In the next two sections we discuss the implementation the synchronizing proportional feedback algorithm to a diode resonator circuit and find that it works remarkably well. The diode resonator exhibits a one dimensional return map so that Equation (2.3) is applicable as stands. In a future paper [15] we show how the synchronization of two chaotic signals can be achieved for more general dynamical systems by means of a generalization of Eq. (2.3) involving earlier iterates, i.e.  $\delta p_n = \alpha(V_n^M - V_n^S) + \beta(V_{n-1}^M - V_{n-1}^S)$ , where again,  $\alpha$  and  $\beta$  are empirically chosen constants.

### III. EXPERIMENT AND RESULTS

#### A. Setup

The basic idea behind the synchronization experiment is depicted in Fig. 1. From the chaotic attractor of a diode resonator circuit we select out an arbitrary chaotic signal which we designate as the master signal  $V^M(t)$ . From another, identical diode resonator circuit operating under the same conditions we wish to select another chaotic signal, designated as the slave  $V^S(t)$ , and synchronize it to  $V^M(t)$ . We accomplish this by measuring the difference between the two signals and feeding back a proportional amount  $\alpha [V^M(t) - V^S(t)]$ , to the voltage which drives the slave resonator. The quantity  $\alpha$  is to be determined experimentally by adjusting the gain of an amplifier which acts on the difference voltage, until the two chaotic signals lock together.

A block diagram of the experimental setup is shown in Fig. 2. Each diode resonator

consists of a 1N4004 diode, a 33mH inductor and a  $90\Omega$  resistor in series. Both circuits were driven by the same Wave Tek 166 waveform generator. The master signal  $V^M$  and the slave signal  $V^S$  were defined as the voltage drop across the respective resistors. For unsynchronized operation, both master and slave signal were approximately 40mVrms. Signals were recorded with a Tektronix RTD710A digitizer. The master resonator was driven solely by the waveform generator with an sine wave of frequency 80.5kHz and amplitude  $V_0$ , of 2.92Vrms. This drove the master resonator into the chaotic regime just below the period three window which occurred at a driving voltage of 3.0Vrms (see arrow in Fig. 3). In Fig 4 we have plotted the first return map for the master signal. This graph was obtained from a long time series recording of the master signal by plotting the  $(m + 1)$ st peak against the  $m$ th peak. The thinness of the attractor indicates that it is nearly one dimensional. However, the extra branch in the attractor and the jump in the size of the attractor at the transition to period three are manifestations of a two dimensional character of the system. Similar observations have been appeared in the literature for the diode resonator [16,17].

In addition to being driven at  $V_0$ , the voltage applied to the slave generator was modified by the addition of a time varying feedback signal,  $\delta V_f(t) = \alpha [V^M(t) - V^S(t)]$ . This feedback signal was obtained by amplifying the voltage difference between the master and slave oscillators and passing this through a window comparator centered on 0V. If  $\delta V_f(t)$  was inside the range of the the window comparator, an analog switch was closed and  $\delta V_f(t)$  was added to the driving voltage through a summing amplifier. If  $\delta V_f(t)$  fell outside the range of the window comparator, the analog switch remained open and no feedback signal was applied.

## B. Observations

Under conditions of zero feedback, the driving voltage for the master and slave circuit were on average identical. Slight variations in the slave driving voltage did exist due the unavoidable noise involved in passing it through the summing amplifier. In Fig. 5a we show

an oscilloscope trace of the  $V^M(t)$  versus  $V^S(t)$ . The resulting wide parallelogram region of phase space demonstrates that each signal was executing a different chaotic trajectory. The  $45^\circ$  slope of the figure is due to the chaotic peaks being approximately in phase as each signal followed the driving voltage. In Fig. 6a we plot the raw (un-amplified) signal difference  $V^M(t) - V^S(t)$ .

In order to achieve synchronization, feedback had to be applied for a minimum duration of  $1\mu s$ . When the slave signal synchronized to the master the slave driving voltage dropped to 2.83Vrms. This implied a feedback of approximately 3.5% relative to the master driving voltage of 2.92Vrms. The oscilloscope trace of  $V^M(t)$  versus  $V^S(t)$  in Fig. 5b clearly demonstrates that synchronization has been achieved. Below this feedback level we were unable to force the signals to synchronize. During synchronization the absolute value of the signal difference  $|V^M(t) - V^S(t)|$ , fluctuated in time, never exceeding 2.5mV as shown in Fig. 6b. We used a gain  $\alpha$ , of approximately 40 so that the value of the feedback signal  $\delta V_f(t)$  never exceeded  $\pm 100\text{mV}$ . Once the signals were locked together, the comparator window became superfluous since the amplified signal difference was always within the window comparator implying that the analog switch then remained continuously closed. The purpose of the comparator window was to insure that we were not feeding back arbitrarily large perturbations to the slave driving voltage. However, the use of a window comparator was not essential for achieving synchronization. We found that the signals would still synchronize in an experimental arrangement in which the window comparator and the analog switch were removed and the amplified signal difference was feed directly into the slave driving voltage. Again the relative feedback level was approximately 3.5%.

We also found that the signals could not be locked together if the feedback exceeded 250mV corresponding to a relative feedback level of 8.5%. We speculate the failure of synchronization above this feedback level stemmed from our use of a constant gain  $\alpha$  as opposed to a time varying gain  $\alpha(t)$  which would depend on the instantaneous values of the structural constants implied by Eq. 2.4. These prefactors which multiply the signal difference required instantaneous knowledge of the system over the whole of the master and

slave chaotic trajectory. Above this feedback level the difference  $\alpha(t) - \alpha$  could probably no longer be considered a small noise which could be tolerated by our algorithm. A further investigation into this point will be forthcoming [15].

We observed that once synchronization had been achieved for a given relative feedback level, the driving voltage  $V_0$  could be varied across the full range of the resonator bifurcation diagram (Fig. 3), without varying the gain, and the synchronization would continue to persist. Thus synchronization could be maintained as the signals were changed freely between chaotic and periodic orbits.

As mentioned above, once synchronization was achieved the amplified signal difference always remained within the window comparator. This implied that the analog switch remained closed so that feedback was applied continuously. In a another experiment we chopped the feedback signal in time once synchronization was achieved so that the feedback was turned off periodically. The largest interruption interval in which the feedback signal could be turned off and synchronization was still maintained was  $10\mu s$ .

Finally, great care was taken to ensure that the two diode resonators were constructed as identically as possible and operated under similar driving voltages. It is noteworthy to point out that synchronization could still be achieved when the resonator circuits differed slightly from each other due to differences in the various circuit components. In addition synchronization could also be achieved when there existed noticeable differences between the master and slave driving voltages. In these cases the synchronization was somewhat degraded in the sense that the waveform of the slave signal showed noticeable differences from that of the master signal. A comparison of  $V^M(t)$  versus  $V^S(t)$  similar to Fig. 5b revealed a straight line which grew thicker towards the higher voltage end. For slightly dissimilar resonator circuits or nearly identical operating conditions, the chaotic trajectory content of the attractors are different for the two circuits. However, the synchronization employed here allows for successfull synchronization of similar chaotic orbits.



#### IV. CONCLUSIONS

We have demonstrated experimentally that two chaotic signals generated by separate but identical diode resonators could be synchronized by a simple proportional feedback algorithm. To achieve synchronization, the feedback must be applied for a minimum duration of  $1\mu\text{s}$ . The synchronization was maintained by applying relative feedback levels between 3.5% and 8.5%. Once synchronization was established, it could be maintained as the driving voltage was altered while the feedback gain was held constant. We found this synchronizing proportional feedback scheme to be robust and easier to implement than other traditional synchronization methods. The combination of this synchronization scheme with current chaotic controlling algorithms could potentially find use in communications applications. These results were reported at the SPIE conference Chaos in Optics and will be published in Physical Review E [18].

#### ACKNOWLEDGMENTS

T.C.N. would like to thank the AFOSR for a summer fellowship.

## REFERENCES

- [1] L.M. Pecora and T.L. Carroll, Phys. Rev. Lett. **64**, 821 (1990).
- [2] H.G. Winful and L. Rahman, Phys. Rev. Lett. **65**, 1575 (1990).
- [3] T.L. Carroll and L.M. Pecora, IEEE Trans. on Circuits and Systems **38**, 453 (1991);  
Int. Journal of Bifurcation and Chaos **2**, 659 (1992).
- [4] K.M. Cuomo and A.V. Oppenheim, Phys. Rev. Lett. **71**, 65 (1993).
- [5] E. Ott, C. Grebogi, and J. A. Yorke, Phys. Rev. Lett. **64**, 1196 (1990).
- [6] N.J. Mehta and R.M. Henderson, Phys. Rev. A **44**, 4861 (1991).
- [7] Y.C. Lai and C. Grebogi, Phys. Rev. E **47**, 2357 (1993).
- [8] E. R. Hunt, Phys. Rev. Lett. **67**, 1953 (1991).
- [9] R. Roy, T.W. Murphy, T.D. Maier, Z. Gills and E.R. Hunt, Phys. Rev. Lett. **68**, 1259 (1992).
- [10] J. Testa, J. Perez and C. Jefferies, Phys. Rev. Lett. **48**, 714 (1982); Z. Su, R.W. Rollins and E.R. Hunt, Phys. Rev. A **40**, 2698 (1989) and references therein.
- [11] In many cases, simple variations the OGY formula using previous iterates can be used to control unstable orbits of higher periods even though these formulas differ from the higher dimensional formulas put forth by OGY themselves using the full set of phase space variables and/or projections onto a one dimensional time series. For the latter cases see E. Ott, C. Grebogi and J.A. Yorke, in *Chaos: Soviet-American Perspectives on Nonlinear Science*, edited by D.K. Campbell (AIP, New York, 1990); D. Auerbach, C. Grebogi, E. Ott and J.A. Yorke, Phys. Rev. Lett. **69**, 3479 (1992).
- [12] B.A. Huberman and E. Lumer, IEEE Trans. on Circuits and Systems **37**, 547 (1990); S. Sinha and R. Ramaswamy, Physica D **43**, 118 (1990).

- [13] Y.C. Lai, M. Ding and C. Grebogi, Phys. Rev. E **47**, 86 (1993).
- [14] P.M. Alsing, A. Gavrielides and V. Kovanis, "Controlling chaos in fast dynamical systems," (submitted to Phys. Rev. E, 1993); P.M. Alsing, A. Gavrielides and V. Kovanis, in *Chaos and Commercialization*, SPIE Proceedings **2037**, (1993).
- [15] T.C. Newell, P.M. Alsing, A. Gavrielides and V. Kovanis (to be published).
- [16] E.R. Hunt in Proceeding of the 1st Experimental Chaos Conference, edited by S. Vohra, M. Spano, M. Shlesinger, L. Pecora and W. Ditto, World Scientific, 333 (1992).
- [17] J.M. Perez, Z. Lu, J.M. Kowalski, G. Albert, C.L. Littler and X.N. Song in Proceeding of the 1st Experimental Chaos Conference, edited by S. Vohra, M. Spano, M. Shlesinger, L. Pecora and W. Ditto, World Scientific, 327 (1992).
- [18] T.C. Newell, P.M. Alsing, A. Gavrielides and V. Kovanis "Synchronization of Chaos Using Proportional Feedback" to be published at Physical Review E.

## FIGURES

FIG. 1. A schematic illustration of the strategy for synchronizing two almost identical chaotic circuits. The output of the master and the slave circuit is feed into a comparator and the resulting difference is amplified and fed back into the slave circuit in order to induce synchronization.

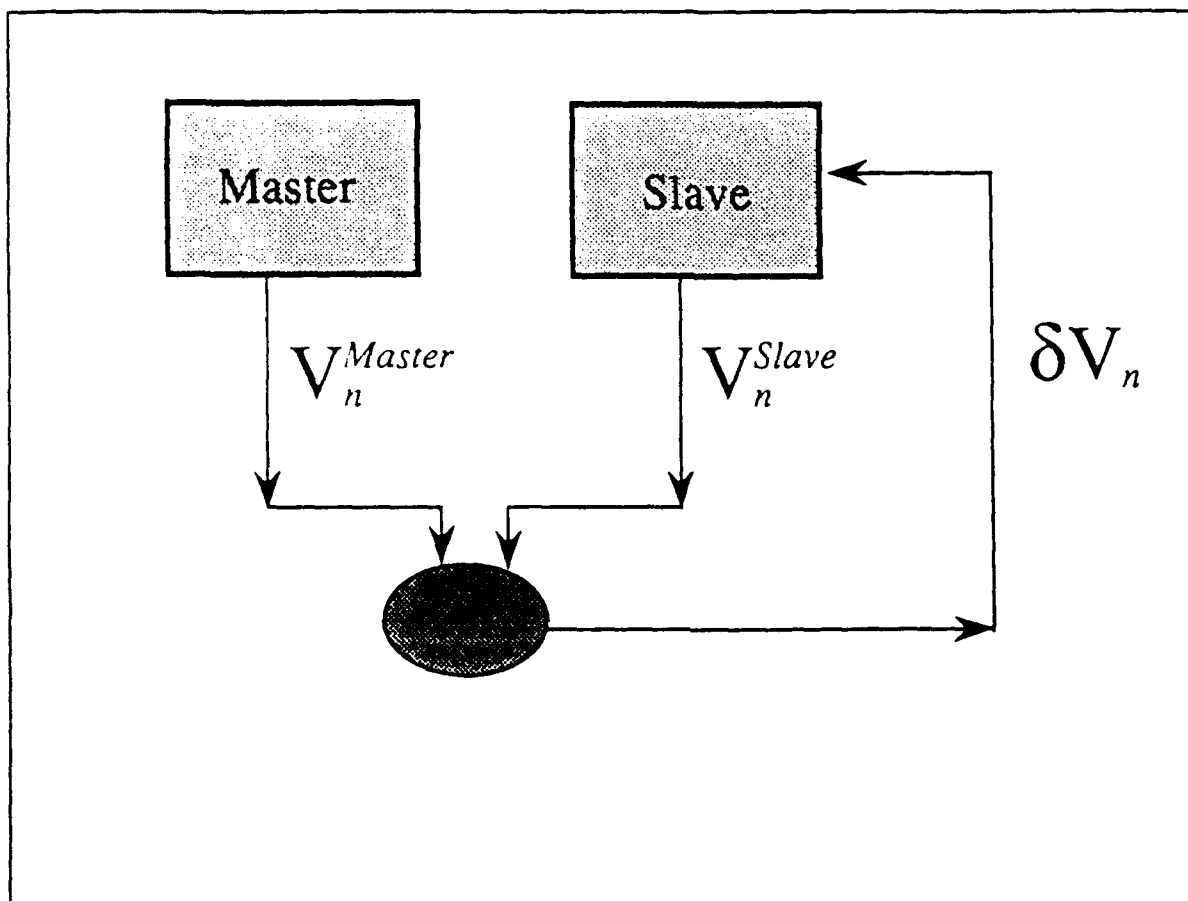
FIG. 2. A block diagram of the experimental apparatus. The setup consists of two identical diode resonators each composed of a 1N4004 diode, 33mH inductor and a  $90\Omega$  resistor. Both circuits are driven by the same Wave Tek 166 function generator at 80.5kHz to ensure that their basic characteristics are the same as much as possible. The chaotic current of each circuit is converted into a voltage and fed into a difference amplifier which is then passed onto a window comparator. If the amplified difference between the two chaotic signals is within an the adjustable window of the comparator, an analog switch is closed and the feedback is then added to the slave driving voltage.

FIG. 3. An oscilloscope trace of the bifurcation diagram for a single diode resonator displaying the period doubling route to chaos. The abscissa is the amplitude of the driving sine wave,  $V_0$  while the ordinate is the voltage converted current across the diode (arbitrary units). The arrow indicates the master circuit driving voltage of 2.92Vrms for which the the majority experiments were performed.

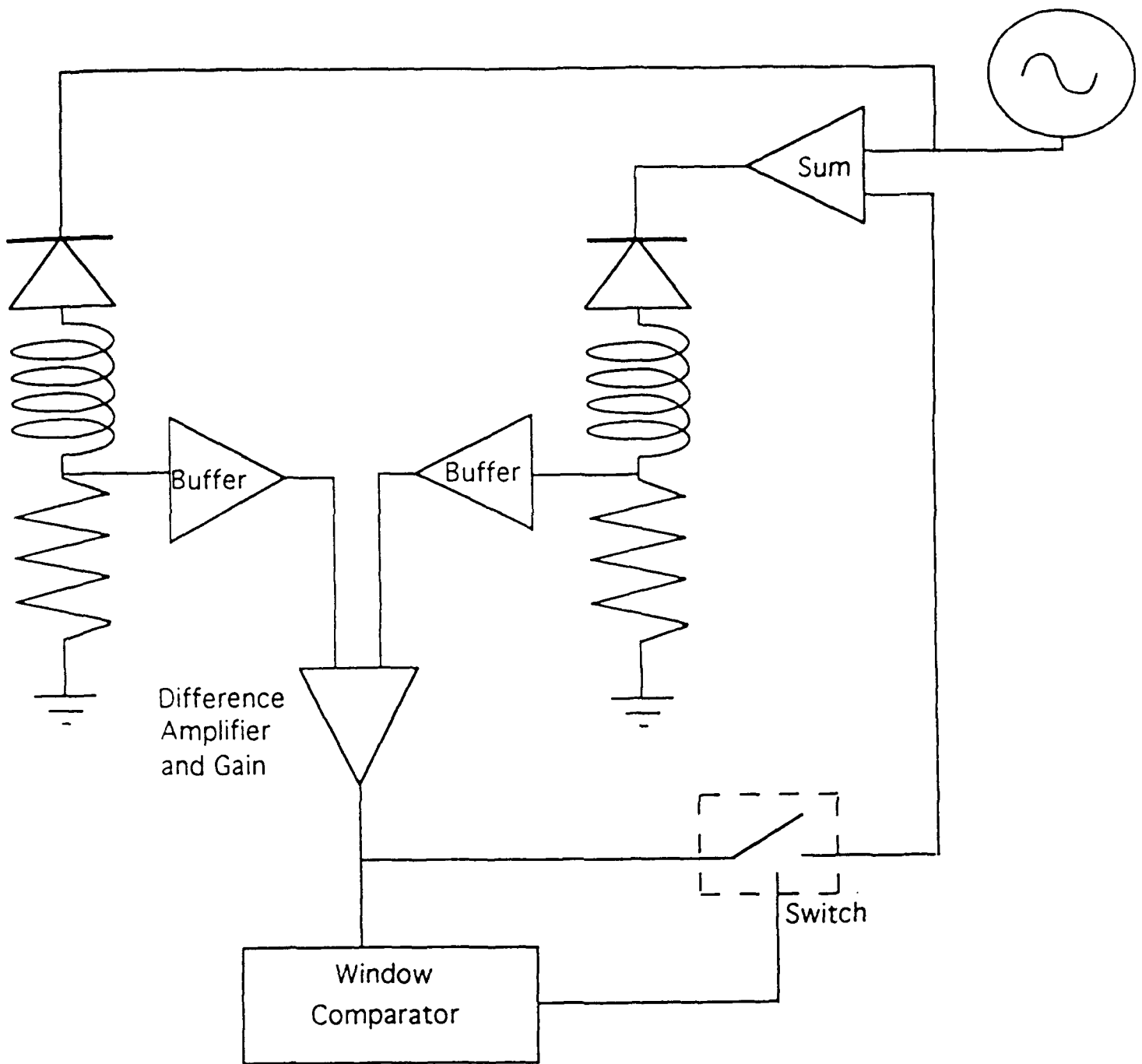
FIG. 4. The first return map for the master circuit driven at 2.92Vrms. This graph was constructed from a long time series recording of the master signal by plotting consecutive pairs of peak values.

FIG. 5. (a) Oscilloscope trace phase portrait  $V^M(t)$  versus  $V^S(t)$  of the chaotic circuits when no feedback is applied, (b) The phase portrait when the when feedback is applied. The thinness of the trace indicates almost perfect synchronization.

FIG. 6. The master-slave signal difference  $V^M(t) - V^S(t)$ , (50MHz sampling rate): (a) no feedback applied, (b) feedback applied. The maximum signal difference is reduced by over a factor of ten when the signals are synchronized.



**Fig. 1**



**Fig. 2**

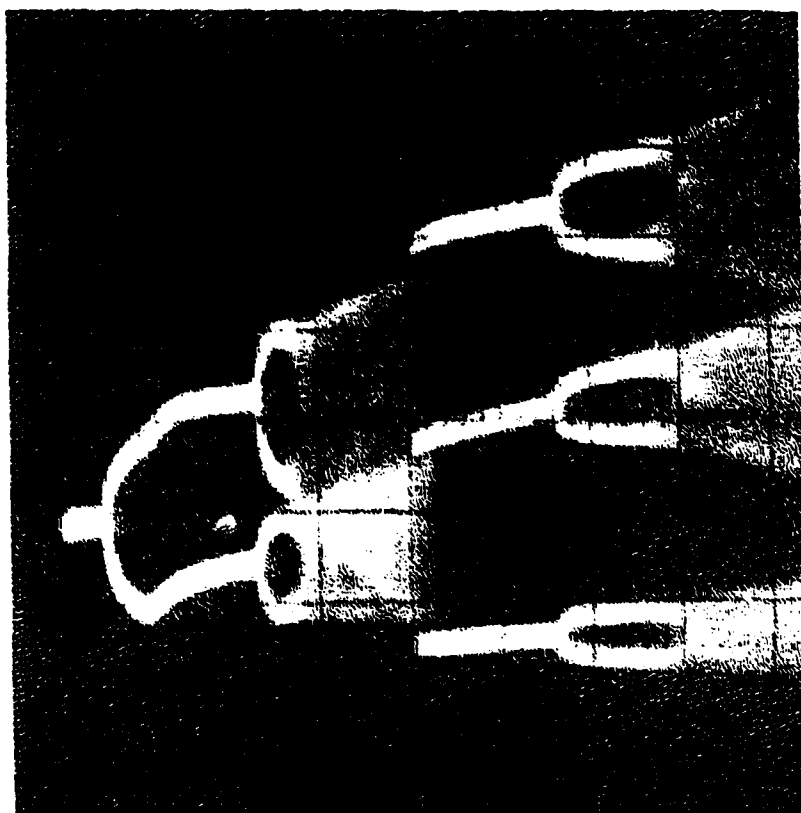


**Fig. 3**



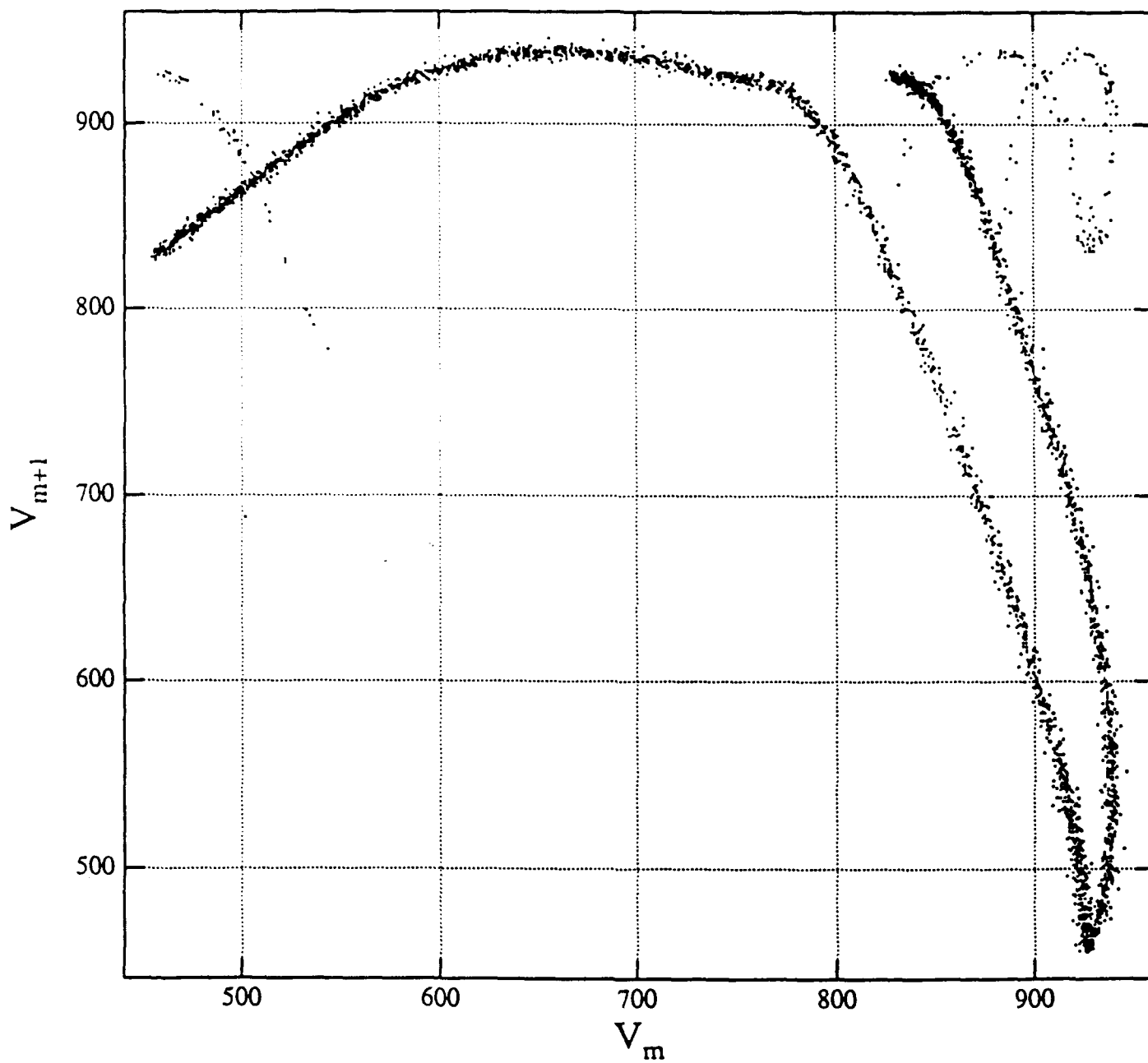
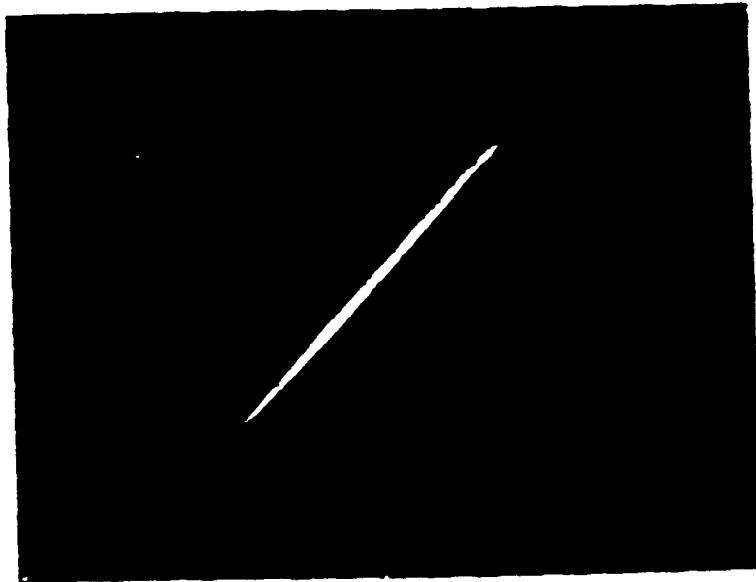
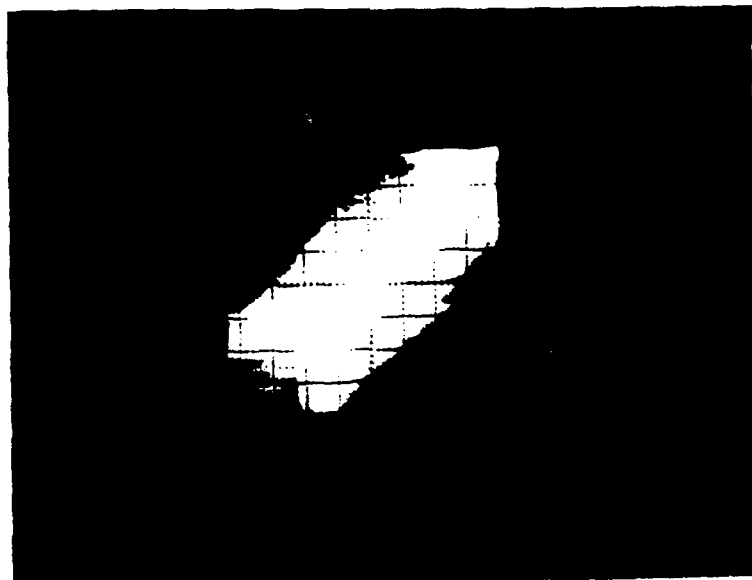


Fig. 4



(b)



(a)

Fig. 5

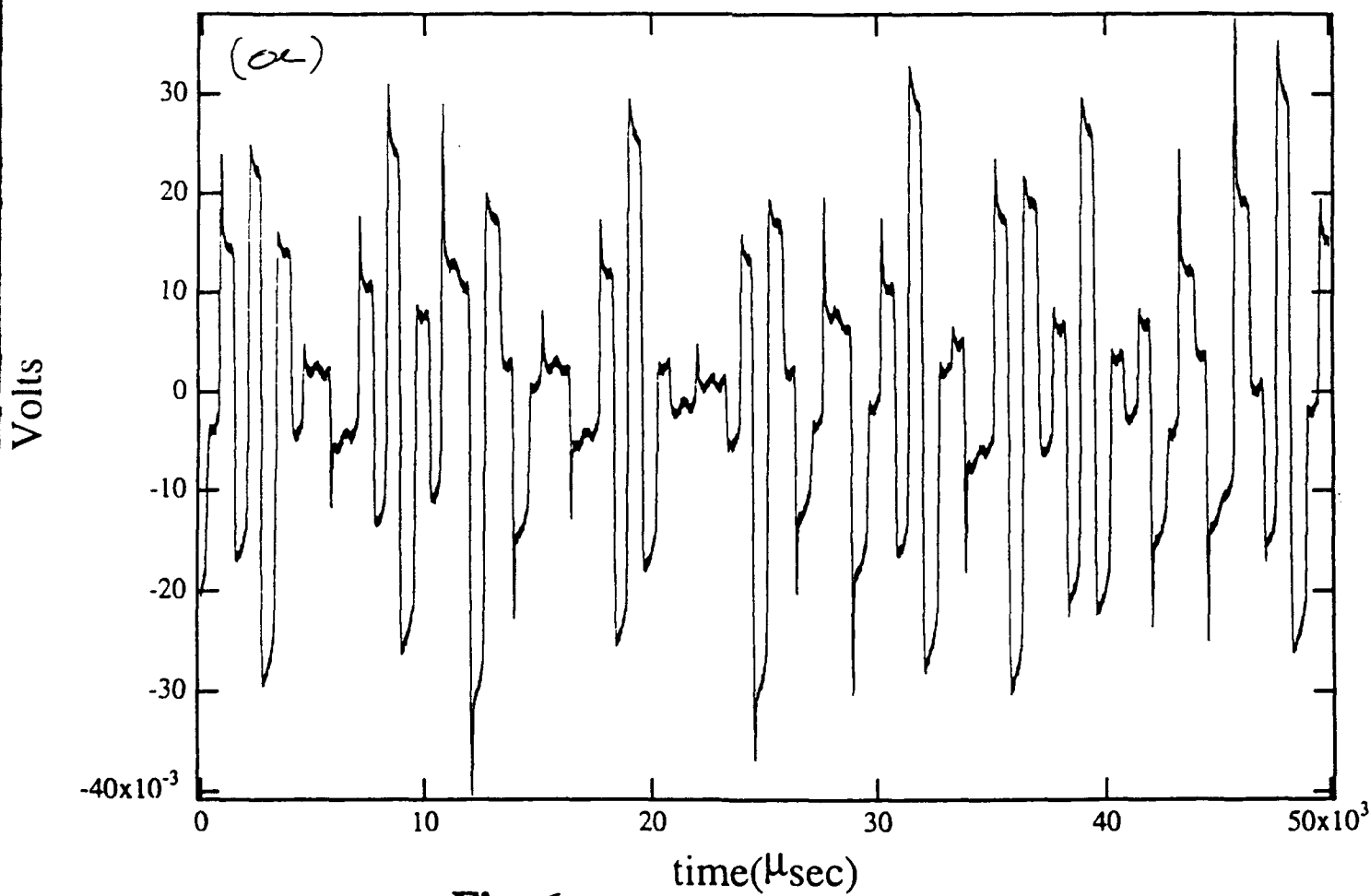
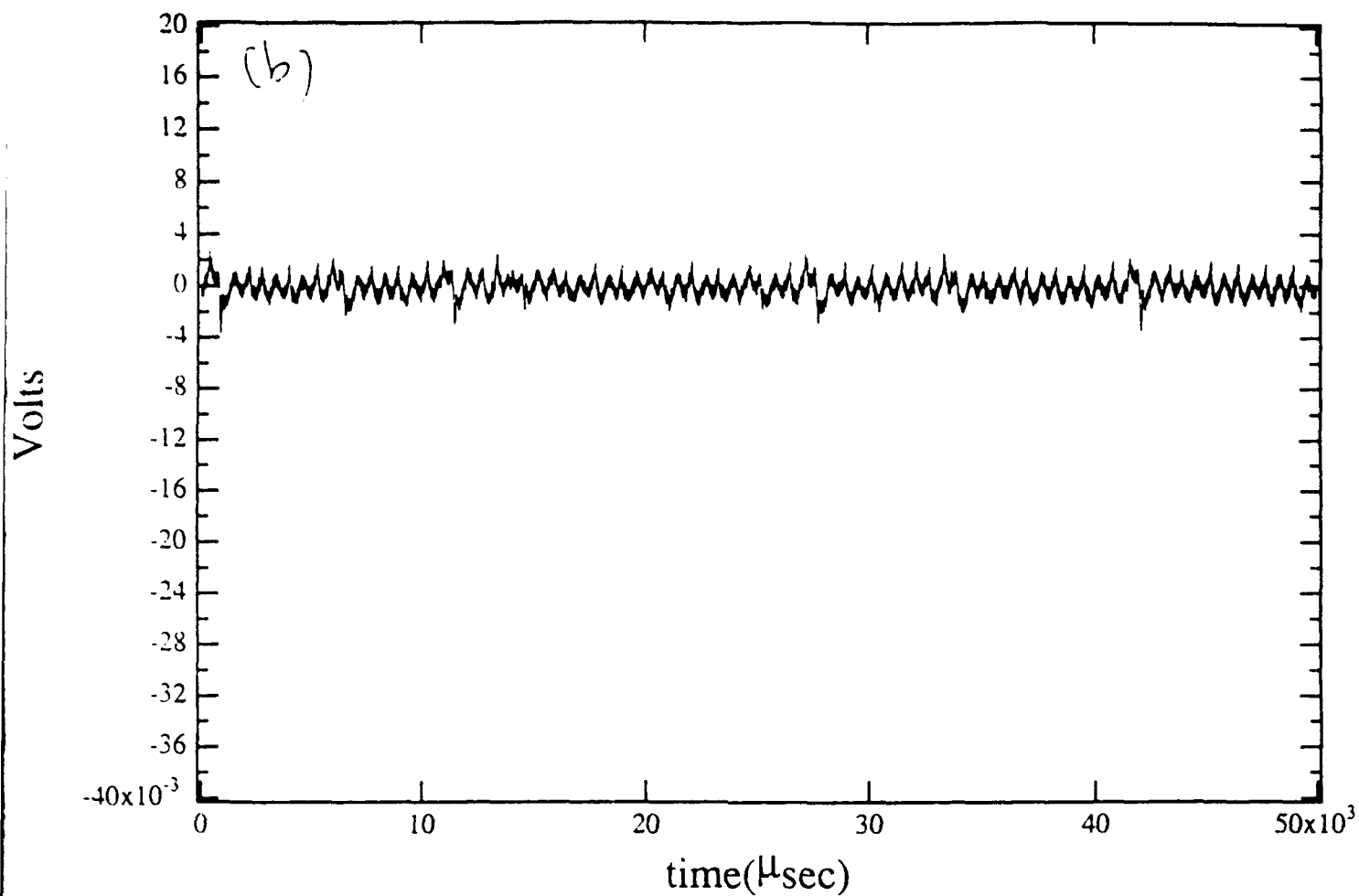


**Fig. 6**

**A PARTICLE IMAGE VELOCIMETRY TECHNIQUE  
FOR SPRAY INJECTORS**

**William W. Brocklehurst  
Research Assistant  
Department of Aerospace Engineering**

**Dr. San-Mou Jeng  
Research Associate**

**University of Cincinnati  
Mail Location #70  
Cincinnati, OH 45221**

**Final Report for:  
Graduate Student Research Program  
Phillips Laboratory**

**Sponsored by:  
Air Force Office of Scientific Research  
Bolling Air Force Base, Washington, D.C.**

**September 1993**

# **A PARTICLE IMAGE VELOCIMETRY TECHNIQUE FOR SPRAY INJECTORS**

**William W. Brocklehurst  
Research Assistant  
Department of Aerospace Engineering  
University of Cincinnati**

## **Abstract**

The droplet field produced by a liquid spray injector was studied using a Particle Image Velocimetry (PIV) technique. By pulsing a laser-sheet through the spray field parallel to the injector centerline, images consisting of droplet pairs were produced on a CCD camera oriented perpendicular to the laser-sheet. In knowing the time between the laser pulses, a two-dimensional droplet velocity vector map was retrieved from the digital image. Although the droplet size distribution will also be obtained from these images in the near future, this report only introduces the concept. This methodology was found to produce high quality images and very detailed velocity maps. The work presented here is the baseline for a more complex and comprehensive system being developed.

# **A PARTICLE IMAGE VELOCIMETRY TECHNIQUE FOR SPRAY INJECTORS**

William W. Brocklehurst

## **Introduction**

Today's combustor computer models are providing very promising results in flow field prediction but are still limited by the empirical data they employ. The injector droplet initial conditions (usually empirical) are one of the major sources of error in these codes. By providing a better estimate of the velocity, size, and distribution contours in the droplet spray field, combustor model accuracy can be greatly increased. The procedure investigated is somewhat more affordable than commercial Phase Doppler Particle Analysis (PDPA) and Laser Doppler Velocimetry (LDV) equipment and will also provide instantaneous droplet size and velocity from a single image. Since the presented measuring process is also non-intrusive (i.e., no physical probes present in the flow), the flow field and droplet formation processes are undisturbed. After constructing the experimental apparatus, one need only change injectors to acquire a database for future use in combustor system design. Another attractive potential of this technique lies in the mapping of continuum fluid flows such as air. If sufficiently small particles are introduced into a flow so as not to disturb the flow structure, a velocity map can be found by the exact same procedure presented in this paper. Although this investigation did not include a seeded-flow analysis, work was done recently and the procedure is identical.

## **Methodology**

The method of non-intrusive PIV requires only a pulsed laser-sheet and a digital camera to provide images for the data reduction software. A double image of the spray field is obtained by setting the camera exposure time to receive two laser pulses. The droplet speed is obtained by dividing the droplet pair separation distance by the laser-pulse separation time; the velocity vector is already represented by the droplet pair

orientation. To determine direction, the first laser pulse duration is set to be twice that of the second laser pulse. This produces a droplet pair image in which one has an intensity twice that of the other. The two dimensional velocity vector is then constructed by tracing a line from the brighter droplet to its partner on the image. In this relatively straight-forward flow however, the pulses are set to equal widths.

Care must be taken to place the laser-sheet along the camera's focal plane when imaging the flow. If the laser-sheet is not properly placed, the droplet's radial velocity will carry it out of the sheet and perhaps out of the camera's focal plane thereby not producing a double image. The images produced are two-dimensional and any deviations out of the 2-D plane cannot be calculated by this procedure as of yet. More sophisticated techniques are required to accurately derive the normal velocity component from the images. Future work may include a camera equipped with a stereoscopic lens using a procedure somewhat like the one developed in Reference 1; although the normal components will be acquired only for a small slice of the field in each image.

Droplet sizes can be calculated from the images in two different ways. One can directly read the droplet size from the image or the droplet diameter can be calculated by using Mie scattering theory.

Directly determining the droplet size by counting *pixels* on the image is quite easy and straight-forward. The droplet smearing distance must simply be subtracted from the diameter obtained from the image. The droplet smearing distance is the enlarging effect caused by the movement of the droplet during a laser pulse. This smearing distance is equal to the product of the droplet velocity and the laser pulse duration and lies along the droplet's path of motion. This method was not used due to the limitations of the imaging equipment. In setting the imaging area to sufficiently cover the flow field, the resulting image resolution becomes approximately 35 by 70 *microns/pixel*. This results in a droplet radius of only one or two *pixels* which is too crude a representation of the droplet to predict size with any acceptable accuracy. Accurately determining the droplet sizes requires a changing of the camera lens and taking another image at a higher magnification; however this defeats the initial goal of determining velocity and size from a single image. In the future, a camera of finer spatial and intensity resolution will be used to accurately calculate the droplet size and velocity from the image.

Though somewhat more involved, analyzing the Mie scattering produced by the droplets allows one to calculate droplet velocity and size from the same image. Mie scattering theory provides a direct relationship between a sphere's diameter and its scattered light intensity. The procedure and equipment needed has been calculated but the discussion is quite lengthy. In this paper it will simply be stated that the camera used at present had only an eight *bit* resolution whereas a resolution of around sixteen *bits* will be needed. This should accurately predict droplet sizing within 10 *microns* using a wide-band laser sheet. Due to the camera's limitations, droplet sizes were not calculated but will definitely be added to this process in the future.

### **Apparatus**

The apparatus shown in Figure 1 was constructed to allow a pulsed laser-sheet to interact with the spray cone produced by a generic spray injector while digitally imaging the flow field. Software was composed to determine the droplet velocity profiles from these digital images.

A laser-sheet generator consisting of two horizontal and two vertical cylindrical lenses in series was used to form a laser-sheet from a 2 watt continuous Argon ion laser. By mounting the cylindrical lenses on rails, it was quite easy to adjust the laser-sheet height and thickness to maximize the energy incident on the area of interest. The laser beam was pulsed before the laser-sheet generator using an acousto-optic modulator and a digital delay/pulse generator; this allows various pulse widths and separations to be prescribed. Note that an acousto-optic modulator does not modulate the entire laser beam. These modulators use a Bragg cell to produce ordered fringes which are then chopped by modulating the power to the cell. By pulling off the 1st order fringe, a beam intensity 10% that of the vertically polarized primary laser beam can be supplied to the sheet generator. Note that a pulse width of 1 *microsecond* results in each droplet only seeing 0.2 *microJoules* of energy which still produces an adequate image.



The laser-sheet was passed through a fixture which encompassed the injector and its spray field. The injector fixture was essentially a 3 inch diameter stainless steel tube open at the ends having a length of 10 inches. The fixture was equip with four 1.5 by 8 inch quartz windows; one of which was replaced by a flat-black aluminum plate to produce an adequate imaging background. The injector fluid was removed by a variable speed vacuum pump attached to the bottom of the fixture.

The injector itself was placed on a traverse so as to accurately place the injector spray cone into the imaging area. This allowed fast and accurate imaging of the entire spray distribution perpendicular to the flow axis. The traverse system was accurate to 10 microns which provided very accurate injector placement.

The injector fluid supply system consisted of a GN<sub>2</sub> pressurized liquid reservoir equip with shutoff and bleed valves. A pressure gauge and regulator assured accurate fluid flow rate control. Figure 2 shows the injector flow rates and bulk velocities as a function of driving (reservoir) pressure for different fluids. The bulk velocity is found by dividing the measured flow rate by the injector exit area. Bernoulli's equation,  $V=(2\Delta P/\rho)^{1/2}$ , was also used to estimate the bulk velocity. Though the bulk velocities do not give exact information, they do allow one to estimate the pulse separation and exposure time required before activating the system. Note that for the final results, denatured ethanol ( $\approx$  5% methanol) was used as the injector fluid. The injector used in the experiment resisted clogging and provided better atomization when ethanol was used.

Flow images were obtained by a CCD camera oriented perpendicular to the laser-sheet. The camera's resolution was 482 by 640 pixels and could provide exposure times as low as 0.05 microseconds. However, the camera was designed to normally operated in interlace mode. To produce an image with no 'blank' lines, the interlace mode was disabled to give a picture resolution of 241 by 640 pixels. Due to the nature of this investigation, the camera was placed so that the injector's axial direction had a 640 pixel resolution. The digital images acquired by the camera were displayed and stored on a Macintosh IIc computer as well as being continuously displayed and recorded on a TV/VCR setup. This allows the runs to be recorded and analyzed later with the camera's frame-grabber software. Pseudo-color contours are possible with the camera's software,

but gray-scale images are stored for a clearer picture and for use with the image analysis software. The camera exposure time was set to trigger and obtain two laser pulses and the average viewing area size was 50 by 35 *millimeters*.

## **Software**

A FORTRAN program was written on a 486 IBM PC to calculate velocity vector maps from the digital images. Since the camera's software requires a Macintosh computer, the images must first be converted to a TIFF gray-scale format so that the PIV software can more efficiently handle the files. Each TIFF image is 154.45 *kilobytes* and can be compressed to between 60 - 80 *kilobytes* for storage compared to the raw Macintosh files of 308.74 *kilobytes* and 75 - 90 *kilobyte* compression capability.

After converting the files into a usable format, the first step of the analysis is to identify and tag the individual droplets on the image so as to ignore background noise. The software first allows the user to view the image for different threshold values. That is, all *pixels* having an intensity value below the input threshold value are set to zero and the image is displayed on the PC monitor. This allows the user to decide what threshold value to use when the program begins to identify droplets and also what to expect from the image.

After setting the actual threshold value, the program begins to identify the droplets. A user input minimum radius (in *pixels*) is used to search for *pixel* clusters representing the droplets. Since the images are taken directly after the injector exit, the liquid sheet on either side of the image will be recorded as a very large droplet. Once identified, each droplet's center of gravity is calculated and stored. The program has now produced an array of droplet center locations.

Now that the droplets have been identified, the initial pair matching is done using the droplet center location data. The program takes a user input box size (in *pixels*) and scans the picture. The box size represents the expected X and Y velocity components; any section of the picture (including the entire picture) can be scanned. The variable

section scan has been included so that the user can ignore the pre-atomization area directly after the injector to increase the program run time. At any point during the scan where there are only two points present in a box, the pair location is stored. If there are not two points present, the scan proceeds to the next box and does not store any location data. The scan results are graphically displayed on the monitor after completion and the user is asked if the results should be stored. More scans can be run if desired and the pair results are accumulated in a file making sure that no pairs are duplicated. More than one scan is usually done since the droplet velocity decreases as they move away from the injector exit. This is represented on the image by decreasing pair separation distances. Please refer to Figure 3 for a representation of the initial droplet pair search procedure.

Although the obvious droplet pairs have now been found, there is still much data left to be extracted from the droplet dense regions. After all of the initial box scans have been run, the program begins an automated dense region search. Essentially, the program looks at every droplet center on the image which was not paired. When a droplet is without a partner, the nearest three pairs are used to interpolate the expected partner location. A 'thick' vector is then set by the program and the expected location is scanned. If a partner is found it is added to the pair list (again making sure there are no pair duplications); else the program moves onto the next droplet center. Figure 4 shows a representation of this interpolation scheme.

Now that all of the droplet pairs are identified, the velocity calculations begin. First of all, *pixel* dimensions are converted to *microns* through the user input conversion factor. The conversion factor is found by imaging a ruler scale or known diameter wire in the laser-sheet plane and measuring its size in *pixels* on the image. Simply geometric relations are then used to calculate the distance between the droplet pair centers. By dividing the distance traveled by the pulse separation time, a droplet speed is calculated along with the unit velocity vector. A velocity vector map has been calculated.

Finally, the velocity vector map is displayed on the monitor and the user has the option of deleting obvious mistakes, changing vector signs, and starting another scan. Figure 5 shows a velocity map format and the final filtering options available. The final results are written out into a TECPLOT™ PC data file for presentation. Contours, histograms, vector maps, and distance curves are all helpful in viewing the velocity field.

The software described here is an image processing technique in its infancy. The software composition, experimental setup, data acquisition, data reduction, and this paper were all accomplished in 11 weeks. There is still tremendous room for improvement and expansion that time has not allowed. The future work and modifications will be discussed at the end of this paper.

## **Results**

PIV data was taken at driving pressures of 40 and 60 *psi* for 40 'slices' of the spray field to provide a three-dimensional representation. At each of these 40 positions, 10 exposures were taken to provide enough information for a reliable velocity map. The multiple exposures were needed due to the nature of the droplet field. One must remember that the human eye accumulates data; when the spray field is imaged on the order of microseconds, the images will contain a smaller number of droplets than expected. On the average, each image contained 20 pairs that were actually used in the final velocity map. The average pulse width, pulse separation, and exposure time were 1.5, 70, and 80 *microseconds* respectively.

Figures 6, 7, 8, and 9 each show a raw TIFF image and its corresponding velocity map for 40 and 60 *psi* at  $z = 0$  and 1.5 cm where  $z$  is perpendicular to the camera focal plane and  $z = 0$  at the injector center. Figure 10 shows the final accumulated velocity vector maps for  $z = 0$  and 1.5 cm at 60 *psi*. These are actually 5 superimposed velocity maps.

## **Future Work**

As stated earlier, there is much room for improvement in the entire procedure presented in this paper. These improvements include the data acquisition techniques, theoretical concepts, image processing, program/user interaction, experimental equipment, and data reduction efficiency techniques.

Droplet sizing was not investigated in this paper due to camera limitations. A system similar to the one already being used has been outlined though not presented. This system will enable one to acquire an instantaneous measurement of the droplet velocity and size fields. The theory has already been developed and the overall procedure looks promising. By using a CCD of sufficient resolution and a wide-band dye-laser rig, size becomes a function of image intensity.

In the area of PIV, two modifications are being considered. It would be of great benefit to apply the PIV technique to a burning spray. Through the use of appropriate optical filters, a relatively clean flame should present little problem. A high soot content could severely reduce the effectiveness of the present system, however the optical filters should lessen the effect. Soot and droplet distribution density are perhaps the two limiting factors of the present system. It is hoped that increasing laser power, accounting for incident sheet intensity extinction through the spray, and shorter exposure times (i.e., less imaged droplets) can counteract these obstacles.

Certainly there is much more to be done with the image processing software. The pair location algorithm is extremely basic. The program presently relies on a fairly detailed knowledge of the flow prior to analysis. To rely less on the user, there are quite a few immediate changes that can be made. The first is in the pair search method. By using different search-box geometry's (squares, rectangles, triangles, etc.) the program can be pre-configured to best analyze a given flow structure (including recirculation zones). Additionally, more up to date processes such as sharpening, blurring, despeckling, and more exotic digital imaging filters can be used to 'clean-up' the image before data extraction. Figure 11 shows a raw TIFF image and the same image below that has been heavily sharpened and despeckled. This was done by a commercially available image editor (PhotoStyler™) which would drastically increase the data reduction time if it were used on all of the files. If sizing procedures are added, they will also provide another parameter for pair matching, not to mention the ability to test droplet evaporation models experimentally.

Patternation (mass flow or flux contour) diagnosis has already been attempted somewhat with the current system and work is being continued at Phillips Laboratory. By mapping intensity contours of multiple ( $\approx 100$ ) exposures, the axial patternation can be compared to cross-sectional patternation and actual fluid collection results. Some theoretical work is still needed to relate these intensities to absolute quantities such as mass flux.

The fundamental change planned for the present system involves three-dimensional velocity measurements. It is hoped that by using a stereoscopic lens, two separate images of different views can be obtained at the same instant without the use of a second camera. By expanding the laser sheet width slightly, a three-dimensional velocity profile (in a small vertical slice of the spray field) can be obtained by modifying the image processing software. This can provide better velocity profiles of swirling sprays and more accurate three-dimensional patternation contours. Three-dimensional PIV will also provide instantaneous measurements of turbulent velocity profiles. This would be of great use to the CFD community in understanding the mechanics of turbulent flows as indicated in Reference 1.

## **Conclusions**

A PIV experimental setup and image processing package was successfully created and tested. Well defined velocity distribution maps were produced for different driving pressures. These two-dimensional maps showed a reduction in droplet velocity as the distance from the injector exit increased. The calculated velocities were also on the order of those indicated by the mass flow rate and Bernoulli's equation. Procedural modifications are planned to create a very useful tool in spray diagnostics and fluid mechanics.

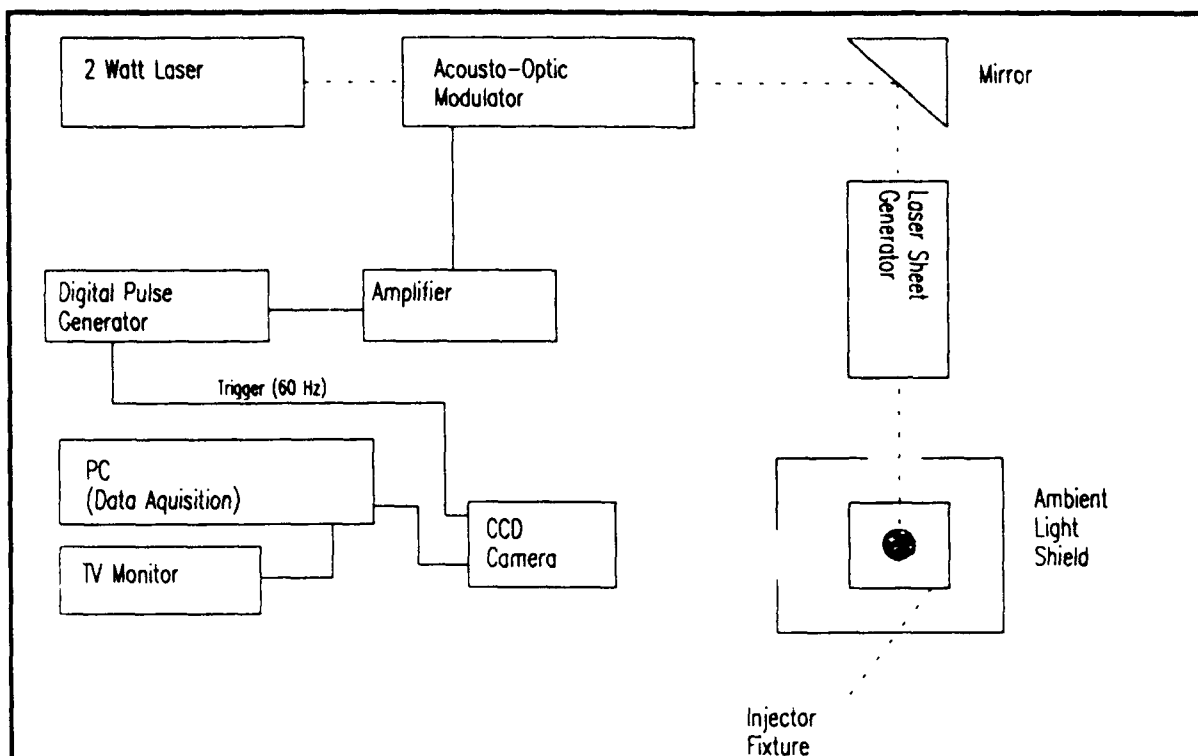


**Figure 1: Experimental Setup**

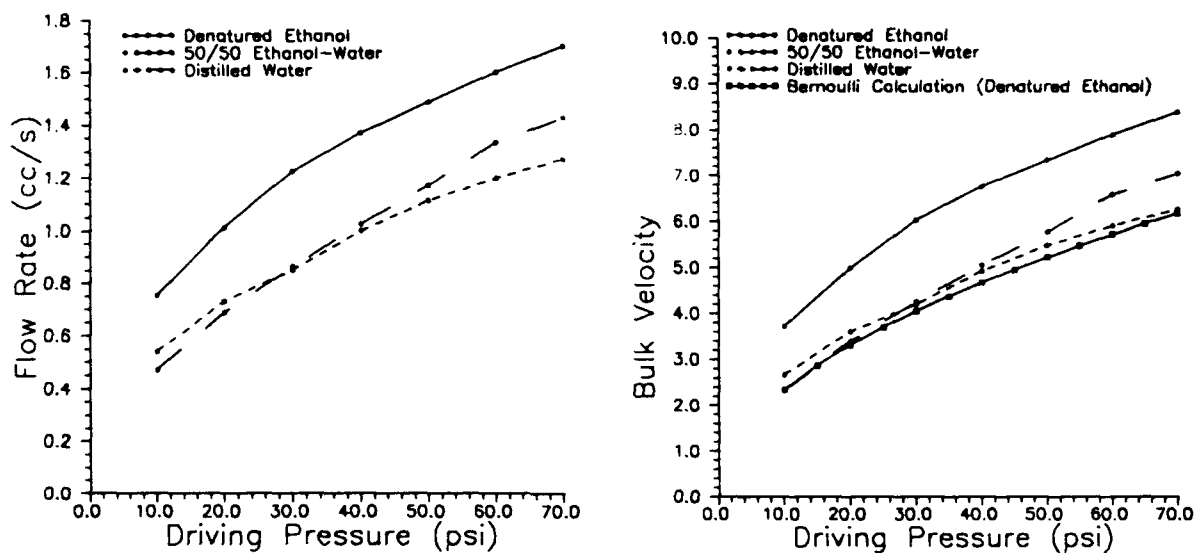


**Figure 2: Flow Rates and Bulk Velocities**

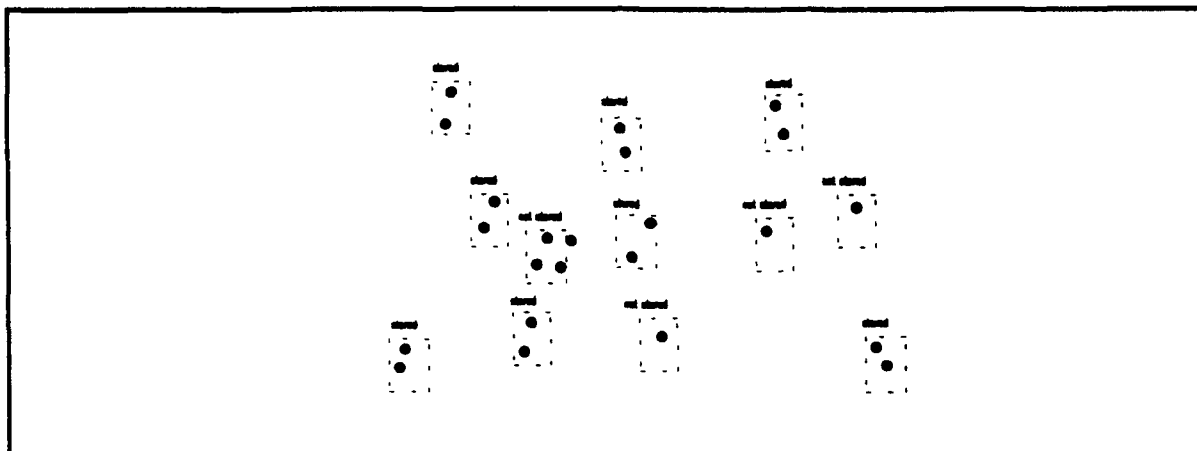


**Figure 3: Scan Procedure**

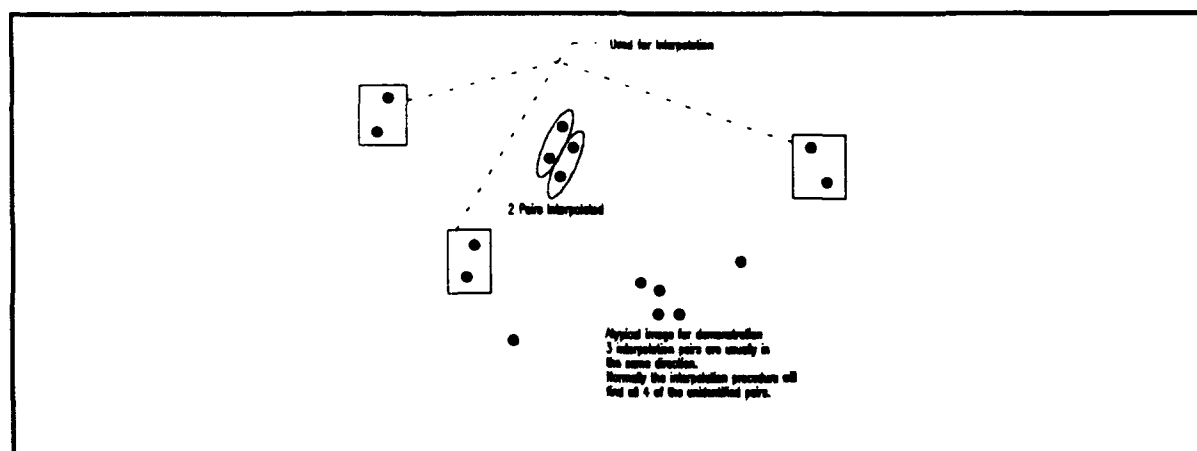


**Figure 4: Interpolation Routine**

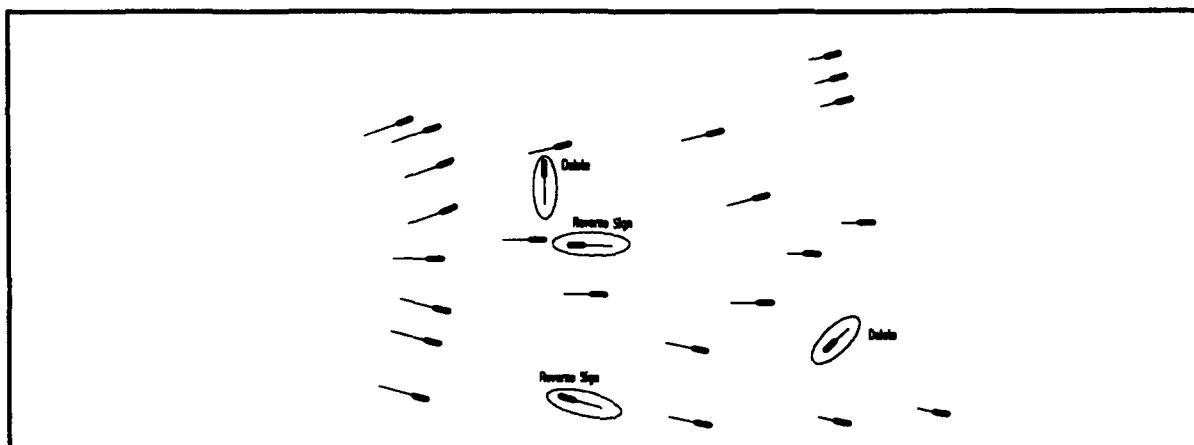


**Figure 5: Final Data Filtering Options**



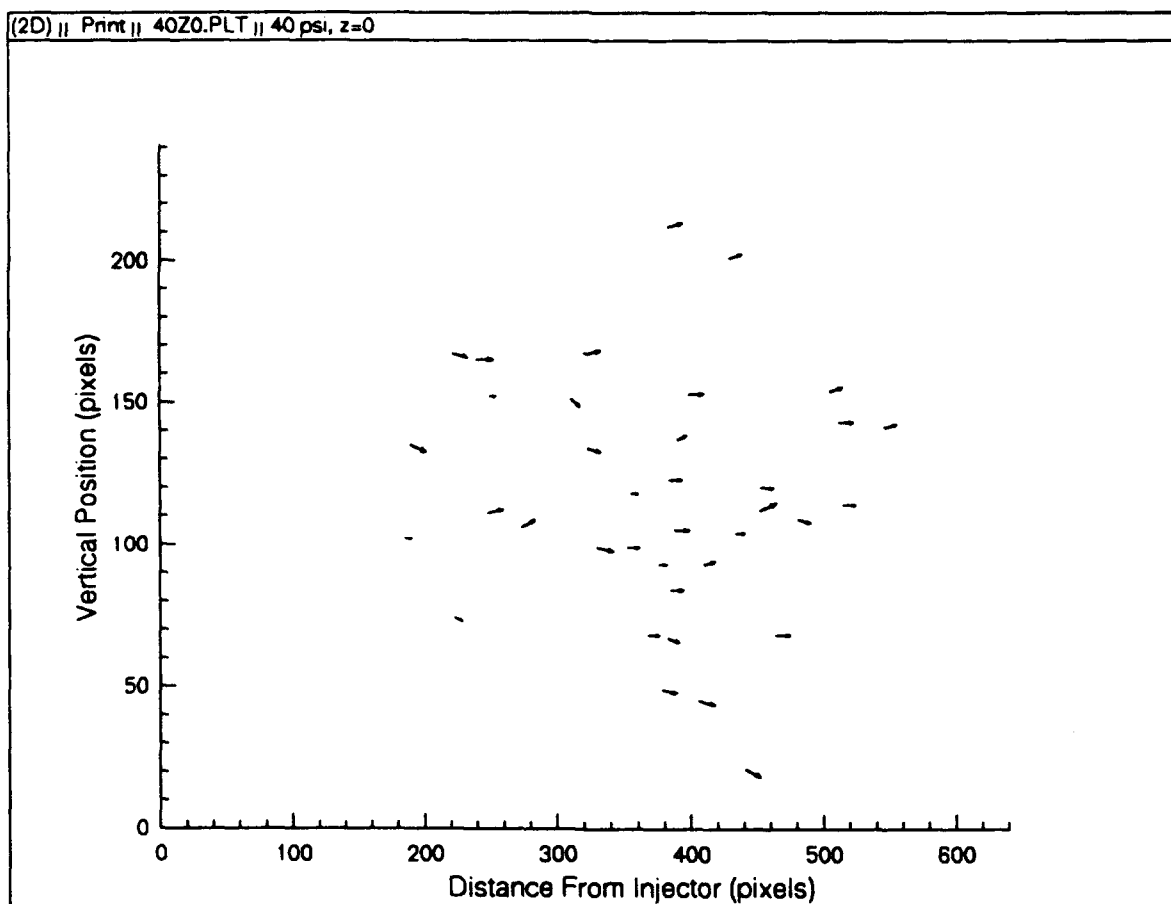


**Figure 6: 40 psi, z = 0 cm**

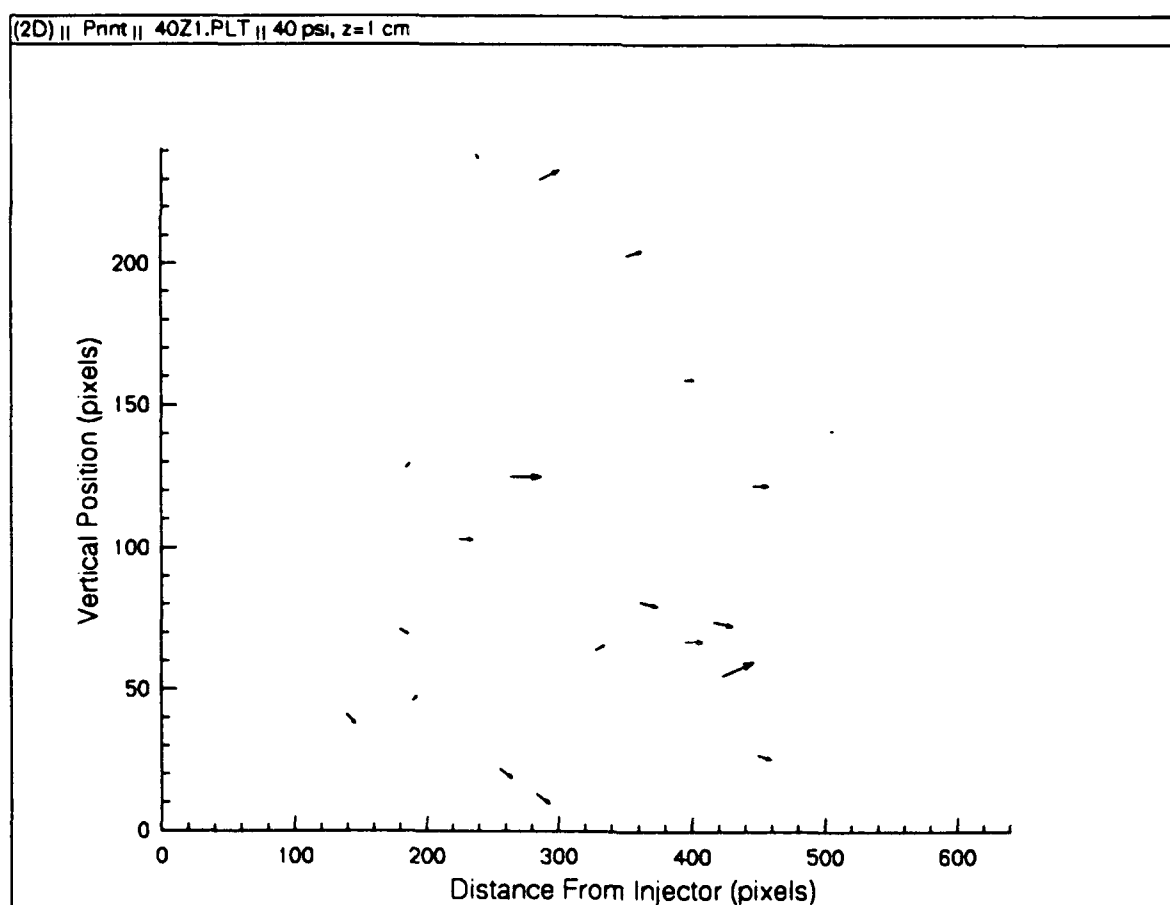
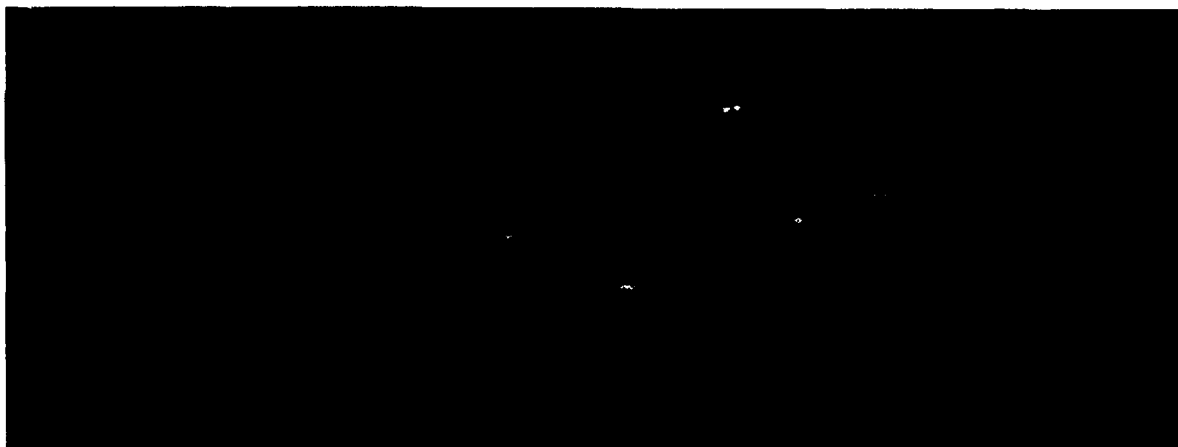


**Figure 7: 40 psi, z = 1 cm**

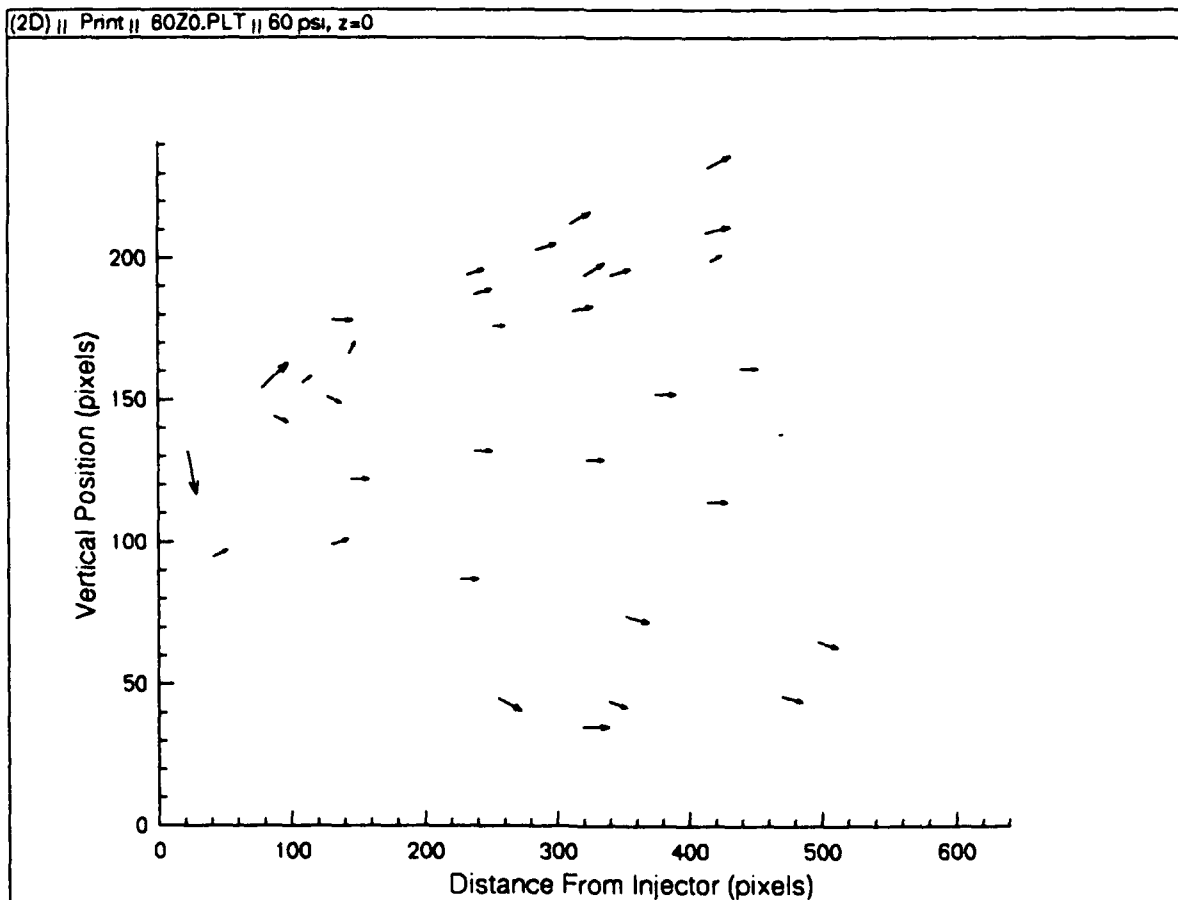


**Figure 8: 60 psi,  $z = 0$  cm**

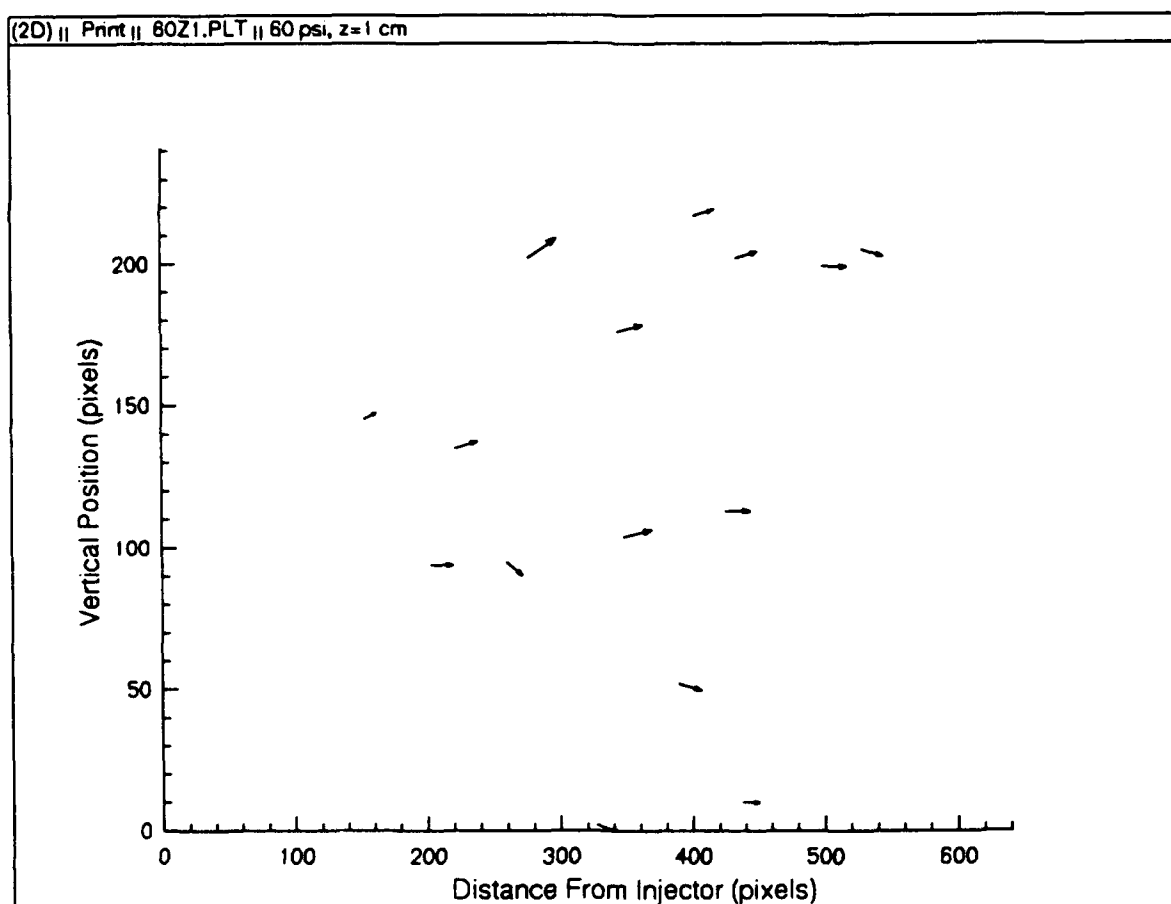
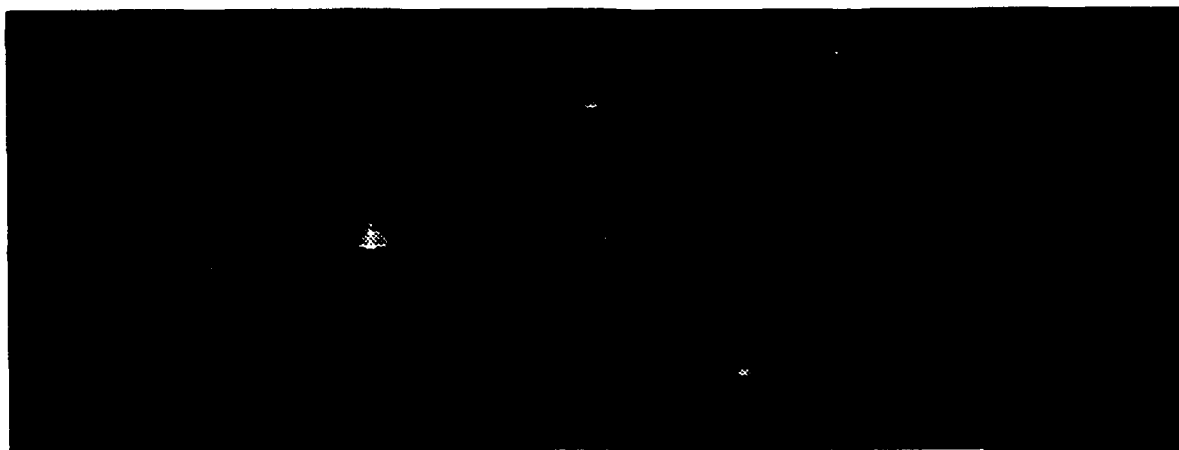
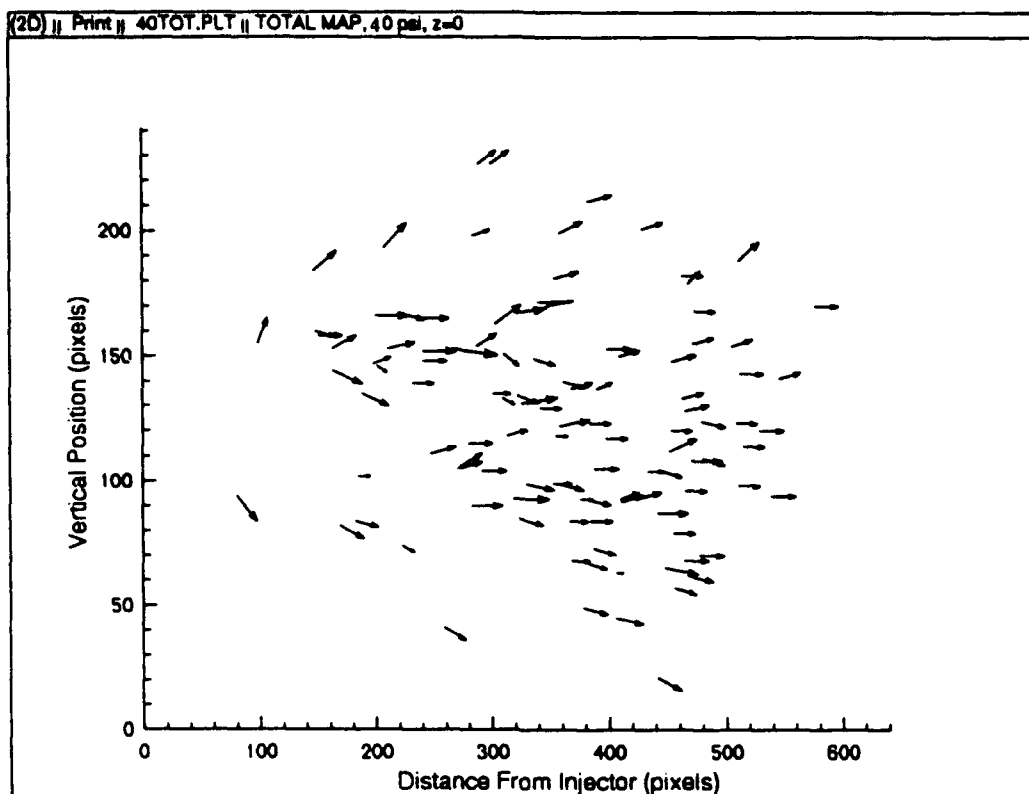
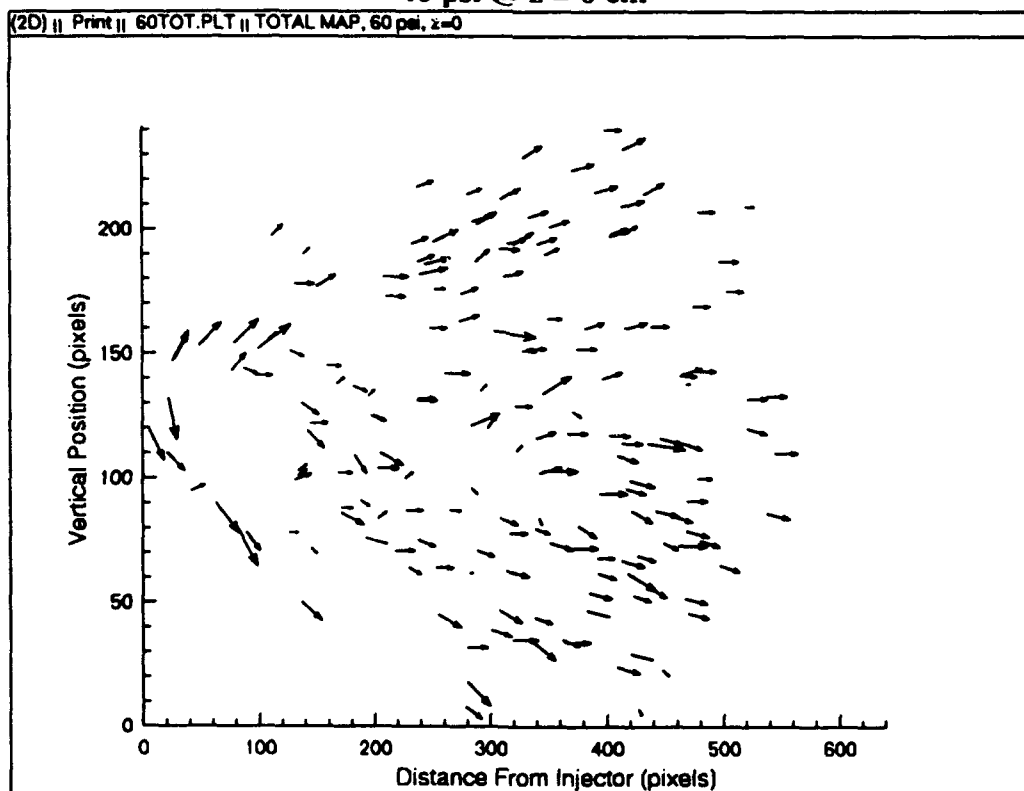


**Figure 9: 60 psi, z = 1.5 cm**

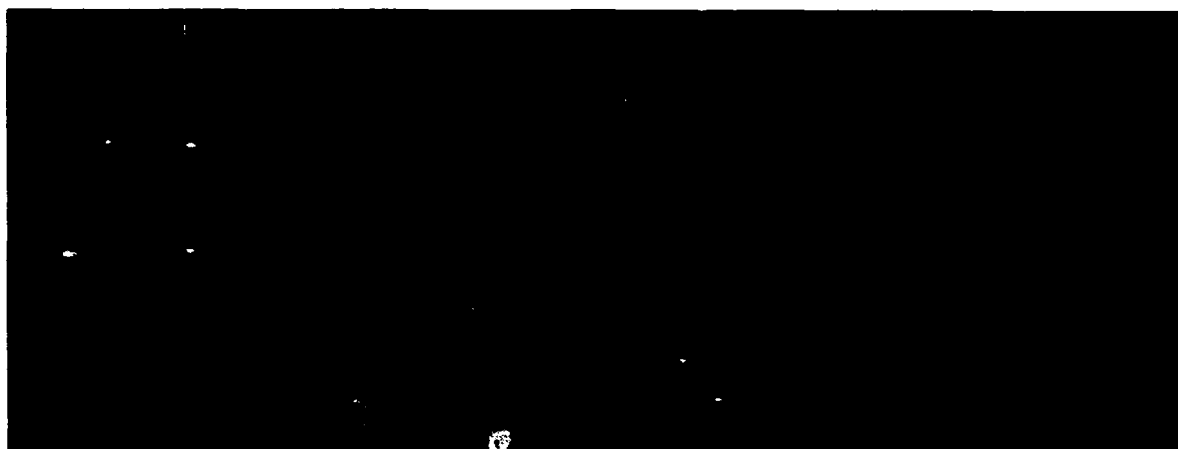


40 psi @ z = 0 cm



60 psi @ z = 0 cm

**Figure 10: Composite Velocity Maps at the Center of the Spray Cone**



**Raw TIFF Image**



**Sharpened Heavily, Despeckled, with Contrast and Brightness Adjustment**

**Figure 11: Digital Image Enhancement**

## **References**

1. N. Trigui, Y. Guezennec, R. Brodkey, and C. Kent, "Algorithms for Fully Automatic Three-Dimensional Particle Image Velocimetry", 13th Symposium on Turbulence, University of Missouri-Rolla, September 1992.
2. C. Bohren and D. Huffman, Absorption and Scattering of Light by Small Particles, John Wiley & Sons, 1983.
3. J. Russ, The Image Processing Handbook, CRC Press, 1992.
4. A. Nussbaum and R. Phillips, Contemporary Optics for Scientists and Engineers, Prentice-Hall Inc., 1976.
5. A. Gupta and D. Lilley, FlowField Modeling and Diagnostics, APO Production Unit Inc., 1985.

ANODE VOLTAGE DROP STUDY IN A QUASI-STEADY MPD THRUSTER  
USING PROBE DIAGNOSTICS

Mohanjit S. Jolly

Graduate Student  
Department of Aeronautics and Astronautics

Massachusetts Institute of Technology  
77 Massachusetts Avenue  
Cambridge, MA 02139

Final Report For:  
Graduate Student Research Program  
Phillips Laboratory, Edwards AFB

Sponsored by:

Air Force Office of Scientific Research  
Bolling Air Force Base, Washington, D.C.

September 1993



# ANODE VOLTAGE DROP STUDY IN A QUASI-STEADY MPD THRUSTER USING PROBE DIAGNOSTICS

Mohanjit S. Jolly

Graduate Student

Department of Aeronautics and Astronautics  
Massachusetts Institute of Technology

## Abstract:

A cylindrical quasi-steady Magnetoplasma-Dynamic (MPD) thruster was used to conduct a voltage drop study. Several probe diagnostics were utilized to determine radial and axial electron temperature, density, magnetic field, current density and plasma potential profiles at 4.4 kA and 4.8 kA current levels with Argon flowing at .5 grams per second. A set of six experiments were conducted during the course of the study. Initially voltage-current characteristics for the thruster were obtained at .5, 1.0 and 1.5 grams per second. Near anode axial traverses were performed with floating probe and Langmuir triple probe to determine the anode voltage drop and the electron temperature and density as a function of increasing thruster current. Radial scans were made with the floating probe and triple probe at three axial location at 4.4 kA and 4.8 kA. Finally, a magnetic induction probe was utilized to determine the magnetic field and subsequently the enclosed current and radial current density profiles at the same two current levels. Measured near-anode voltage drop varied from 16 V to 33 V as a function of increasing thruster current (2.2 kA - 5.34 kA). During the radial floating probe scans, cathode voltage drops of 35 V and 43 V were measured near the backplate and at the mid-thruster locations, respectively. The measured anode voltage drops during the radial scans varied from 6.1 V to 21 V near the backplate and mid-thruster locations, respectively. The electron density varied throughout the thruster from  $1.4 \times 10^{20} \text{ m}^{-3}$  to  $5 \times 10^{20} \text{ m}^{-3}$ . The electron temperature varied from 1 eV to 4.25 eV radially, being highest near the cathode. Current concentration was observed near the cathode root with a current density of  $250 \text{ A/cm}^2$  and the anode tip with a current density of  $180 \text{ A/cm}^2$ .

# ANODE VOLTAGE DROP STUDY IN A QUASI-STEADY MPD THRUSTER USING PROBE DIAGNOSTICS

## I. INTRODUCTION:

With the mindset of the National space program leaning towards interplanetary missions, increasingly more emphasis is being placed on high efficiency, low cost methods of space propulsion. High specific impulse (Isp) and a consequent increase in the payload fraction has shown electric propulsion as a viable option for these missions. MagnetoPlasma-Dynamic (MPD) propulsion, a subset of Electric Propulsion (EP) has been a subject of numerous experimental and numerical studies for the past twenty years. MPD propulsion relies on ionized propellant being accelerated by the interaction of electric current driven through the propellant with magnetic fields that are induced by the current and/or supplied externally via solenoids. This interaction is referred to as the Lorentz force ( $\mathbf{J} \times \mathbf{B}$  force). [1]

Significant advances have been made in the EP field on both the theoretical and the experimental fronts, but much of the physics remains poorly understood. In order to test the validity of numerical models and guide their future development, accurate measurement of plasma parameters such as electron temperature, density, plasma potential and current density is crucial. To prove the advantages of MPD systems, high efficiency (~60%) must be achieved. Although these thrusters show theoretical efficiencies on the order of 80%, experimentally, the efficiency values have been calculated to be 35% at best [2]. Two major loss mechanisms prevent the high theoretical efficiency from being reached: frozen flow losses, which are dominant at high (> 1 MW) power, and anode losses. Previous studies have shown that below the 1 MW level, a significant portion of the thruster power gets deposited into the anode [3]. Therefore, anode voltage drop study along with measurement of overall plasma parameters was conducted.

## II. FACILITY:

The pulsed multi-megawatt facility used for this study is located at the Phillips Electric Propulsion Laboratory, Edwards Air Force Base, California. A 1.625 in. long, 3.0 in. diameter cylindrical device with a copper anode and a 1.0 in. long, .375 in. diameter throated tungsten cathode was used as shown in Fig. 1. The exterior of the thruster was insulated with plexiglass. Argon propellant was injected into the thruster through a Boron-nitride backplate via 16 .125 in. diameter holes, 8 each at a radius of .5 in. and .9375 in. and through an .1875 in. annulus at the base of the cathode. Mass flow was distributed to the holes via a high precision orifice through which the gas enters. Since the propellant flow through the orifice was choked, the mass flow rate could be deduced from the pressure drop in the

spherical plenum that was placed outside the chamber. Copper coaxial cables were used to establish connection between the Pulse Forming Network (PFN) and the thruster electrodes.

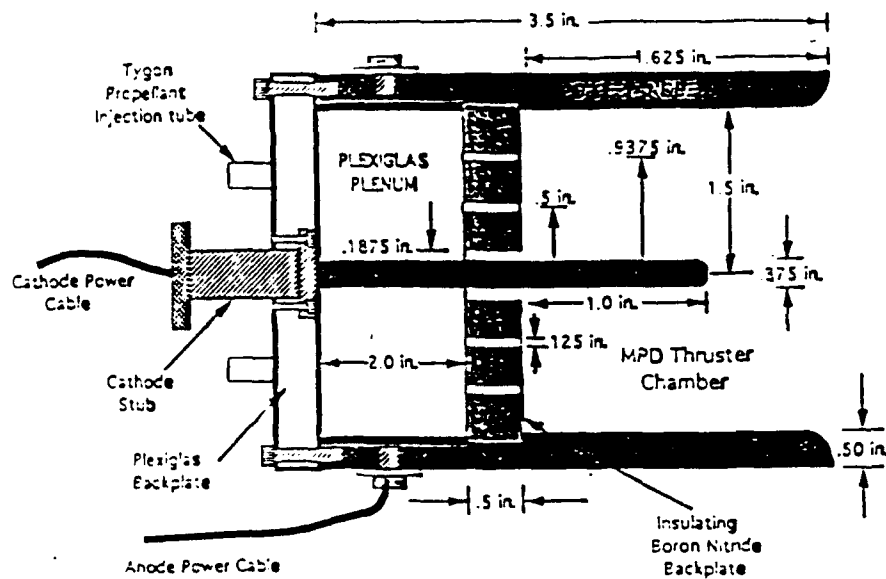


Fig. 1: MPD Thruster Schematic

The plasma generation system consisted of three different subsystems: The MPD vacuum system, the propellant feed system and the electrical system.

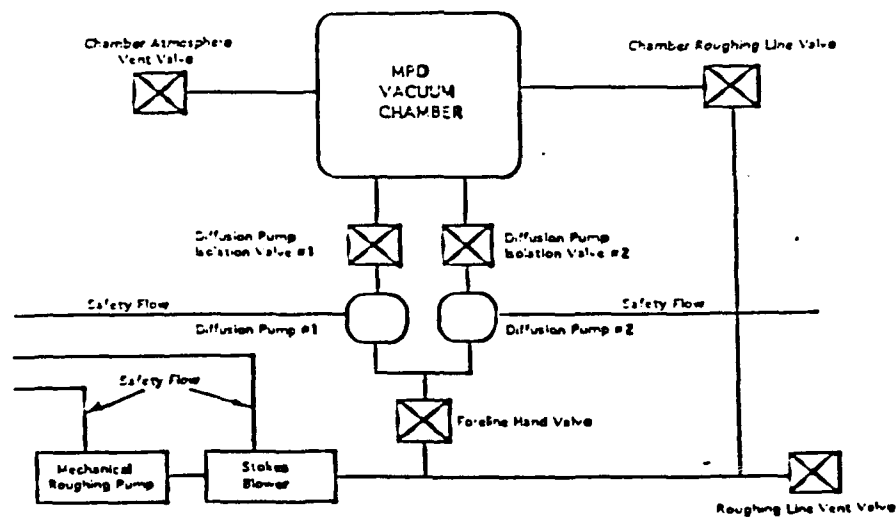


Fig. 2: The MPD Vacuum System

The vacuum facility as shown in Fig. 2 consisted of a stainless steel cylinder which was 8 feet in diameter and 12 feet long. Optical access to the chamber was possible through two plexiglass and one quartz portals. A mirror was placed inside the chamber to obtain head-on shots of the thruster. A stokes mechanical pump in series with a Roots blower and a ten inch diffusion pump were used to bring the chamber pressure to  $3 \times 10^{-4}$  Torr range.

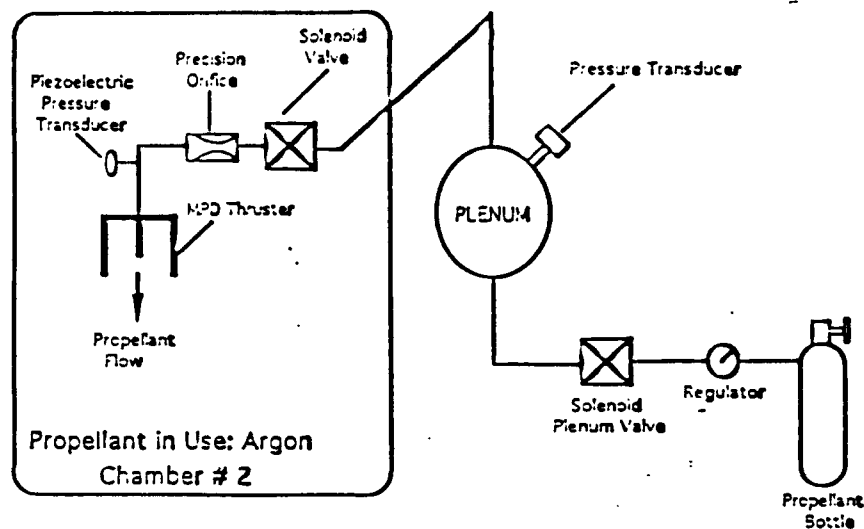


Fig. 3: The MPD Propellant System

The propellant system shown in Fig. 3 was a choked flow pulsed gas system which consisted of an Argon T-bottle and regulator supply. A .25 in. propellant line fed from the bottle into a steel spherical plenum located outside the vacuum chamber. The chamber pressure was measured with an Omega pressure gauge.

From the plenum, a .25 in. steel propellant line fed through the vacuum chamber to a Valcor solenoid valve. Following the valve was a 2 mm. diameter Fox precision orifice used to choke the flow. A Kistler piezoelectric pressure transducer was used to measure the gas pulse profile. The propellant line finally fed into two .25 in. Tygon tubes leading to the thruster plenum.

During thruster operation, a fast acting solenoid valve was used to release a 60 millisecond gas pulse, which achieved steady-state in 15 milliseconds. The thruster was fired 20 milliseconds after the initiation of the gas pulse. A Stanford Research Systems signal generator was used to regulate the timing between the gas pulse initiation and the actual thruster firing.

The power source for the quasi-steady MPD thruster was a Pulse Forming Network (PFN) shown in Fig. 4. The PFN is a ten section LC network with a nominal .01 ohm output impedance. Each section consists of three, 2000 microfarad, 800 volt Maxwell electrolytic capacitors connected in parallel and a 5-turn, .53 microhenry inductor. The PFN is capable of releasing a one to two millisecond current pulse at up to 40 kA and 400 volts, assuming a matched load. All experiments conducted in this study utilized a 1 millisecond pulse with roughly a 700 microsecond steady-state region.

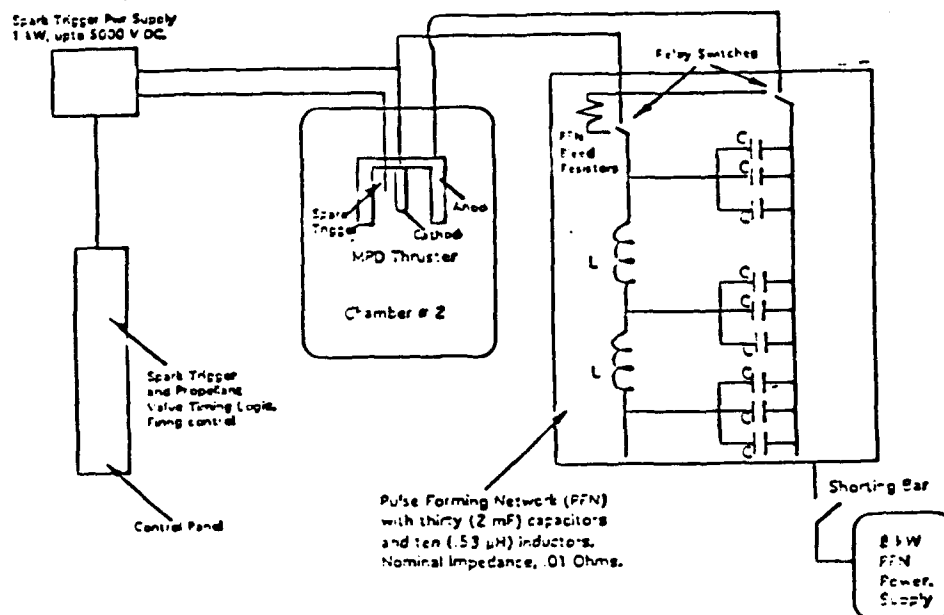


Fig. 4: The MPD Electrical System

The thruster firing sequence begins with the charging of the PFN until a desired voltage is reached, at which time the PFN is disconnected from the charging power supply. All the controls for the thruster firing were mounted on a console next to the chamber. Once the "Fire" button is pushed, a TTL logic pulse acts as a trigger for the signal generator to send out two square pulses: namely, the gas pulse and the spark pulse. The gas pulse is an 80 msec pulse that opens the solenoid valve. Twenty milliseconds later, the spark pulse is initiated. The spark occurs once the gas pulse has reached steady state. This spark initially ionizes the propellant to create a current path for the PFN discharge. The spark trigger is a .01 in. diameter tungsten wire fed through a thruster propellant injection hole. This spark trigger wire is used to provide an initial high voltage spark initiates thruster operation. Thruster current is measured with a Pearson Electronics current pulse transformer. Voltage across the thruster was measured using two Tektronix 1000:1 high voltage probes attached to the thruster feed-throughs outside the chamber. A Tektronix DSA 601 digital signal analyzer was used to record the thruster current and voltage profiles.

The following set of six experiments were conducted during the course of this investigation:

1. Thruster characterization (V-I curves at .5, 1.0, 1.5 g/sec).
2. Axial traverse of the thruster with a floating probe to determine the voltage drop near the anode as a function of increasing current.
3. Axial traverse of the thruster with a triple probe to determine electron temperature and density near the anode as a function of thruster current.
4. Radial floating probe traverses at three axial locations.
5. Radial triple probe traverses at three axial locations.
6. A current mapping of the entire thruster using an induction probe.

### III. EXPERIMENTAL RESULTS:

#### III.1 MPD Characterization:

Initial set of experiments were conducted in order to determine a voltage current characteristic of the MPD thruster at three different mass flow rates (.5, 1.0, 1.5 g/sec). Experiments in the past have shown an unstable regime of thruster operation commonly referred to as Onset where profound voltage oscillations and electrode erosion are visible. This particular series of firings were conducted to identify the Onset level for the given mass flow rates. Since operation at or beyond the Onset level tends to physically damage the thruster, the identification of the stable and unstable (post-onset) regimes was important. Care was taken to insure that the probe experiments would be kept in the stable region, thereby extending the thruster lifetime.

The Onset current levels for the .5, 1.0 and 1.5 grams per second were determined to be 5 kA, 5.5 kA and 6.0 kA, respectively. The Voltage-Current characteristics for the three mass flow rates are shown in Figs. 5, 6, and 7, respectively.

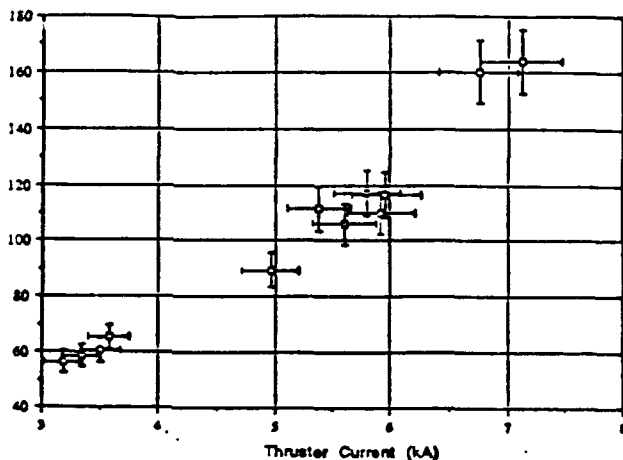


Fig. 5: V-I Curve At .5 grams/sec

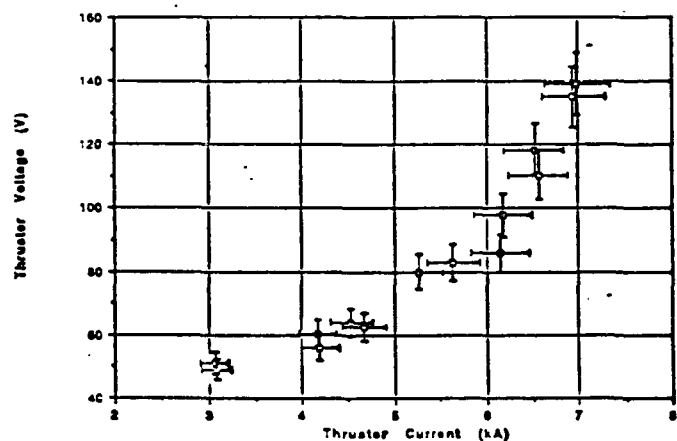


Fig. 6: V-I Curve At 1.0 grams/sec

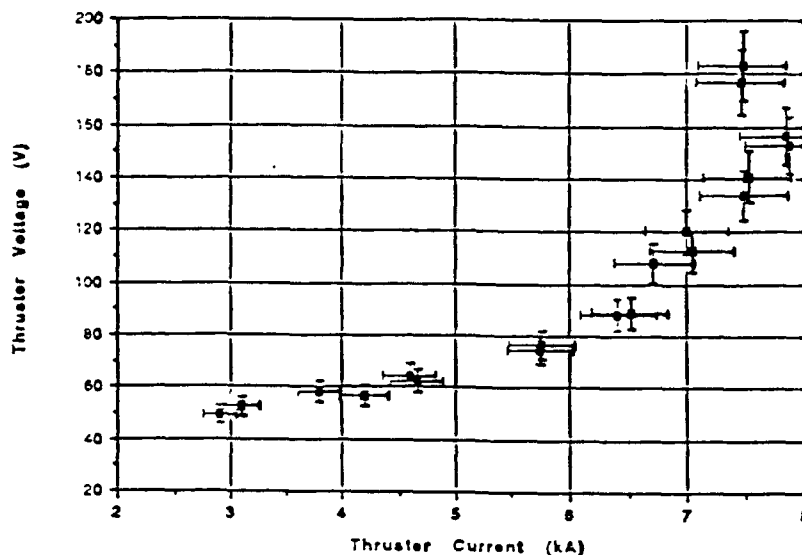


Fig. 7: V-I Curve At 1.5 grams/sec

The primary objective of this investigation was to study the anode voltage drop which constitutes a major efficiency loss mechanism for MPD thrusters. The mass flow rate of .5 g/sec was chosen as the operational mass flow rate for the experiments to follow. With a low mass flow rate, then, high anode voltage drop would be noticed at a lower power level than for higher mass flow rates. One theory suggests anode starvation (lack of charge carriers) near the anode as the mechanism for the voltage drop. To increase electrical conductivity near the anode, therefore, large electric fields need to be created leading to a high voltage drop in the area.

### III.II Near Anode Experiments:

Anode voltage drop measurements were made as a function of varying thruster current. Thruster current was varied from 2.2 kA to 5.34 kA by varying the PFN voltage from 100 V to 200 V, respectively. Initially, a floating probe was inserted roughly 1 mm. from the anode surface and traversed axially. A floating probe consists of a single electrode inserted into an Alumina housing, aligned with the thruster axis and connected via a BNC cable to an electronic comparator. The probe was referenced with respect to the anode but since the probe was floating, no net charge interaction took place between the plasma and itself. Measurements were made at twelve axial locations separated by .125 in. Thruster operation was kept below the onset level for .5 grams per second determined previously to be 5.5 kA. The goal of the floating probe experiments was to determine the anode voltage drop as a function of increasing thruster current and determine the thruster current where the anode drop rose rapidly, which could be used as the operating condition for further probe experiments.

The floating probe results are shown in Fig. 8 which represents the floating potential drop with respect to the anode rather than the plasma potential which is needed to determine the actual anode fall.

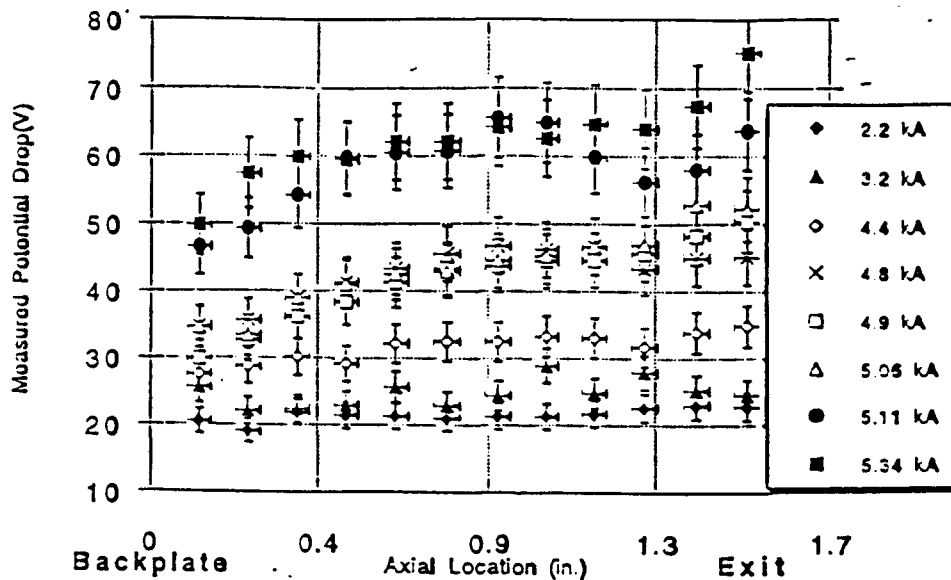


Fig. 8: Near-Anode Floating Potential Drop as a Function of Thruster Current

Fig 8 does, however, shows two distinct transition points. A considerable jump in the floating potential was noticed between 150 V and 160 V PFN (4.4 and 4.8 kA) and again between 180 V and 190 V PFN (5.06 and 5.11 kA). To convert from the measured floating potential to the desired plasma potential, an electron temperature correction factor is necessary as given by the following equation [4]:

$$V_p = V_f - 5kT_e/e$$

where  $V_p$  is the plasma potential,  $V_f$  is the measured floating potential,  $k$  is the Boltzmann constant and " $e$ " is the electron charge. The measured anode drop varied from 16.1 V to 33.2 V as a function of increasing thruster current. The second set of near anode experiments were conducted with a Langmuir triple probe to determine the electron temperature and density.

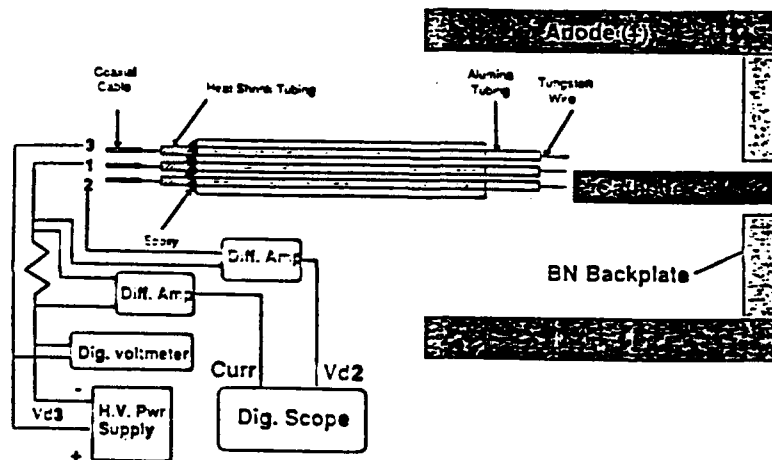


Fig. 9: A Langmuir Triple Probe Schematic

A triple probe consists of three metallic electrodes supported by three parallel thin alumina tubes as shown in Fig. 9. One of the electrodes is floating while the other two are biased with respect to each



other. The simultaneous measurements of the current flowing between electrodes 1 and 3 and the voltage difference between electrodes 1 and 2, values for the electron density and temperature, respectively, can be obtained. This particular probe technique nullifies the use of voltage ramping to obtain a V-I characteristic to deduce the  $T_e$  and  $N_e$ , as is the case with a traditional Langmuir probe. Since the MPD firings were pulsed, triple probe provided the source for instantaneous measurements of the  $T_e$  and  $N_e$ .

Due to the physical dimensions of the probe, during the near anode traverse, the electrodes were placed approximately 1.25 mm. from the anode surface with an inter-electrode separation of 1.6 mm. Measurements were obtained at the same twelve axial locations as used for the floating probe measurements. Near anode electron temperature varied from .2 eV to over 6 eV with increasing thruster current as shown in Figs. 10-13. All axial temperature profiles displayed a dual hump behavior corresponding to a sharp rise in temperature at .375 in. and 1.25 in. axial locations. The behavior was repeatable at all current levels.

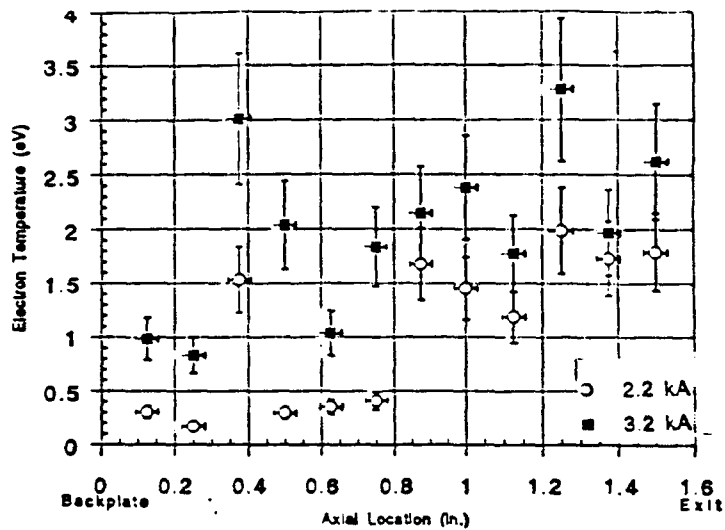


Fig. 10:  $T_e$  at 2.2 and 3.2 kA

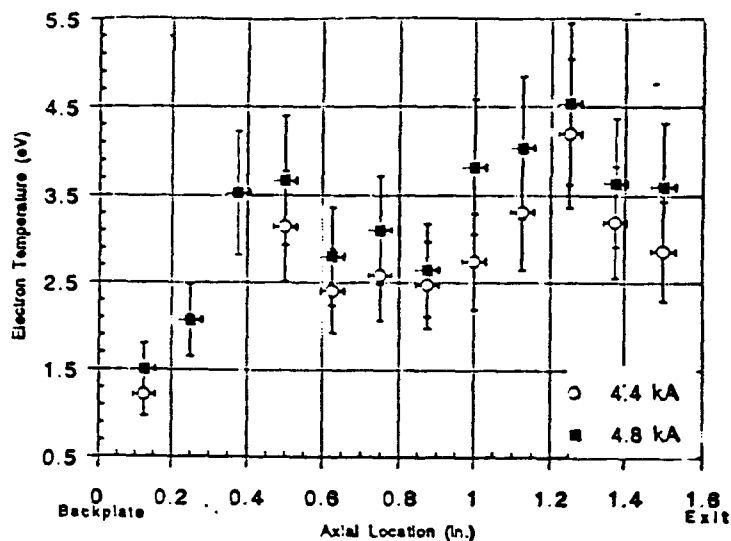


Fig. 11:  $T_e$  at 4.4 and 4.8 kA

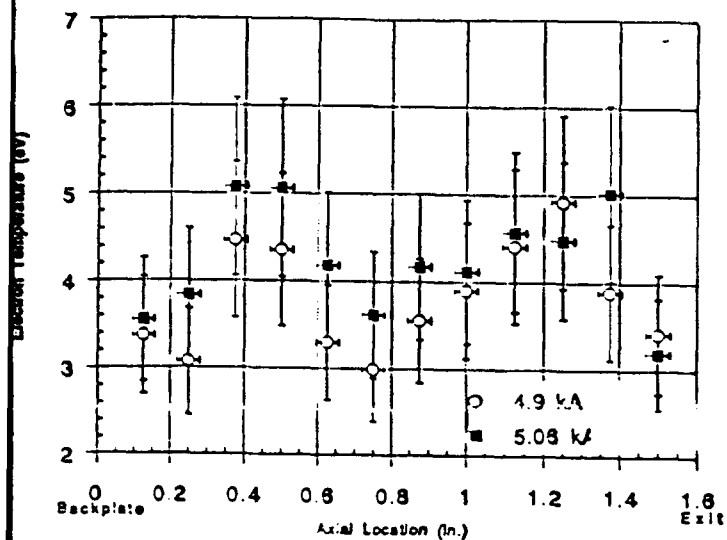


Fig. 12: Te at 4.9 and 5.06 kA

Although electron temperature increased dramatically with current, no such behavior was observed in the density profiles as shown in Figs. 14-17.

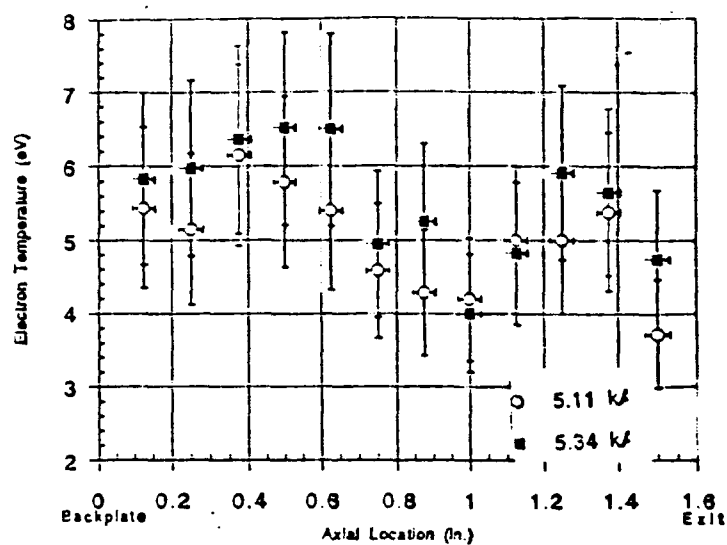


Fig. 13: Te at 5.11 and 5.34 kA

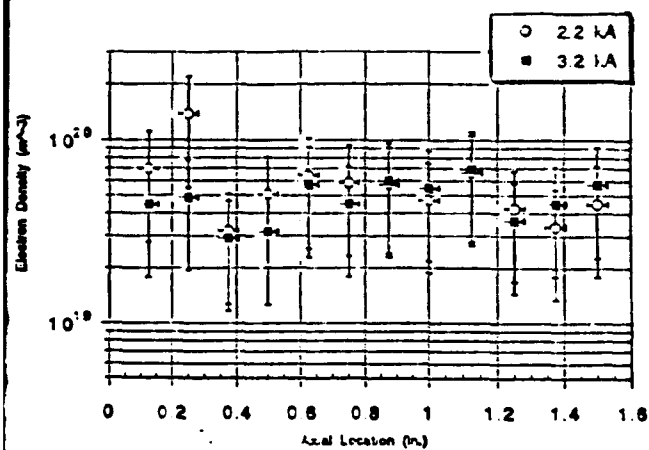


Fig. 14: Ne at 2.2 and 3.2 kA

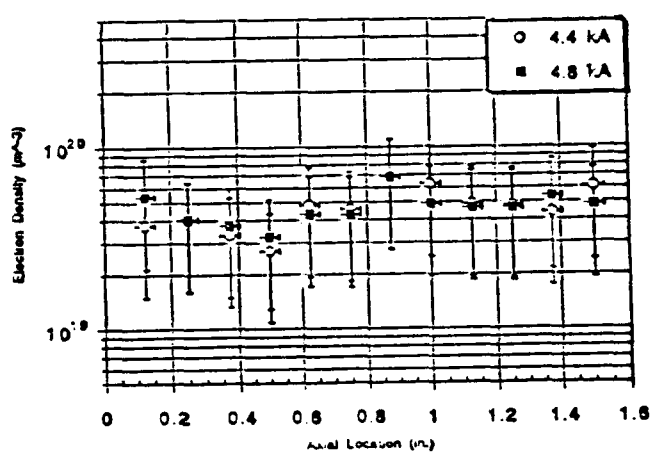


Fig. 15: Ne at 4.4 and 4.8 kA

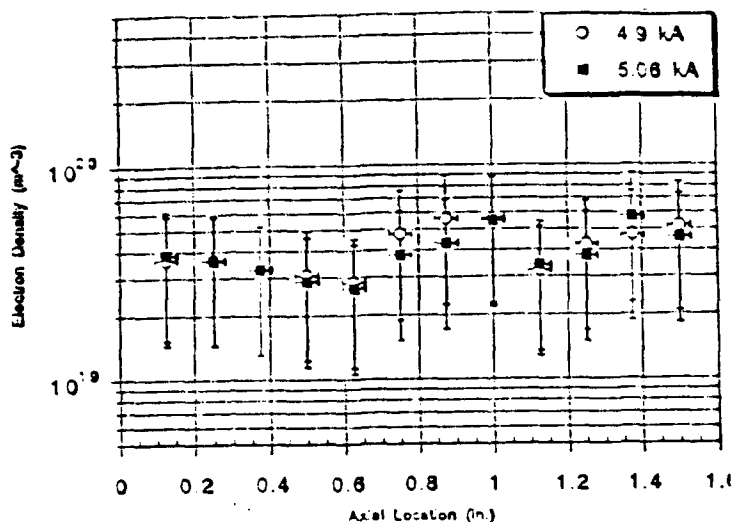


Fig. 16: Ne at 4.9 and 5.06 kA

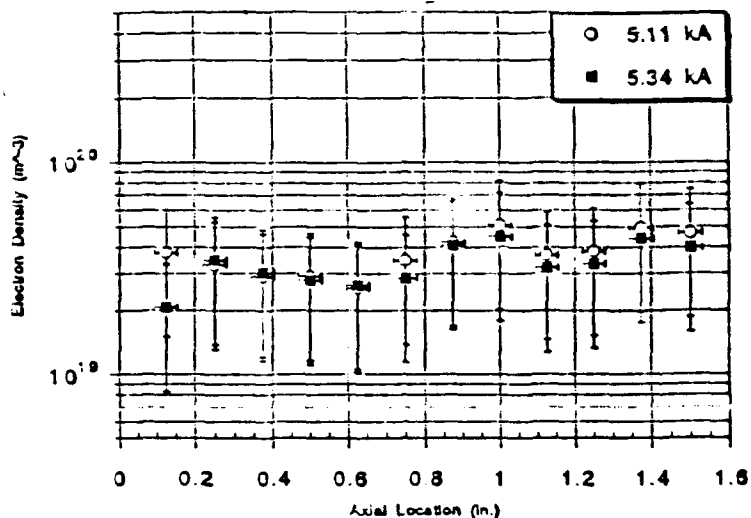


Fig. 17: Ne at 5.11 and 5.34 kA

In general, the electron density near the anode decreased with increasing current. For nearly all current levels, the density dropped from the backplate to roughly .5 in. axial location rising gradually thereafter to 1.0 in. location followed by another slight dip at 1.125 in. and a subsequent rise to the exit. The electron density varied from  $3 \times 10^{19} \text{ m}^{-3}$  to  $7 \times 10^{19} \text{ m}^{-3}$  for both current levels.

Once the electron temperature had been determined, the conversion from floating potential to the plasma potential could be made. The axially averaged anode fall varied from 15.8 V at 2.2 kA to 33 V at 5.34 kA. Due to the humps noticed in the temperature profile, the plasma potential axial profiles showed large dips at the .375 and 1.25 in. locations. Two regions of transition were visible from the anode fall profiles: the first between 4.4 and 4.8 kA and again between 5.06 and 5.11 kA current levels. The voltage drops measured were significant fractions of the total thruster voltage. The axially averaged anode voltage fraction ( $V_{\text{anode}}/V_{\text{thruster}}$ ) varied from 19% to 30.6 %. There was a large deviation in the anode fall observed from one axial location to another, however. At 200 V PFN (5.34 kA), the anode drop varied from 18.9 V near the backplate to 50 V near the exit. Near the backplate, however, similar anode drop values were observed (18.9 V for 100 V PFN (2.2 kA) to 18.85 V for 200 V PFN (5.34 kA)). This particular behavior seems to indicate that the mechanism(s) for the anode fall magnifies with current everywhere except near the backplate.

### III.III Radial Floating Probe Results:

After the initial near anode tests, the first anode fall jump observed between 4.4 kA and 4.8 kA was used as the operating condition for the remaining probe experiments. Three axial locations, .23 in.,

.97 in. and 1.47 in. from the backplate were chosen for radial floating probe and triple probe experiments. The three axial locations represented three very distinct regions of the thruster, namely a near-backplate, a mid-thruster and a near-exit location. Research in the field has indicated different plasma behavior in the three general regions of the thruster. Near the backplate, the incoming gas is cold and the gas is in the process of going from completely unionized to nearly fully ionized. The mid-thruster represents the bulk of the thruster where the gas is fully ionized and free from current or temperature concentrations. the near-exit location allows for the measurement of temperature and density gradients in the region of high current concentration near the anode lip. The experiments were conducted at 4.4 kA and 4.8 kA. 4.4 kA level represents the pre-transition (anode fall jump) current level while the 4.8 kA represents the post-transition operation. The question to be answered was whether a global change in the electron temperature, density or plasma potential profiles is observed as the anode fall increases drastically.

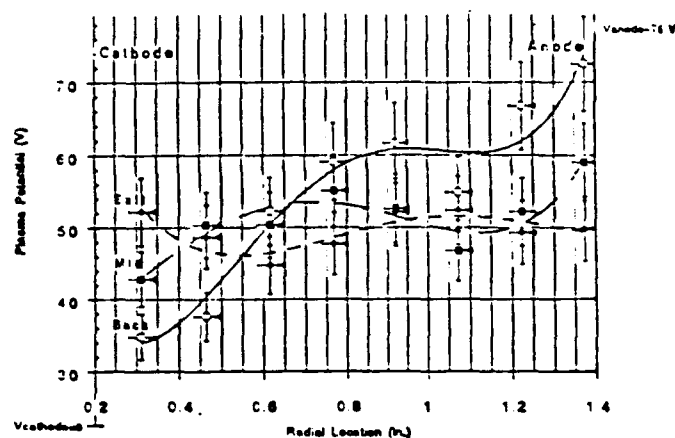


Fig. 18: Radial Vp For 4.4 kA

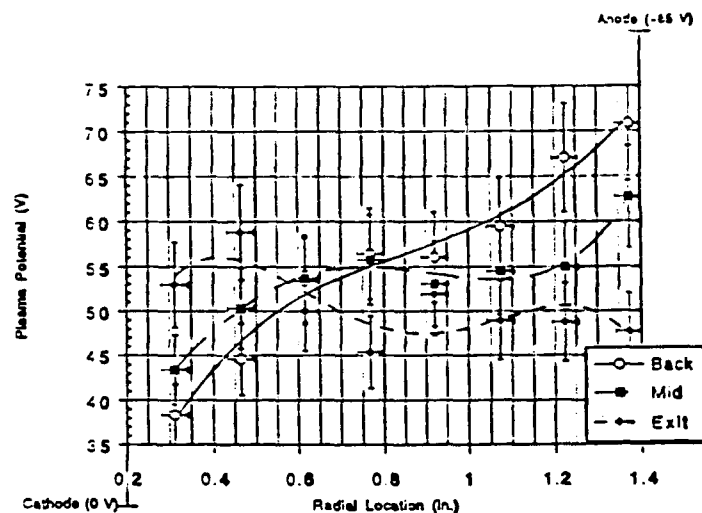


Fig. 19: Radial Vp For 4.8 kA

The measurements were conducted at eight radial locations separated by .15 in. with Argon flowing at .5 g/sec. The probe was again referenced with respect to the anode. Electron temperature measurements gotten with the triple probe (described in a later section) were used to obtain the plasma potential from the measured floating potential. Radial plasma potential profiles for 4.4 kA and 4.8 kA are shown in Figs 18 and 19, respectively. During the radial scan, the near electrode measurements were conducted with the probe approximately .125 in. away. The cathode drop in the mid-thruster and near backplate axial locations was much greater than the anode drop. At 4.4 kA, the cathode voltage drop was 34.8 V near the backplate and 42.9 V at the mid-thruster location. The anode drop was found to be 6.2 V near the backplate and 18.1 V at the mid-thruster location. The

corresponding cathode drops for 4.8 kA were 38.3 V and 43.4 V at the near-backplate and mid-thruster locations, respectively, while the anode drop was 11.35 V and 21.1 V for the near-backplate and mid-thruster locations, respectively.

#### III.IV Radial Triple Probe Results:

A series of triple probe experiments were conducted at 4.4 kA and 4.8 kA at the same three axial locations as used for the floating probe experiments (.23 in., .98 in. and 1.47 in. from the exit plane). The resulting electron density measurements are shown in Figs 20 and 21 for 4.4 kA and 4.8 kA, respectively.

Electron density was maximum closest to the cathode and decreased radially in all cases. Numerical simulations of MPD thruster behavior have shown a so-called anode starvation regime near the anode. The density profile in the near exit plane experiments shows a drop only near the anode, however. The reason that there is no obvious decline in electron density near the centerline of the thruster in Fig. 20 and 21 is that even at the centerline of the thruster the probe is still .4 in. from the cathode surface. The cathode was recessed in the thruster such that the cathode tip was .625 in. inside the thruster and not aligned with the thruster.

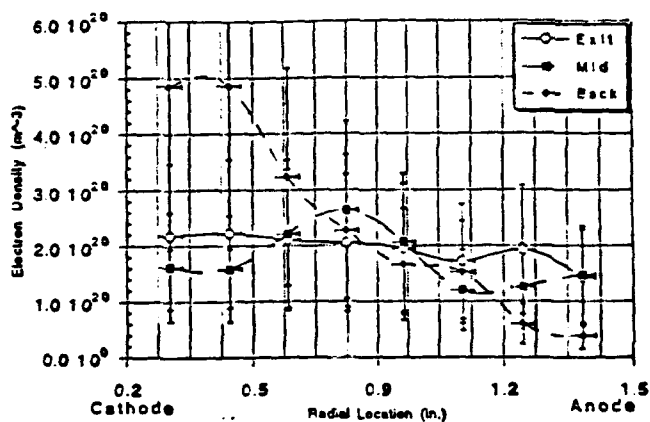


Fig. 20: Radial Ne For 4.4 kA

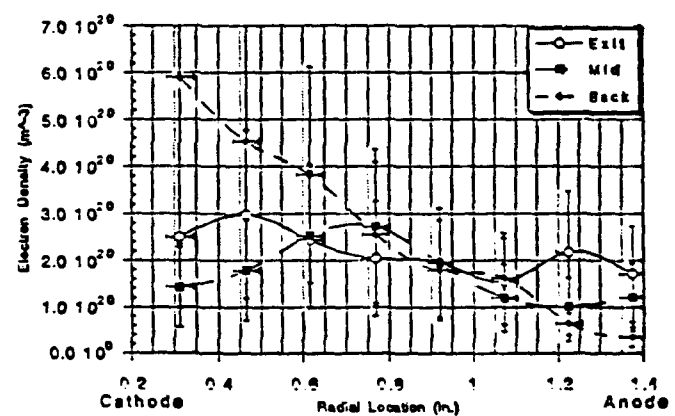


Fig. 21: Radial Ne For 4.8 kA

Density profiles and magnitudes for the two current levels are very similar. The jump in the near anode voltage drop from 4.4 kA to 4.8 kA current levels did not seem to correspond to any change in the electron density profile away from the anode. A high deviation in electron density between axial locations was observed. Near the backplate, the density is extremely high near the cathode and drops

sharply radially towards the anode. The near backplate electron density varied from  $5 \times 10^{20} \text{ m}^{-3}$  near the cathode to  $3.5 \times 10^{19} \text{ m}^{-3}$  near the anode. The reason for the high density near the cathode root is twofold: Nearly half the gas enters the MPD chamber through the .1875 in. thick annulus around the cathode; in addition, a high current concentration near the cathode root leads to high ionization and rise in electron density. The mid-thruster radial profile shows a sharp drop in electron density near both electrodes with the electron density rising from  $1.6 \times 10^{20} \text{ m}^{-3}$  near the cathode to  $2.64 \times 10^{20} \text{ m}^{-3}$  at the mid-radius level and dropping again to  $1.47 \times 10^{20} \text{ m}^{-3}$  near the anode. The electron density near the exit plane varied from  $2.2 \times 10^{20} \text{ m}^{-3}$  near the cathode to  $1.4 \times 10^{20} \text{ m}^{-3}$  near the anode.

In addition to the electron density, electron temperature was measured. The radial electron temperature profiles at 4.4 and 4.8 kA are given in Figs 22 and 23. Near the backplate, the electron temperature varied from 4.2 eV near the cathode to 1 eV near the anode for the 4.4 kA current level. For the 4.8 kA current level, the variation was from 4.25 eV to 1.2 eV. At the mid-thruster location, the temperature decreased a bit near the cathode to 3.7 eV for both current levels dropping to 1 eV near the anode for both cases. During the near-exit scan, the profiles looked very different from the other two cases. Te decreased from 3.2 eV at the thruster centerline to 2.6 eV midway between the two electrodes and then rose again near the anode to 3.3 eV for both 4.4 and 4.8 kA.

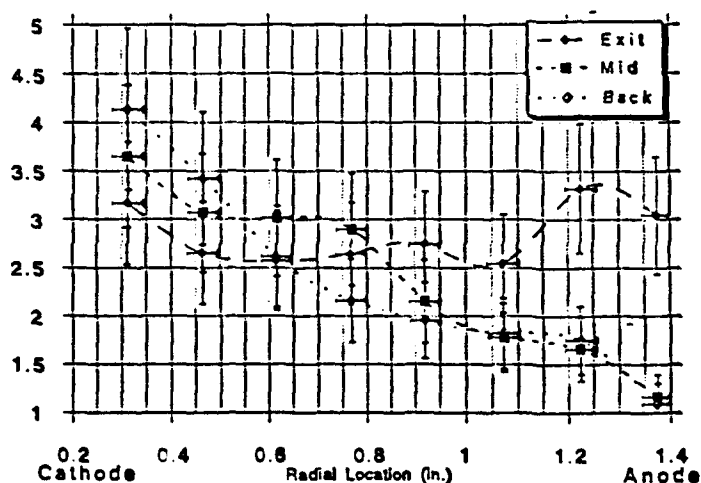


Fig. 22: Radial Te For 4.4 kA

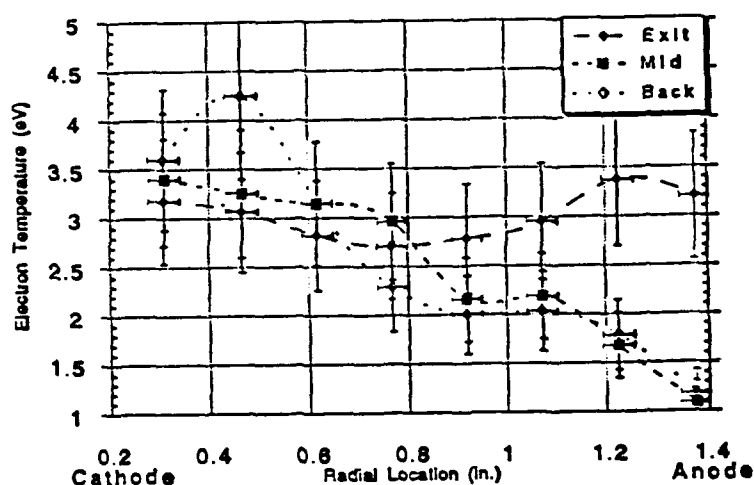


Fig. 23: Radial Te For 4.8 kA

### III.V Induction Probe Results:

Induction probe measurements were conducted within the thruster on a grid of seven axial and eight radial locations. The magnetic field measurements could be used to yield values for current densities

and plasma characteristics such as the Hall parameter and electrical conductivity. The Hall parameter which is a measure of the tendency of charge carriers to move perpendicular to both the electric and magnetic fields, has been linked to high anode falls by several researchers [5].

$$\beta = eB/mev_e$$

where "e" is the electron charge, B is the measured magnetic field in Tesla,  $m_e$  is the electron mass and  $v_e$  is the electron collision frequency. Knowing the current density profiles and the Hall parameter, ohmic dissipation can be calculated near the anode to determine whether the temperature rise measured at .375 in. and 1.25 in. near-anode axial locations were due to high ohmic heating.

The magnetic field measurements were obtained throughout the thruster via a magnetic probe consisting of a 75 turn cylindrical copper coil sealed within a quartz tube as shown in Fig. 24. The probe was calibrated to yield magnetic field strengths from the measured probe voltage output [6]. Since the probe signal itself was a function of the time derivative of the magnetic field, an integrator had to be used to deduce the actual magnetic field. Constant magnetic field contours are shown in Figs. 25 and 26 for 4.4 and 4.8 kA, respectively.

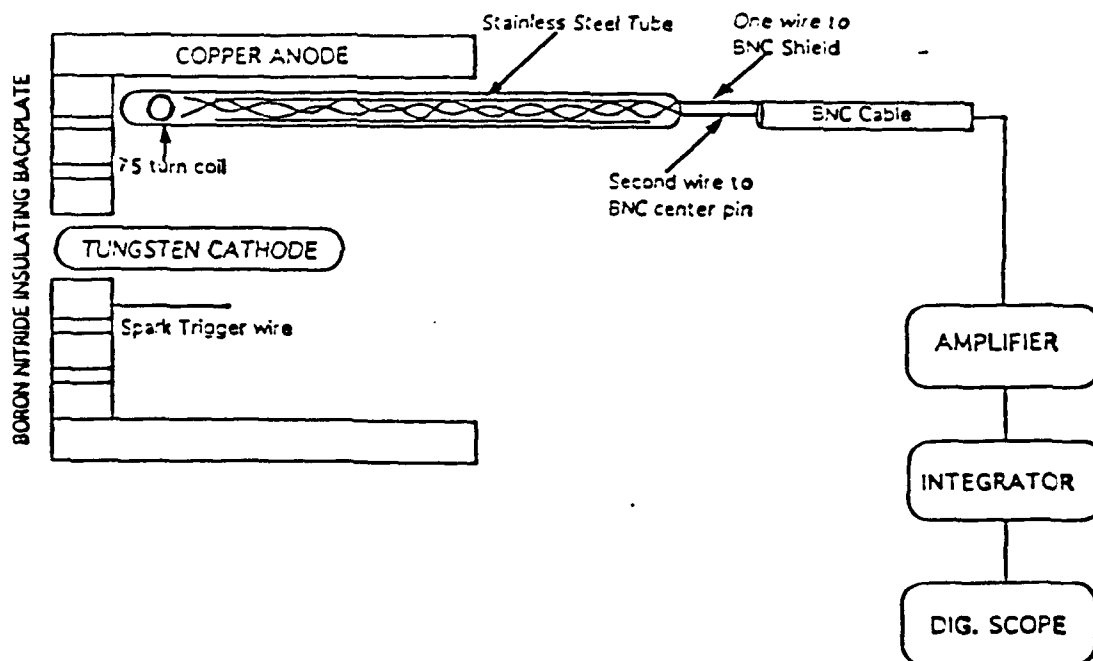


Fig. 24: Magnetic Induction Probe Schematic

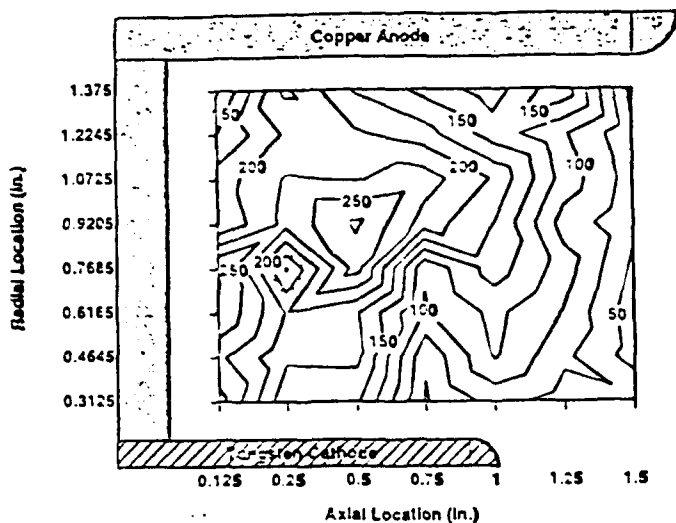


Fig. 25: B-Field Contours at 4.4 kA

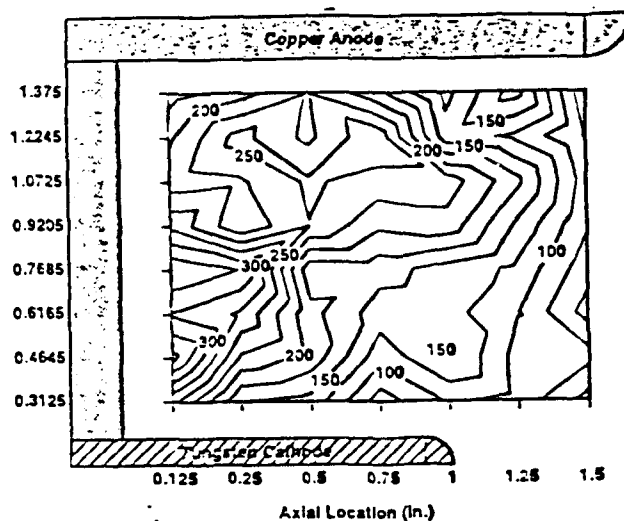


Fig. 26: B-Field Contours at 4.8 kA

The magnetic field, in general, decreased radially from the cathode to the anode and axially from the backplate towards the exit plane. Knowing the magnetic field, radial Hall parameter profiles at the three axial locations were obtained for 4.4 and 4.8 kA. The Hall parameter varied from .8 to 5.4 during the radial traverses, dropping under one only for the near-exit shots near thruster centerline. Near the anode, the Hall parameter varied from 1.0 to 9.6 axially for 4.4 kA and from 1.8 to 13.0 for 4.8 kA.

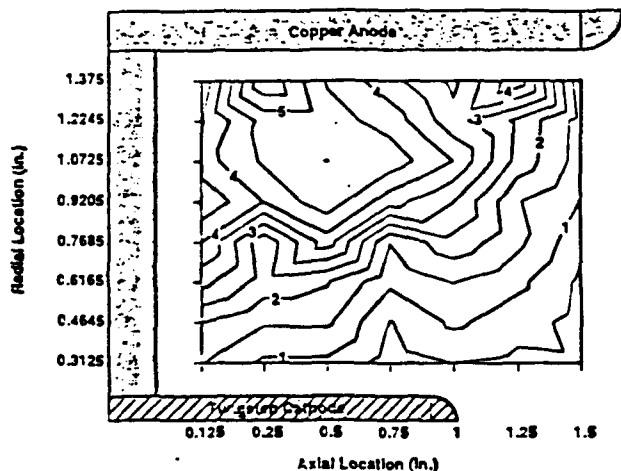


Fig. 27: Current (kA) Contours at 4.4 kA

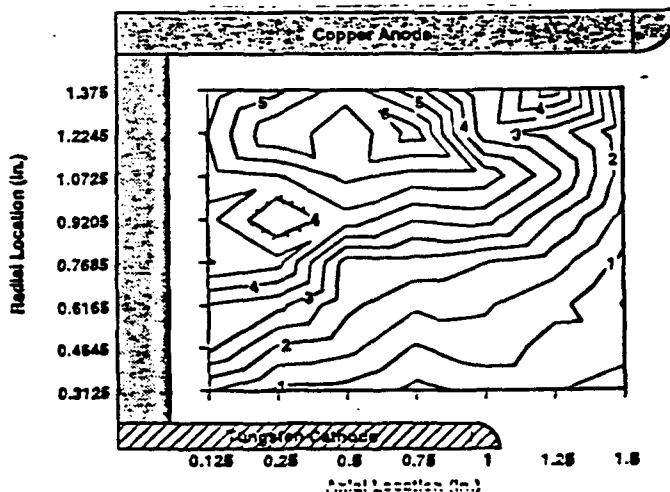


Fig. 28: Current (kA) Contours at 4.8 kA

Magnetic field measurements could be incorporated into Ampere's law to determine enclosed current profiles. The enclosed current contours are shown in Figs. 27 and 28 for 4.4 kA and 4.8 kA,



respectively.

To further verify the current concentration behavior, radial current density near the two electrodes was calculated using the following equation [1]:

$$J_y = 1/\mu_0(dB/dx)$$

The current density varied from over 250 A/cm<sup>2</sup> near the cathode root to about 50 A/cm<sup>2</sup> near the exit plane. Near-anode current density rose gradually from roughly 100 A/cm<sup>2</sup> for 4.4 kA and 65 A/cm<sup>2</sup> for 4.8 kA near the backplate to a value of 180 A/cm<sup>2</sup> for both current levels at the anode lip. Measured values of current densities were used to determine the anode power fractions, along with the floating probe data (anode fall) using the following equation:

$$P_{\text{anode}} = \sum \Delta V_i (J_i 2\pi r_{\text{anode}} \Delta x)$$

where  $i$  represents a slice of thruster of thickness  $\Delta x$  and  $r_{\text{anode}}$  is the magnetic probe near-anode radial location,  $J_i$  is the radial component of the current density and  $\Delta V_i$  is the measured anode fall for each thruster slice. The anode power fraction, due only to the anode fall, was calculated to be 33% and 40% for 4.4 and 4.8 kA, respectively.

#### IV. SUMMARY AND CONCLUSIONS:

Extensive experimental data have been provided for important plasma parameter including electron temperature, electron density, enclosed current and plasma potential. The objectives set forth for the investigation were met. The stable regime (below Onset) for the thruster was identified for .5, 1.0 and 1.5 g/sec Argon flow rates. .5 g/sec was chosen as the flow rate for the study. Anode fall data were obtained using a floating probe in conjunction with a Langmuir triple probe to determine the electron temperature correction factor needed to convert from the measured floating potentials to plasma potentials. Anode fall was seen to increase with thruster current at all axial locations accompanied by an increase in electron temperature and a gradual decrease in number density. A direct correlation between anode fall and reduction in number density was therefore obtained. Two transition points (jumps) in the anode fall were observed corresponding to 4.8 and 5.11 kA current levels. 4.8 kA was chosen as the point of operation for the remaining probe experiments. Experiments were also conducted at 4.4 kA to get an idea of both pre and post-transition global plasma properties. Radial plasma potential measurements were obtained at three axial locations corresponding to near-backplate, mid-thruster and near-exit locations. The measured temperature decreased sharply from the cathode to the anode. A rise in temperature was observed near the anode lip. Induction probe measurements showed a considerable current concentration at the anode lip which

could presumably be causing localized ohmic dissipation resulting in higher temperature at that location.

The electron density varied considerably both radially and axially. Near the cathode root, where high current concentration and a resulting high ionization exists, the number density was highest dropping sharply towards the anode. At the mid-thruster location, however, a drop in density was seen both near the cathode and the anode. The mechanisms for the voltage drop near the two electrodes are quite different, however. Starvation or lack of charge carriers due to the Lorentz pumping force can be cited as a reason for the reduced density near the anode. To maintain current continuity, large electric fields are created in the region very close to the anode leading to large voltage drops. The reason for a low number density near the cathode may be reduced ionization in the region due to lack of current concentration that is seen at the cathode root and the anode lip. There is no observable ionization mechanism, therefore, in the near-cathode region. A higher voltage drop was observed near the cathode than the anode. The fact that the cathode is cold and cannot thermionically emit can be cited as the cause for the large drop. For the electrons to be detached from the cathode, therefore, large electric fields are created.

Induction probe experiments identified large current concentrations near the cathode root and the anode lip. The Hall parameter which has been related to large anode drops and skewing of the current lines, was calculated from measured plasma parameters. It exceeded unity everywhere near the anode. No consistent radial pattern in the Hall parameter was observed, however. "Unexpected" behavior was observed at .375 in. and 1.25 in. axial near-anode locations throughout the series of probe experiments. A large jump in electron temperature was seen at the two locations corresponding to a large temperature correction factor for the floating potentials. As a result, the anode fall dropped considerably at the two locations for all current levels. In addition, current contours obtained from the induction probe measurements show the enclosed current being highest at the .375 in. location and increasing sharply at the 1.25 in. axial location as well. It may be concluded, then, that a transition in the plasma flow (perhaps a sonic transition) takes place .375 in. from the backplate causing the charge carriers to flow perpendicular to the probe rather than give the desired parallel flow. Ion flow perpendicular to the probe has been shown to result in unusually high values for  $T_e$  [7]. The fact that both triple probe and induction probe results yielded unexpected behavior at the two axial location seemed to indicate a plasma effect rather than probe error.

## BIBLIOGRAPHY:

1. Jahn, R. Physics of Electric Propulsion, McGraw Hill Book Company, New York, 1968.
2. Lawless J. L. and V. V. Subramaniam. "A Review of the Theory of Self-Field MPD Thrusters". AIDAA/AIAA/DGLR/JSASS 22nd International Electric Propulsion Conference, (IEPC-91-019), October 14-17, 1991.
3. Gallimore A., Myers R. and R. Jahn. "Anode Power Deposition in an Applied Field Segmented Anode MPD Thruster". 21st International Electric Propulsion Conference, (AIAA-90-2668), July 18-20, 1990.
4. Tilley, D. "The Application of The Triple Probe Method to MPD Thruster Plumes". 21st International Electric Propulsion Conference, (AIAA-90-2667), July 18-20, 1990.
5. Niewood, E. H. The Hall Effect in a Numerical Model of MPD Thrusters. 22nd International Electric Propulsion Conference, (AIAA-91-099), October 14-17, 1991.
6. Huddleston R. H. and S. L. Leonard. Plasma Diagnostic Techniques. Academic Press, New York, NY, 1965.
7. Gallimore A. "Anode Power Deposition in Coaxial MPD Thruster". Ph. D. Thesis. Dept. of Mechanical and Aerospace Engineering, Princeton Univ., 1992.

ABSOLUTE OPTICAL SPECTROSCOPY OF METAL VAPORS  
ADDING ALUMINUM TO PREVIOUSLY-CHARACTERIZED CHEMICAL SYSTEMS

Jeffrey D. Mills

Candidate for the Degree of Doctor of Philosophy

Department of Chemistry  
Indiana University  
Bloomington, IN 47403

Final Report for:  
Graduate Student Research Program  
Phillips Laboratory

Sponsored by:  
Air Force Office of Scientific Research  
Bolling Air Force Base, Washington, D.C.  
and  
Indiana University  
Bloomington, IN 47405

September 1993

ABSOLUTE OPTICAL SPECTROSCOPY OF METAL VAPORS  
ADDING ALUMINUM TO PREVIOUSLY-CHARACTERIZED CHEMICAL SYSTEMS

Jeffrey D. Mills

Candidate for the Degree of Doctor of Philosophy

Department of Chemistry  
Indiana University  
Bloomington, IN 47405

**Abstract**

The optical properties of high-temperature aluminum vapors were modelled using an established theoretical and computational framework, in conjunction with attempts to measure light absorption in these samples with the Plasma Spectroscopy Cell. In addition, the most promising physical conditions and the spectroscopic region most likely to reveal the presence of the hitherto unobserved molecule, LiAl, were established. In this pursuit, experimental and theoretical energy levels and vapor pressures were used to characterize the densities of atomic lithium and aluminum, diatomic homonuclear lithium and aluminum, and the heteronuclear lithium aluminum molecule expected under a variety of conditions. Also, calculated molecular transition dipole moments allowed the absorption due to bound-bound and bound-free processes in the homonuclear diatomics to be added to the atomic contributions in order to provide the background spectrum upon which LiAl might be observed. Specifically, diatomic aluminum is predicted to yield a weak but distinctively-structured band profile and to interfere little with the search for the LiAl molecule among the strong absorption bands of atomic and diatomic lithium and atomic aluminum.

# ABSOLUTE OPTICAL SPECTROSCOPY OF METAL VAPORS

## ADDING ALUMINUM TO PREVIOUSLY-CHARACTERIZED CHEMICAL SYSTEMS

Jeffrey D. Mills

### Introduction

Metals highly dispersed in cryogenic fuels show considerable promise as High Energy Density Materials (HEDM's) for rocket propulsion.[1] Either via the large energy release upon direct oxidation or their large light-absorbing capacities, these additives can lead to significant increases in specific impulse in either conventional combustion or solar-powered rockets. In the development of these materials, optical spectroscopy is indispensable not only in predicting their specific utility but also in characterizing their properties and optimal means of production.[2,3,4]

Because of the ease of preparation and relative simplicity of the operant physical environment, high-temperature, rare-gas-buffered metal vapors allow convenient and accessible insight into the nature and prospects of these materials and provide an important first step to understanding the conditions and processes important in their production and use. Building on previous experimental and theoretical work with the Li/Li<sub>2</sub> system, it was hoped that the same theoretical framework might be of some use in predicting the results of and, to some extent, guiding the intensive experimental labors required to investigate other mixtures of such substances. In the course of this research program, the thermodynamic and spectral characteristics of the aluminum and mixed lithium and aluminum systems were considered.

### Apparatus and Discussion of the Experimental Problem

The Plasma Spectroscopy Cell (PSC), the subject of these theoretical studies, has been rather fully described elsewhere.[5] Briefly, it is comprised of a large containment vessel equipped to prepare high-temperature (up to 2200K in these experiments) and high-pressure metal vapors and allow them to be studied under flow conditions with the tools of molecular spectroscopy. For this work, an additional apparatus to allow the combination of two metals of widely divergent boiling points was developed (see Figure 1). Herein relatively cooler samples of a low boiling point metal (here lithium, bp  $\approx$  1600K) vapor in an inert buffer and contained in

the inner tube, may be heated and mixed at the tip of the apparatus with similar vapors of metals which are much higher boiling (here, aluminum, bp  $\approx$  2750K) and are evaporated from the cylindrically symmetric boats which surround the inner tube. Near the region of the tip, chemical equilibrium among all possible reacting species is established at a near constant temperature and optical observations are conducted. As either lithium or aluminum are incompatible with a great number of common refractory materials, and since liquid aluminum is highly corrosive, the PSC was first run with aluminum only in order to address and overcome some of the daunting materials problems involved. An account of the theoretical characterization of these experiments and the initial work in assisting in the future search for the unknown molecule LiAl, comprise the bulk of this report.

### Theoretical Background

The theoretical exigencies of determining the absolute absorption of gaseous atomic and diatomic samples under known thermodynamic samples has been extensively described elsewhere.[6,7] Briefly, the goal is to calculate the transmission of light (the ratio of passed to incident light intensity)

$$\frac{I(\nu)}{I_0(\nu)} \equiv T(\nu) = e^{-k(\nu)\Delta x} \quad (1)$$

through a uniform sample of length,  $\Delta x$ , (taken to be approximately 3.5 mm for the PSC) at wavelengths across the entire visible spectrum, in terms of individual atomic and molecular properties, as:

$$k(\nu) = \sum_{\substack{q \\ \text{species}}} \sigma_q(\nu) \left(\frac{N}{V}\right)_q. \quad (2)$$

Both the per molecule (or atom) optical absorption cross-section,  $\sigma_q$ , which allows the connection between the macroscopic, measurable optical properties of a sample and the microscopic characteristics of its constituent chemical species,  $q$ , and the number density,  $\left(\frac{N}{V}\right)_q$ , of each of these species can be treated to several levels of approximation and are treated in turn in what follows.

For atoms, the absorption cross section is simply given by:

$$\sigma_q(E) = \frac{2\pi^2 e^2 \hbar}{m_e c} \sum_{I,F} f_{If} \frac{\left(\frac{N}{V}\right)_I}{\left(\frac{N}{V}\right)_q} \phi_{IF}(E) \quad (3)$$

where  $f_{if}$  is the oscillator strength which determines the overall strength of a transition between initial state  $i$  and final state  $f$ ,  $\phi_{IF}(E)$ , the unity-normalized line shape function, contains the overall distribution of intensity in the transition, and the density of particles in a level of degenerate initial states,  $(\frac{N}{V})_I$ , relative to the total atomic species density is given by statistical mechanics, as:

$$\frac{(\frac{N}{V})_I}{(\frac{N}{V})_q} = \frac{g_I e^{-E_I/k_B T}}{\sum_K g_K e^{-E_K/k_B T}} \quad (4)$$

in terms of state energies,  $E$ , level degeneracies,  $g$ , and the temperature,  $T$ , of the observation zone.

For diatomic molecules, approximations of various sophistication are convenient and necessary. At the simplest level, for transitions involving two bound electronic states, the molecule's electronic, vibrational, and rotational states can be grouped in such a way that all transitions with the same nominal electronic and vibrational character are considered to occur at a uniform effective transition energy. This leads to a molecular absorption cross section independent of rotational state:

$$\sigma_q(E) = \frac{2\pi^2 e^2 h}{m_e c} \sum_{\epsilon_I, \epsilon_F} \overline{f_{\epsilon_I \epsilon_F}} \sum_{v_I, v_F} \chi_{v_I, v_F} \frac{\overline{E_{v_I v_F}}}{\overline{E_{\epsilon_I \epsilon_F}}} \frac{(\frac{N}{V})_I}{(\frac{N}{V})_q} \phi_{IF}(E) \quad (5)$$

where  $\chi$  is a measure of the effective strength of each transition between the averaged electronic-vibrational levels denoted by  $\epsilon$  and  $v$ , with transition energy,  $\overline{E_{v_I v_F}}$ . Likewise,  $\overline{f_{\epsilon_I \epsilon_F}}$  and  $\overline{E_{\epsilon_I \epsilon_F}}$  can be thought of as an average oscillator strength and transition energy for all transitions in the electronic transition band. Even more simply, for the purposes of rough illustration, the line shape function, which should represent the envelope of substructure due to rotational degrees of freedom, can be combined with the strength and taken to be a simple "stick" or "spike" with length proportional to the transition propensity.

In a more exact treatment, the rotational structure of transition bands must be considered. At the next most extensive level, transitions of different energy,  $E_{IF}$  between individual rovibronic states of angular momentum,  $J$ , are considered, but their intrinsic strengths,  $\chi$  are taken to be the same for all rotational transitions between states with the same nominal vibronic assignment, and are calculated for some representative transition. Thus,



$$\sigma_q(E) = -\frac{2\pi^2 e^2 \hbar}{m_e c} \sum_{\epsilon_i, \epsilon_f} \overline{f_{\epsilon_i, \epsilon_f}} \sum_{v_i, v_f} \sum_{J_i, J_f} \chi_{v_i, J_i, v_f, J_f} \frac{E_{IF}}{E_{\epsilon_i, \epsilon_f}} \phi_{J_i, J_f}^{\text{rot}} \frac{(\frac{N}{V})_I}{(\frac{N}{V})_q} \phi_{IF}(E) \quad (6)$$

where  $\phi_{J_i, J_f}^{\text{rot}}$  are the known Hönl-London factors which account for the angular momentum degeneracies in each type of electronic transition and are normalized to the initial state angular momentum degeneracy. The rotation independent vibronic band strengths used in this and previous expression are of two customary types. Franck-Condon Factors are calculated assuming the value of the transition dipole doesn't vary over the vibrational coordinate of the diatomic (the Franck-Condon Approximation) and can be shown to be just the overlap of the initial and final effective vibrational eigenfunctions. In a more exact accounting, these strength factors are given by the expectation value of the electronic transition dipole moment along the vibrational coordinate, relative to its average value for all transitions in the electronic band.

Finally, in the most exact treatment allowed within the fixed nuclei or Born-Oppenheimer Approximation, the full rotational state dependence of the rovibronic transition strength must be included in an expression identical to the previous.

The molecular information needed for these calculations of the molecular cross section include the Born-Oppenheimer molecular potential energy curves, the electronic transition dipole moment, the Hönl-London Factors, and the molecular transition line shapes (usually taken to be the same for each transition in an electronic band). The molecular state energies (and transition energies), and the vibrational-eigenfunction-dependent strength factors of the two types can be considered to be derived from these, by first solving the one-dimensional problem of the diatomic vibrational potential, and then calculate integrals over the appropriate quantities. Further averages or effective values are then considered of selected from these more complete values. Finally, Boltzmann state population fractions are given by the usual expressions of statistical mechanics:

$$\frac{(\frac{N}{V})_I}{(\frac{N}{V})_q} = \frac{g_{\epsilon_I} (2J_I + 1) g_I^{\text{ns}} e^{-E_I/k_B T}}{\sum_K g_{\epsilon_K} (2J_K + 1) g_K^{\text{ns}} e^{-E_K/k_B T}} \quad (7)$$

where  $g_{\epsilon}$ ,  $(2J + 1)$ , and  $g^{\text{ns}}$  are the electronic, rotational and nuclear spin degeneracies, respectively.

Finally, it should be noted that expressions similar to those given in Equations (5) and (6) have been constructed which allow the treatment of transitions from bound to continuum (i.e. repulsive) molecular states. In these cases, the only change which is required involves replacing the combinations of a usually relatively narrow line shape function and discrete transition strength with a generalized transition strength broadly varying with the infinitely variable transition energy. Also, in this case, the strength factors involve integrals over unbounded vibrational eigenfunctions which can be approximated in various ways.

Having described the construction of atomic and molecular absorption cross sections, it remains only to specify the total species particle densities of all types in Equation (2). In the experimental apparatus, materials are evaporated from quantities of the liquid metal at one temperature, and may travel to a region of the apparatus with a different temperature, there to react with other species to form an equilibrium mixture according to a reaction for each molecule,  $m$ , from the component atoms,  $p \in \{A, B, C, \dots\}$ , as represented by:



where  $\nu$  is the stoichiometric coefficient for each atom in the molecule. The total atomic particle density,  $(\frac{N}{V})_p^0$ , of each atom initially established at the known evaporator temperature can usually be taken from the results of previous experiments. Then, expressions for the mass conservation of the initial vaporized atomic particle densities,

$$\left(\frac{N}{V}\right)_p + \sum_m \nu_{p,m} \left(\frac{N}{V}\right)_m = \left(\frac{N}{V}\right)_p^0, \quad (9)$$

and knowledge of the equilibrium constants,

$$K_m = \frac{(\frac{N}{V})_m}{\prod_p (\frac{N}{V})_p^{\nu_{p,m}}}, \quad (10)$$

provide an equation of constraint for each chemical species in the mixtures. Solution of these equations gives the desired particle densities. Although the equilibrium constants of some common systems have been measured and reported, it was discovered that they are often most accurately determined using the results of chemical statistical mechanics and the degeneracies and state energies previously utilized as:

$$K_m = \frac{\left(\frac{Q_m^{\text{mol}}}{V}\right)}{\prod_p \left(\frac{Q_p^{\text{atom}}}{V}\right)^{\nu_{p,m}}} \quad (11)$$

where the atomic and molecular partition functions,  $Q$ , are given by:

$$Q_p^{\text{atom}} = V \left( \frac{2\pi m_p k_B T}{h^2} \right)^{\frac{3}{2}} \sum_K g_K e^{-E_K/k_B T} \quad (12)$$

$$Q_p^{\text{mol}} = V \left( \frac{2\pi m_m k_B T}{h^2} \right)^{\frac{3}{2}} \sum_{\epsilon_K \nu_K J_K} g_{\epsilon_K} (2J_K + 1) g_K^{\text{ns}} e^{-E_K/k_B T} \quad (13)$$

for observation zone temperature,  $T$ , and particle masses,  $m$ .

By combining these elements, the per atom or molecule absorption cross section and the particle densities of each species in the observation zone, the optical absorption of an arbitrary mixture of atomic and diatomic absorbers can be absolutely predicted with no dependence upon arbitrary factors or information outside the thermodynamics or quantum mechanics of the system. Further, by comparing the results of the various levels of theoretical approximation with each other and with actual experimental results, the essential features of the minimal theoretical framework required to accurately describe the optical absorption of different sorts of samples, will gradually become identified. (By similar methods, other optical properties (in particular, the refractive index and the optical emission) of these systems can be deduced. Interested readers are referred to reference [7] for a detailed description.)

## Results

The aforementioned theoretical framework was applied to three areas of interest: the optical absorption due to diatomic aluminum by itself, the species densities of all atoms and diatoms in a mixture of lithium and aluminum as a function of observation and evaporator temperature, and the optical absorption of such a sample due to only the atomic and homonuclear diatomic components.

In modelling the spectroscopy of the aluminum dimer, the required potential energy curves and electronic transition dipole moments were obtained from a recent theoretical investigation.[8] (While the energy values from experimental studies [9,10] seemed to be more accurate for the low-lying states, they could not be extended to

the high vibrational and rotational levels populated at the extremely high temperatures ( $\approx 2100\text{K}$ ) of the experiment. In the present approach, vibrational levels up to dissociation were included and rotational levels with  $J \approx 120$  were found to be significant.) The allowed electronic transitions in the optical spectrum involve one bound-bound absorption ( $((1)^3\Sigma_g^- \rightarrow (1)^3\Sigma_u^-)$  and one bound-free (or bound-continuum) transition ( $((1)^3\Pi_u \rightarrow (1)^3\Pi_g)$ ). Exact or appropriate effective Hönl-London Factors for these transitions can be determined from established sources.[11]

For the bound-bound transition, if the line shape function of Equation (5) is taken to be a spike or stick with length proportional to the strength of the vibronic transition, the effect of the Franck-Condon Approximation on the strength factors can be gauged. Figures 2 and 3 show on a common arbitrary intensity scale and for observation temperature around  $2100\text{K}$ , the spectrum using the two types of strength factors. Clearly, for this transition in the diatomic aluminum system (and unlike the diatomic lithium and sodium systems), the Franck-Condon Approximation used in generating Figure 2 is somewhat deficient in describing the molecular absorption more completely described by the inclusion of actual transition dipole moments in Figure 3. (This is born out by the rapid change which can be seen in the electronic transition dipole moment as the internuclear separation deviates slightly from its equilibrium value.) Thus, at least here, the distance dependence of this transition parameter must be treated correctly in order to gain a realistic picture of system absorption.

Addition of a realistic line shape to the bound-bound spectrum and incorporation of the bound-free absorption requires more detailed consideration of the absorption profiles for the system. In general, both homogeneous (natural and collisional) and inhomogeneous (Doppler and instrumental) line broadening are important. Of these, the width due to the finite instrumental resolution and the collisional width due to the perturbation of absorbers by collision with atoms of the same (resonance broadening) and different (foreign gas broadening due to the inert buffer) types are the most important of each class. Although no quantitative measures of either type of collision broadening seem to exist for the diatomics, reasonable values extrapolated from similar molecules put this factor at least an order of magnitude below the instrumental resolution ( $0.5 \text{ nm}$  or  $8\text{--}30 \text{ cm}^{-1}$  depending upon the energy). For the bound-bound transition, the homogeneous and inhomogeneous broadening mechanisms can be both accounted for by using the symmetric Voigt

profile. [12] Figure 4 shows (on an arbitrary intensity scale) the band head for the  $v'' = 0 \rightarrow v' = 0$  manifold of rovibronic transitions broadened with a Voigt line shape of predominant instrumental width. As the rotational substructure is totally obscured at this experimental resolution, an effective vibrational band width can be extracted and used in determining the bound-bound molecular cross section of Eq. (5). Incorporating this line width ( $\approx 88\text{cm}^{-1}$ ) into a simple Lorentzian profile leads to bound-bound absorption as shown in Figure 5 for an aluminum evaporator and observation temperature of 2100K.

The bound-free transition can then be added to the absorption profile by methods described in the previous section. This leads to the spectrum shown in Fig. 6. Although at these evaporator temperatures (constrained from above by the maximum temperature which the material of the PSC can withstand before degrading) the paucity of aluminum diatomics leads to an extremely weak optical absorption, the characteristic shape of the profile should make it distinctly recognizable if present and measurable in an experimental spectrum. Calculation of the rovibronically-resolved spectrum of Eq. (6) and advances in overcoming the difficult problems involved in preparing aluminum vapors may allow further comparison between theory and experiment and provide a prediction of the results of high-resolution spectroscopy on this system.

In the search for the lithium aluminum molecule, the theoretical framework described above can be useful in ways preparatory to predicting actual optical absorption profiles. Via Equations (9)-(13) above, known evaporator and observation temperatures, along with the state energies and degeneracies involved in the statistical mechanical sums can lead to predictions of the particle densities of absorbers in the observation zone without requiring knowledge of transition moments or strengths. With initial evaporator vapor pressures[13] and atomic energy levels[14] derived from standard compilations, and only the state energies of diatomic aluminum,[8] lithium,[15] and lithium aluminum[16] determined from the Born-Oppenheimer potential energy curves, these populations can be easily calculated. In Figures 7 and 8 can be seen the results of two such calculations. For fixed, identical aluminum evaporator and observation temperatures (2000K and 2200K, respectively) the particle densities of all important species are plotted as a function of lithium evaporator temperature. In this way, conditions for which the effects of known, strongly interfering materials are minimized and the particle density of the material of interest are

maximized, may be approximately determined without labor-intensive experimental searches over the entire parameter space or unmotivated, disappointing guesses.

Proceeding one more step in aiding the search for new molecules, the particle densities thus determined can be combined with the transition strengths of known materials to predict the expected "spectral background" provided by known absorbers against which absorption of a novel species is to be determined. For the mixed lithium and aluminum system, atomic transition strengths,[17,18] known or estimated atomic line widths,[19,20,21] Hönl-London Factors,[11] and diatomic electronic transition moments[22,8] allow the construction of the absorption profiles shown with two different vertical scales in Figures 9 and 10 for a lithium evaporator temperature of 1350K and aluminum evaporator and observation temperatures of 2100K. The atomic aluminum  $3p \rightarrow 4s$  resonance transition at around 395 nm, the strong atomic Li resonance transition  $2s \rightarrow 2p$  around 670 nm with weaker, higher excitations at around 615 nm, 460 nm, 440 nm, and 420 nm along with the weak  $\text{Li}_2$   $((1)^1\Sigma_g^+ \rightarrow (1)^1\Pi_u)$  transition distributed broadly around 500 nm and the extremely weak  $(1)^1\Sigma_g^+ \rightarrow (1)^1\Sigma_u^+$  transition also due to  $\text{Li}_2$  which can be seen on the low energy shoulder of the Li resonance line, provide the expected absorption in this system, minus the LiAl contribution. It would seem that the LiAl molecule with strong optical transitions predicted[23] in the region 620-650 nm should be observable in such a mix. Further, as expected from the results of modelling it by itself, the aluminum diatomic appears to be essentially unobservable in this mixture and, if the theoretical studies are correct, should interfere little with the detection of LiAl.

As the above preliminary results and examples illustrate, the present theoretical framework allows improved insight and increased efficiency in the experimental search for new molecules. Further progress in experimental areas and the final determination[23] of the theoretical electronic transition dipole moment and Born-Oppenheimer potential energy curves for LiAl will lead to a calculation of the model optical absorption in this molecule and permit the comparison with real results so necessary for the further evaluation and refinement of this computational schema.

## Conclusions

Most broadly, a very general computational and theoretical framework for the prediction of the optical absorption of arbitrary mixtures of atomic and diatomic

molecules has been shown to be applicable. It shows promise, not only for the prediction of the actual absolute absorption of known samples and the absorption profile of unknown molecules, but also for characterizing the thermodynamic parameters governing mixtures of molecules, in preparation to their discovery.

For the specific system of interest in the current study, if theoretical studies are correct, diatomic aluminum should be a relatively minor absorber in a lithium/-aluminum mixture. Thus, the search for the lithium aluminum diatomic should be able to proceed in those areas of the optical spectrum not blocked by strong Li, Al, and Li<sub>2</sub> transitions. The calculation of the transition dipole moment in this new molecule will allow the construction of its absolute optical absorption profile.

### References

- [1] N. Presser and A.T. Pritt, Jr., in *Proceedings of the High Energy Density Matter (HEDM) Conference*, edited by W.J. Lauderdale and W.A. Sowell (AFAL-CP-002, USAF Astronautics Lab, Edwards AFB, California, 1987).
- [2] M.E. Fajardo and P.G. Carrick, *J. Chem. Phys.*, **94**, 5812 (1991).
- [3] M.E. Fajardo, *J. Chem. Phys.*, **98**, 110 (1993).
- [4] S. Tam and M.E. Fajardo *J. Chem. Phys.*, **99**, 854 (1993).
- [5] C.W. Larson, *The Spectroscopy of Hydrogen/Metal Vapor Mixtures at High Temperatures and Pressures*, Research Report (AL-TR-88-080), August 1990.
- [6] Jeff Mills, C500 Research Report, Indiana University, May 1992.
- [7] Jeff Mills, Candidacy Research Report, Indiana University, available Nov. 1993.
- [8] S.R. Langhoff and C.W. Bauschlicher, Jr., *J. Chem. Phys.*, **92**, 1879 (1990).
- [9] Z. Fu, G.W. Lemire, G.A. Bishea, and M.D. Morse, *J. Chem. Phys.*, **93**, 430 (1990).
- [10] M.F. Cai, C.C. Carter, T.A. Miller, and V.E. Bondybey, *Chem. Phys.*, **155**, 155 (1991).
- [11] G. Herzberg, *Molecular Spectra and Molecular Structure: I. Spectra of Diatomic Molecules*, 2nd Ed., (Van Nostrand, New York, 1950), pp. 209-9 and references cited therein.
- [12] J.I. Steinfeld, *Molecules and Radiation*, Second Ed., (MIT Press, Cambridge, MA, 1986), pp. 31-36.
- [13] A.N. Nesmeyanov, *Vapour Pressure of the Elements*, edited and transl. by J.I. Carasso, (Academic, New York, 1963).
- [14] C.E. Moore, *Atomic Energy Levels*, Nat. Bur. Stand. Circ. 467, (U.S. G.P.O, Washington, D.C., 1949).

- [15] For this and a previous investigation, highly accurate hybrid experimental and theoretical curves have been constructed for lithium. See Ref. 7 for details.
- [16] M.E. Rosenkrantz, *unpublished*.
- [17] W.L. Wiese, M.W. Smith, and B.M. Glennon, *Atomic Transition Probabilities*, Nat. Stand. Ref. Data Ser., Nat. Bur. Stand. Circ. 4, (U.S. G.P.O, Washington, D.C., 1966), Vol I.
- [18] W.L. Wiese, M.W. Smith, and B.M. Miles, *Atomic Transition Probabilities*, Nat. Stand. Ref. Data Ser., Nat. Bur. Stand. Circ.22, (U.S. G.P.O, Washington, D.C., 1969), Vol II.
- [19] B. Ya'akabi, *J. Quant. Spectrosc. Radiat. Transfer*, **9**, 309 (1969).
- [20] K. Niemax and G. Pichler, *J. Phys. B Atom. Molec. Phys*, **8**, 179 (1975).
- [21] N. Allard and J. Kielkopf, *Rev. Mod. Phys.*, **54**, 1103 (1982).
- [22] L.B. Ratcliff, J.L. Fish, and D.D. Konowalow, *J. Mol. Spectrosc.*, **122**, 293 (1987).
- [23] M.E. Rosenkrantz, *in progress*.



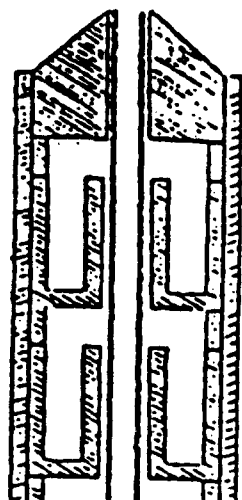


Figure 1— New apparatus at the PSC jet tip to allow controlled addition of a material with a much elevated boiling point

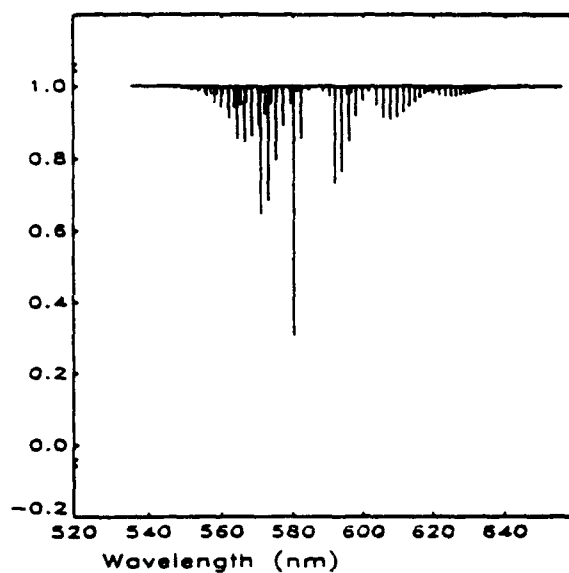


Figure 2— Stick vibronic spectrum utilising the Franck-Condon Approximation (scaled arbitrarily but identically to Figure 3), evaporator and observation temperature, 2100K

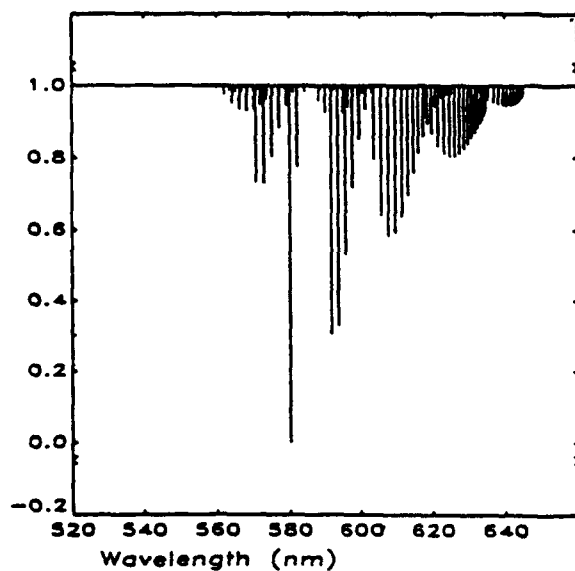


Figure 3— Stick vibronic spectrum calculated with strength factors from an internuclear-distance-dependent transition dipole (scaling as in Figure 2)  $T=2100K$

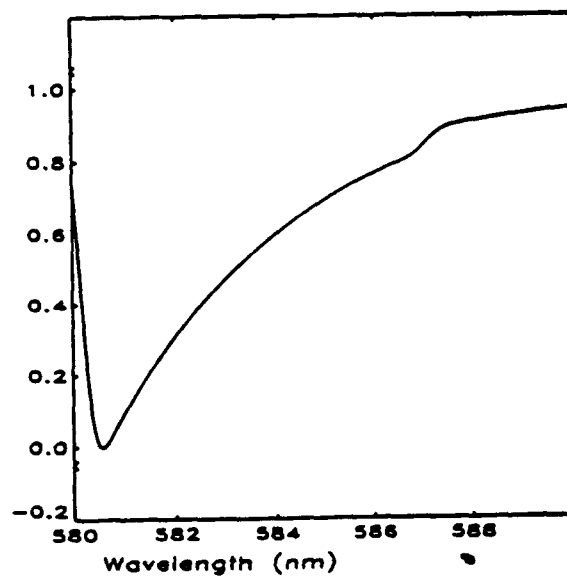
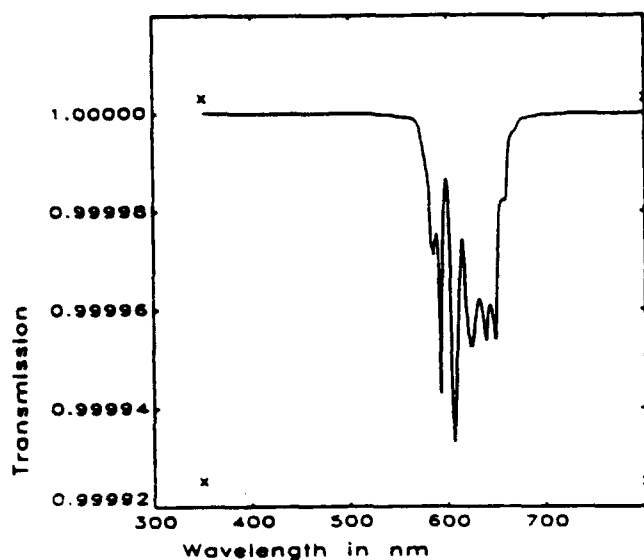
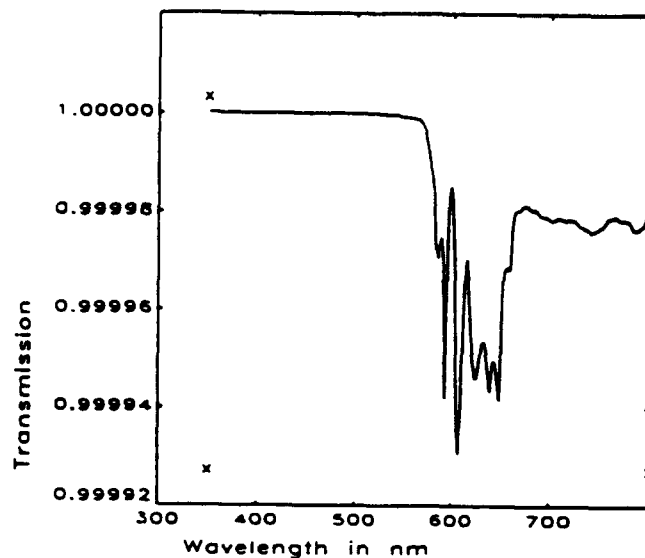


Figure 4— The  $v''=0 \rightarrow v'=0$  rovibronic manifold of transitions broadened with a Voigt function of predominant Gaussian width, 0.5 nm (arbitrary scaling),  $T=2100$



**Figure 5**— Vibronic transmission spectrum of the bound-bound transition in diatomic aluminum,  $T=2100\text{K}$



**Figure 6**— Combined vibronic transmission spectrum of the bound-bound and bound-free transitions in diatomic aluminum,  $T=2100\text{K}$

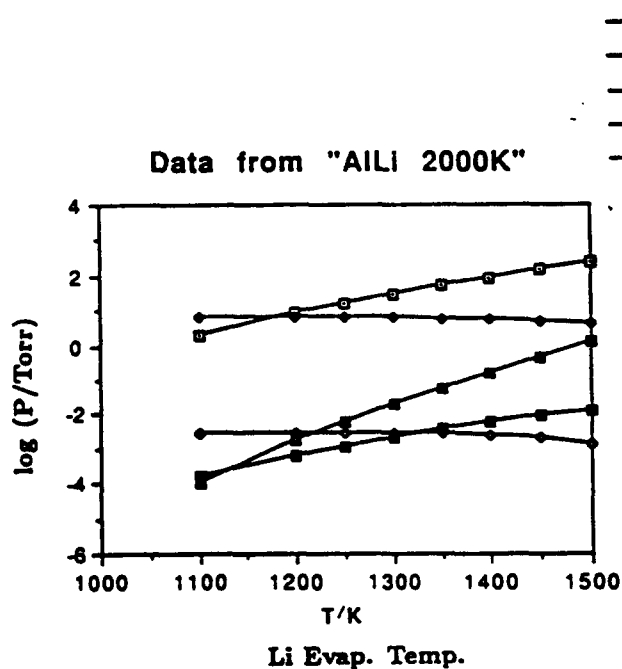


**Figure 7**— Vapor pressures of atomic and diatomic species in a mixture of lithium and aluminum at identical aluminum evaporator and observation temperatures of  $2000\text{K}$  as a function of the temperature of the lithium evaporator upstream

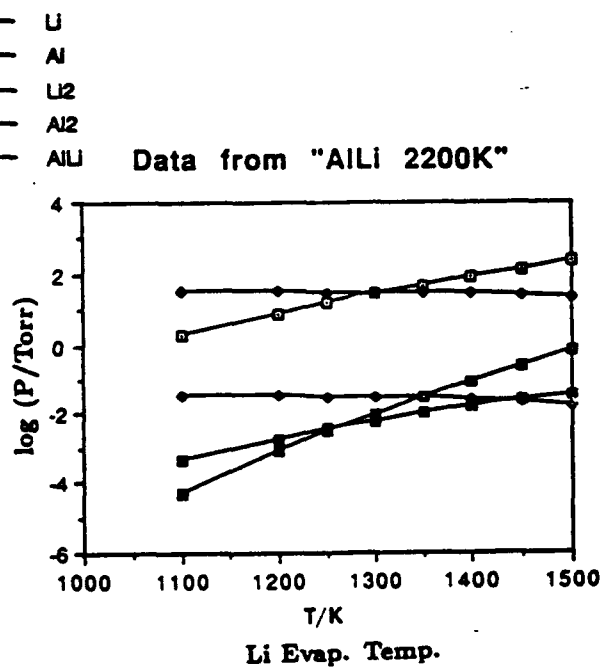


**Figure 8**— Vapor pressures as in Figure 7 but for aluminum evaporator and observation temperatures of  $2200\text{K}$

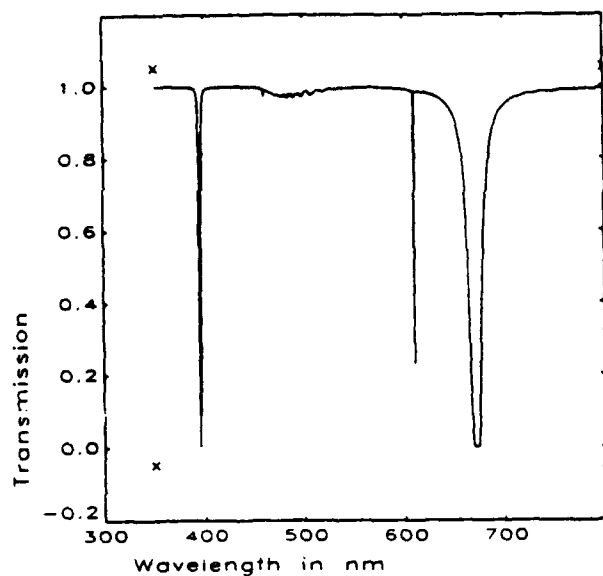


**Figure 9**— Background transmission spectrum of Li, Al,  $\text{Li}_2$ , and  $\text{Al}_2$  in a mixture at 2100K created with evaporator temperatures of 1350K for lithium and 2100K for aluminum

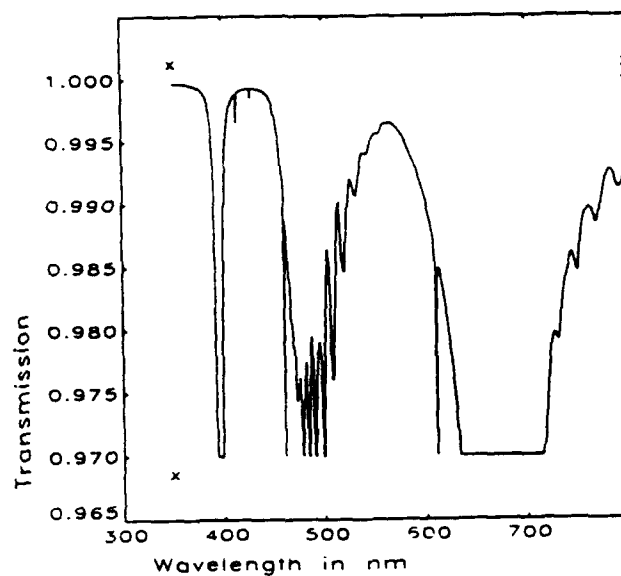


**Figure 10**— The spectrum of Figure 9 on an enlarged scale

INVESTIGATION OF ARCJET-POWER PROCESSING UNIT  
INTERACTION: EMISSION RIPPLE VELOCIMETRY I

Jeffrey A. Pobst  
Research Assistant  
Department of Aerospace Engineering

University of Southern California  
Los Angeles, California 90089-1191

Final Report for:  
Graduate Student Research Program

Sponsored by:  
Air Force Office of scientific Research  
Bolling Air Force Base, Washington, D.C.

August 1993

INVESTIGATION OF ARCJET-POWER PROCESSING UNIT  
INTERACTION: EMISSION RIPPLE VELOCIMETRY I

Jeffrey A. Pobst  
Research Assistant  
Department of Aerospace Engineering  
University of Southern California  
Los Angeles, California 90089-1191

Abstract

The behavior of the arcjet space thruster plume was studied using the emission ripple velocimetry method whereby the gas plume is observed to be radiating in conjunction with the change in power-processing-unit current levels as a function of time. The diagnostic method itself is investigated as is the experimental setup required for the measurements. In addition, appropriate data acquisition software was written. The effects of the high-frequency (16 kHz) 17% peak to peak current ripple of the PPU on the plume emission is examined and found to be 30-50% ripple peak to peak. This modulation of the emission is found to convect with the plume and lead to a velocity diagnostic method whereby the convection of the emission ripple leads to a velocity determination when the ripple phase is extracted as a function of position. As this method is examined it is found that the accuracy of the technique degrades as measurements are taken farther downstream from the nozzle. Modifications to the measurement technique are suggested and will be implemented should further funding accommodate such work.

INVESTIGATION OF ARCJET-POWER PROCESSING UNIT  
INTERACTION: EMISSION RIPPLE VELOCIMETRY I

Jeffrey A. Pobst

Introduction

The arcjet thruster for space applications is currently in a state of optimization and refinement. One of the ways to understand the behavior of the device is to probe the plume for information that leads to device efficiency and operation characteristics. To date, little work has been done to link the characteristics of a typical flight-ready power supply unit, known as the PPU or power-processing-unit to the behavior of the device itself at a high enough time resolution to examine the temporal changes of the flowfield due to the fluctuations in power supplied to the arcjet from the PPU.

The PPU supplies a pseudo-constant-current power to the arcjet to support an electrical arc between two electrodes. Gas propellant flows through the arc and the energy deposition into the gas causes the gas to accelerate. The gas then flows through a converging-diverging nozzle and is ejected out of the device at high velocity. While the thrust of the device is very low (on order of Newtons) constant operation in space along with the high specific impulse (on order of 1000 seconds on hydrogen) lead to a device that can be used as an efficient station keeping thruster or orbit transfer thruster for satellites and spacecraft.

The effect of PPU switching operation is apparent in the arcjet current profile, which exhibits a sawtooth-shaped current ripple at the PPU switching frequency. The optical emission from the plume has a corresponding ripple. This indicates that the energy deposited in molecular excited states (frozen flow losses) is modulated by the current ripple. Investigation of this requires the use of optical diagnostic techniques with time resolution of microseconds or better.

## Technique

The work described here is part of the ongoing investigation of the interaction between the arcjet and its power supply unit. This paper centers on the diagnostic technique of emission ripple velocimetry.

Emission ripple velocimetry (or ERV) is a way of measuring the velocity of the flow of gas by watching the emission ripple (created through variations in input current) convect with the gas flow. Its axial progress is then measured in time relative to the current profile from the PPU to determine a bulk gas flow velocity. This technique was developed by Spores, Pobst, Schilling, and Erwin.<sup>1</sup>

Potential drawbacks of the ERV technique include the fact that the emission detection is a line-of-sight measurement and integrates the signal across the optical path focusing to a point at the centerline of the plume.

Several recent papers<sup>2-4</sup> have presented investigations of arcjet thruster operation using laser-induced fluorescence (LIF) techniques to determine flow velocities in arcjets. Though the LIF results have demonstrated exceptional accuracy, time dependent resolution of velocity has not been demonstrated. The most accurate of the techniques have been continuous wave (CW) and are not applicable to temporal change measurements as a velocity measurement may take several seconds to perform.

Demonstration of pulsed laser-induced fluorescence (PLIF) has been shown to ascertain good velocity distributions, but usually at a cost of repetitive measurements that are then averaged to a velocity value.<sup>4-5</sup> Averaging of data points also prevents temporal measurements if the velocity field is not repetitive.

## Background

The use of arcjets, and electric thrusters in general, has become vastly more feasible in recent years. This is due, not so much to progress in the thrusters themselves, as to progress in prime power (solar and nuclear) and in power processing. Transformation from one DC voltage to another (DC-DC

conversion) using high-frequency ( $\sim 10$  kHz-10 MHz) switching<sup>o</sup> now has efficiency well in excess of 90%, compared with  $\sim 50\%$  for traditional linear supplies. This efficiency gain is due to the use of current regulation through on-off switching rather than series resistive elements: the switches dissipate significant power only during the short transition between on and off. The high switch frequency allows the use of much smaller magnetic components (inductors and transformers) than with low-frequency (e.g. 60 Hz) units. While these benefits are general to all power applications, switching PPU's have an additional feature: they can drive plasma devices, even with negative small-signal impedance, without the use of a ballast resistor.

Use of switching PPU's in space applications, however, gives rise to serious questions. The switch frequency is in the radiofrequency range, possibly causing RF emission from the plume as well as from the PPU itself. Moreover, the parts count in a switching PPU is quite large, which will lead to high space-rating costs. Finally, the PPU can affect the properties of the thruster itself: electrode erosion, frozen-flow losses, and momentum flux. These phenomena will be studied and analyzed as this work progresses.

### Experiment

To examine arcjet plume characteristics, a low-power (1 kW class) arcjet and PPU (designed by NASA Lewis Research Center) were operated on hydrogen gas in an optical diagnostic vacuum facility at the Electric Propulsion Lab of Phillips Laboratory at Edwards Air Force Base, California. The chamber was pumped by two 10,000 cfm Roots-Stokes combinations in parallel that lead to chamber pressures as low as 35 mTorr while flowing 8-10 slm of hydrogen through the arcjet thruster. The propellant flow was measured with a thermal-conductivity mass flow meter (MKS), calibrated with accuracy  $\pm 3\%$  by filling the known plenum volume to a known pressure and temperature. Engine operating voltage and current were obtained using a parallel 100-k $\Omega$  resistive divider and 0.01- $\Omega$  series resistor, respectively.



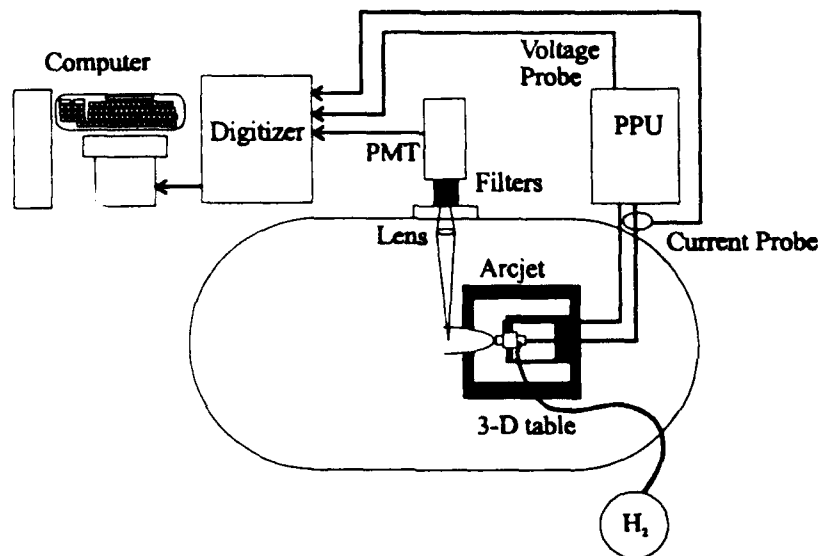


Figure 1: Experimental setup for emission diagnostics.

The diagnostic setup is shown in Figure 1. The arcjet is mounted on a three-axis translation stage, while the optics are fixed. Light is collected in the radial direction using only narrowband interference filters to select the entire Balmer  $\alpha$  line ( $\lambda=6563 \text{ \AA}$ ) of atomic hydrogen as well as several orders of neutral density filters and an aperture to select a roughly 1-mm-diameter cone of emission. A photomultiplier tube (PMT) (Hamamatsu R943) was the detector. The PMT signal was terminated in  $10\text{k}\Omega$  and acquired on a digitizing oscilloscope (Tektronix DSA 601) where the emission signal, the voltage signal, and the current trace were downloaded to an Intel 486 personal computer for analysis. The trigger for the experiment was the PPU current ripple as measured by a current probe (Tektronix AM 503).

When first developed by Spores et al<sup>1</sup>, the results given through the use of the ERV technique were brought under question due to the high back pressure (~1 Torr) of the vacuum chamber during the previous experiments. Through the AFOSR Summer Graduate Research Program, this author has been allowed to investigate further use of the technique in understanding arcjet flowfield

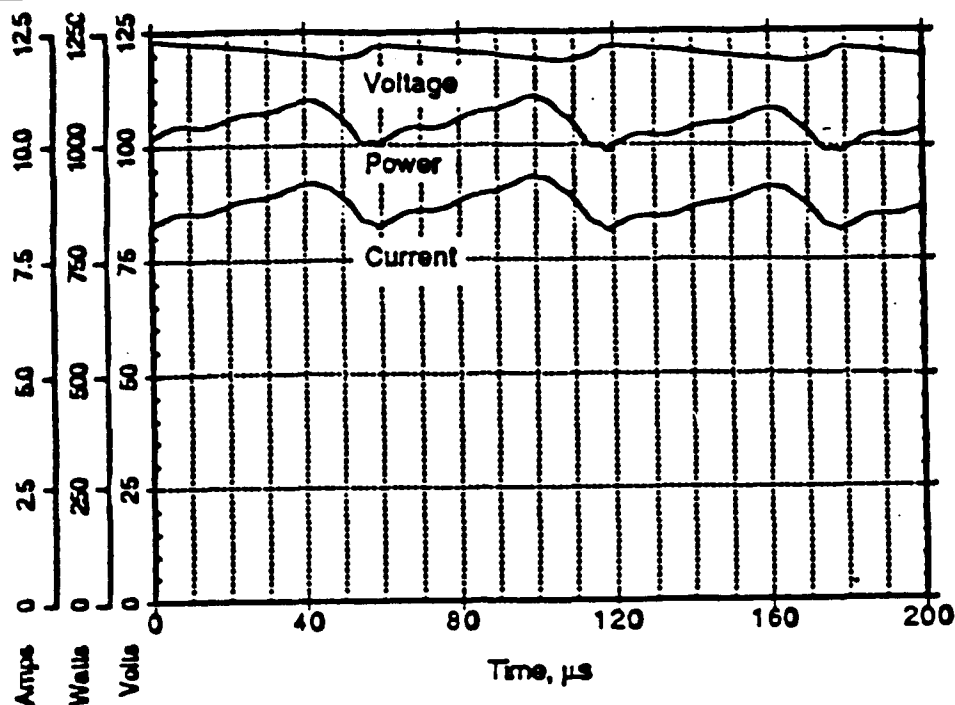


Figure 2: Arcjet voltage, current and power waveforms under typical operating conditions

behavior in a low background pressure facility ( $\sim 35$  mTorr) at the Electric Propulsion Lab at Phillips Laboratory, Edwards Air Force Base.

To bring the low pressure facility to a point where the ERV experiments could be conducted, a new data acquisition system was assembled including the authoring of Microsoft Windows software using C++ for the i486 microcomputer to initiate and control the experiment as well as post-process the raw data into velocity measurements.

The ERV software was an important part of data acquisition as automation of the data taking was required for the large number of data points that were needed to determine velocities and changes in velocity. Through the user interface, digitizer configuration and operation, as well as arcjet positioning and monitoring, could easily be done from a single location. Data storage and classification is also performed. When single shot experiments had determined the proper operating conditions for taking data, the automated scanning software ran the entire set of experiments unattended.

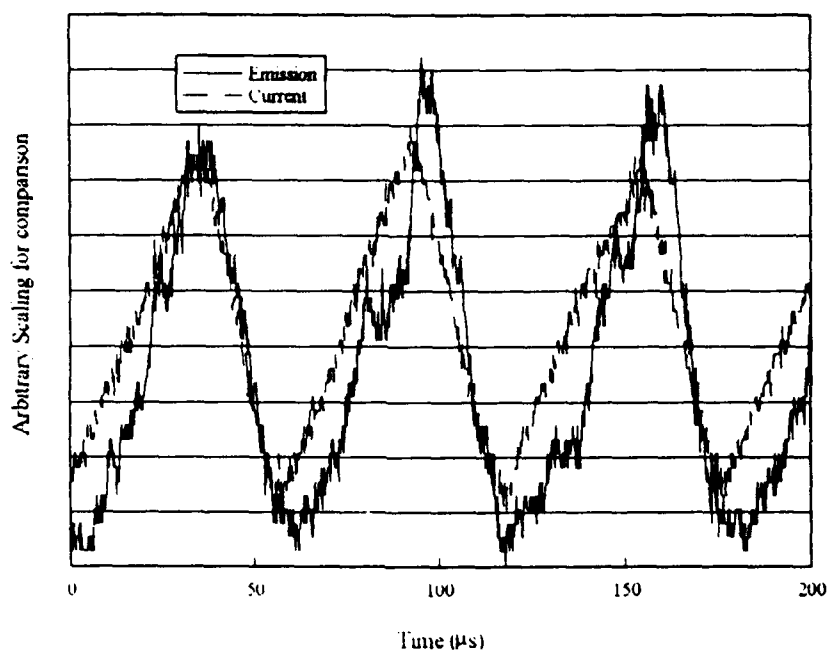


Figure 3: Typical Balmer- $\alpha$  curve with current trace shown.

### Results

A typical plot of arcjet voltage, current and power is shown in Figure 2. In this figure, the current ripple is seen to be about 17%. The voltage ripple is much smaller, about 3%, and in the opposite direction from the current ripple. This is consistent with DC operating characteristics of arc devices. The power, then, exhibits approximately 14% ripple, which may be considered an AC component of the propellant heating mechanism.

Figure 3 shows a typical plot of Balmer measured optically with the PMT at an axial location just outside the arcjet nozzle exit. The emission ripple is roughly in phase with the current except for a small phase delay. Amplitude values are not demonstrated in the figure as the two waveforms have been scaled for a phase comparison. The current ripple absolute value, though, is found to be about 45% of its average value, much larger ripple in the emission than the ripple in the applied current. The presence of an emission ripple would seem to indicate a modulation of excited-state density (hence of frozen-flow loss) by the PPU switching as discussed in [1].

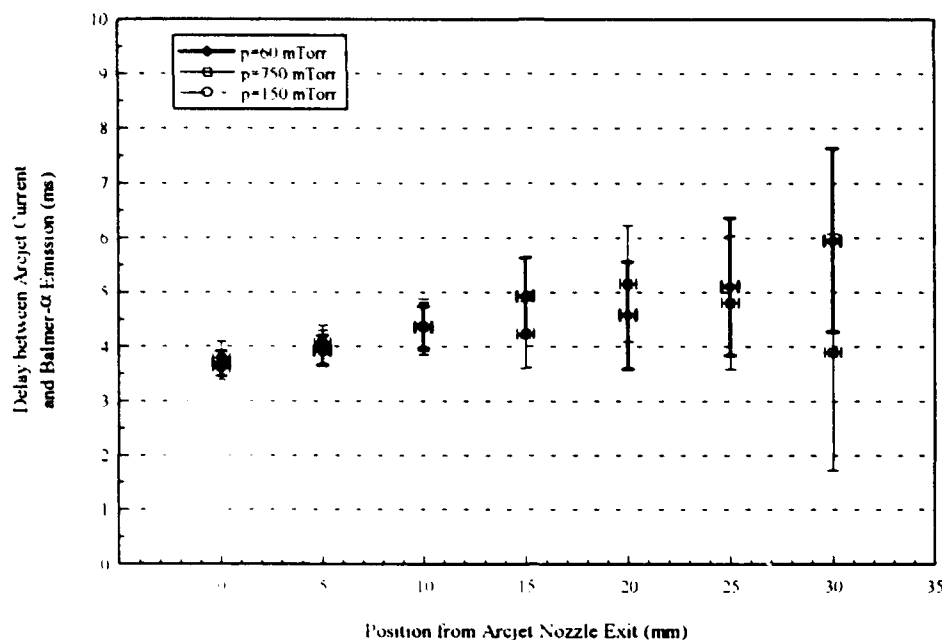


Figure 4: Time resolved delay deviations shown at various axial locations

As the PMT images at different locations downstream of the arcjet nozzle exit, the delay between the emission ripple and the current ripple increases.<sup>1</sup> This phenomenon of convection of ripple phase was demonstrated by Spores to be a feasible diagnostic technique known as emission ripple velocimetry or ERV where the distance from the nozzle exit of the probe volume divided by the time delay between emission at each location leads to an average velocity to that location. Through this summer graduate program, I have further explored the ERV technique at a variety of vacuum background pressures. In addition to this, the new facility provided equipment whereby the data taken could be time resolved and not time averaged. This allowed for a demonstration of a standard distribution of data values to be displayed. The results of this are shown in Figure 4. The error bars in position (x) demonstrate the uncertainty of the light collection volume, while the vertical error bars in time depict the variation with different phase delays from the PPU current. As can be seen, the variation near the nozzle exit is very small and seems to be independent of background pressure, but as light is collected downstream of

the nozzle the errors grow rapidly, calling into question the value of time averaged velocities and the effect on the gas due to the background pressure. The downstream measurements lead one to believe that the time delays are changing from data point to data point and indicate perhaps some rapidly changing fluid dynamic properties.

### Analysis

The presence of luminous species far out in the plume, and of the modulation of their density by the PPU ripple, deserves explanation. The plume convects at a rate of order 10 km/s ( 1 cm/ $\mu$ s) or lower. Since the plume is optically thin to Balmer radiation, the radiative 1/e decay times are 23 ns for Balmer- $\alpha$  which is too short for the plume emission to be due solely to the decay of atoms excited within the engine nozzle. Therefore, a mechanism for production of excited states in the plume is needed.

As is described in more full detail in [1], the plume modulation is local in the sense that a perturbation in the plasma state caused by arc modulation remains fixed in the frame of the plasma as the plume convects. Recombination of the electrons, which cool as the plume drifts, takes place preferentially to the upper levels of atomic hydrogen.<sup>8</sup> This produces a cascade from upper to lower levels which is visible as the plume radiation.

On the topic of data analysis, the method whereby the actual time delay of the emission is determined must be called into question. At greater distances from the nozzle large fluctuations in time delay are measured. Remembering that this is an integral method in determining velocity to this point, any fluid dynamic effects that took place at a specific location downstream of the nozzle will affect all measurements further downstream as its phase is compared to that of the initial current ripple which created the emission ripple in the plasma. Therefore, if we expect to determine time accurate measurements of velocity distributions downstream of the arcjet nozzle we will have to measure the time delay relative to some event unrelated

to the area upstream of the location that is being probed. As this is not possible with the current setup, it is my intention to pursue an extended experimental setup utilizing two photomultiplier tubes whose collection areas are focused at two different locations some small distance apart. As these two collection volumes can have a known fixed distance apart and as the emission ripple phase will be different at each location an average velocity for the area between only the two collection volumes can then be determined. If this is made small enough, a determination of changes in the velocity irrespective of any upstream behavior can be made. It is also expected that since the location of the two probed areas will be closer together than the measurements presented, a more accurate technique for determining time delay may be necessary. Some ideas on the subject include enhancing the current ripple of the PPU so that the waveform is more distinct down to the hundreds of nanoseconds and can therefore allow a separation of millimeters for the two collection volumes where the phase difference of the waveforms would be more distinct than is currently seen.

### Conclusions

The current ripple from a switching PPU is shown to cause a modulation in the excited state population of the hydrogen propellant. This excited state variation can be used as a way of following the flow and determining how fast the flow expands out of the arcjet nozzle. The current emission ripple velocimetry technique has been extended using time specific data acquisition techniques and lower background pressures. While the pressure difference does apparently influence the flowfield the data presented do not depict the flowfield accurately enough to determine to what extent this effect may be. The reason that the data is not accurate enough stems from the integrating nature of the diagnostic technique over position from the arcjet nozzle exit even when time dependent measurements are taken. A new extension of ERV is proposed using two light detection devices focused at two locations near each other so that the integrating nature of the technique is minimized. Using

this technique it is hoped that time accurate measurements of flow velocity distributions may be obtained axially downstream of the arcjet nozzle.

#### References

1. R. A. Spores, J. A. Pobst, J. H. Schilling, D. A. Erwin, "Performance Effects of Interaction Between a Low-Power Arcjet and its Power Processing Unit," 28th JPC, AIAA 92-3238, 1992.
2. D. A. Erwin, G. Pham-Van-Diep, and W. D. Deininger, "Laser Induced Fluorescence measurements of flow velocity in high-power arcjet thruster plumes," AIAA J. 29, 1298, 1991.
3. J. G. Liebeskind, R. K. Hanson, and M. A. Cappelli, 30th Aerospace Sciences Mtg, AIAA 92-0678, 1992.
4. W. M. Ruyten and D. Keefer, 22nd IEPC, AIAA 91-093, 1991.
5. M. W. Crotton, R. P. Welle, S. W. Janson, and R. B. Cohen, 22nd Plasmadynamic and Lasers Mtg, AIAA 91-1491, 1991.
6. G. C. Chryssis, *High Frequency Switching Power Supplies: Theory and Design*. McGraw-Hill, New York, 1989.
7. E. Pfender, in *Electric ARCs and Arc Gas Heaters*, edited by M. N. Hirsh and H. J. Oskam, Academic, New York, 1978, p. 291.
8. C. G. Braun, D. A. Erwin, and M. A. Gundersen, "Fundamental processes affecting recovery in hydrogen thyratrons," *Appl. Phys. Lett.* 50, 1325, 1987.

FORCED VIBRATION OF A TWO-SPAN FREE-FREE BEAM  
JOINED BY A NONLINEAR ROTATIONAL SPRING

David Bard  
Doctoral Candidate  
Department of Mechanical Engineering

Columbia University  
500 W. 120th Street  
S. W. Mudd, Room 220  
New York, NY 10027

Final Report for:  
Graduate Student Research Program  
Phillips Laboratory, Hanscom Air Force Base, Massachusetts

Sponsored by:  
Air Force Office of Scientific Research  
Bolling Air Force Base, Washington, D.C.  
August 1993



FORCED VIBRATION OF A TWO-SPAN FREE-FREE BEAM  
JOINED BY A NONLINEAR ROTATIONAL SPRING

David Bard  
Doctoral Candidate  
Department of Mechanical Engineering  
Columbia University

Abstract

The forced vibration characteristics of a two-span free-free beam joined by a nonlinear Duffing type rotational spring were investigated. The exact solutions of the linear problem were found and used as a basis to find an approximate solution to the nonlinear problem. This was accomplished by using a harmonic balance technique to handle the nonlinear boundary condition. The beam responses were determined for different nonlinear stiffness conditions for loadings at various frequencies. The relationship between amplitude and forcing frequency revealed a multiplicity of jump and oscillation hysteresis phenomena normally associated with Duffing type systems.

FORCED VIBRATION OF A TWO-SPAN FREE-FREE BEAM  
JOINED BY A NONLINEAR ROTATIONAL SPRING

David Bard

Introduction

The free and forced vibration of continuous beams have been widely investigated in the literature. Most texts develop solutions for the forced vibration problem by using exact solutions such as modal expansion and approximate solutions such as Galerkin and assumed mode methods. An exact technique discussed by Leissa [1] does not rely on the expansion of the applied loads in terms of the modes of free vibration, but rather relies on separating variables and evaluating a particular solution. This direct technique can be used without difficulty to analyze conditions such as a beam clamped at one end and supported by a linear spring at the other. Also, the method is much easier to employ for systems that contain multiple spans since particular solutions are calculated for each span independently of the loading on the other spans.

In an attempt to analyze the vibration of a two-stage rocket, a model was developed using a two-span free-free beam connected by a Duffing type nonlinear spring. Leissa's direct solution technique is applied and a solution is developed for spans with different loadings, lengths and material properties. A harmonic balance technique demonstrated by Porter and Billett [2] for longitudinal vibration is extended to bending vibration and is employed to handle the nonlinear boundary condition. Another reason for choosing the direct method was that the harmonic balance technique was easily applied, but it is unclear if applying the harmonic balance technique to modal expansion would have been possible.

Theory

The fourth order partial differential equation governing transverse vibration of an Euler-Bernoulli beam is

$$\frac{\partial^2}{\partial x^2} \left[ EI(x) \frac{\partial^2 w(x, t)}{\partial x^2} \right] + \frac{m(x)}{g_c} \frac{\partial^2 w(x, t)}{\partial t^2} = f(x, t) \quad (1)$$

For given boundary conditions, initial conditions, and applied load, equation (1) describes the beam's motion for all time. According to Leissa [1], if the applied load is sinusoidal in time then it is reasonable to assume the forced displacement will also be sinusoidal in time with the same frequency. Therefore, for a force given as

$$f(x, t) = P(x) \sin(\Omega t) \quad (2)$$

it is assumed that the displacement can be expressed as

$$w(x, t) = W(x) \sin(\Omega t) \quad (3)$$

Equation (3) allows the displacement to be in phase or 180 degrees out of phase with the applied load. For a beam that has a uniform mass distribution, constant modulus of elasticity and constant cross section, substituting equations (2) and (3) in equation (1) yields

$$EI \frac{d^4 W(x)}{dx^4} - \frac{m}{g_c} \Omega^2 W(x) = P(x) \quad (4)$$

A new dimensionless variable  $\zeta_i$  is defined as

$$\zeta_i = \frac{x_i}{L_i} \quad (5)$$

where the subscript has been added so that multiple spans can be analyzed. Now for any uniform prismatic span, equation (4) may be rewritten as

$$W_i^{IV}(\zeta_i) - \beta_i^4 W_i(\zeta_i) = Q_i(\zeta_i) \quad (6)$$

where

$$\beta_i^4 = \frac{m_i \Omega^2 L_i^4}{g_c (EI)_i}, \quad Q_i(\zeta_i) = \frac{P_i(\zeta_i) L_i^4}{(EI)_i} \quad (7)$$

and the differentiation is with respect to  $\zeta_i$ .

The solution of equation (6) is the sum of a complementary and particular solution which is given as

$$W_i(\zeta_i) = W_{p_i}(\zeta_i) + A_i \sin(\beta_i \zeta_i) + B_i \cos(\beta_i \zeta_i) + C_i \sinh(\beta_i \zeta_i) + D_i \cosh(\beta_i \zeta_i) \quad (8)$$

For a given load, a particular solution is found and then the four unknown constants are determined by using the four boundary conditions. This method of solution can be applied to boundary conditions such as a linear rotational spring attached at an end of a beam. However, if the spring has nonlinear restoring moments then equation (8) is only an approximate solution. Such an approximate solution can be obtained by using a harmonic balance technique demonstrated by Porter and Billett [2] for nonlinear boundary conditions.

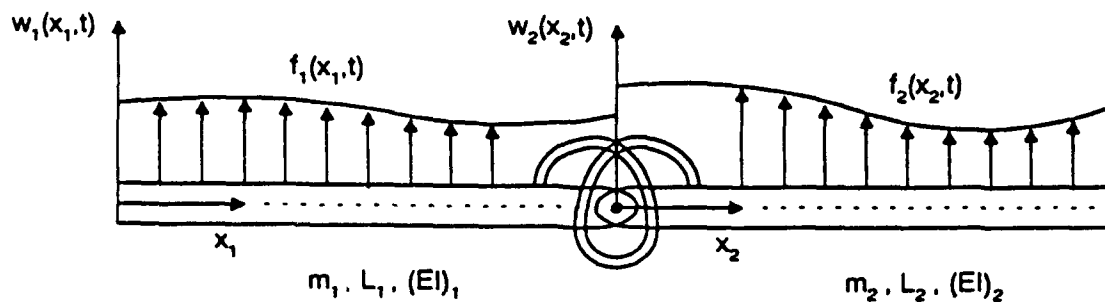


Figure 1. Two-span free-free beam connected by a nonlinear torsional spring.

## Analysis

In an attempt to analyze a two stage rocket a model was developed using two free beams connected at their ends by a nonlinear Duffing type torsional spring as shown in Figure 1. A Duffing torsional spring is one for which the restoring moment is proportional to the angular rotation and angular rotation cubed. As stated above it is assumed that the solution can be expressed as

$$\begin{aligned} w_1(\zeta_1, t) &= [w_{p_1}(\zeta_1) + A_1 \sin(\beta_1 \zeta_1) + B_1 \cos(\beta_1 \zeta_1) + C_1 \sinh(\beta_1 \zeta_1) + D_1 \cosh(\beta_1 \zeta_1)] \sin(\Omega t) \\ w_2(\zeta_2, t) &= [w_{p_2}(\zeta_2) + A_2 \sin(\beta_2 \zeta_2) + B_2 \cos(\beta_2 \zeta_2) + C_2 \sinh(\beta_2 \zeta_2) + D_2 \cosh(\beta_2 \zeta_2)] \sin(\Omega t) \end{aligned} \quad (9)$$

The eight boundary conditions for the two span beam are

$$\begin{aligned} \frac{(EI)_1}{L_1^2} w_1''(0, t) &= 0 \\ \frac{(EI)_1}{L_1^3} w_1'''(0, t) &= 0 \\ \frac{(EI)_2}{L_2^2} w_2''(1, t) &= 0 \\ \frac{(EI)_2}{L_2^3} w_2'''(1, t) &= 0 \\ w_1(1, t) &= w_2(0, t) \\ \frac{(EI)_1}{L_1^2} w_1''(1, t) &= \frac{(EI)_2}{L_2^2} w_2''(0, t) \\ \frac{(EI)_1}{L_1^3} w_1'''(1, t) &= \frac{(EI)_2}{L_2^3} w_2'''(0, t) \\ \frac{(EI)_2}{L_2^2} w_2''(0, t) &= k_1 \left[ \frac{w_2'(0, t)}{L_2} - \frac{w_1'(1, t)}{L_1} \right] + k_2 \left[ \frac{w_2'(0, t)}{L_2} - \frac{w_1'(1, t)}{L_1} \right]^3 \end{aligned} \quad (10)$$

To help simplify equations (10) several dimensionless variables are defined. The variables  $\alpha$ ,  $\beta$  and  $\gamma$  are used to relate the properties of the two spans and are defined as

$$\alpha^4 = \frac{(EI)_1}{(EI)_2}, \quad \beta = \frac{L_1}{L_2}, \quad \gamma^4 = \frac{m_1}{m_2} \quad (11)$$

Two other dimensionless variables are also defined. The first variable is the relationship of beam stiffness to the linear torsional spring constant and is defined as

$$R = \frac{(EI)_1}{k_1 L_1} \quad (12)$$

The second variable is the ratio of the nonlinear to linear spring constant and is defined as

$$K = \frac{k_2}{k_1} \quad (13)$$

Another useful equation is derived by combining equations (7) and (11) to give

$$\frac{\beta_1}{\beta_2} = \frac{\beta \gamma}{\alpha} \quad (14)$$

The first seven boundary conditions in equation (10) are linear and homogeneous. However, the eighth condition is nonlinear and requires special attention. The first seven simplified linear boundary conditions are attained by substituting equations (3) and (11) in equation (10) and are

$$\begin{aligned} w_1''(0) &= 0 \\ w_1'''(0) &= 0 \\ w_2''(1) &= 0 \\ w_2'''(1) &= 0 \\ w_1(1) &= w_2(0) \\ \frac{\alpha^4}{\beta^2} w_1''(1) &= w_2''(0) \\ \frac{\alpha^4}{\beta^3} w_1'''(1) &= w_2'''(0) \end{aligned} \quad (15)$$

In the eighth equation, unlike the others, the  $\sin(\Omega t)$  term does not vanish. The relationship

$$\sin^3(\Omega t) = \frac{3}{4}\sin(\Omega t) - \frac{1}{4}\sin(3\Omega t) \quad (16)$$

is used to expand the cubic term and simplify the equation. Applying equations (3), (11), (12), (13) and (16) to the eighth boundary condition yields

$$\left[ \frac{\beta}{\alpha^4} R W_2''(0) - \left[ W_2'(0) - \frac{W_1'(1)}{\beta} \right] - \frac{3\beta^2 K}{4L_1^2} \left[ W_2'(0) - \frac{W_1'(1)}{\beta} \right]^3 \right] \sin(\Omega t) + \frac{\beta^2 K}{4L_1^2} \left[ W_2'(0) - \frac{W_1'(1)}{\beta} \right]^3 \sin(3\Omega t) = 0 \quad (17)$$

Since the solution is approximate in that we assumed the displacement was expressible in terms of only  $\sin(\Omega t)$ , the coefficient of the  $\sin(\Omega t)$  term is used as the eighth boundary condition. In actuality, if the solution were exact it would be necessary for both the coefficient of  $\sin(\Omega t)$  and  $\sin(3\Omega t)$  to be zero. For a discussion of exact solutions including all sub-harmonic and super-harmonic vibrations see Porter and Billett [2].

### Discussion

A two-span model was created to test the above analysis. The two spans were assigned lengths, flexural rigidities, and mass distributions. Also, both spans were loaded with the same uniform distribution

$$f_i(\zeta_i, t) = P_0 \sin(\Omega t) \quad (18)$$

For the load of equation (18), the corresponding particular solution is

$$W_{pi}(\zeta_i) = -\frac{P_0 g_c}{m_i \Omega^2} \quad (19)$$

Since the load is constant, it is convenient to define a dimensionless load parameter as

$$F = \frac{P_o L_1^3}{(EI)_1} \quad (20)$$

To aid in plotting solutions, a dimensionless forcing frequency is defined as

$$\omega = \frac{\Omega}{\sqrt{\frac{g_c (EI)_1}{m_1 L_1^4}}} \quad (21)$$

To solve for the eight unknown constants, numerical techniques were employed. The first seven linear equations are solved algebraically to evaluate all the unknowns  $B_1$ ,  $C_1$ ,  $D_1$ ,  $A_2$ ,  $B_2$ ,  $C_2$  and  $D_2$  in terms of  $A_1$ . The eighth equation which is cubic is then solved numerically for the unknown  $A_1$ . The seven other constants are then evaluated using the calculated  $A_1$ . Care must be taken to determine if the three roots of the cubic are all real or a complex conjugate pair and a real. If three real roots exist then there are three possible behaviors for the system at the driven frequency.

The following table summarizes the property values assigned to span #1 for the test. The properties of span #2 are varied by specifying values for the dimensionless variables  $\alpha$ ,  $\beta$  and  $\gamma$ . In this paper all the tests were performed for  $\alpha=1$ ,  $\beta=1$  and  $\gamma=1.189$ .

Table 1. Span #1 properties.

$(EI)_1$	$L_1$	$m_1$	$P_o$
$10^9$ lbf-in <sup>2</sup>	100 in	2 lbm/in	100 lbf/in

It was desired to load the spans at frequencies between consecutive (i.e. between the first and second, second and third, etc.) natural frequencies in bending. However, since the system is nonlinear the exact natural frequencies



are not known. To approximate the unknown frequencies two methods were employed. For the first method the linear eigenvalue problem was solved by setting the coefficient K to zero. The value of R was also set to zero so that the two beams act like a single beam twice as long while retaining its nonuniform mass distribution. This method, though straight forward, is not a trivial matter since this process leads to evaluating an 8x8 determinant to get the desired natural frequencies. The second method is much simpler and uses the formula for the eigenvalues of a free-free beam which according to Meirovitch [3] is

$$\Omega_n = (n + 0.5)^2 \pi^2 \sqrt{\frac{EI g_c}{mL^4}} \quad (22)$$

where  $n=1,2,\dots$ . Using equation (22), the nth natural frequency for the two beam system is approximated by assuming the two beams are replaced by a single beam twice as long ( $L=200$  in) with uniform mass distribution ( $m=2$  or  $m=1$  lbm/in). The frequencies obtained using both methods are listed in Table 2.

Table 2. Approximate natural frequencies.

n	Eigenvalue problem	Equation (22) with $m=2$ lbm/in	Equation (22) with $m=1$ lbm/in
1	287 rad/s	244 rad/s	345 rad/s
2	813 rad/s	678 rad/s	958 rad/s
3	1544 rad/s	1328 rad/s	1878 rad/s

Examining Table 2 for all three modes, as expected, it is seen that the frequencies determined from the eigenvalue problem fall between the values obtained using equation (22) for the different mass distributions. The values calculated with equation (22) and  $m=1$  lbm/in give an approximate upper bound for the frequencies of a very stiff linear or nonlinear system. Based on the values in Table 2, it was decided to analyze the response of the nonlinear system at frequencies of 10, 500, 1000, 1500, and 2000 rad/s. Using equation (21) the frequencies could be non-dimensionalized, but there is no benefit here.

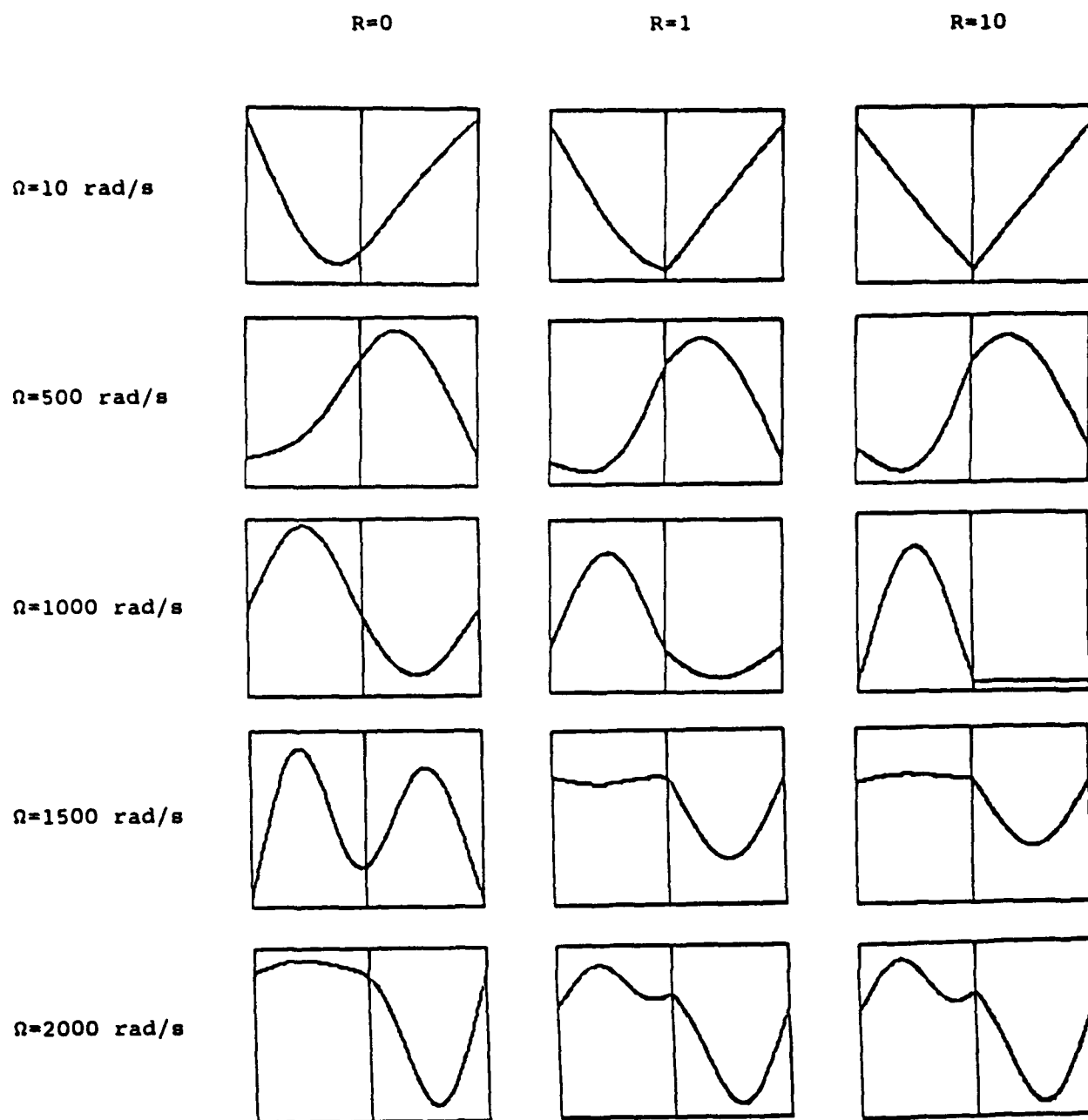


Figure 2. Deflected shapes for  $K=0$ ,  $\alpha=1$ ,  $\beta=1$  and  $\gamma=1.189$  for various values of  $R$  and  $\Omega$ .

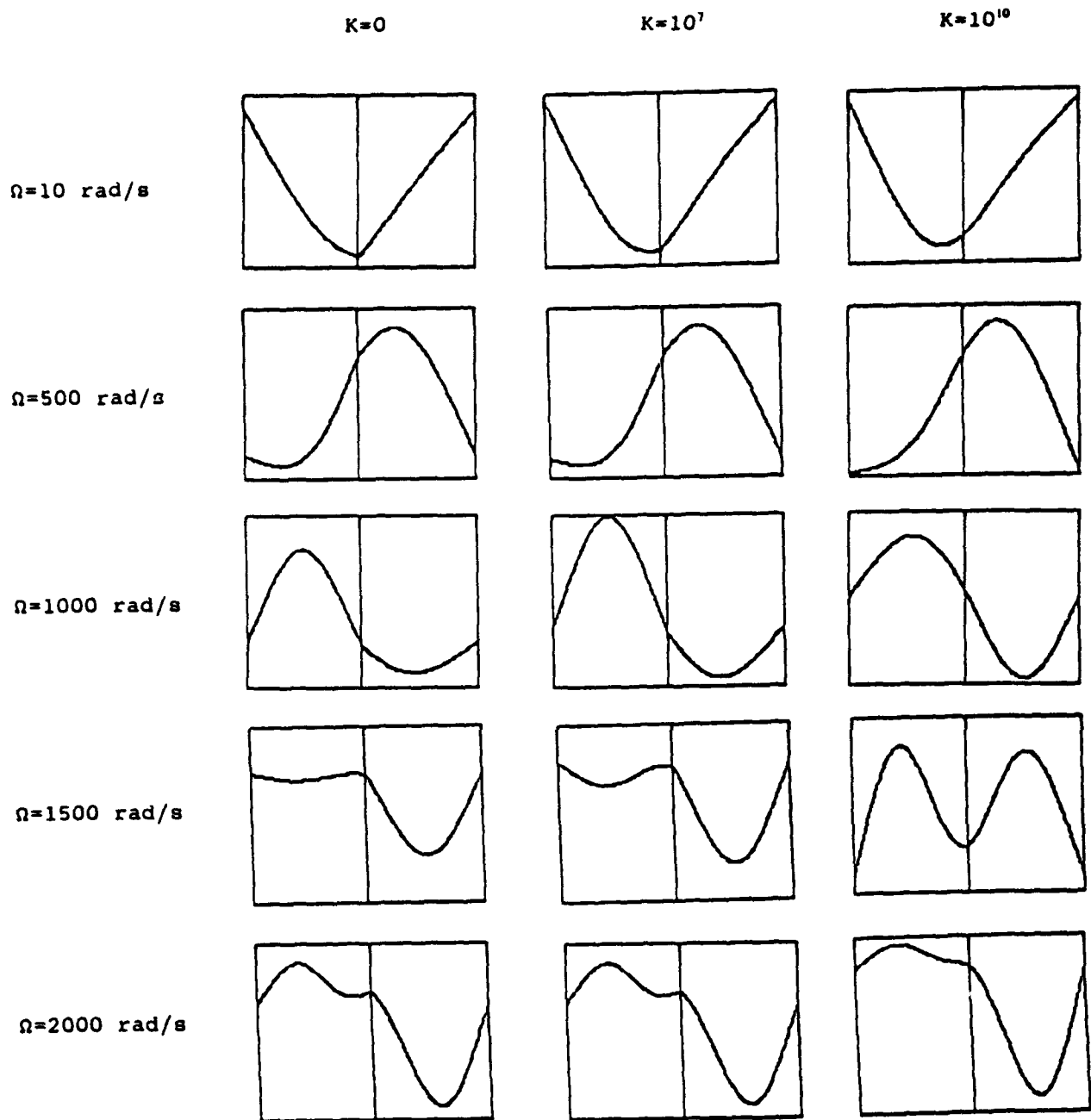


Figure 3. Deflected shapes for  $R=1$ ,  $\alpha=1$ ,  $\beta=1$  and  $\gamma=1.189$  for various values of  $K$  and  $\Omega$ .

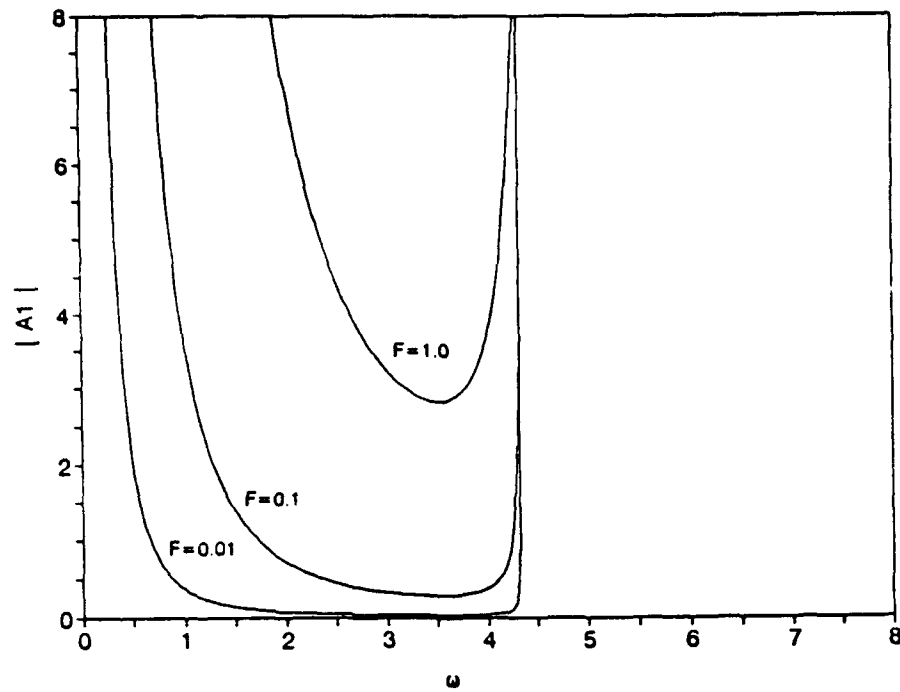


Figure 4. Amplitude  $A_1$  versus forced frequency  $\omega$  for values of  $F$  of 0.01, 0.1 and 1.0 when  $R=1$  and  $K=1$ .

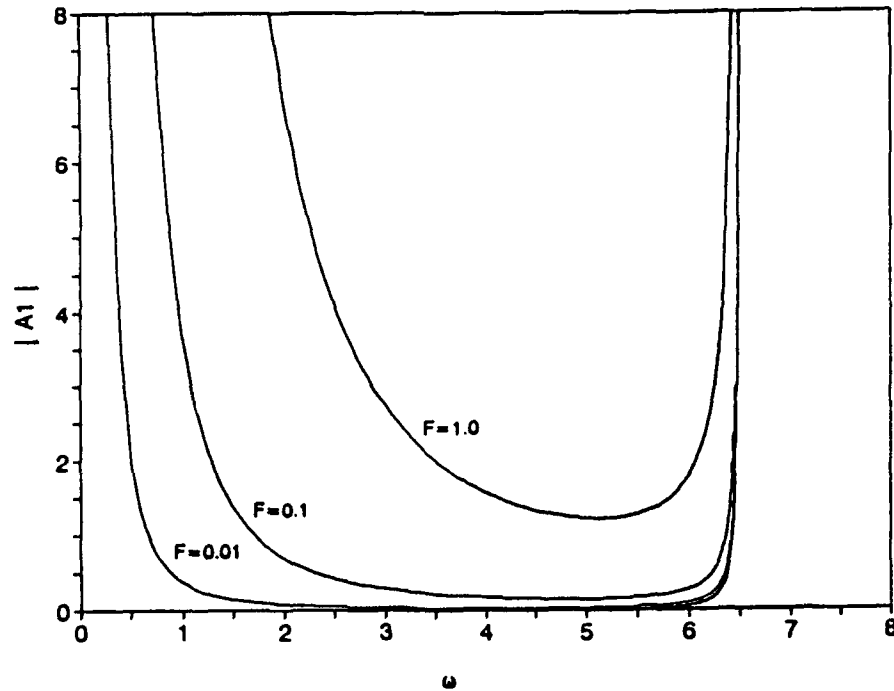


Figure 5. Amplitude  $A_1$  versus forced frequency  $\omega$  for values of  $F$  of 0.01, 0.1 and 1.0 when  $R=1$  and  $K=10^7$ .

Figure 2 shows the deflected shapes of a linear ( $K=0$ ) two beam system for various values of  $R$  when loaded at the five frequencies listed above. Since a direct solution method was employed to obtain these plots, it was necessary to subtract out the rigid body translation and rotation from the solution in order to find the final deflected shape. This is similar to the modal expansion technique where the rigid body modes are not included in the expansion. Most of the behavior shown in Figure 2 is as expected. Inspecting the  $R=0$  column, it is seen that the slope at the beam connection is constant, but a kink is noticeable in the  $R=10$  column. This kink occurs when  $R=10$  because the beams remain almost rigid due to the connection by a soft torsion spring, but when  $R=0$  the beams bend as a single continuous beam. Another expected result is the response change from in phase to out of phase as the forcing frequency was increased. For example, the free ends of the beams deflect up at  $\Omega=10$  rad/s, but deflect down at  $\Omega=500$  rad/s.

Figure 3 shows the deflected shapes for  $R=1$  for various values of  $K$  when loaded at the same five frequencies. It was found that the general nonlinear behavior can be quite similar to the linear case at certain frequencies. However, at the frequency  $\Omega=1500$  rad/s increasing  $K$  not only reversed the phase, but totally changed the response shape. This strange occurrence is directly related to the existence of three real roots of the cubic equation as described above.

To study this effect, the roots of the cubic equation for  $A_1$  were plotted versus dimensionless frequency  $\omega$  for  $R=1$  at force levels  $F$  of 0.01, 0.1 and 1.0 which respectively correspond to constant loads of 10, 100 and 1000 lbf/in. Figure 4 shows the roots of a slightly nonlinear system ( $K=1$ ) and Figure 5 shows those of a nonlinear system ( $K=10^7$ ). Since the vertical asymptotes in these plots occur at the natural frequency, this method provides a method for finding the natural frequencies of a nonlinear system. The respective dimensionless natural frequencies for the  $K=1$  and  $K=10^7$  systems are  $\omega=4.31$  and  $\omega=6.51$  which correspond to actual frequencies of about 190 and 286 rad/s. Recalling Table 2, the first frequency predicted by the linear eigenvalue problem was 287 rad/s

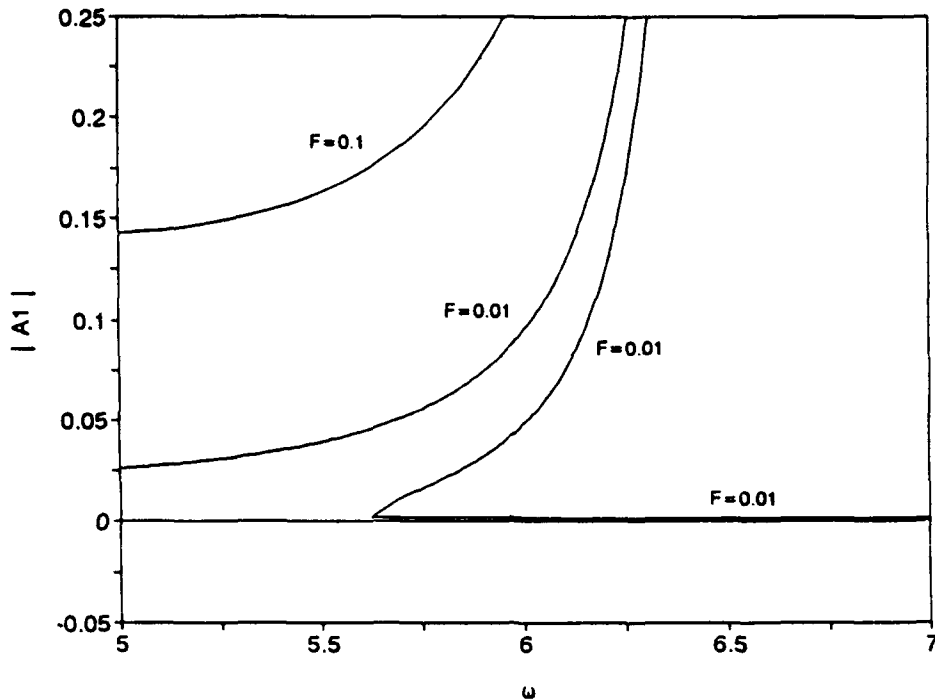


Figure 6. Magnification of three root region of Figure 5.

which turns out to be an excellent approximation for a stiff nonlinear system. Although not shown in Figure 4 or 5, the demonstrated behavior of  $A_1$  repeats within an infinite number of ranges each enclosed by asymptotes corresponding to higher natural frequencies.

Figure 4 shows that the roots for the  $K=1$  case turn out to be a pair of complex conjugates and a real. This means that for all practical purposes the behavior resembles a linear system. However, for the  $K=10^7$  case it is noticed that the solution of the cubic has a region with three real roots when  $F=0.01$ . Figure 6 shows a magnified view of the region in which the three roots exist. The existence of multiple roots lead to so called "jump" phenomena characteristic of Duffing type systems. The fact that jumps in amplitude can occur at different frequencies depending on the direction of approach of  $\omega$  shows that the system exhibits oscillation hysteresis. The figure shows the absolute value of  $A_1$ , but actually the root of largest magnitude is negative. The possibility that two roots can have almost identical magnitude, but opposite sign, means the system

can respond in a similar manner whether in or out of phase. Also, there must exist a point at which there are two equal real roots. In Figure 6 this occurs for a value of about  $\omega=5.63$ . Below this frequency a pair of complex conjugates and a real exist.

### Conclusions

The preceding analysis showed that direct solution of the differential equation for forced vibration along with harmonic balancing can generate accurate results. Although the method was applied only to a system with constant loads, more complicated varying load problems can similarly be solved with the developed theory. The values of  $\alpha$ ,  $\beta$  and  $\gamma$  can also be varied to study alternative configurations. For the parameters chosen for this study, various kinds of phenomena associated with a nonlinear rotational spring were demonstrated. Investigation of amplitude versus forcing frequency curves revealed a multiplicity of jump and hysteresis phenomena that can occur over an infinite range of frequencies.

### Acknowledgements

This study was sponsored by the Air Force Office of Scientific Research, Bolling Air Force Base, Washington, D.C. and was performed at Phillips Laboratory, Hanscom Air Force Base, Massachusetts, while participating in the Graduate Student Research Program.

### References

1. Leissa, A. W., "Closed Form Exact Solutions for the Steady State Vibrations of Continuous Systems Subject to Distributed Exciting Forces," *Journal of Sound and Vibration*, Vol. 134, 1989, pp. 435-453.
2. Porter, B. and Billett, R. A., "Harmonic and Sub-harmonic Vibration of a Continuous System Having Nonlinear Constraint," *International Journal of Mechanical Science*, Vol. 7, 1965, pp. 431-439.
3. Meirovitch, L., *Analytical Methods in Vibration*, Macmillan, New York, 1967.

4. Biggs, J. M., *Introduction to Structural Dynamics*, McGraw-Hill, New York, 1964.
5. Nayfeh, A. H. and Mook, D. T., *Nonlinear Oscillations*, Wiley, New York, 1979.
6. Paslay, P. R. and Gurtin, M. E., "The Vibration Response of a Linear Undamped System Resting on a Nonlinear Spring," *ASME Journal of Applied Mechanics*, Vol. 27, 1960, pp. 272-274.
7. Stoker, J. J., *Nonlinear Vibrations*, Interscience, New York, 1954.



ON THE CALCULATION OF THE COMPONENTS OF THE RIEMANN TENSOR  
BY NEUTRAL PARTICLE INTERFEROMETRY

Ralph R. Craig  
Department of Mathematics

North Carolina State University  
Raleigh, NC 27695

Final Report for:  
Graduate Student Research Program  
Phillips Laboratory

Sponsored by:  
Air Force Office of Scientific Research  
Bolling Air Force Base, Washington, D.C.

September 1993

ON THE CALCULATION OF THE COMPONENTS OF THE RIEMANN TENSOR  
BY NEUTRAL PARTICLE INTERFEROMETRY

Ralph R. Craig  
Department of Mathematics  
North Carolina State University  
Raleigh, NC 27695

Abstract

It is known that the six independent components of the electromagnetic field tensor may be determined by charged particle interferometry. The process may be thought of as sending the particles along six paths or loops through spacetime and observing the change in quantum phase as the particles traverse these loops. An analogous method for determining the components of the Riemann curvature tensor by means of neutral particle interferometry is examined. We wish to know if it is possible to construct enough spacetime loops to determine the twenty-one independent components of the Riemann tensor. This question remains open.

# ON THE CALCULATION OF THE COMPONENTS OF THE RIEMANN TENSOR BY NEUTRAL PARTICLE INTERFEROMETRY

Ralph R. Craig

## Introduction

The possibility that curvature effects may be observed in interferometric experiments using ultracold neutrons is proposed by Anandon [1], based on the experiment performed by Colella, Overhuser and Werner [2] in which gravitationally induced quantum interference was observed in an experiment involving thermal neutrons. We wish to determine whether it is theoretically possible to perform interferometry experiments such that the results may yield all independent components of the Riemann curvature tensor. We shall begin by considering the analogous problem of the calculation of the components of the electromagnetic field tensor using charged particle interferometry.

## Electromagnetic Field Tensor

The quantum phase of a beam of charged particles is given in [3] by  $\Phi[x(t)] = (\text{constant})e^{(i/\hbar)S[x(t)]}$  where  $S[x(t)]$  is the classical action along the path,  $S[x(t)] = \int L(\dot{x}, x, t) dt$ . For the electromagnetic force, the Lagrangian of interaction is given by  $L = eu^\mu A_\mu$  where  $A$  is the four-vector potential. The phase change around a spacetime loop is given by:

$$\Delta\Phi_{loop} = (e/\hbar) \oint A_\mu u^\mu d\tau = (e/\hbar) \oint A_\mu dx^\mu$$

Applying Stokes' Theorem:

$$\Delta\Phi_{loop} = (e/\hbar) \iint_S A_{\mu,\nu} dx^\mu \wedge dx^\nu = (e/\hbar) F_{\mu\nu} (\text{Area of loop}),$$

considering  $F_{\mu\nu}$ , the components of the electromagnetic tensor, to be constant within the loop.

$$(F_{\mu\nu}) = \begin{pmatrix} 0 & -E_x & -E_y & -E_z \\ E_x & 0 & B_z & -B_y \\ E_y & -B_z & 0 & B_x \\ E_z & B_y & -B_x & 0 \end{pmatrix}$$

The simplest of our spacetime loops consists of emitting particles in opposite directions along a coordinate axis,  $x^i$ , a distance  $\ell$  and reflecting them back to the origin. This results in a spacetime loop of area  $2(\ell^2/v)$  where  $v$  is the velocity of the particles in units where  $c = 1$ . See Figure 1 a). We now have the

electric components of  $F$  in terms of the measured phase difference between the two beams.

$$\Delta\Phi_i = (e/\hbar) F_{0i} (2\ell^2/v), \quad E_i = (\Delta\Phi_i \hbar/e) (v/2\ell^2)$$

To obtain the magnetic components, we consider loops in which the particles beams are emitted along different axes,  $x^i$  and  $x^j$ , a distance  $\ell$  and reflected at right angles so the beams cross at the point  $(\ell, \ell)$  in the  $x^i - x^j$  plane. See Figure 1 b). The differential along the legs of the loop which are parallel to the  $x^i$  axis is given by  $\alpha = v dx^0 \wedge dx^i$  and for the legs parallel to the  $x^j$  axis,  $\beta = v dx^0 \wedge dx^j$ . Note that  $\alpha \wedge \beta = v dx^0 \wedge dx^i - v dx^0 \wedge dx^j + dx^i \wedge dx^j$ . The spacetime area encompassed by this loop is  $\ell^2(1+2/v^2)^{1/2}$ . Resulting in:

$$\Delta\Phi_{ij} = \iint_S A_{\mu\nu} \alpha \wedge \beta = (e/\hbar) \ell^2(1+2/v^2)^{1/2} [vF_{0i} - vF_{0j} + F_{ij}].$$

This process results in the following six independent equations:

$$\Delta\Phi_x = (e/\hbar) E_x 2(\ell^2/v), \quad \Delta\Phi_{x,y} = (e/\hbar) \ell^2(1+2/v^2)^{1/2} [vE_x - vE_y + B_z]$$

$$\Delta\Phi_y = (e/\hbar) E_y 2(\ell^2/v), \quad \Delta\Phi_{x,z} = (e/\hbar) \ell^2(1+2/v^2)^{1/2} [vE_x - vE_z - B_y]$$

$$\Delta\Phi_z = (e/\hbar) E_z 2(\ell^2/v), \quad \Delta\Phi_{y,z} = (e/\hbar) \ell^2(1+2/v^2)^{1/2} [vE_y - vE_z + B_x]$$

### Gravitation

We now wish to apply this method to the gravitational field. The action is given by  $\int \sqrt{g_{\mu\nu} dx^\mu dx^\nu}$ . In an inertial reference frame we may find a Riemann-normal coordinate system, i.e. one in which the first derivatives of the  $g_{\mu\nu}$  tensor vanish [4]. We may then expand the expression for the action to

$$\int \sqrt{\eta_{\mu\nu} dx^\mu dx^\nu + (1/2)g_{\mu\nu,\kappa\lambda} x^\kappa x^\lambda dx^\mu dx^\nu}.$$

The components of the Riemann tensor may be expressed as linear combinations of the  $g_{\mu\nu,\kappa\lambda}$  terms. It is these terms which we hope to compute.

First consider the simple loop consisting of a beam of neutral particles split so that each part goes in one direction of the  $x^i$  axis a distance  $\ell$  and is reflected back to the origin. Unfortunately, Stokes' Theorem is not applicable in this case so we must parameterize each of the four legs of the loop and integrate. The parameterization of the first leg (See Figure 1 a)) is:

$$x^0 = t \quad x^i = vt \quad dx^0 = dt \quad dx^i = v dt$$

The expression for the phase shift along the first leg of the loop is

$$\begin{aligned}\Delta\Phi_{i(\text{first leg})} = (1/\hbar) \int_{t=0}^{\ell/v} & \sqrt{dt^2 - v^2 dt^2 + (1/2)[g_{00,00} x^{02} dx^{02} + g_{00,i0} x^0 x^i dx^{02} \\ & + g_{00,0i} x^0 x^i dx^{02} + g_{00,ii} x^{i2} dx^{02} + g_{0i,00} x^{02} dx^0 dx^i \\ & + g_{0i,i0} x^0 x^i dx^0 dx^i + g_{0i,0i} x^0 x^i dx^0 dx^i + g_{0i,ii} x^{i2} dx^0 dx^i \\ & + g_{i0,i0} x^0 x^i dx^i dx^0 + g_{i0,ii} x^{i2} dx^i dx^0 + g_{ii,00} x^{02} dx^{i2} \\ & + g_{ii,i0} x^0 x^i dx^{i2} + g_{ii,0i} x^0 x^i dx^{i2} + g_{ii,ii} x^{i2} dx^{i2}]} \end{aligned}$$

Taking advantage of symmetries of the metric tensor and parameterizing,

$$\begin{aligned}\Delta\Phi_{i(\text{first leg})} = (1/\hbar) \int_{t=0}^{\ell/v} & \sqrt{(1-v^2)dt^2 + [g_{00,00} + 2g_{00,0i} v + g_{00,ii} v^2 \\ & + 2g_{0i,00} v + 4g_{0i,0i} v^2 + 2g_{0i,ii} v^3 \\ & + g_{ii,00} v^2 + 2g_{ii,0i} v^3 + g_{ii,ii} v^4] t^2 dt^2} \end{aligned}$$

Let  $\gamma = (1-v^2)^{1/2}$  and assume that the second term is small so we may make the approximation,

$$\begin{aligned}\Delta\Phi_{i(\text{first leg})} = (1/\hbar\gamma) \int_{t=0}^{\ell/v} & 1 - (1/4)\gamma^2 [g_{00,00} + 2g_{00,0i} v + g_{00,ii} v^2 \\ & + 2g_{0i,00} v + 4g_{0i,0i} v^2 + g_{0i,ii} v^3 \\ & + g_{ii,00} v^2 + 2g_{ii,0i} v^3 + g_{ii,ii} v^4] t^2 dt^2 \end{aligned}$$

Upon integration, this yields a linear combination of  $g_{\mu\nu,\kappa\lambda}$  terms. After each leg of the loop is similarly integrated, we obtain the equation

$$\Delta\Phi_{0i} = (1/2\hbar)\gamma(g_{00,0i} + g_{ii,0i} v^2)(\ell^3/v^2), \quad i = 1 \dots 3.$$

In the case of the electromagnetic tensor, another loop of this type (sending the particles out and back along the same axis) in the  $x^i - x^j$  plane would only yield a linear combination of the equations obtained from loops aligned along the  $x^i$  and  $x^j$  axes respectively. However, in the case of the gravitational field, additional

terms may be found by considering an interferometric experiment in which the arms of the intrferometer are aligned at a  $45^\circ$  angle to the axes. See Figure 1 c). In this case we get the equation

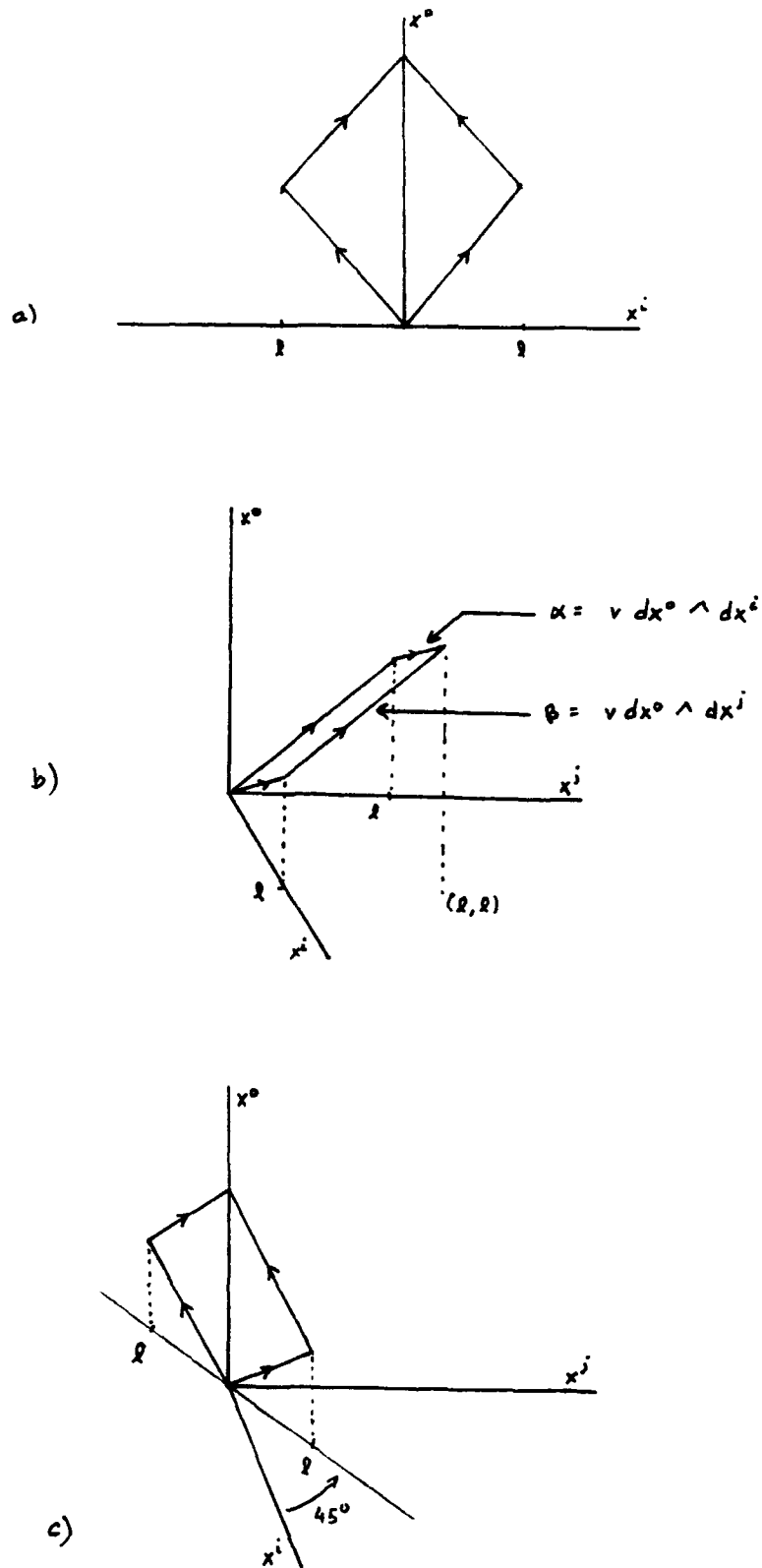
$$\begin{aligned}\Delta\Phi_{ij\angle 45^\circ} = & (1/4\hbar)\gamma(\sqrt{2} g_{00,0i} \ell + \sqrt{2} g_{00,0j} \ell + \frac{\sqrt{2}}{2} g_{ii,0i} \ell v^3 \\ & + \frac{\sqrt{2}}{2} g_{ii,0j} \ell v^3 + \frac{\sqrt{2}}{2} g_{jj,0i} \ell v^3 + \frac{\sqrt{2}}{2} g_{jj,0j} \ell v^3 \\ & + \sqrt{2} g_{ij,0i} \ell v^2 + \sqrt{2} g_{ij,0j} \ell v^2) (ell^2/v^2), \quad i, j = 1 \dots 3\end{aligned}$$

which includes four mixed terms not found in the loops aligned with the coordinate axes.

### Conclusion

As we continue and explore more complicated loops in spacetime the computations rapidly increase with complexity to the point where they are very inefficiently done by hand. During the term of the research program, the proper software for handling this type of complicated tensor manipulation was not available. The question of whether enough spacetime loops may be found to generate equations which may be solved for all components of the Riemann tensor remains unanswered at this time.

Figure 1



- [1] Anandan, J.. 1984, "Curvature effects in Interferometry," *Phys. Rev. D* 8, 1615-1624.
- [2] Colella, R., A.W. Overhauser, and S. A. Werner, 1975, "Observation of Gravitationally Induced Quantum Interference," *Phys. Rev. Lett.* 23, 1472-1474.
- [3] Feynmann, R., 1961, *Quantum Electrodynamics* W.A. Benjamin, New York.
- [4] Misner, C., K. Thorne, and J. Wheeler, 1970, *Gravitation*, W. H. Freeman and Co., San Francisco.



**DATA ACQUISITION AND CONTROL OF  
CRYOGENIC COOLERS  
DURING EXTENDED LIFE TESTING**

**Steven E. Griffin, E.I.T.  
Mechanical Engineering  
Division of Engineering**

**University of Texas at San Antonio  
6900 N Loop 1604 West  
San Antonio, TX 78242-0665**

**Final Report for:  
Graduate Summer Research Program  
Phillips Laboratory**

**Sponsored by:  
Air Force Office of Scientific Research  
Bolling Air Force Base, Washington, D.C.**

**and**

**University of Texas at San Antonio**

**Summer 1993**

## Table of Contents

ABSTRACT.....	3
INTRODUCTION.....	4
DISCUSSION OF PROBLEM.....	5
METHODOLOGY.....	6
APPARATUS.....	7
RESULTS.....	10
CONCLUSIONS.....	11
ACKNOWLEDGMENTS.....	11
APPENDIX.....	12
REFERENCES.....	18

DATA ACQUISITION AND CONTROL OF  
CRYOGENIC COOLERS  
DURING EXTENDED LIFE TESTING

Steven E. Griffin  
Mechanical Engineering Graduate Student  
Division of Engineering  
University of Texas at San Antonio

Abstract

The Space Thermal Technologies Branch (PL/VTPT) has undertaken a life performance testing laboratory for cryogenic refrigeration studies and associated efforts. The overall vision includes the development of a state-of-the-art cryogenic refrigeration database to demonstrate reliable and predictable behavior, identify and predict failure modes, and evaluate long term performance changes while making statistical inferences over extended life periods.

To successfully automate initial performance and endurance characterizations of cryogenic coolers, a complete data acquisition and control environment is being designed and evaluated. This capability represents a critically enabling achievement in terms of monitor and control. Using LabVIEW graphical programming for instrumentation, virtual instruments can be developed to completely monitor and control transient response characteristics of long-life coolers during a planned five year study. While acquiring data, the virtual instruments will evaluate and independently control the testing process via standardized instrumentation and cabling.

To date, several successful LabVIEW instruments have been developed and are currently undergoing preliminary testing and monitoring capabilities. Initial data acquisition and control instrumentation includes programs for ultra-low temperature chillers, ion-vacuum turbo pumps, cryogenic sensors, and temperature controllers. The computer emulates these instruments through panels which can be designed to look and function exactly like their "real world" counterparts with two exceptions -- LabVIEW graphics and analysis can be performed in "real time" during testing.

Virtual instruments provide a unique opportunity to completely automate the testing process. Essentially, they provide a graphical icon-based capability to replace existing acquisition instruments and control devices. By using analog to digital I/O boards and accompanying peripherals, LabVIEW is considerably more powerful than any of its acquisition predecessor.

DATA ACQUISITION AND CONTROL OF  
CRYOGENIC COOLERS  
DURING EXTENDED LIFE TESTING

Steven E. Griffin

Introduction

Recent satellite technology, with its solar cells and low temperature electronics, has placed immediate demand for satellite thermal control. The use of heat pipes and phase change materials to remove waste heat has become extremely important, but low temperature applications, such as infrared sensors, need cryogenic coolers which operate anywhere from 10 to 150 K for efficient operation. As a result, satellite thermal endurance tests on cryogenic coolers are needed to characterize long-life performance.

Cryogenic cooler tests provide a challenging task for data acquisition and system control. Using a Macintosh driven software such as LabVIEW (by National Instruments), a direct interface can be developed to completely monitor transient response characteristics of long-life coolers continuously without interruption. While acquiring data, the virtual instruments (VIs) will evaluate, analyze, store, and respond to either a selected data point or an averaging of past data.

The experiment consists of four vacuum chambers ( $\sim 10^{-7}$  torr) connected independently to a chiller system using fluorinert near 300 K. The chambers are completely insulated and reject waste heat through a thermal shunt connecting the chiller loop and cryocooler. Studies will include simulated pulse-load duty cycles and environmental heating. The rejection temperature and waste heat will be monitored and controlled closely to determine both optimum and critical heat loads encountered during satellite earth orbits.

The experimental set-up provides a powerful tool for measuring, monitoring, and controlling the testing process. The benefit from stringent thermal control plays a key role in predicting the durability of cryogenic coolers in space power applications.

### Discussion of Problem

SDIO and the Air Force has tasked Air Force Phillips Laboratory's Space Thermal Technologies Branch with developing cryogenic refrigeration testing and analysis capabilities. The initiative will define and establish a state-of-the-art cryogenic refrigeration database which will be used to demonstrate reliable behavior, identify and predict failure modes, and evaluate cryogenic refrigerators for military and commercial space efforts.

At the present time, all the data regarding specific cryogenic refrigerators remains as privileged information within the company that developed the cooler. By establishing the capability to observe, operate, test, and evaluate a variety of typical cryogenic refrigerators, informed judgments regarding important parameters can be made to improve the operating efficiency, effectiveness, and durability of current and future devices.

To accomplish a cryogenic refrigeration database, a data acquisition system must be developed to completely monitor and control the testing process. Fail-safes must be included to prevent unforeseen, inadvertent, or maintenance shutdown problems.

System failures due to independent devices are unacceptable. The environmental system must be monitored quickly and maintained to provide flexible computer and user interfacing. Initially, all parameters will be set as default values within each instrument and device, but each device should be capable of remote login and control via the computer.

### Methodology

Data acquisition and analysis begins with an understanding of each instrument's role: monitor and/or control. To achieve total system control, an overall system approach has to be developed based on integrating hardware specifications with the computer via cabling and monitor/control interfacing commands. The selection, design, and implementation of all the software requirements must follow a general guideline for each instrument.

- 1) Data requirements -- While the experiment is on the drawing boards, decide what general data requirements (temperature, pressure, etc.) are needed.
- 2) Data acquisition -- Does the experiment require monitoring only, or does it need controlling also?
- 3) Data storage -- Decide what computer will be required for data acquisition and information storage. (i.e. HP, PC, MacIntosh, etc).
- 4) Interfacing compatibility -- The Macintosh doesn't support RS-232 and the PC doesn't support RS-422. But interface convertors for IEEE 488 to RS-232/RS-422 protocol can be obtained for a reasonable price.
- 5) Software requirements -- Several graphics interface programs exists to expedite data acquisition and computer interfacing. Pick one that offers good support and meets user needs.
- 5) Instrument protocol -- Each device supports its own command or communication protocol if it offers computer interfacing (IEEE, RS-232, or RS-422).

Develop a VI that is flexible and capable of concatenating commands strings which will both monitor and control the individual instrument. Later, after all the instruments have been considered, assemble each virtual instrument into a command VI that will operate the testing process through the computer. The process is rather cumbersome, but the end results will improve both research and test capabilities. Eventually, a store house of old virtual instruments can be applied to new experiments because the VI is flexible and can be either used again or modified for a newer version of the instrument.

In the past, several problems have occurred with interfacing. General purpose interface boards (GPIB) offer excellent versatility for most systems. They are extremely common and can be added to most computer systems. The IEEE 488 cabling is extremely durable and well insulated; however, the cables are very expensive ( $\approx$  \$85/2 meters) and limited to less than 5 meters. Regulated standard cabling such as RS-232 and RS-422 can be very long and flexible, but shielding is poor; especially with ribbon cables.

## Apparatus

The cryogenic refrigeration systems were provided by Jet Propulsion Laboratories. Four thermal/vacuum cryocooler test chambers were designed and built to isolate and dampen vibrations of 10 Hz or less by using hydraulic floor mounts and a high stiffness stand. The test stands consists of twenty-four inch diameter bell jar assemblies connected to a central vacuum system which uses a Leybold Inficon turbo vacuum pump. A second system is connected as a standby unit in case of an unforeseen maintenance shutdown of the primary vacuum system (See Fig 1). Other fail-safes are included to prevent system failure and reduce shutdown time.

Each chamber is equipped with an instrument feedthrough collar capable of accommodating electrical and cooling fluid loop systems via a set of eighteen Conflat 1 3/4" feedthroughs. The electrical collars may include thermocouples, silicon diodes, or power sources for the cryocoolers. Two fluid loops are set up to provide independent entrance and exit flows for each cryocooler (see Fig. 2). The chiller loops use Flourinert; a trade name refrigerant. A third chiller system will be available in case of pump failure or maintenance and provide a minimum shutdown period.

The temperature control of each cryocooler is provided either locally by the device or remotely by the computer. For example, the chiller loop is locally controlled by the PID capabilities found in the PTS Ultra Low Single Loop Chiller. The computer only monitors the fluid loop bath temperature and alarms if specific values are exceeded. An Athena AT-16 temperature controller is also used locally. It monitors the chiller loop temperature and actuates a MacMaster-Carr 1500 Watt in-line immersion heater to fine tune individual heat rejection temperatures. Though initially preset values are determined, a complete feedback and control system is expected by using IEEE 488 and Serial RS-232 /RS-422 interfacing to the MacIntosh using LabVIEW software.

LabVIEW is a highly flexible and well maintained software developed and distributed by National Instruments. Although all the work has been done via the MacInstosh, LabVIEW is now available on both the PC and Sun/SPARC workstations. Eventually, virtual instruments will be developed for each device and then compiled into a main operating panel. These complex systems may result in endless loops, information storage problems, or system monitoring difficulties based on priority.

Other instruments include LakeShore Cryogenic scanners, controllers, and sensors which accommodate silicon diodes and provide heater output. Instruments like the FLUKE Hydra and National Instruments AMUX-64T provide accurate readings for analog input signals; however, each device has its own problems which must be addressed.

Two problems encountered with the AMUX-64T data acquisition board were resolved. The first problem was the result of a poorly shielded ribbon cable. Noise from power supplies and other electrical devices strongly affects low voltage signals. By using signal conditioning, wrapping aluminum foil around the ribbon cable, or purchasing a shielded cable, significant improvements can be made. The second problem resulted from applying a differential mode to thermocouple connections. Procedure II of the AMUX User's Manual describes how to use the board, but does not provide the means to do it. The procedure follows:

- 1) Read and scale the cold-junction compensation voltage in differential mode (i.e. read Ch 0). The compensation voltage is then multiplied by 100 to provide the temperature in Celsius. (i.e. 0.25 V = 25°C).
- 2) Read and Scale the offset thermocouple voltage of a specific channel. For example, Ch 1 may use a type T Thermocouple and give a reading of 7.718 mV.
- 3) Convert the cold junction temperature into a corresponding type T voltage. This is either done through look-up tables or taking the inverse of the NBS polynomials provided by National Instruments. A look-up table shows 25°C corresponds to 0.789 mV for a type T thermocouple.
- 4) Add step 2 and 3 to get a differential thermocouple voltage and convert the voltage into a corresponding type T thermocouple temperature. For example,  $0.789 + 7.718 = 8.507$ , which corresponds to 185.2°C.

One might consider step 3 completely unrealistic because, data acquisition should be continuous and uninterrupted monitor and control. If one is forced to use look-up tables every time they are needed to convert the cold junction temperature into a corresponding thermocouple voltage, then testing is interrupted. Furthermore, taking an inverse of a 9<sup>th</sup> order polynomial, as is the case for E and S-type thermocouples, is an impossible task.

Step 3 was solved by first plotting  $T = f(v)$  using the NBS polynomial coefficients in the following equation.

$$T = a_0 + x(a_1 + x(a_2 + x(a_3 + xa_4)))$$



Afterwards, the information was exported from a spreadsheet and imported into a graphics and analysis package such as AXUM. The plots along with the coefficients for each thermocouple type were reevaluated as  $v = f(T)$ . New coefficients were then generated and printed with the graph. The results gave exceptional approximations to the standard equations and are provided in the Appendix.

The goal to achieve a continuous, self-contained data acquisition system is quite challenging. Since little details work to impede the progress of on-going experiments, project and experiment timelines maybe pushed back.

Planned testing begins in December and will continue through the destructive stage of life-long testing. The goal for each chiller is to apply expected and harsh duty cycles to determine durability, performance, and failure modes. Some of the coolers which will be received are included in Table 1.

**Table 1. Cryogenic Test Articles**

Company	Temp	Power	Description
Hughes	65 K	2 Watt	"Split" Stirling Cycle - Compression/Expander
Creare	65 K	2 Watt	Integral Stirling - Diaphragm Actuated
Creare	65 K	5 Watt	Reverse Brayton Cycle - SSSF
Creare	35 K	300 W	Compressor: 2 Stage Stirling
Boll Aero	35 K	300 W	2 Stage Stirling
Boll Aero	----	-----	Multistage, Closed Cycle, Joule-Thompson Refrig.
TRW	35 K	-----	Stirling "Pulse Tube" - 20cc Displ. Compressor
TRW	150	1 W	Integral Stirling

## Results

Although actual experimentation has not begun, a trial investigation was assembled to simulate a cryogenic refrigeration control system. The test included an FTS Chiller, a 1000 Watt in-line heater, an Athena AT-16 Temperature Controller, FLUKE Hydra and AMUX-64T acquisition units, and a heat sink to feign waste heat removal from a cryogenic cooler. Individual virtual instruments were created to operate each device and then connected to monitor and control the test's outcome.

The heat sink was controlled manually with a voltage variac that applies power input across a known electrical resistance wire. The wire, along with a variable inlet valve, was used to adjust the flow rate and the exit temperature. The heat sink's exit temperature was fine tuned by the in-line heater which was monitored and controlled by the Athena temperature controller.

The entire virtual instrument system was integrated along with the hardware to provide valid results specific to the test article. No results are shown in this paper because they are specific to the testing needs of the simulation and not the actual cryogenic cooler experiments. However, by looking at the Figure 2, in the appendix, one can see how the hardware and software requirements were integrated to provide good chamber evaluation capabilities.

### Conclusion

Developing a cryogenic refrigeration database for SDIO and associated users requires extensive planning and long term testing to provide experimental and statistical inferences. The programming and data acquisition requisites have been generally described and should help demonstrate the basic conditions needed to begin new tests.

LabVIEW Graphical Programming for Instrumentation, developed and distributed by National Instruments, is extremely versatile. As a data acquisition tool, it is well maintained and provides easy hardware/software interfacing. Although, other data acquisition software exists, LabVIEW's virtual instruments can be designed and connected much easier than previous packages.

### Acknowledgements

Special thanks to Air Force Phillips Laboratory's Space Thermal Technologies Branch. They are developing a top-notch facility and providing the necessary support needed to complete the task.

## Appendices

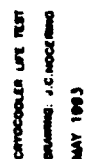
FIGURE 1. Turbo Pump Assembly.

FIGURE 2. Cryogenic Chamber Assembly w/Instrument Allocation

FIGURE 3. Type E and J Thermocouple Curves  $\rightarrow v = f(T)$

FIGURE 4. TYPE K and R Thermocouple Curves  $\rightarrow v = f(T)$

FIGURE 5. TYPE S and T Thermocouple Curves  $\rightarrow v = f(T)$



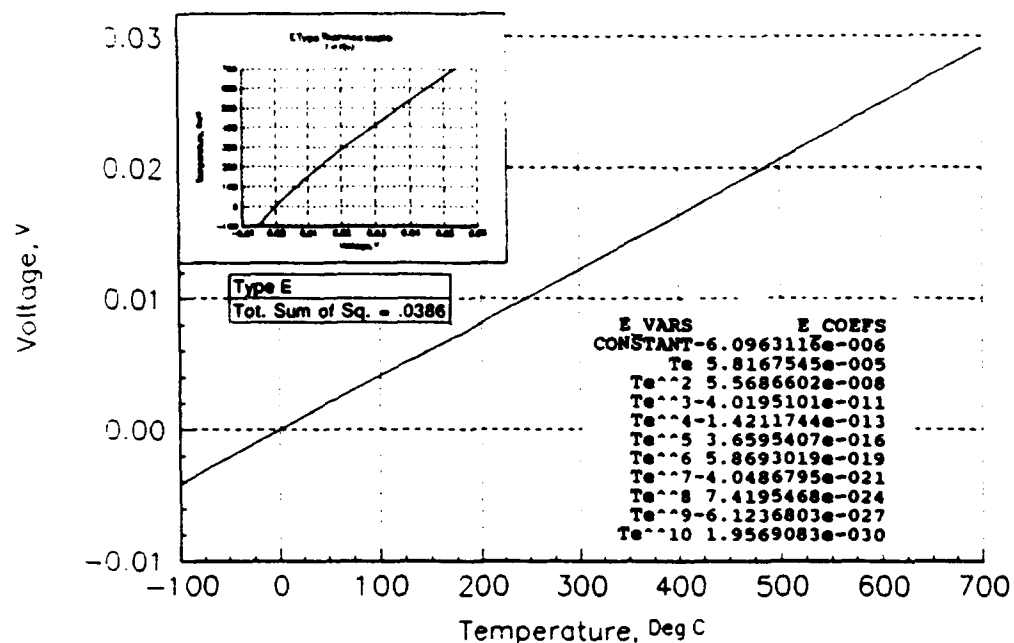
**16-13**



**DONOR JUDITH A. JOHNSON**

FIGURE 3. Type E and J Thermocouple Curves  $\rightarrow v = f(t)$

E Type Thermocouple  
 $v = f(T)$



J Type Thermocouple  
 $v = f(T)$

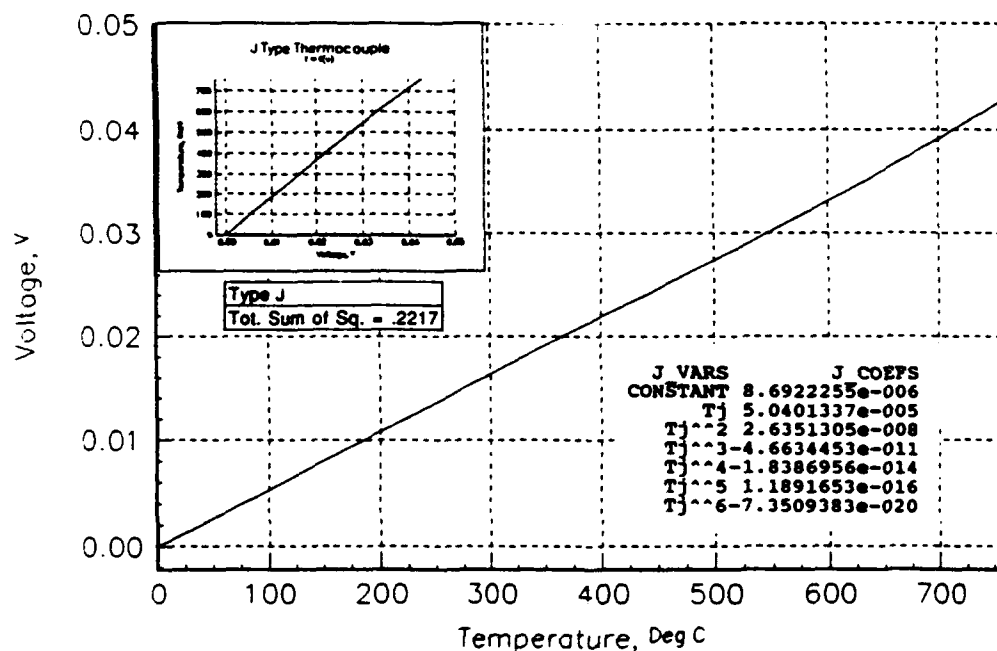
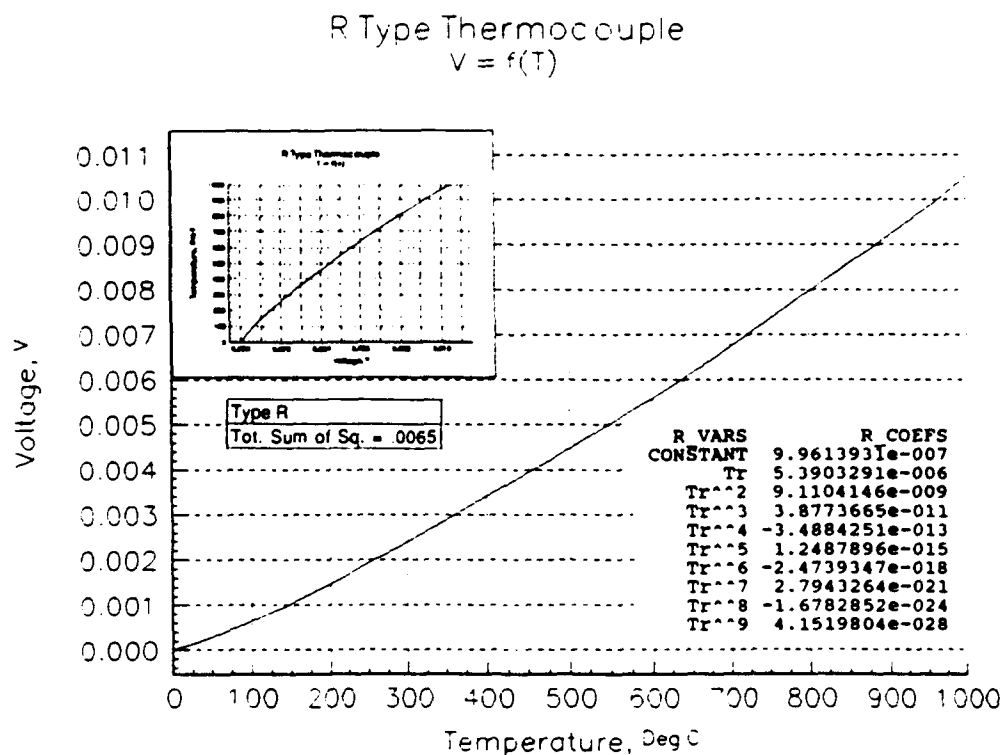
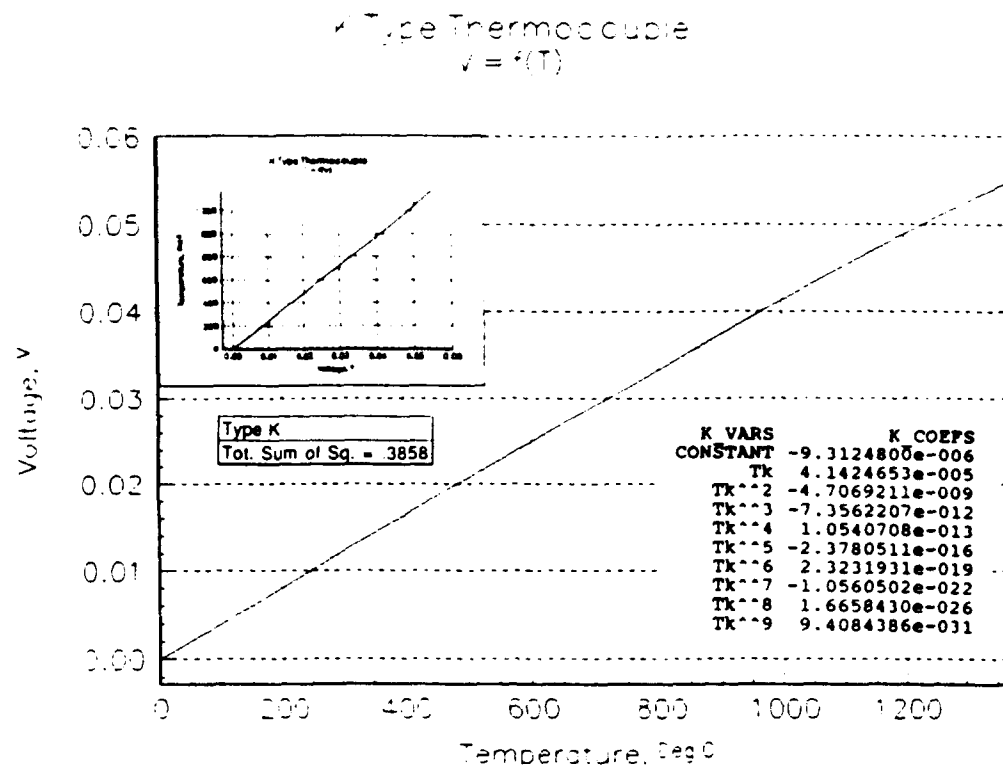
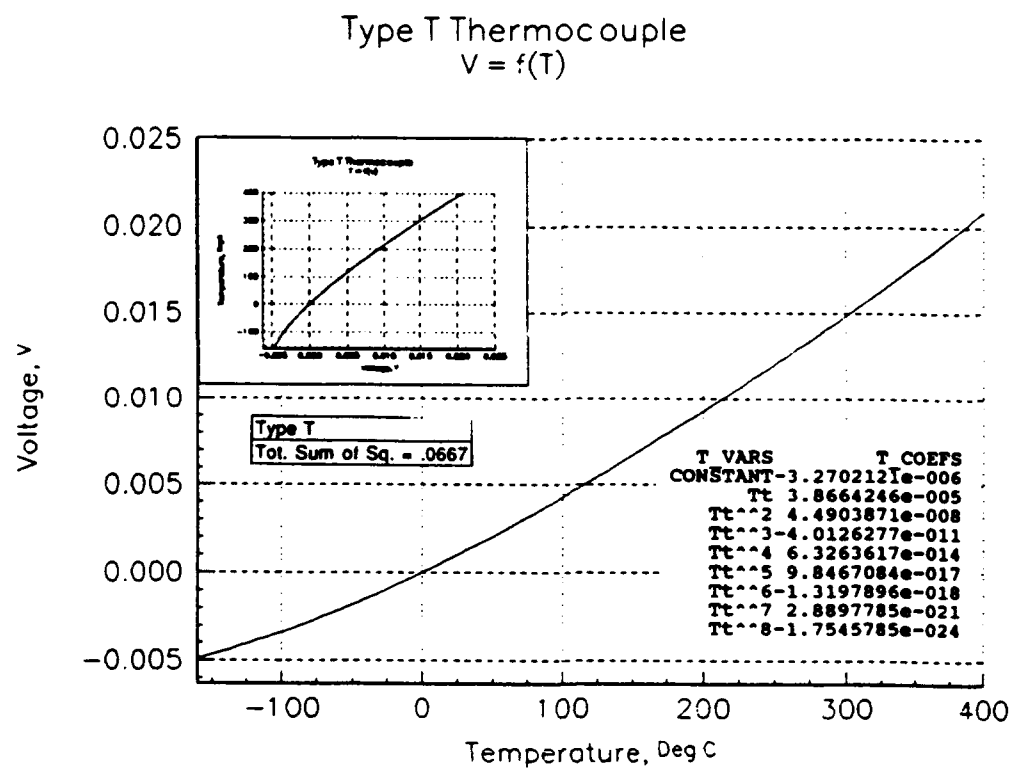
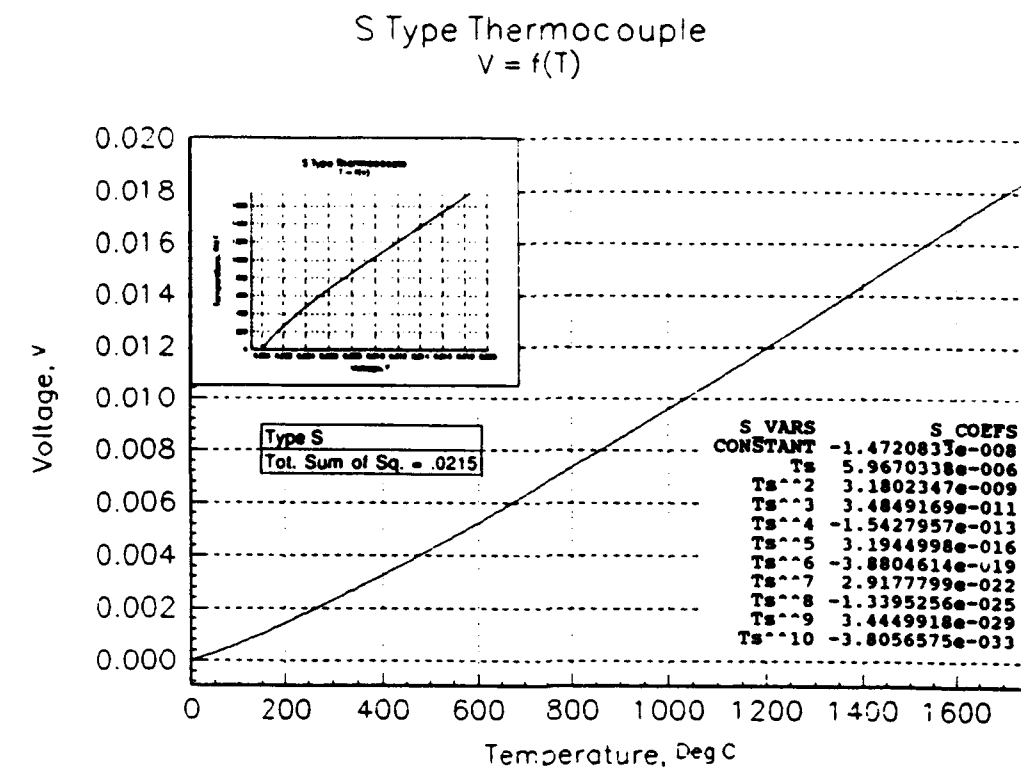


FIGURE 4. Type K and R Thermocouple Curves  $\rightarrow v = f(T)$





**Figure 5. Type S and T Thermocouple Curves  $\rightarrow v = f(T)$**



### References

- [1] National Instruments. "LabVIEW Training Manuals - Basics and Advanced". Austin, TX. 1992.
- [2] National Instruments. *LabVIEW User's Manual*. Ver 2.1. Austin, TX. 1992.
- [3] Thomas, Pete. "Cryogenic Refrigerator Systems Test Plan - Space Thermal Technologies Branch". DRAFT - Kirtland AFB, NM. 1992.

**THERMAL MODELING OF BEAM HEATING OF A  
CRYSTALLINE SOLID**

**Jonathan Stohs  
Graduate Student  
Dept. of Physics  
University of New Mexico  
Albuquerque, New Mexico**

**Final Report for:  
Summer Research Program  
Phillips Laboratory  
Kirtland Air Force Base  
Albuquerque, New Mexico**

**Sponsored by:  
Air Force Office of Scientific Research  
Bolling Air Force Base, Washington, D.C.**

**September, 1993**

## **Thermal Modeling of Beam Heating of Solids**

**Jonathan Stohs**  
Graduate student in the physics department at  
The University of New Mexico

### **Abstract**

Two methods for calculating the temperature rise in a crystalline (thermally isotropic) solid due to heating from a laser beam or other kind of beam, such as electrons or protons, are discussed. The first method uses an equation that is evaluated numerically. The second method described is the modeling of the solid and the way it is heated using the finite element code ANSYS. Tables and graphs are presented, and the two methods are compared regarding their advantages and disadvantages. The models may be effective in helping to determine the heating effects of radiation on crystals used in electronic, optical, and acousto-optic devices.

## INTRODUCTION

In the space environment experienced by satellites and the space shuttle, electronic and optical devices are exposed to radiation such as electrons, protons, and gamma rays. At the present time experiments are being carried out in a laboratory setting on acousto-optic devices in order to evaluate how their performance is affected by exposure to radiation. Here these acousto-optic devices are exposed to beams of electrons, protons, neutrons, or gamma rays in order to simulate what they may experience in space. The Photonics Research Group of the Directorate of Space and Missiles Technology at the Phillips Laboratory at Kirtland Air Force Base in Albuquerque, New Mexico finds that one of the most important influences upon the operation of these devices is the heat generated when they absorb radiation [1]. It was desired that a theoretical model of the heating of the crystal in a device be developed. That is, the temperatures at various points in the crystal were to be found.

## DISCUSSION AND ANALYSIS

The heating of a crystal by a beam of radiation was approximated at first by a CO<sub>2</sub> laser directed at it. Then the theory of laser heating of solids was applied.

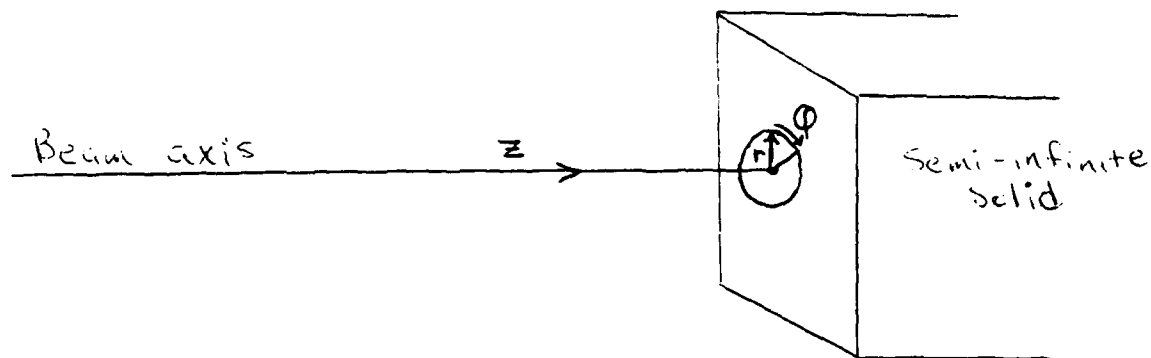
In the early 1970s aspects of the theory of laser heating of solids were worked out in order to help determine techniques for the drilling and welding of metals using high-power CO<sub>2</sub> lasers. The situations encountered involved large temperature changes in the materials. In the case considered here only small temperature increases (5-20 Kel) were of interest. However, the general theory of heating applies without difficulty.

In his book CO<sub>2</sub> Lasers, Effects and Applications [2], W.W. Duley gives an equation for the temperature in a semi-infinite solid upon which a CO<sub>2</sub> laser is directed:

$$T(r, z, t) = \frac{P \epsilon}{2\pi A k} \int_0^{\infty} J_0(\lambda r) J_1(\lambda A) \left\{ e^{-\lambda z} \operatorname{erfc} \left[ \frac{z}{2\sqrt{k t}} - \lambda \sqrt{k t} \right] - e^{-\lambda z} \operatorname{erfc} \left[ \frac{z}{2\sqrt{k t}} + \lambda \sqrt{k t} \right] \right\} \frac{d\lambda}{\lambda} \quad (1)$$

$P$  is the power of the beam (Watts);  $\epsilon$  is the fraction of energy absorbed from the beam ( $\epsilon = \text{absorbed energy/incident energy}$ );  $A$  is the beam radius (cm);  $K$  is the thermal conductivity of the material (Watts/(cm\*Kel)); and  $\kappa$  is the thermal diffusivity ( $\kappa = K/(\rho \cdot c)$  where  $\rho$  is the density of the material, and  $c$  is its specific heat.  $J_0$  and  $J_1$  are Bessel functions, and  $\text{erfc}$  is the complimentary error function.  $\epsilon$  was taken to be 1 here.

The coordinate system is cylindrical with coordinates  $r, \phi, z$ . The surface of the solid is at  $z = 0$ . Since the material is semi-infinite, it occupies all space for  $z > 0$ . The laser beam shines from some point on the negative  $z$  axis and hits the surface at  $z = 0$ . The center of the beam at the surface is then at the origin,  $r = z = 0$ :



There is cylindrical symmetry so the temperature has no dependence on  $\phi$ .

The equation originally comes from Carslaw and Jaeger [3] and describes the temperature in the solid as a function of position ( $r$  and  $z$ ) and time for a circular heat source on the surface. It is assumed that the heat is generated at the surface in the circular area of the beam. The temperature can be calculated numerically for any given  $r, z$ , and  $t$ .

The numerical evaluation of this equation entails calculation of special functions and numerical integration. Routines for doing this are available within the mathematical software libraries of the computer, but the user doesn't know how long these routines are, how long they

might take to run when called, or how they actually work. Therefore, it was determined to get routines from the literature and incorporate them into a program that would evaluate this equation.

A good numerical integration routine may be able to handle satisfactorily the integration in equation (1), but it may be helpful to consider special cases such as  $r = 0$  and  $z = 0$ , in which the equation takes different forms. These forms may be easier to work with. Details of the special cases and the equations involved can be found in Appendix A.

The routines for calculating  $J_0$ ,  $J_1$ ,  $\text{erfc}$ , and the Gaussian quadrature routine for carrying out the numerical integration were taken from Numerical Recipes by W.H. Press et al. [4]. Double precision was used throughout. The integration routine originally evaluated the integrand at 10 points. It was enhanced by increasing the number of points to 96 according to Abramowitz and Stegun, Table 25.4 [5].

All programming was done on an IBM RS6000. The results of the program, the temperatures according to position, are shown in Appendix B.

Duley also gives an equation for the temperature in a semi-infinite solid for a Gaussian beam in which the intensity falls off as  $\exp(-r^2/d^2)$  [6] and [7]:

$$\frac{\epsilon I d^2}{\rho C \sqrt{\pi} k} \int_0^t \exp \left[ \frac{-z^2}{4k(t-t')} - \frac{r^2}{4k(t-t') + d^2} \right] \frac{dt'}{\sqrt{t-t'} [4k(t-t') + d^2]} \quad (2)$$

Here  $d$  is the Gaussian beam radius,  $\rho$  is the density of the material, and  $I$  is the intensity of the beam at its center. The results for this case are shown in Appendix C. They are very similar to those for a circular beam but, of course, the temperatures are slightly lower because the intensity of the Gaussian beam decreases from the center, whereas the intensity for the circular beam is uniform over the entire circle. The intensity at the center of the Gaussian beam equals that of the circular beam but is less everywhere else.

Obviously, a crystal in an acousto-optic device is not semi-infinite. For this reason another

computer model was developed using the finite element system called ANSYS [8]. With ANSYS a three-dimensional system of points (called nodes) is set up in a coordinate system, in this case, cartesian. Then, using ANSYS commands, the node system is filled with square elements (like bricks) so that the corners of the bricks are the nodes. A crystalline block thus becomes layers of small bricks. The elements and nodes match the size and shape of the crystal. By carefully setting up a system of nodes, a variety of crystal shapes can be modeled. Here a simple rectangular block was set up.

Again using the ANSYS commands a group of nodes on a surface of the crystalline block was chosen so that the nodes were approximately within a circular area. These nodes were specified to have heat flowing into them. This represents a laser beam hitting the surface and heating it up. Now if not told otherwise, the computer assumes the block of bricks to be perfectly insulated. So some sort of heat sink must be included or else the solid would heat up without bound. A heat sink was modeled by determining all the nodes on the surface opposite the heat input to be fixed at a temperature of zero. This approximately matches the actual device configuration in which the crystal is attached by one surface to a metal heat sink.

The computer then went through its calculations and solved for the temperature at each node. A steady state situation was modeled in which the temperatures at the nodes were those reached after a long period of time. With ANSYS, analysis of transient, that is, time-dependent cases is also possible.

The graphs in Appendix D show the temperature along a path through the crystal. Since the temperature at every node has been calculated and stored in the computer, any path through the crystal may be chosen along which to plot the temperature.

The following table compares temperatures calculated with ANSYS to those found using the analytic model for a circular laser beam. The time used in the analytic model calculation was taken to be long enough so that a steady state situation was achieved. In the ANSYS model the surface hit by the beam is at  $z = 0$  and the heat sink is on the surface  $z = 1.0$  cm.



Table I

Temperature rise along z axis ( $r = 0$ ):

z (cm)	Temp rise	
	Analytic model	ANSYS model
0.0	18.3	17.9
0.1	11.0	10.9
0.2	7.11	7.19
0.3	4.98	4.96
0.4	3.71	3.59
0.5	2.89	2.63
0.6	2.31	1.92
0.7	1.89	1.35
0.8	1.57	0.858
0.9	1.32	0.418
1.0	1.12	0.00

One can see that the temperatures are similar, except that when getting close to the heat sink ( $z = 1$ ) the temperatures decrease faster in the ANSYS case.

One last note: the discussion here has referred to laser heating of solids. Actually the models only know that there is a circular heat source at the surface. It could be caused by anything, any kind of beam. Also, if one wished to know the temperatures in the crystal for heat generated inside instead of at the surface, for example, if the crystal absorbs energy from the beam as it passes through, ANSYS would be the system to use.

## CONCLUSION

The discussion here has been about two methods for thermal modeling of beam heating of solids: an analytic method and the ANSYS finite element method. Both yield similar results. The analytic method works well when the beam is small compared to the crystal dimensions and when the temperatures desired are not too close to a surface of the crystal (other than the surface hit by the beam). Under these circumstances the actual situation resembles the case of the semi-infinite solid.

For other cases ANSYS gives better results. ANSYS is more versatile because one can construct node and element systems that correspond closely to actual crystal shapes. It can handle crystal shapes where one surface may not be perpendicular to another. It also can take into account the presence of a heat sink on one surface, or part of a surface, various positions of the beam upon the impacted surface, and absorption of heat inside the material rather than on the surface. This comes at the price of time to construct the node and element model and time for the computer to go through its calculations. The model described above took a Cray-2 about three minutes of CPU time to calculate the temperatures. So for quick, general results the analytic model is probably better, but ANSYS will be appropriate for more accurate analyses of special configurations.

#### ACKNOWLEDGMENTS

Special thanks to Edward Taylor for directing the project, Dr. Mike Kelly for helpful discussions, Dr. Ernie Paxson for consultation regarding ANSYS, Andrew Fant for general computer advisement, and Tony Sanchez for direction of funding for computer accounts.

## APPENDIX A

The general temperature equation is again:

$$T(c, z, t) = \frac{P\varepsilon}{2\pi AK} \int_0^\infty J_0(\lambda r) J_1(\lambda A) \left\{ e^{-\lambda z} \operatorname{erfc}\left[\frac{z}{2\sqrt{kt}} - \lambda\sqrt{kt}\right] - e^{-\lambda z} \operatorname{erfc}\left[\frac{z}{2\sqrt{kt}} + \lambda\sqrt{kt}\right] \right\} \frac{d\lambda}{\lambda} \quad (\text{A-1})$$

According to Duley [9], if  $r = 0$  then

$$T(c, z, t) = \frac{2P\varepsilon\sqrt{kt}}{\pi A^2 K} \left[ \operatorname{ierfc}\left(\frac{z}{2\sqrt{kt}}\right) - \operatorname{ierfc}\left(\frac{\sqrt{z^2 + A^2}}{2\sqrt{kt}}\right) \right] \quad (\text{A-2})$$

where  $\operatorname{ierfc}(x) = \int_x^\infty \operatorname{erfc}(y) dy$

which is a repeated integral of the complimentary error function. Using Abramowitz and Stegun, section 7.2.5 [10] equation (A-2) can be worked out to become:

$$T(c, z, t) = \frac{2P\varepsilon\sqrt{kt}}{\pi A^2 K} \left[ (-v) \operatorname{erfc}(v) + \frac{1}{\sqrt{\pi}} \exp(-v^2) + (w) \operatorname{erfc}(w) - \frac{1}{\sqrt{\pi}} \exp(-w^2) \right] \quad (\text{A-3})$$

where  $v = \frac{z}{2\sqrt{kt}}$

and  $w = \frac{\sqrt{z^2 + A^2}}{2\sqrt{kt}}$

## APPENDIX A

Now if  $r \neq 0$  and  $z = 0$  equation (A-1) works out to:

$$T(r, 0, t) = \frac{PE}{2\pi AK} \int_0^{\infty} J_0(\lambda r) J_1(\lambda A) \left\{ \operatorname{erfc}(-\lambda \sqrt{k t}) - \operatorname{erfc}(\lambda \sqrt{k t}) \right\} \frac{d\lambda}{\lambda} \quad (\text{A-4})$$

By using the properties

$$\operatorname{erfc}(-x) = 1 - \operatorname{erf}(-x)$$

and

$$\operatorname{erfc}(x) = 1 - \operatorname{erf}(x)$$

(A-4) yields:

$$T(r, 0, t) = \frac{PE}{\pi AK} \int_0^{\infty} J_0(\lambda r) J_1(\lambda A) [1 - \operatorname{erfc}(\lambda \sqrt{k t})] \frac{d\lambda}{\lambda} \quad (\text{A-5})$$

The first term of the integrand may be evaluated in terms of complete elliptic integrals (see [11] and [12]), and a book that has good routines for calculating these functions is Computer Approximations by J.F. Hart et al. [13].

# APPENDIX B

## CIRCULAR BEAM

File: circ60

Data for lead molybdate:

thercon = .0150 Watt/(cm\*Kel)  
 density = 6.9500 gm/cm^3  
 sp. ht. = .0719 joul/(gm\*Kel)  
 power = .1800 Watt  
 eps = 1.0000 (absorbed energy)/(incident energy)  
 beam radius = .2000 cm  
 time = 60.0000 sec

\*\*\*\*\*  
 \*\*\*\*\*

z = .0000 cm

r (cm)	temp rise (Kel)
.0000	18.2964
.1000	15.6201
.2000	11.3579
.3000	1.6448

\*\*\*\*\*  
 \*\*\*\*\*

z = .1000 cm

r (cm)	temp rise (Kel)
.0000	11.0018
.1000	10.1509
.2000	7.8211
.3000	5.4499
.4000	3.9536
.5000	3.0193
.6000	2.3914

\*\*\*\*\*  
 \*\*\*\*\*

z = .2000 cm

r (cm)	temp rise (Kel)
.0000	7.1102
.1000	6.7037
.2000	5.6715
.3000	4.4897
.4000	3.5133
.5000	2.7901
.6000	2.2587
.7000	1.8598
.8000	1.5526

\*\*\*\*\*  
 \*\*\*\*\*

z = .3000 cm

r (cm)	temp rise (Kel)
.0000	4.9838
.1000	4.7875
.2000	4.2769
.3000	3.6330
.4000	3.0155
.5000	2.4937
.6000	2.0733
.7000	1.7380
.8000	1.4690
.9000	1.2510
1.0000	1.0721

# APPENDIX B

\*\*\*\*\*  
\*\*\*\*\*

z = .4000 cm

r (cm)	temp rise (Kel)
-----	
.0000	3.7123
.1000	3.6088
.2000	3.3306
.3000	2.9541
.4000	2.5568
.5000	2.1877
.6000	1.8664
.7000	1.5946
.8000	1.3670
.9000	1.1765
1.0000	1.0165
1.1000	.8814
1.2000	.7665

\*\*\*\*\*  
\*\*\*\*\*

z = .5000 cm

r (cm)	temp rise (Kel)
-----	
.0000	2.8851
.1000	2.8256
.2000	2.6613
.3000	2.4276
.4000	2.1644
.5000	1.9026
.6000	1.6600
.7000	1.4441
.8000	1.2557
.9000	1.0929
1.0000	.9527
1.1000	.8320
1.2000	.7278
1.3000	.6376
1.4000	.5593

# APPENDIX C

## GAUSSIAN BEAM

File: gaus60

Data for lead molybdate:

```
thercon      = .0150 Watt/(cm*Kel)
density      = 6.9500 gm/cm^3
sp. ht.      = .0719 joul/(gm*Kel)
power        = .1800 Watt
eps          = 1.0000 (absorbed energy)/(incident energy)
beam radius  = .2000 cm
time         = 60.0000 sec
```

\*\*\*\*\*  
\*\*\*\*\*

z = .0000 cm

r (cm)	temp rise (Kel)
.0000	15.4704
.1000	13.6853
.2000	9.8777
.3000	6.5094
.4000	4.4143
.5000	3.2251
.6000	2.4985
.7000	2.0067
.8000	1.6493
.9000	1.3774
1.0000	1.1639

\*\*\*\*\*  
\*\*\*\*\*

z = .1000 cm

r (cm)	temp rise (Kel)
.0000	9.6301
.1000	8.9149
.2000	7.2339
.3000	5.4492
.4000	4.0560
.5000	3.0946
.6000	2.4383
.7000	1.9728
.8000	1.6280
.9000	1.3631
1.0000	1.1538

\*\*\*\*\*  
\*\*\*\*\*

z = .2000 cm

r (cm)	temp rise (Kel)
.0000	6.4374
.1000	6.1255
.2000	5.3383
.3000	4.3870
.4000	3.5159
.5000	2.8176
.6000	2.2850
.7000	1.8804
.8000	1.5681
.9000	1.3221
1.0000	1.1246

# APPENDIX C

\*\*\*\*\*  
\*\*\*\*\*

z = .3000 cm

r (cm)	temp rise (Kel)
.0000	4.6449
.1000	4.4893
.2000	4.0778
.3000	3.5363
.4000	2.9848
.5000	2.4929
.6000	2.0825
.7000	1.7489
.8000	1.4790
.9000	1.2595
1.0000	1.0792

\*\*\*\*\*  
\*\*\*\*\*

z = .4000 cm

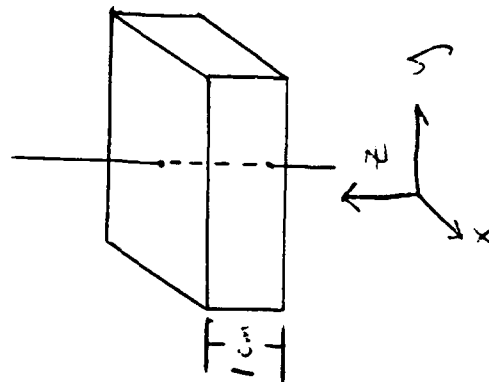
r (cm)	temp rise (Kel)
.0000	3.5272
.1000	3.4412
.2000	3.2065
.3000	2.8793
.4000	2.5205
.5000	2.1747
.6000	1.8650
.7000	1.5981
.8000	1.3722
.9000	1.1819
1.0000	1.0215

\*\*\*\*\*  
\*\*\*\*\*

z = .5000 cm

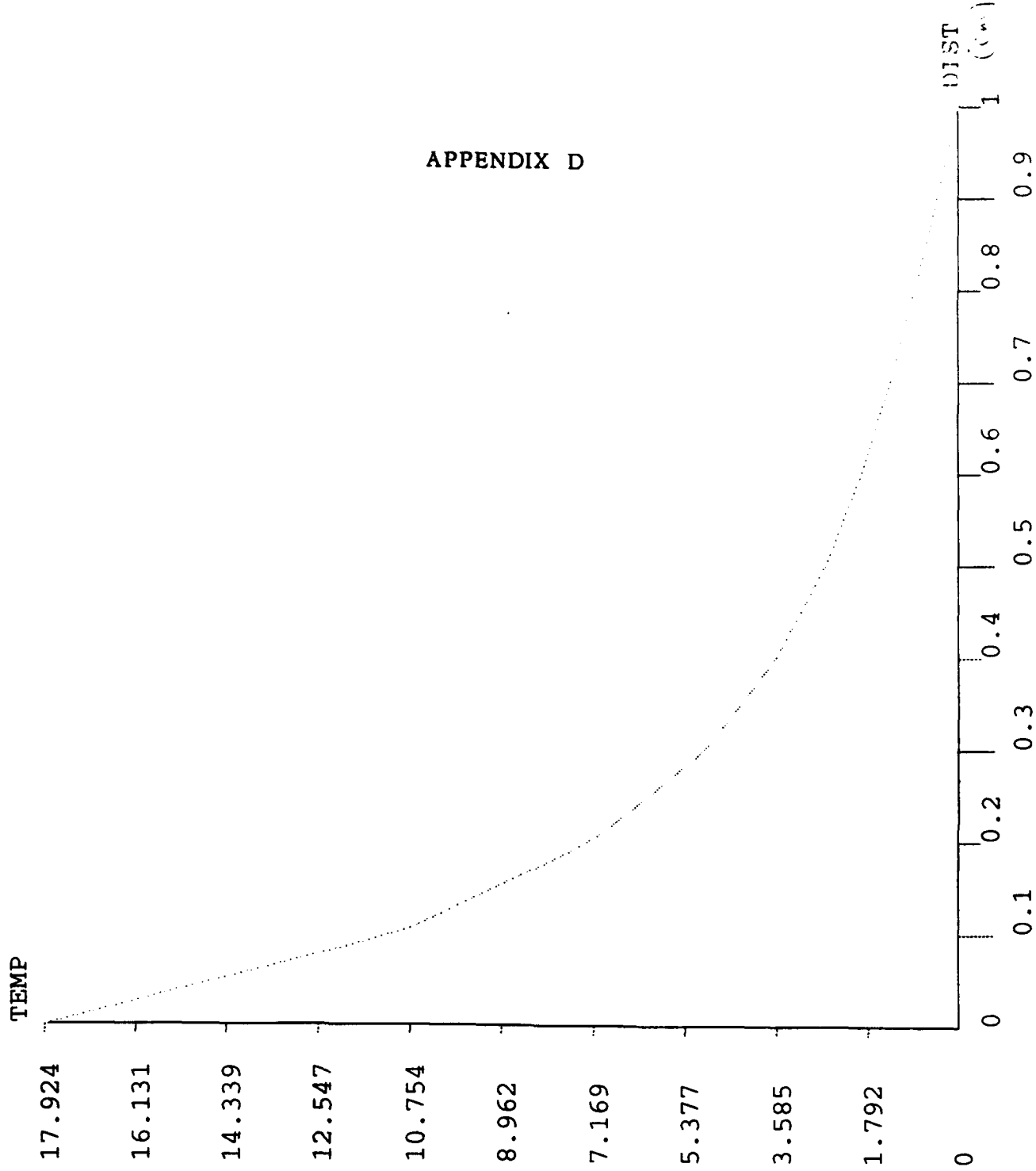
r (cm)	temp rise (Kel)
.0000	2.7758
.1000	2.7243
.2000	2.5808
.3000	2.3724
.4000	2.1316
.5000	1.8859
.6000	1.6533
.7000	1.4428
.8000	1.2572
.9000	1.0956
1.0000	.9558



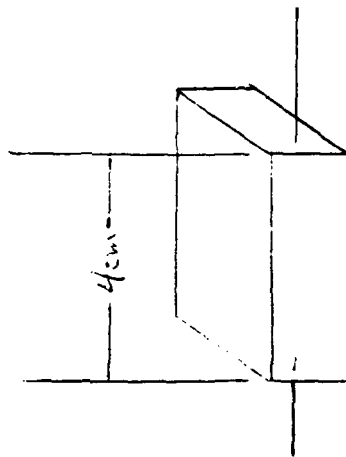


Path is along the z axis of  
of the heating beam.

## APPENDIX D



crystal heated by laser



Path is 5mm from front face. Heating beam is centered on bottom face.

# APPENDIX D

TEMP

1.756

1.607

1.457

1.308

1.159

1.009

0.860148

0.71085

0.561553

0.412256

0.262958

DIST (C)

4

3.6

3.2

2.8

2.4

2

1.6

1.2

0.8

0.4

0

crystal heated by laser

## **REFERENCES**

- [1] E.W. Taylor, A.D. Sanchez, and S.A. DeWalt, Radiation Induced Effects in Acoustooptic Devices, SPIE vol. 1784, Sept. 1992.
- [2] W.W. Duley, CO<sub>2</sub> Lasers, Effects and Applications, Academic Press, New York, 1976, chapter 4, section 5.1, equation (33), p. 144.
- [3] H. S. Carslaw and J. C. Jaeger, Conduction of Heat in Solids, 2nd ed., Oxford University Press, Oxford, 1959, chapter 10, section 5, equation (4), p. 264.
- [4] W. H. Press, B. P. Flannery, S. A. Teukolsky, and W. T. Vetterling, Numerical Recipes, The Art of Scientific Computing, Cambridge University Press, Cambridge, 1986, chapter 4, section 5, p. 122, routine QGAUS, and chapter 6, section 2, p. 164, routine ERFCC, and section 4, pp. 172-174, routines BESSJO and BESSJ1.
- [5] M. Abramowitz and I. Stegun ed., Handbook of Mathematical Functions, Dover, New York, 1965, p. 919.
- [6] Duley, chapter 4, section 6, equations (46) and (50), pp. 159-150.
- [7] Carslaw and Jaeger, chapter 10, section 3, equation (7), p. 260.
- [8] ANSYS Engineering Analysis System, Revision 4.4, Swanson Analysis Systems, Inc., P. O. Box 65, Houston, Pennsylvania, 15342, 1989.
- [9] Duley, chapter 4, section 5, equation (34), p. 144.
- [10] Abramowitz and Stegun, p. 299.
- [11] G. N. Watson, A Treatise on the Theory of Bessel Functions, 2nd ed., Cambridge University Press, Cambridge, 1966, chapter 13, section 4, equation (2), p. 401.
- [12] W. Magnus, F. Oberhettinger, and R. P. Soni, Formulas and Theorems for the Special Functions of Mathematical Physics, 3rd ed. Springer-Verlag, New York, 1966, chapter 2, section 5, p. 54, and chapter 10, section 1, p. 366.
- [13] J. F. Hart, E. W. Cheney, C. L. Lawson, H. J. Maehly, C. K. Mesztenyi, J. R. Rice, H. G. Thacher, Jr., and C. Witzgall, Computer Approximations, John Wiley and Sons, New York, 1968, chapter 6, section 9, pp. 150-154, and routines ELLPE 7308, p. 337, and ELLPK 7408, p. 339.

MATRIX ELEMENT COMPUTATION USING RECTANGULAR  
PATCH FIELD COMPUTATION FOR ELECTROMAGNETIC  
SCATTERING FROM BODIES OF REVOLUTION

Charles T. Widener  
Department of Electrical and Computer Engineering

Syracuse University  
121 Link Hall  
Syracuse, NY 13244-1240

Final Report for:  
Graduate Student Research Program  
Phillips Laboratory

Sponsored by;  
Air Force Office of Scientific Research  
Bolling Air Force Base, Washington, D.C.

August 1993

MATRIX ELEMENT COMPUTATION USING RECTANGULAR  
PATCH FIELD COMPUTATION FOR ELECTROMAGNETIC  
SCATTERING FROM BODIES OF REVOLUTION

Charles T. Widener  
Department of Electrical and Computer Engineering  
Syracuse University

Abstract

Computation of the matrix elements for a method of moments solution to the electric field formulation of electromagnetic scattering from bodies of revolution using rectangular field patch computation is investigated. The rectangular patch method uses a series summation to calculate the electric field due to a small, uniform amplitude, rectangular patch of surface current. Typically, computations of this type have used delta function approximations to ease the computational burden and reduce computer solution time. While the rectangular patch field method is computationally slower and more cumbersome, its use relieves other problems associated with a delta function current approximation.

MATRIX ELEMENT COMPUTATION USING RECTANGULAR  
PATCH FIELD COMPUTATION FOR ELECTROMAGNETIC  
SCATTERING FROM BODIES OF REVOLUTION

Charles T. Widener

I. Introduction

In this report the problem of electromagnetic scattering from a body of revolution (BOR) excited by an incident plane wave is reviewed. In particular only scattering in the resonance region is considered. In scattering problems the resonance region is identified by the condition that the dimensions of the body are on the order of the incident wavelength  $\lambda$ . In this region the echo area of the body oscillates as the ratio of the mean radius  $a$  to the wavelength  $\lambda$  is varied, finally converging to the physical optics solution as the dimensions of the body becomes much greater than the incident wavelength.

It is also assumed that the method of moments will be used to solve the field equations resulting from the application of boundary conditions to the surface of the body. Method of moment solutions have the distinct advantage of being able to yield solutions for BORs of arbitrary shape illuminated by plane waves of arbitrary relative orientation.

As a further specialization, only perfectly conducting bodies will be considered. This specialization is hardly restrictive as the scattering problem for dielectric and/or magnetic media have forms which are similar to that of perfectly conducting bodies.

Once the main ideas of BOR scattering problems have been highlighted, the more basic problem of calculating the matrix elements is discussed. These calculations are at the heart of the BOR scattering problems and they represent the majority of the computation. The essence of these elements is the integration of the product of a current on one part of the body with the electric field due to a current on another part of the body. The method discussed here requires the approximation of the surface by rectangular patches, each with its own current distribution (assumed uniform). The electric field from any patch can then be evaluated at any point on the body. The utility of this method is

that it relieves the problem of integrating across singularities introduced by certain approximation techniques. This same feature has promise for the analysis of scattering by chiral bodies, which is complicated by the addition of a  $\nabla \times \nabla$  term in the wave equation.

## II. Problem Statement

The problem is to find the far scattered field from a perfectly conducting body of revolution illuminated by an incident plane wave. A body of revolution is formed when a two dimensional curve (called the generating curve) is swung around an axis to form a closed surface,  $S$ . Common examples of BORs include spheres, cones, cylinders, and ellipsoids. A typical BOR is shown in Fig. 1. Because of the axial symmetry it is natural to use cylindrical coordinates  $\rho$ ,  $\phi$ ,  $z$  when describing the geometry of the surface. However since it is necessary to define functional quantities on the surface and take surface integrals thereof it is also useful to define the unit vectors  $\hat{u}_t$ ,  $\hat{u}_\phi$  on  $S$ . These two vectors along with a third unit vector  $\hat{u}_z$  form an orthogonal, curvilinear coordinate system. Since we are basically dealing with a two dimensional surface area, coordinates in the  $t$  and  $\phi$  directions are sufficient to uniquely specify a point anywhere on the surface. They will likewise be good choices to describe surface currents and similar functions.

It is also necessary to define the directions of the incident and scattered waves. The incident wave by assumption is a plane wave and the scattered wave in the far field is also essentially a plane wave. The directions of these waves are most conveniently defined in a spherical coordinate system. Figure 2 shows the transmitter angle  $\theta_t$ , the incident propagation vector  $k_i$ , the receiver coordinates  $\theta_r$ ,  $\phi_r$ , and the propagation vector  $k_r$  of a fictitious plane wave that travels from the receiver to the origin. The  $\phi$  coordinate of the transmitter can be taken as zero without loss of generality due to the axial symmetry of the problem.

In the most general case the input wave could be of any polarization. An arbitrary incident plane wave would have components of polarization in both the





$\theta$  and  $\phi$  directions. However, due to the linearity of electromagnetic fields it suffices to study each polarization separately assuming unit amplitude waves. Once results for  $\theta$  and  $\phi$  polarizations are obtained, results for an arbitrary incident polarization can be obtained by taking a linear combination in the correct proportions of  $\theta$  and  $\phi$  components. With this in mind we define a  $\theta$  polarized wave as

$$\vec{E}^i = \vec{u}_\theta^t \exp(-j \vec{k}_t \cdot \vec{r}) \quad (1)$$

and a  $\phi$  polarized wave as

$$\vec{E}^i = \vec{u}_\phi^t \exp(-j \vec{k}_t \cdot \vec{r}) \quad (2)$$

where  $E^i$  denotes the incident electric field,  $r$  is the position vector from the coordinate origin, and  $t$  implies the transmitted or incident wave (should not be confused with the  $t$ -component of the surface vectors). Either polarization will induce both  $t$  and  $\phi$  currents on the surface  $S$ . These induced currents in turn cause a scattered far field of both  $\theta$  and  $\phi$  polarizations.

### III. Field Integral Formulation

The field equations for this problem (and similar problems) have been discussed in detail and solved by several authors [1-5]. For a more in depth discussion of the field equations the interested reader is referred to the aforementioned sources. The field equations can be set up using an H-field formulation, an E-field formulation, or a linear combination of H- and E-fields. For simplicity only the E-field formulation is considered here.

The E-field integral equation is derived by applying the boundary condition for an electric field at a perfectly conducting surface, i.e. setting the tangential component of the total E-field on the surface  $S$  to zero. The total E-field will be the sum of the incident field  $E^i$  and the scattered field  $E^s$ . This

condition can be written as

$$-\vec{E}_{\text{tan}}^s = \vec{E}_{\text{tan}}^i \quad \text{on } S \quad (3)$$

Another way to express the condition denoted by (3) is to say that  $E^i$  induces surface currents on the perfectly conducting surface  $S$ . These surface currents in turn are the source of the scattered field  $E^s$ . The magnitude and direction of these currents are just sufficient so that  $E^s$  is equal but opposite to  $E^i$  on  $S$ . It's important to note that the incident field  $E^i$  portion of this equation remains unchanged whether or not there is a scattering body present, while  $E^s$  is dependent on the induced surface current  $J$ . Specifically the functional dependence of  $E^s$  on the surface current  $J$  is commonly expressed through the intermediate vector quantity  $A$ , called the magnetic vector potential, and is given by

$$\vec{E} = -j\omega\mu\vec{A}(\vec{J}) + \frac{1}{j\omega\epsilon}\nabla(\nabla\cdot\vec{A}(\vec{J})) \quad (4)$$

where the dependency of  $A$  on  $J$  is given by

$$\vec{A}(\vec{J}) = \frac{1}{4\pi} \iint_S \vec{J}(\vec{r}') \frac{e^{-jk|\vec{r}-\vec{r}'|}}{|\vec{r}-\vec{r}'|} ds \quad (5)$$

The problem is to determine the values of  $J$  which satisfy (3).

#### IV. Method of Solution

The first step in solving the field equations is to recognize that any surface current induced on  $S$  can be decomposed into orthogonal components, in the  $\hat{u}_t$  and  $\hat{u}_\phi$  directions, with each component having a dependence on both  $t$  and  $\phi$ . Explicitly this decomposition is expressed by

$$\bar{J}(\bar{r}) = \hat{a}_t J^t(t, \phi) + \hat{a}_\phi J^\phi(t, \phi) \quad (6)$$

The next step is to approximate the surface of revolution S by frusta. This is easily done by choosing a number of points along the generating curve C of the body of revolution and connecting them by straight line segments (see figure 3). By choosing enough points, the curvature of any BOR can be well represented. The more points taken, the better the approximation. The decision of how many points to use generally must be balanced against desired accuracy and the overall computer solution time. Considering this approximation, the surface current can now be expressed as the summation of a set of expansion functions

$$\bar{J}(\bar{r}) = \sum_{n,j} (I_{nj}^t \bar{J}_{nj}^t(t, \phi) + I_{nj}^\phi \bar{J}_{nj}^\phi(t, \phi)) \quad (7)$$

where  $J_{nj}^t(t, \phi)$  and  $J_{nj}^\phi(t, \phi)$  are functions defined by

$$\bar{J}_{nj}^t = \hat{a}_t f_j(t) e^{jn\phi} \quad (8)$$

$$\bar{J}_{nj}^\phi = \hat{a}_\phi f_j(t) e^{jn\phi} \quad (9)$$

and  $I_{nj}^t$  and  $I_{nj}^\phi$  represent the amplitude of each current component.

Also, in eqs. (7), (8), and (9) the subscript n takes the values ...-3, -2, -1, 0, 1, 2, 3... and the subscript j refers to the frusta segments that approximate the surface S. When the expanded form of J given by (7) is substituted into (3) the result is a summation of scattered field terms, each multiplied by a yet unknown coefficient  $I_{nj}^b$  where b denotes either t or  $\phi$ , as shown in (10)

$$-\sum_{n,j} [I_{nj}^t \bar{E}(\bar{J}_{nj}^t) + I_{nj}^\phi \bar{E}(\bar{J}_{nj}^\phi)]_{\tan} = \bar{E}_{\tan}^i \quad \text{on } S \quad (10)$$

According to the method of moments the undetermined coefficients  $I_{nj}^b$  are determined in the following fashion, a set of testing functions is chosen as well

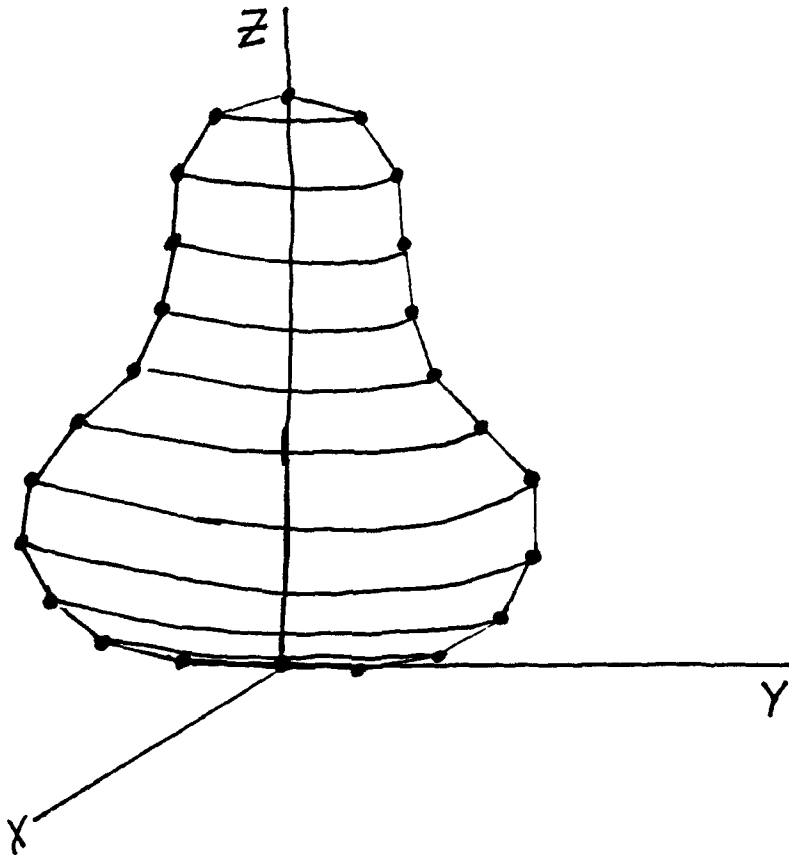


Figure 3. Approximation of BOR by frusta

a suitable inner product. The inner product of each testing function is taken with (10) to form a system of matrix equations. The set of testing functions in this case are defined by

$$\vec{W}_{mi}^t = \hat{U}_t f_i(t) e^{-jn\phi} \quad (11)$$

$$\vec{W}_{mi}^\phi = \hat{U}_\phi f_i(t) e^{-jn\phi} \quad (12)$$

For this problem a suitable inner product is the dot product of two vector functions integrated over the surface S. Each resulting matrix equation of the system will have the following form

$$\begin{bmatrix} Z_{mn}^{tt} & Z_{mn}^{t\phi} \\ Z_{mn}^{\phi t} & Z_{mn}^{\phi\phi} \end{bmatrix} \begin{bmatrix} \vec{I}_n^t \\ \vec{I}_n^\phi \end{bmatrix} = \begin{bmatrix} \vec{V}_m^t \\ \vec{V}_m^\phi \end{bmatrix} \quad (13)$$

where each Z is a square matrix whose ij-th elements are defined by

$$(Z_{mn}^{ab})_{ij} = \iint_S \vec{W}_{mi}^a \cdot \vec{E}(\vec{J}_{nj}^b) ds \quad (14)$$

where a and b may each be t or  $\phi$ . The source vectors  $V_m^t$  and  $V_m^\phi$  are column vectors whose i-th elements are expressed as

$$V_{mi}^a = \iint_S \vec{W}_{mi}^a \cdot \vec{E}^i ds \quad (15)$$

where again a can be t or  $\phi$ . Finally, the column vectors  $I_n^t$  and  $I_n^\phi$  are the unknown current coefficients from (7).

Of distinct advantage in body of revolution problems is the choice of the  $\phi$  dependence function,  $e^{jn\phi}$  which appears in both the expansion functions and the testing functions. It is well known from Fourier analysis that the set of

functions  $e^{jn\phi}$   $n=0, \pm 1, \pm 2, \dots$  are orthogonal on the interval  $[0, 2\pi]$ . This has the effect of causing the matrices  $Z_{mn}$  to be identically zero unless  $m=n$ . Effectively, each frequency mode corresponding to a particular  $n$  is decoupled from all the other modes. Therefore the surface current will be a sum of surface currents each having a different, independent azimuthal variation. For the same reason the scattered field will also be a sum of modal field terms. This allows computation of field contributions starting with  $n=0$  until the sum converges to within some predetermined limit. This greatly reduces the number of matrix equations that need to be considered.

It is clear that the matrix eq. (13) is of the form  $[Z][I]=[V]$ . To solve for the unknown coefficients  $[I]$  it is necessary to find  $Z^{-1}$ , the inverse of  $Z$ , and from straightforward calculation,  $[I]=[Z^{-1}][V]$ . Once these coefficients are found, it is a small step to calculate the scattered field or the radar cross section of the BOR.

This concludes the review of the general methodology used to solve perfectly conducting BOR scattering problems. What will be discussed in the following sections will be the method of computing the matrix elements  $Z_{mn}$  of (13) using a rectangular patch field method.

#### V. The Rectangular Field Patch Method

The rectangular patch field method is based on the calculation of the electromagnetic field at a given point in space due to a uniform current distribution on the patch. Exact analytic expressions for the field computation, suitable for computer computation, were developed by Mahadevan and Auda [6].

As has been mentioned, the BOR surface is approximated by frusta, with the assumption that the surface current is expanded in terms of  $t$  and  $\phi$  directed currents (see figure 4). Each element of the matrix  $Z$  is the integral of the dot product of the field due to the current on one frusta with the conjugate of the current on another frusta. Regarding the method of moments, the conjugate of the currents in this case are the testing functions. For computational purposes, each frusta (as well as the currents on each frusta) can be expanded into a

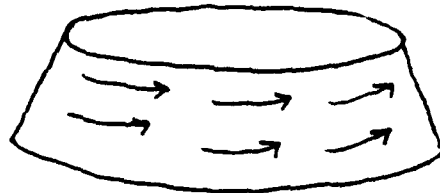
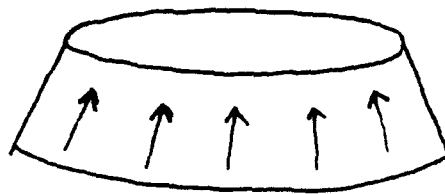
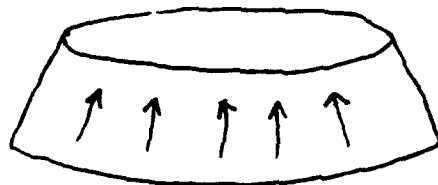
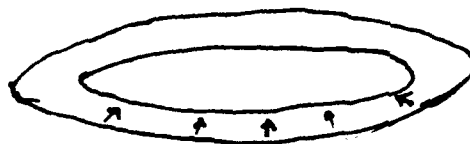


Figure 4. Examples of  $t$  and  $\phi$  directed current on a segment



||



+

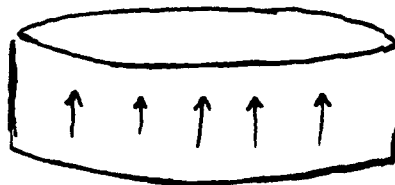


Figure 5. A vector decomposition of a segment

cylindrical segment and a flat, annular segment (see figure 5). These component segments of each frusta are then approximated by small, flat plate, segments (see figure 6). At this point the cylindrical portion of the frusta needs no further preparation for use with the rectangular patch field calculation. The components of current in the  $t$  and  $\phi$  directions are also shown in figure 6. However, the annular portion requires one more level of approximation in order the rectangular field patch method. Here we note that if the annulus is divided into  $M$  equal segments, the area of each segment is

$$AREA_{seg} = \frac{\pi}{M} (r_o^2 - r_i^2) \quad (16)$$

where  $r_o$  and  $r_i$  are the outer and inner radius of the annulus. This area can be expressed in terms of the average radius  $r_{av}$  and the difference of radii  $\Delta r$  as

$$AREA_{seg} = \frac{2\pi}{M} r_{av} \Delta r \quad (17)$$

The area of each annular sub-segment now has the form of a rectangular patch. If  $M$  is large, and  $\Delta r$  is small compared to  $r_{av}$ , then modelling the components of current on the annulus by a uniform distribution on each sub-segment is an excellent approximation.

Here we return to the matrix element formulation and begin applying the proposed approximations to the element calculation. The form of the general matrix element (14) is repeated for clarity

$$(Z_n^{ab})_{ij} = \iint_S \vec{W}_{ni}^a \cdot \vec{E}(\vec{J}_{nj}^b) ds \quad (14)$$

Note that the double subscript  $mn$  on the matrix element  $Z$  has been replaced by the single subscript  $n$ . This simplification is due to the orthogonality of the expansion functions in  $\phi$ , previously mentioned, i.e. unless  $m=n$ , the matrix  $Z_{mn}$  is identically zero, therefore only the single subscript  $n$  is needed.

The first step in approximating the integral in (14) is to rewrite the



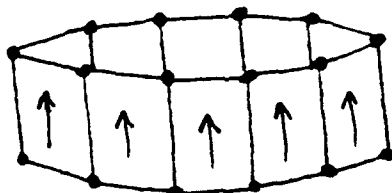
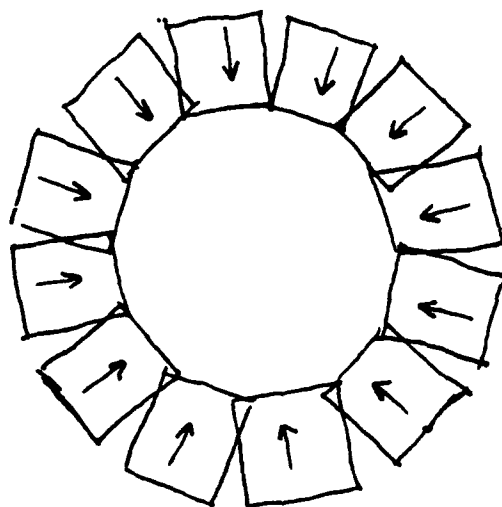


Figure 6. Rectangular patch approximations of segment components

integral as a summation of M smaller integrals, each covering an angular span of  $2\pi/M$ , corresponding to the small, flat plates of the segmented frustum

$$(Z_n^{ab})_{ij} = \sum_M \int_{\Delta s_i} \int \hat{u}_s f_i(t) e^{-j n \phi} \cdot \vec{E}(\vec{J}_{nj}^b) ds \quad (18)$$

where a generalized expression for the testing function has been used instead of W and  $\Delta s_i$  denotes an integration over one small segment. Note that the simplest choice for the function  $f_i(t)$  is a unit pulse function. This simply means we are approximating the surface currents on each frusta as having a constant amplitude. The variation in amplitude from frusta to frusta is taken care of by the coefficients  $I_n^i$  and  $I_n^j$  which we are trying to find. Computationally this means that  $f_i(t)=1$  on the i-th frustum and is zero elsewhere. Now the E-field in (18) is due to the surface current on the j-th frustum, evaluated on the surface of the i-th frustum. But the E-field can also be written as a summation of terms, one from each of the small, frustum patches. Each matrix term is then approximated by a double summation of integrals over small portions on a frustum

$$(Z_n^{ab})_{ij} = \sum_M \sum_M \int_{\Delta s_i} \int \hat{u}_s f_i(t) e^{-j n \phi} \cdot \vec{E}(\vec{J}_{nj}^b) ds \quad (19)$$

If a sufficient number of points on the generating curve of the BOR are taken, then the slant length of each frustum will be less than a wavelength. If the number of sub-segments comprising each frustum is also sufficiently large, then the change in  $\phi$  across each sub-section will be small and its span will also be less than a wavelength. This means that the E-field from one small patch will be approximately constant across the extent of any other small patch. It also means that  $\hat{u}_s$  and  $e^{-j n \phi}$  are approximately constant across each small patch. Given these assumptions are true, the mean value theorem can be applied. The integrand can be evaluated at a single point (the midpoint of the patch for simplicity) and the approximate value of the integral is just that single integrand value times the surface area of the patch. The final computational form of the matrix

element is

$$(Z_n^{ab})_{ij} = \sum_{l=1}^M \sum_{k=1}^M a_{al} \exp(-jn\phi_l) \text{area}_l \cdot \vec{E}(\vec{J}_{aj}^b(k)) \quad (20)$$

where the additional subscript (or functional dependence on)  $l$  indicates the  $l$ -th flat segment of the  $i$ -th frustum and the  $k$  indicates the E-field due to the current on the  $k$ -th flat segment of the  $j$ -th frustum.

## VI. Discussion

In essence the approximation described in the preceding section is nothing more than the definition of an integral, taken without letting the number sub-intervals go to infinity. However, it must be determined how small each flat segment on each frustum should be in order that the approximation is valid, or rather, how large they can be before the approximation becomes invalid.

Directly related to the angular span of each flat segment (in an azimuthal sense) is the number of segments,  $M$ , each frustum is approximated by. The dependence of the validity of the approximation on  $M$  will be examined for each of the factors in the integrand of (19). First consider the complex exponential,  $e^{-jn\phi}$ , which can be expressed as  $\cos n\phi - j \sin n\phi$  via Euler's identity. This is multiplied by the additional dot product factor  $\hat{u}_i \cdot (\hat{e}_r + \hat{e}_\phi + \hat{e}_z)$ , where  $\hat{e}_r$ ,  $\hat{e}_\phi$ , and  $\hat{e}_z$  represent the vector components of  $E$  in a cylindrical coordinate system, and are assumed constant. It can be shown that each of the dot products required contributes only a factor of either  $\sin \phi$  or  $\cos \phi$ . If  $M$  is the number of segments comprising each frustum, and if the segments are equal, then each segment spans  $2\pi/M$  radians.

To check the validity of the approximation, the exact integrals of  $\cos \phi$ ,  $\cos n\phi$  and  $\cos \phi \sin n\phi$  over a span of  $2\pi/m$  were evaluated and compared against the mid-angle approximation for  $n=0,1,2,3,4,5$ . It was found that for up to  $n=3$  the error was less than 5% taking  $M=20$ . Even for  $n=5$ , the error was only 15% (again for  $M=20$ ). While 15% error is unacceptable in many cases, in this case, as the mode number increases, the contribution of mode to the overall scattering

decreases, similar to higher order harmonics in a Fourier series. However, if it is found that the overall error is too gross, taking  $M=40$  reduces the error to less than about 6% (also for  $n=5$ ).

These results are encouraging, and while the effects of assuming the  $E$  field is constant from one small patch across another has not been evaluated, it should be remembered that the summation process itself will tend to smear out errors and yield values close to the actual.

## REFERENCES

- [1] J.R. Mautz and R.F. Harrington, "Radiation and Scattering from Bodies of Revolution," Appl. Sci. Res., vol.20, June 1969, pp. 405-435
- [2] P.L.E. Uslenghi, "Computation of Surface Currents on Bodied of Revolution," Alta Frequenza, vol. 39, No. 8, 1970, pp. 1-12
- [3] J.R. Mautz and R.F. Harrington, "H-Field, E-Field, and Combined Field Solutions for Bodies of Revolution," Technical Report TR-77-2, Department of Electrical and Computer Engineering, Syracuse University, Syracuse, NY 13210, February 1977
- [4] J.R. Mautz and R.F. Harrington, "Electromagnetic Scattering From a Homogeneous Body of Revolution", Technical Report TR-77-10, Department of Electrical and Computer Engineering, Syracuse University, Syracuse, NY 13210, November 1977
- [5] S. Govind, D.R. Wilton, A.W. Glisson, "Scattering From Inhomogeneous Penetrable Bodies of Revolution", IEEE Trans. Ant. and Prop., vol 32, No.11, 1984, pp. 1163-1173
- [6] K. Mahadevan and H.A. Auda, "Electromagnetic Field of a Rectangular Patch of Uniform and Linear Distributions of Current", IEEE Trans. Ant. and Prop., vol. 37, No. 12, December 1989, pp. 1503-1509

ELECTRIC FIELD MEASUREMENTS BY USING  
ELECTROOPTIC SAMPLING SYSTEM

Imad S. Ahmad  
Research Associate  
Department of Electrical Engineering

Portland State University  
P.O.Box 751  
Portland, OR 97207

Final Report for:  
Graduate Student Research Program  
Phillips Laboratory

Sponsored by:  
Air Force Office of Scientific Research  
Bolling Air Force Base, Washington, D.C.

September 1993

# ELECTRIC FIELD MEASUREMENT BY USING ELECTROOPTIC SAMPLING SYSTEM

*Imad S. Ahmad*  
*Graduate Associate*  
*Department of Electrical Engineering*  
*Portland State University*

## Abstract

The electric field has been measured by using electrooptic sampling system. The system uses an  $\text{LiTaO}_3$  electrooptical crystal and a YAG laser pumped by a laser diode whose output power is 13 mW to measure the electrical field of RF sources. An applied electric field nearby the  $\text{LiTaO}_3$  crystal changes the polarization state of YAG laser beam as it propagates through it. The output emerging beam of the  $\text{LiTaO}_3$  has been characterized. A wideband photodetector and a high frequency signal detector have been used to detect the change in the polarization fields at varies values of the electric field applied nearby the  $\text{LiTaO}_3$  crystal. A computer program (MathCad) has been developed to verify the accuracy of the system.

# ELECTRIC FIELD MEASUREMENT BY USING ELECTROOPTIC SAMPLING SYSTEM

*Imad S. Ahmad*

## Introduction

Since the beginning of this decade, rapid progress has been made in the development of ultrafast electronic and optoelectronic devices that will be the fundamental elements of the next generation of high frequency devices. However, commercially available measurement systems are quite inadequate for the characterization of these devices at such high frequencies; therefore, there is a definite need for new electronic measurement techniques. Most previous electrooptic sampling systems relied on a hybrid connection between the device under test and a transmission line formed on electrooptic substrate such as  $\text{LiTaO}_3$  [1],[2],[3]. The electric field of the transmission line was then probed transversely with ultrashort optical pulses from a mode-locked laser. Although these systems demonstrated outstanding speed and sensitivity, their hybrid nature represents a compromise when very wide bandwidth measurements are anticipated. The physical connection between the device under test and an  $\text{LiTaO}_3$  transmission line will introduce parasitic capacitances and inductances that could seriously affect the accuracy of the measurement. So a new approach is called for.

In this report, an electrooptic sampling system has been developed to measure the electric field of high frequency devices (up to 100 GHz) by using an  $\text{LiTaO}_3$  electrooptic crystal. The sampling relied on placing the electrooptic crystal close proximity to the transmission line to be sampled.



## METHODOLOGY

The method of measuring the electric field by using an electrooptic sampling system relied on the propagation of laser light in  $\text{LiTaO}_3$  electrooptic crystal. An applied electric field nearby the crystal causes a change in the polarization field of a propagating laser beam in the dielectric [4], [5]. This change in the polarization field can be displayed in a wideband photodetector and high frequency signal detector for characterization. Figure 1 shows a simplified diagram of the electrooptic sampling technique.

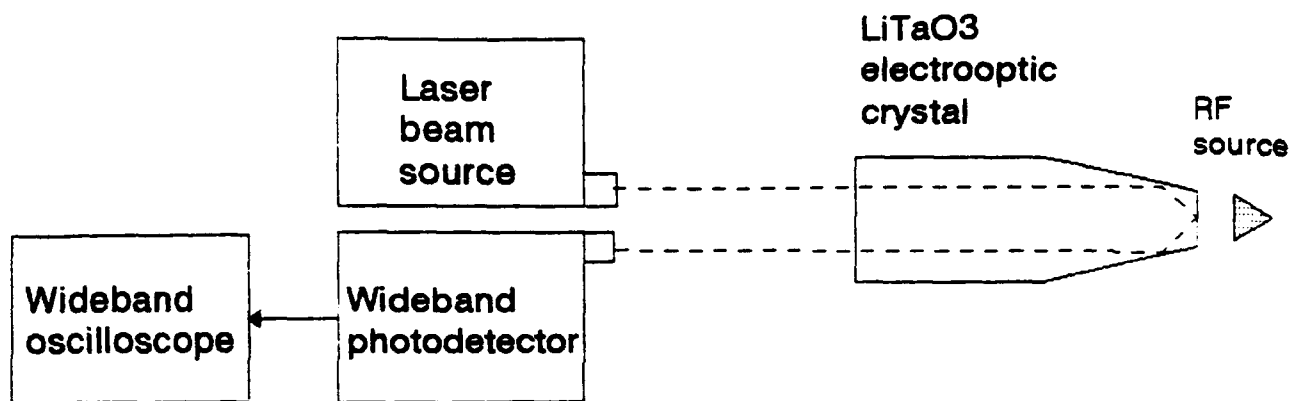


Figure 1. Simplified diagram of the electrooptic sampling technique

## THEORY AND DISCUSSION OF PROPOSED SYSTEM

The overall electrooptic sampling system configuration is shown in Fig. 2.

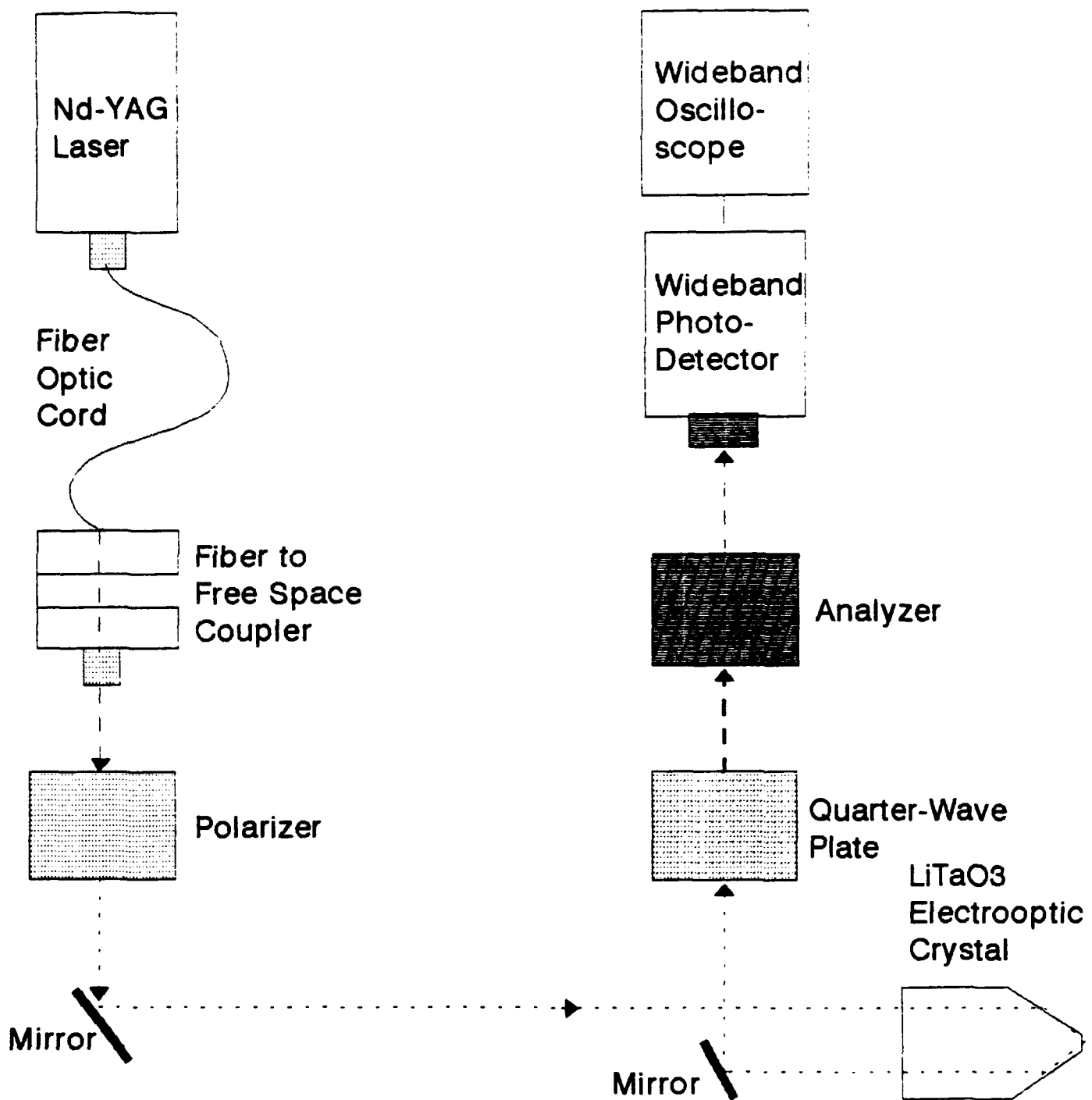


Figure 2. An overall electrooptical sampling system configuration.

### A. Laser Beam Transmission

The system uses a neodymium-doped yttrium-aluminum-garnet (Nd-YAG) laser as an input source. The Nd-YAG has a wavelength of 1320 nm and 13 mW of power [5]. The laser beam is then transmitted through a fiber optic patch cord and then coupled to a fiber-to-free space coupler.

### B. Polarization

The laser beam transmitted through the fiber optic can be partially polarized or unpolarized [5]. So a polarizer was placed in front of the laser beam for the production of linearly polarized light beam. To check the polarization state, a cardboard was placed in front of a polarizer. A slight darkening of the projected laser beam occurs. As a polarizer disk rotated on its axis, the darkening effect becomes more dominant. When this effect is at maximum, the polarization of the beam is at right angles to the planes of the polarizing crystals in the polarizing disk material. The polarization state of polarized light beam is described by Jones vector

$$V = \begin{bmatrix} V_x \\ V_y \end{bmatrix} \quad (1)$$

where  $V_x$  and  $V_y$  are two complex numbers. The x and y axes are fixed laboratory axes. The light propagates in the polarizer can be decomposed into a linear combination of the "fast" and "slow" eigenwaves of the crystal [6]. This is done by the coordinate transformation:

$$\begin{bmatrix} V_s \\ V_f \end{bmatrix} = \begin{bmatrix} \cos\psi & \sin\psi \\ -\sin\psi & \cos\psi \end{bmatrix} \begin{bmatrix} V_x \\ V_y \end{bmatrix} = R(\psi) \begin{bmatrix} V_x \\ V_y \end{bmatrix} \quad (2)$$

$V_s$  and  $V_f$  are the slow and fast components of the polarization vector  $V$ .

The polarization state of the emerging beam in the crystal coordinate system, where the transmission axis is set to be

parallel to the laboratory x axis, is given by

$$\begin{vmatrix} \hat{V}_s \\ \hat{V}_f \end{vmatrix} = e^{-i\Phi} \begin{vmatrix} 1 & 0 \\ 0 & 0 \end{vmatrix} \begin{vmatrix} V_s \\ V_f \end{vmatrix} \quad (3)$$

where  $\Phi$  is the absolute phase accumulated due to the finite optical thickness of the polarizer.

The Jones vector of the polarization state of the emerging beam in the xy coordinate is given by transforming back from the crystal sf coordinate system

$$\begin{vmatrix} \hat{V}_x \\ \hat{V}_y \end{vmatrix} = \begin{vmatrix} \cos\psi & -\sin\psi \\ \sin\psi & \cos\psi \end{vmatrix} \begin{vmatrix} \hat{V}_s \\ \hat{V}_f \end{vmatrix} = R(-\psi) \begin{vmatrix} \hat{V}_s \\ \hat{V}_f \end{vmatrix} \quad (4)$$

By combining Eqs. 2, 3, and 4, the Jones vector for the emerging beam is

$$\begin{vmatrix} \hat{V}_x \\ \hat{V}_y \end{vmatrix} = R(-\psi) P_0 R(\psi) \begin{vmatrix} V_x \\ V_y \end{vmatrix} \quad (5)$$

where  $R(\psi)$  is the rotation matrix and  $P_0$  is the Jones matrix of the polarizer oriented with its transmission axis parallel to the laboratory x axis. These are given, respectively, by

$$R(\psi) = \begin{vmatrix} \cos\psi & \sin\psi \\ -\sin\psi & \cos\psi \end{vmatrix} \quad (6)$$

and

$$P_0 = e^{-i\Phi} \begin{vmatrix} 1 & 0 \\ 0 & 0 \end{vmatrix} \quad (7)$$

The phase factor  $e^{-i\Phi}$  can be neglected since it is not observable. The Jones matrix of a polarizer rotated by an angle  $\psi$  is given by

$$P = R(-\psi) P_0 R(\psi) \quad (8)$$

The polarization state of the emerging beam at the output of the polarizer is obtained by multiplying Eqs. 8 and 1 and is given by

$$E = P \cdot V = \begin{vmatrix} E_x \\ E_y \end{vmatrix} \quad (9)$$

The intensity is calculated as

$$I = \text{abs}(E_x)^2 + \text{abs}(E_y)^2 \quad (10)$$

The polarized laser beam will then hit a spherical mirror with 100% reflectivity and then reflected into electrooptical crystal for electrooptic modulation.

### C. Electrooptic Sampling

The polarized laser beam then propagates in an electrooptical lithium tantalate ( $\text{LiTaO}_3$ ) crystal. The propagation of laser beam in  $\text{LiTaO}_3$  can be described in term of the index ellipsoid form [6]

$$\frac{x^2}{n_x^2} + \frac{y^2}{n_y^2} + \frac{z^2}{n_z^2} = 1 \quad (11)$$

where  $x$ ,  $y$ , and  $z$  are the principal axes and  $n_x$ ,  $n_y$ , and  $n_z$  are the principal refractive indices.

Applying an electric field nearby the crystal changes the index ellipsoid to the form

$$\left(\frac{1}{n_x^2} + r_{1k}E_k\right)x^2 + \left(\frac{1}{n_y^2} + r_{2k}E_k\right)y^2 + \left(\frac{1}{n_z^2} + r_{3k}E_k\right)z^2 \quad (12)$$

$$+ 2yzr_{4k}E_k + 2zxr_{5k}E_k + 2xyr_{6k}E_k = 1$$

where  $E_k$  ( $k=1, 2, 3$ ) is a component of the applied electric field and 1, 2, 3 correspond to the principal dielectric axes  $x$ ,  $y$ ,  $z$ . The equation of the new index ellipsoid (Eq. 12) reduces to Eq. 11 when  $E_k=0$ .

The  $\text{LiTaO}_3$  crystal has a 200 $\mu\text{m}$  thickness and an electrooptic coefficients listed in Table 1 [6], [7].

Table 1. LiTaO3 Electrooptic Coefficients

Material	Symmetry	Wavelength (nm)	Electrooptic Coefficients				Index of Refraction	
			r13	r22	r33	r51	no	ne
			(10-12m/v)					
LiTaO3	3m	1320	7.5	1	33	20	2.176	2.18

Since the LiTaO<sub>3</sub> has a crystal symmetry of 3m, then the electrooptic coefficients are presented in this form

$$\begin{pmatrix} 0 & -r_{22} & r_{13} \\ 0 & r_{22} & r_{13} \\ 0 & 0 & r_{33} \\ 0 & r_{51} & 0 \\ r_{51} & 0 & 0 \\ -r_{22} & 0 & 0 \end{pmatrix} \quad (13)$$

Letting the electric field to be applied along the z axis of the crystal, so the equation of the index ellipsoid can be written, according to Eq. 12 and Eq. 13, as

$$x^2 \left( \frac{1}{n_o^2} + r_{13}E \right) + y^2 \left( \frac{1}{n_o^2} + r_{13}E \right) + z^2 \left( \frac{1}{n_e^2} + r_{33}E \right) = 1 \quad (14)$$

where  $n_o$  and  $n_e$  are the ordinary and extraordinary refractive indices of the crystal, and  $r_{13}$  and  $r_{33}$  are the relevant electrooptic coefficients. The principal refractive indices, according to Eq. 14, are given by

$$n_x = n_o - \frac{1}{2} n_o^3 r_{13} E \quad (15)$$

$$n_y = n_o - \frac{1}{2} n_o^3 r_{13} E \quad (16)$$

$$n_z = n_e - \frac{1}{2} n_e^3 r_{33} E \quad (17)$$

since the laser beam is propagating in the y direction, the birefringence seen by laser beam is

$$n_z - n_x = (n_e - n_o) - \frac{1}{2}(n_e^3 r_{33} - n_o^3 r_{13})E \quad (18)$$

The phase retardation of the crystal is then given by

$$\Gamma = \frac{2\pi}{\lambda}(n_z - n_x)L \quad (19)$$

where  $\lambda$  is the wavelength of the laser beam, and  $L$  is the length of the propagating laser beam in the  $\text{LiTaO}_3$ .

The laser beam propagates in the  $\text{LiTaO}_3$  along the y direction as shown in Fig. 3 and has the length, twice the thickness of the crystal, 400  $\mu\text{m}$ .

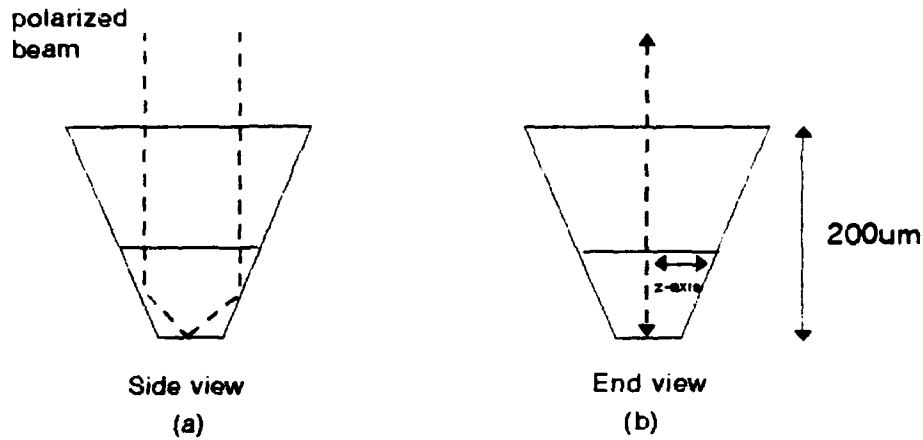


Figure 3. (a) side and (b) cross-sectional views of internal polarized beam reflection in the  $\text{LiTaO}_3$  crystal

The Jones matrix of the crystal is given by

$$W_0 = \begin{bmatrix} e^{j\Gamma/2} & 0 \\ 0 & e^{j\Gamma/2} \end{bmatrix} \quad (20)$$

where  $\Gamma$  is given by Eq. 19.

The Jones matrix of the crystal rotated by an angle  $\psi$  is given by

$$W_1 = R(-\psi) W_0 R(\psi) \quad (21)$$

The polarization state of the emerging beam at the output of the crystal is given by multiplying Eqs. 21 and 9 and is given by

$$E_1 = W_1 \cdot E \quad (22)$$

The output emerging beam of the  $\text{LiTaO}_3$  crystal has the form of ellipse at various values of the phase retardation  $\Gamma$ . The output emerging beam of the crystal is needed to be converted into linearly polarized beam to obtain proper interference, so a quarter-wave plate is needed.

#### D. A Quarter-Wave Plate

A quarter-wave plate is placed at a 90 degrees right angle of the  $\text{LiTaO}_3$  crystal. The emerging beam at the output of the  $\text{LiTaO}_3$  crystal is directed to the quarter-wave plate by using two mirrors as shown in Fig. 2.

A quarter-wave plate has a phase retardation of  $\Gamma = \frac{1}{2}\pi$  and azimuth angle of  $\psi = 45^\circ$  [6]. The Jones matrix of the quarter-wave plate is given by

$$W_2 = R(-\psi) W_0 R(\psi) \quad (23)$$

where  $R(\pm\psi)$  is the rotation matrix given in Eq. 6 with  $\psi = 45^\circ$  and  $W_0$  is the Jones matrix of the plate given in Eq. 20 with  $\Gamma = \frac{1}{2}\pi$ . The polarization state of the emerging beam is obtained by multiplying Eqs. 23 and 22 and is given by

$$E_2 = W_2 \cdot E_1 \quad (24)$$

The emerging beam at the output of the quarter-wave plate is now linearly polarized.



### E. Analysis & observation

In order to measure the changes in the polarization field of the emerging beam an analyzer is placed in front of the quarter-wave plate.

An analyzer is basically a polarizer. It is called an analyzer simply because it analyze the polarization state of the emerging beam [6]. The wollaston prism is used as an analyzer in this system. It splits the polarized beam into two rays (o-ray and e-ray)[8].

The Jones matrix of the analyzer oriented with its transmission axis parallel to the laboratory y axis (crossed with respect to the input polarizer) is given by

$$P_{out} = \begin{bmatrix} 0 & 0 \\ 0 & 1 \end{bmatrix} \quad (25)$$

The polarization state of emerging beam after it passes through the analyzer is obtained by multiplying Eqs. 25 and 24 and is given by

$$E_{out} = P_{out} \cdot E_2 = \begin{bmatrix} \acute{E}_x \\ \acute{E}_y \end{bmatrix} \quad (26)$$

The intensity of the emerging beam after it passes through the analyzer is calculated as

$$I_{out} = abs(\acute{E}_x) + abs(\acute{E}_y) \quad (27)$$

The transmissivity of the electrooptical system is calculated by dividing the output intensity (Eq. 27) by the input intensity (Eq. 10) and is given by

$$T = \frac{I_{out}}{I} = \frac{abs(\acute{E}_x) + abs(\acute{E}_y)}{abs(E_x) + abs(E_y)} \quad (28)$$

The intensity is measured by a wideband photodetector and the amplitude of the modulated intensity versus voltage applied is displayed by a wideband oscilloscope.

## CALCULATION AND RESULTS

The calculation for the electrooptic sampling system has been developed by using a mathcad program and is given by:

A. Assuming the laser beam (incident beam) has the polarization state of:

$$V := \begin{bmatrix} 1 \\ 0 \end{bmatrix}$$

B. Laser beam polarization

The rotation angle is set to:

$$\psi := 0 \cdot \frac{\pi}{180}$$

$$RO(\psi) := \begin{bmatrix} \cos(\psi) & \sin(\psi) \\ -\sin(\psi) & \cos(\psi) \end{bmatrix}$$

$$RO(\psi) = \begin{bmatrix} 1 & 0 \\ 0 & 1 \end{bmatrix}$$

$$RO(-\psi) = \begin{bmatrix} 1 & 0 \\ 0 & 1 \end{bmatrix}$$

The Jones matrix of the polarizer oriented with its transmission axis parallel to the laboratory x axis is given by

$$P0 := \begin{bmatrix} 1 & 0 \\ 0 & 0 \end{bmatrix}$$

The Jones matrix of the polarizer rotated by an angle= 0 degrees is given by

$$P := RO(-\psi) \cdot P0 \cdot RO(\psi)$$

$$P = \begin{bmatrix} 1 & 0 \\ 0 & 0 \end{bmatrix}$$

The polarization state of the emerging beam at the polarizer output is given by

$$E_{in} := P \cdot V$$

$$E_{in} = \begin{bmatrix} 1 \\ 0 \end{bmatrix}$$

The transmitted beam after the first polarizer has the intensity:

$$I := \left[ \left[ |E_{in_0}|^2 \cdot |E_{in_1}|^2 \right] \cdot 100 \right] \quad I = 100 \quad \%$$

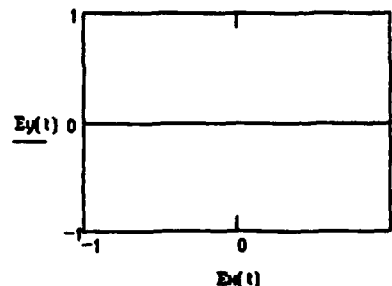
The polarization state is plotted below:

$$t := 0..360$$

$$w_t := t \cdot \frac{\pi}{180} \quad i := \sqrt{-1}$$

$$E_x(t) := \operatorname{Re} \left[ E_{in_0} \cdot e^{i \cdot w_t} \right]$$

$$E_y(t) := \operatorname{Re} \left[ E_{in_1} \cdot e^{i \cdot w_t} \right]$$



### C. Electrooptic Sampling

LiTaO3 electrooptic coefficients:

$$r_{13} := 7.5 \cdot 10^{-12} \quad r_{33} := 33 \cdot 10^{-12} \quad r_{51} := 20 \cdot 10^{-12} \quad r_{22} := 1 \cdot 10^{-12}$$

$$n_o := 2.176 \quad n_e := 2.16 \quad \lambda := 1320 \cdot 10^{-9} \quad L := 400 \cdot 10^{-6}$$

Electric field applied nearby the crystal:

$$i := 0.5000$$

$$E_1 := 10^4 \cdot i$$

The birefringence is:

$$n_{x2} := (n_e - n_o) - \frac{1}{2} \cdot [n_e^3 \cdot r_{33} - n_o^3 \cdot r_{13}] \cdot E_1$$

The phase retardation of the crystal is:

$$\Gamma_1 := 2 \cdot \frac{\pi}{\lambda} \cdot n_{x2} \cdot L$$

The half wave Electric field and voltage for the LiTaO3 which yields a phase retardation of Gamma = Pi is given by:

$$E_x := \frac{1}{L} \cdot \frac{\lambda}{n_e^3 \cdot r_{33} - n_o^3 \cdot r_{13}} \quad E_x = 1.247 \cdot 10^7 \quad \frac{V}{m}$$

Assuming the separation between the electrodes (d) is 0.1mm

$$d := 10^{-4}$$

$$V := \frac{d}{L} \cdot \frac{\lambda}{n_e^3 \cdot r_{33} - n_o^3 \cdot r_{13}} \quad V = 1.247 \cdot 10^3 \quad V$$

The rotation angle is set to:

$$\psi := 45 \cdot \frac{\pi}{180}$$

$$R2(\psi) := \begin{bmatrix} \cos(\psi) & \sin(\psi) \\ -\sin(\psi) & \cos(\psi) \end{bmatrix} \quad R2(\psi) = \begin{bmatrix} 0.707 & 0.707 \\ -0.707 & 0.707 \end{bmatrix} \quad R2(-\psi) = \begin{bmatrix} 0.707 & -0.707 \\ 0.707 & 0.707 \end{bmatrix}$$

The Jones matrix of the crystal is given by

$$W0(i) := \begin{bmatrix} e^{-j \cdot \frac{\Gamma_1}{2}} & 0 \\ 0 & e^{j \cdot \frac{\Gamma_1}{2}} \end{bmatrix}$$

The Jones matrix of the crystal rotated by an angle = 45 degrees

$$W1(i) := R2(-\psi) \cdot W0(i) \cdot R2(\psi)$$

The polarization state of the emerging beam at the output of the crystal is given by

$$Z1(i) := W1(i) \cdot Zin$$

Polarization ellipse of the output beam of the crystal at various values of the electric field:

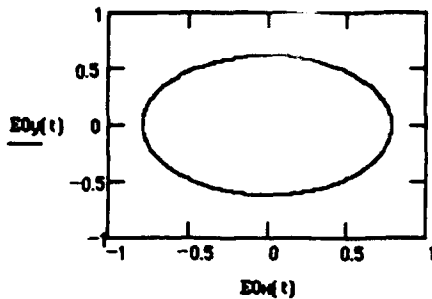
$$t := 0.360$$

$$w(t) = t \cdot \frac{\pi}{180}$$

At  $E = 0$  V/m

$$E0x(t) := \operatorname{Re} \left[ E1(0)_0 \cdot e^{j \cdot w(t)} \right]$$

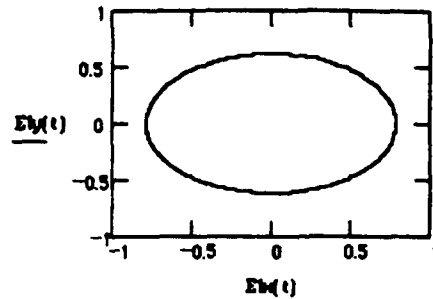
$$E0y(t) := \operatorname{Re} \left[ E1(0)_1 \cdot e^{j \cdot w(t)} \right]$$



At  $E = 10$  kV/m

$$E1x(t) := \operatorname{Re} \left[ E1(1)_0 \cdot e^{j \cdot w(t)} \right]$$

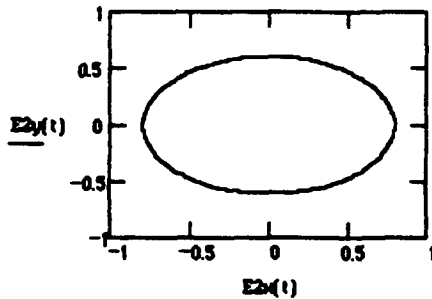
$$E1y(t) := \operatorname{Re} \left[ E1(1)_1 \cdot e^{j \cdot w(t)} \right]$$



At  $E = 100$  kV/m

$$E2x(t) := \operatorname{Re} \left[ E1(10)_0 \cdot e^{j \cdot w(t)} \right]$$

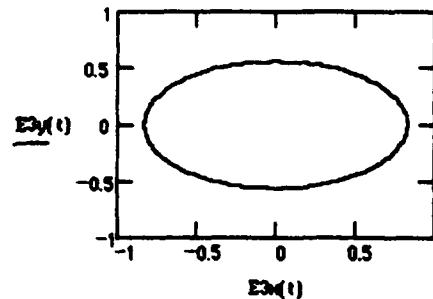
$$E2y(t) := \operatorname{Re} \left[ E1(10)_1 \cdot e^{j \cdot w(t)} \right]$$



At  $E = 10$  MV/m

$$E3x(t) := \operatorname{Re} \left[ E1(1000)_0 \cdot e^{j \cdot w(t)} \right]$$

$$E3y(t) := \operatorname{Re} \left[ E1(1000)_1 \cdot e^{j \cdot w(t)} \right]$$



#### D. A Quarter-Wave Plate

The azimuth angle and the phase retardation of the quarter-wave plate are:

$$\psi := 90 \cdot \frac{\pi}{180} \quad \Gamma := \frac{\pi}{2}$$

$$R3(\psi) = \begin{bmatrix} \cos(\psi) & \sin(\psi) \\ -\sin(\psi) & \cos(\psi) \end{bmatrix}$$

$$R3(\psi) = \begin{bmatrix} 0 & 1 \\ -1 & 0 \end{bmatrix}$$

The Jones matrix of the quarter-wave plate

$$W0 = \begin{bmatrix} e^{-j\frac{\pi}{2}} & 0 \\ 0 & e^{j\frac{\pi}{2}} \end{bmatrix} \quad W0 = \begin{bmatrix} 0.707 - 0.707j & 0 \\ 0 & 0.707 + 0.707j \end{bmatrix}$$

The Jones matrix of the quarter-wave plate with a 90 degrees rotation:

$$W2 = R3(-\psi) \cdot W0 \cdot R3(\psi) \quad W2 = \begin{bmatrix} 0.707 + 0.707j & 0 \\ 0 & 0.707 - 0.707j \end{bmatrix}$$

The polarization state of the emerging beam at the output of the quarter-wave plate:

$$E2(i) := W2 \cdot E1(i)$$

The polarization state plots of the output beam of the quarter wave plate at various electric field values:

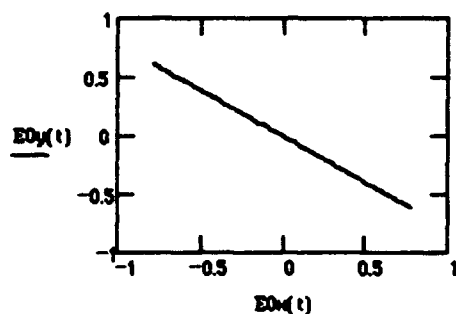
$$t := 0..360$$

$$w(t) := t \cdot \frac{\pi}{180}$$

At E = 0 V/m

$$E0x(t) := \operatorname{Re} [E2(0)_0 \cdot e^{j \cdot w(t)}]$$

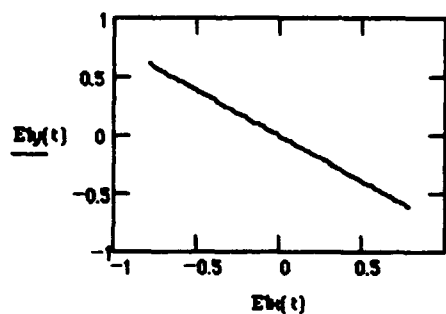
$$E0y(t) := \operatorname{Re} [E2(0)_1 \cdot e^{j \cdot w(t)}]$$



At E = 10 kV/m

$$E1x(t) := \operatorname{Re} [E2(1)_0 \cdot e^{j \cdot w(t)}]$$

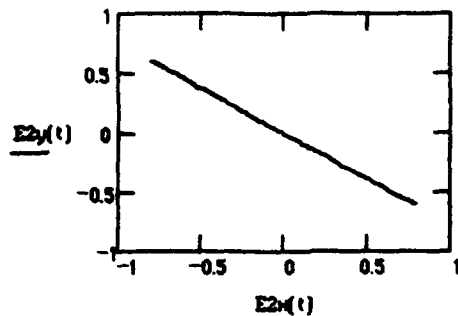
$$E1y(t) := \operatorname{Re} [E2(1)_1 \cdot e^{j \cdot w(t)}]$$



At E = 100 kV/m

$$E2x(t) := \operatorname{Re} \left[ E2(10)_0 \cdot e^{j \cdot w(t)} \right]$$

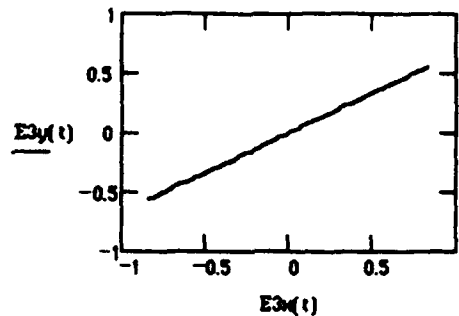
$$E2y(t) := \operatorname{Re} \left[ E2(10)_1 \cdot e^{j \cdot w(t)} \right]$$



At E = 10 MV/m

$$E3x(t) := \operatorname{Re} \left[ E2(1000)_0 \cdot e^{j \cdot w(t)} \right]$$

$$E3y(t) := \operatorname{Re} \left[ E2(1000)_1 \cdot e^{j \cdot w(t)} \right]$$



#### E. Analyzer

The Jones matrix of the analyzer oriented with its transmission axis parallel to the y axis (input polarizer and analyzer are crossed):

$$P_{out} := \begin{bmatrix} 0 & 0 \\ 0 & 1 \end{bmatrix}$$

The polarization state representation of the emerging beam after it passes through the analyzer:

$$E_{out}(i) := P_{out} \cdot E2(i)$$

The intensity of the emerging beam after it passes through the analyzer:

$$I_{out}(i) := \left[ |E_{out}(i)_0|^2 + |E_{out}(i)_1|^2 \right] \cdot 100 \quad \%$$

The transmissivity of the electrooptical system:

$$T(i) := \frac{I_{out}(i)}{I} \cdot 100$$

The polarization state plots of the output beam of the electrooptical system at various electric field values:

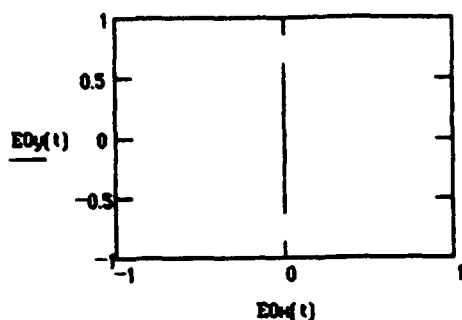
$$t := 0..360$$

$$w(t) := t \cdot \frac{\pi}{180}$$

At  $E = 0$  V/m

$$E0x(t) := \operatorname{Re} [Eout(0)_0 \cdot e^{j \cdot \omega(t)}]$$

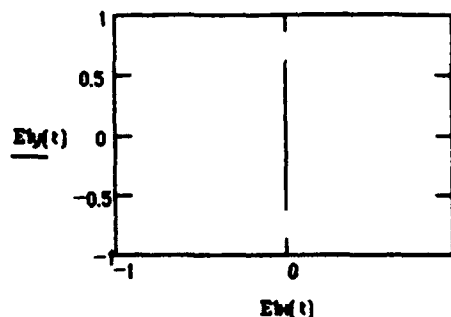
$$E0y(t) := \operatorname{Re} [Eout(0)_1 \cdot e^{j \cdot \omega(t)}]$$



At  $E = 10$  KV/m

$$E1x(t) := \operatorname{Re} [Eout(1)_0 \cdot e^{j \cdot \omega(t)}]$$

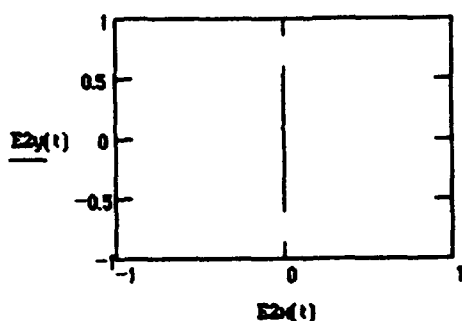
$$E1y(t) := \operatorname{Re} [Eout(1)_1 \cdot e^{j \cdot \omega(t)}]$$



At  $E = 100$  KV/m

$$E2x(t) := \operatorname{Re} [Eout(10)_0 \cdot e^{j \cdot \omega(t)}]$$

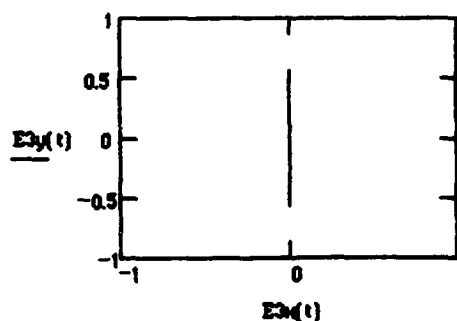
$$E2y(t) := \operatorname{Re} [Eout(10)_1 \cdot e^{j \cdot \omega(t)}]$$



At  $E = 10$  MV/m

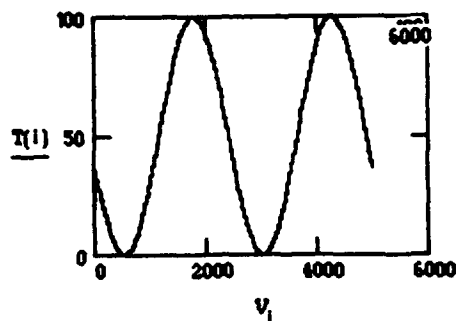
$$E3x(t) := \operatorname{Re} [Eout(1000)_0 \cdot e^{j \cdot \omega(t)}]$$

$$E3y(t) := \operatorname{Re} [Eout(1000)_1 \cdot e^{j \cdot \omega(t)}]$$



The transmission  $T$  versus voltage  $V$  is plotted below:

$$V_i := L_i \cdot d$$



## CONCLUSION

The electrooptic sampling system has been constructed using LiTaO<sub>3</sub> crystal. The measurement accuracy of the system has been investigated by using a MathCad program.

Applying varies values of electric field nearby the LiTaO<sub>3</sub> crystal caused a change in the polarization field at the output emerging beam of the system. A wideband photodetector and a wideband oscilloscope have been used to detect the changes in the polarization field in the form of intensity transmission changes. Table 2. shows some electric fields and their intensity transmission values.

**Table 2. Electric fields and transmission intensity values**

Electric fields (V/m)	Intensity (%)	Electric fields((V/m)	Intensity (%)
0	38.212	$1 \cdot 10^7$	31.246
$5 \cdot 10^5$	32.201	$1.5 \cdot 10^7$	88.379
$1 \cdot 10^6$	26.473	$2 \cdot 10^7$	92.261
$2 \cdot 10^6$	16.218	$2.5 \cdot 10^7$	37.505
$3 \cdot 10^6$	8.097	$3 \cdot 10^7$	0.086
$4 \cdot 10^6$	2.62	$3.5 \cdot 10^7$	31.924
$5 \cdot 10^6$	0.134	$4 \cdot 10^7$	88.843
$6 \cdot 10^6$	0.796	$4.5 \cdot 10^7$	91.867
$7 \cdot 10^6$	4.564	$5 \cdot 10^7$	36.80
$8 \cdot 10^6$	11.2		
$9 \cdot 10^6$	20.285		



## REFERENCES

1. J. A. Valdmanis, G. Mourou, and C.W. Gabel, "Picosecond electrooptic sampling system," Appl. Phys. Lett., Vol. 41, pp. 211-212, 1982.
2. B. H. Kolner, D. M. Bloom, and P. S. Cross, "Electro-optic sampling with picosecond resolution," Electron. Lett., vol. 19, pp. 574-575, 1983.
3. G. A. Mourou and K. E. Meyer, "Subpicosecond electrooptic sampling using coplanar strip transmission lines," Appl. Phys. Lett., vol. 45, pp. 492-494, 1984.
4. J. A. Valdmanis and G. Mourou, "Subpicosecond electrooptic sampling: principles and applications," IEEE J. Quantum Electron., vol. QE-22, pp. 69-78, Jan. 1986.
5. H. M. Muncheryan, Laser and optoelectronic engineering, Prentice-Hall, Englewood Cliffs, NJ, 1984.
6. A. Yariv and P. Yeh, Optical waves in crystals, A Wiley-Interscience Publication, NY, 1986.
7. M. Gottlieb, C. L. Ireland, and J. M. Lay, Electro-optic and acousto-optic scanning and deflection, Marcel Dekker, Inc., NY, 1983.
8. H. A. Haus, HECOT optics, Prentice-Hall, Englewood Cliffs, NJ, 1983

**PREVENTION OF MAGNETIC INDUCTIVE STORE LEAKAGE PAST A  
QUASI-STATICALLY COMPRESSED COMPACT TORUS**

**Robert John Leiweke  
Graduate Research Associate  
Department of Aeronautical & Astronautical Engineering**

**The Ohio State University  
2036 Neil Avenue Mall, Room 326  
Columbus, Ohio 43210**

**Final Report for:  
AFOSR Summer Research Program  
Phillips Laboratory**

**Sponsored by:  
Air Force Office of Scientific Research  
Kirtland Air Force Base, Albuquerque, New Mexico**

**September, 1993**

# **PREVENTION OF MAGNETIC INDUCTIVE STORE LEAKAGE PAST A QUASI-STATICALLY COMPRESSED COMPACT TORUS**

**Robert John Leiweke**  
**Graduate Research Associate**  
**Department of Aeronautical & Astronautical Engineering**  
**The Ohio State University**

## **Abstract**

A one-dimensional (1D) analytic model was used in conjunction with a two-dimensional (2D) model to study conditions under which inductively stored magnetic energy leaks past a Quasi-Statically Compressed (QSC) Compact Toroid (CT) in the MARAUDER (Magnetically Accelerated Rings to Achieve Ultrahigh Directed Energy and Radiation) experiment. This phenomenon has is called "blowby". QSC means to slowly compress a CT in order to prevent elongation and high inductive impedances. By hypothesis, blowby may be prevented by keeping the ratio of piston field to CT self-field,  $\alpha$ , greater than 0.35 but less than unity. The 1D model either assumes  $\alpha$  constant or a function of time only, and does not take into effect CT compressibility. This model calculates a current waveform compatible with ideal magnetohydrodynamics (MHD) for use as a driver current in the 2D model. All 2D simulations were accomplished using MACH2, a 2D Arbitrary Lagrangian Eulerian (ALE) MHD code. The 1D  $\alpha$ -constant model provided a sinusoidal waveform with a moderate risetime compatible with the idea of QSC, however blowby occurred in many of the associated 2D simulations. This is may be due to inappropriate values of  $\alpha$  chosen (0.60 - 0.80) and developing Rayleigh-Taylor instabilities. The single time dependant  $\alpha$  case studied did not exhibit blowby, but also did not conform to QSC. In general, the 2D trajectories did not compare well with their predicted 1D trajectories, for either  $\alpha$  case, because of severe blowby. The 1D model was discovered to be ill-posed for the  $\alpha$ -constant studies since it is impossible for the CT to be in an initial equilibrium state, as assumed in the 2D models. However, the 1D model does provide a waveform that, with the appropriate initial conditions, can be matched by the Shiva Star capacitor bank to provide a starting point for QSC experiments.

# PREVENTION OF MAGNETIC INDUCTIVE STORE LEAKAGE PAST A QUASI-STATICALLY COMPRESSED COMPACT TORUS

Robert John Leiweke

## INTRODUCTION

The MARAUDER (Magnetically Accelerated Rings to Achieve Ultrahigh Directed Energy and Radiation) program at Phillips Laboratory studies the formation, compression, and acceleration of low beta Compact Toroid (CT) plasmas for use as possible sources of intense x-rays, high-power microwaves, very fast opening switches, and as an alternative path to inertial confinement fusion.<sup>1</sup> MARAUDER utilizes Shiva Star, a 9.4 MJ capacitor bank (1300 $\mu$ F, 120 kV) at lower capacitance and voltage to create CT formation and compression discharge energies of 0.25MJ and 1.9MJ, respectively. Acceleration is achieved by releasing the magnetic energy stored inductively behind the CT during the compression phase, quite analogous to the release of a coiled spring.

Formation of a CT begins with the radial injection of a neutral gas (such as argon, hydrogen, or neon) into the gap of an evacuated coaxial electrode gun permeated with a 0.1 to 0.2 T poloidal magnetic field. During the formation discharge, toroidal magnetic flux fills the volume behind the injected gas, which is subsequently ionized by the induced current across the radial gap.<sup>2</sup> The toroidal magnetic pressure, varying as  $1/r^2$ , acts as a massless piston to accelerate the plasma downstream.<sup>2</sup> Magnetic and hydrodynamic boundary layers leave some mass remaining at the walls within the muzzle.

As illustrated in Figure 1, about 60% of the low beta plasma expands into the formation volume as a second discharge pinches this "bubble" off from the flux remaining in the muzzle.<sup>2,3</sup> This initiates full magnetic re-connection, forming a relaxed plasma torus existing in a minimum energy Taylor state configuration of non-zero magnetic field helicity.<sup>2</sup> As shown in Figure 1, the second discharge also serves as a source of compression field. A Taylor state CT is rather robust under conditions of extreme compression and acceleration because perturbations tend to decay rather than grow.<sup>2</sup> The mass left behind in the muzzle bridges the radial gap and becomes an efficient current return path as shown in Figure 1.

Magnetic flux from the second discharge pushes the CT down a bicone in order to achieve high number densities. The bicone is designed to so that in the absense of resistive losses, CT

magnetic flux is conserved during compression and thus maintains its original compact cross-sectional shape (this is known as "self-similar"). Although a CT is somewhat robust, it tends to lose compactness by axial elongation if the center of mass speed is relatively large.<sup>2</sup> For this and among other reasons it is desirable to compress the CT slowly, termed "Quasi-Static Compression" (QSC).<sup>4</sup> Furthermore, MARAUDER experimental data and two-dimensional numerical simulations show that the CT may be pushed against the outer electrode<sup>2</sup> during the QSC phase, releasing magnetic piston energy stored inductively behind the CT armature. This phenomenon has been termed "blowby" because it is quite similar to a blown gasket.<sup>2</sup> A fundamental cause of blowby is the development of a Rayleigh-Taylor instability near the inner electrode/piston interface (the piston field is strongest here)<sup>5</sup>. However, numerical simulation suggests that if the maximum compression "piston" field is less than the maximum CT field in magnitude, then blowby is generally prevented.<sup>6</sup> An understanding of the conditions in which blowby occurs is important because of its disadvantages as well as potential advantages in some applications. For example, blowby has been controlled well enough to become an advantage in two dimensional numerical simulations of a Magnetically-confined Plasma Opening Switch (McPOS). Here, the bicone is designed to induce the CT armature to leak the inductively stored energy to a load at a predetermined geometric location and phase of the QSC current discharge.<sup>1,2,4</sup>

In this study, blowby is considered to be a hinderance to QSC efficiency. Thus an attempt has been made to calculate the proper current waveform consistent with blowby prevention and QSC criteria using a simple one-dimensional analytic dynamical model. The QSC current waveform is then used as an external circuit within a two dimensional ideal MHD numerical model to drive a mature CT into a 9:1 compression bicone.

## **METHODOLOGY**

To focus on the physics of blowby, all details of CT formation are ignored and ideal MHD is assumed to be valid. The CT is assumed to be initially in a relaxed Taylor state at the base of the bicone. Hydrodynamic drag at the electrode boundaries is ignored because it is not a fundamental cause of blowby. As shown in Figure 2b, the 9:1 compression geometry used for this study consists of a bicone of height  $\rho_0 = 52.39$  cm, a  $30^\circ$  mean angle  $\theta$  with an acute angular deviation  $\Delta\theta$  from the central radius  $r$  of  $4.84954^\circ$ . The initial voltage across the gap is 55 kV, bank capacitance is 1300

$\mu\text{F}$ , and a line inductance of 50 nH. Initial QSC current is determined from the one dimensional analytic model.

### The 2-d model

All two dimensional (2D) dynamic simulations were performed with MACH2, a 2D Arbitrary-geometry Lagrangian Eulerian (ALE) magnetohydrodynamics (MHD) code.<sup>7</sup> MACH2 ignores hydrodynamic viscosity since thermal conductivity plays a more dominant role.<sup>7</sup> Figure 2a shows the computational grid, consisting of the right half cross-section (r-z plane) of a 9:1 compression bicone and stagnation region. All computational boundaries are defined to be closed and conducting. The equation of state is that of an ideal gas. Hydrogen was chosen to be the working fluid, with a total mass is no greater than 2 mg. The initial mass density distribution within the CT was scaled proportionally to lines of constant self-field magnetic flux, shown in Figure 2b. Computation begins at time zero with a compression current discharge across the back boundary of the cone and runs until 10 $\mu\text{s}$  has elapsed. The system is modeled as nearly ideal MHD (the fluid upstream of the CT was granted a small amount of resistivity, enabling the current sheet to diffuse up to the CT trailing edge). The usual RLC circuit routine within MACH2 that is used to model the capacitor discharge was substituted with a QSC current waveform computed from the one-dimensional model.

### The 1-d model

#### $\alpha = \text{constant}$

Several assumptions have been made within the 1D CT QSC model. First, the CT is reduced to a point where the self-field magnitude may be represented by a single number. Second, CT self-field flux is conserved. This is consistent with the ideal MHD assumption of no resistive losses. Next, the energy source that drives the system is the Shiva Star capacitor bank. Fourth, the CT kinetic energy is negligible compared to the self-field, inductive store, and capacitor bank energies (this turns out to be a quite valid assumption for a low mass CT). Lastly, the CT starts at the base of the bicone at time zero with zero initial velocity.

By observing 2D numerical experiments with MACH2, it has been hypothesized that the severity of blowby in a self-similar compression bicone may be reduced or even eliminated if the ratio of the piston field to CT self-field is less than unity.<sup>6</sup> Thus, this relationship is to form the basis for computing the QSC current waveform. The global physical model is that of an LC circuit.

The total inductance is the sum of a constant line inductance and the temporally changing cone inductance. The capacitor is initially charged to a voltage  $V_0$ . By Kirchoff's rule, the inductor voltage is equivalent to that of the capacitor for all time. Time dependant unknowns of the system are the CT self field,  $B^{ct}$ , the piston field,  $B^p$ , the combined external line and bicone inductance,  $L$ , The CT field energy,  $U^{ct}$ , the source (Shiva Star capacitor) voltage,  $V$ , the discharge current,  $I$ , and the distance from the bicone centerline to the CT,  $\rho = r \sin(\theta)$ . Here,  $r = r(t)$  is defined as the temporally dependant radial distance of the CT Center-of-Mass (CM) to the cone vertex on the geometrical centerline (see Figure 2b). Thus there are six unknowns requiring six independant relationships to obtain a unique solution for current as a function of time. These relationships are<sup>8</sup>:

#### Energy conservation

$$U_0^{ct} + \frac{1}{2}L_0 I_0^2 + \frac{1}{2}C V_0^2 = U^{ct}(r) + \frac{1}{2}L(r) I(r)^2 + \frac{1}{2}C V(r)^2 \quad (1)$$

#### CT magnetic flux conservation

$$\Phi^m(r) = B_0^{ct} A_0 = B^{ct}(r) A(r) = \text{constant}, \quad \text{where} \quad (2)$$

$A(r)$  = CT cross-sectional area

#### Piston field

$$B^p(r) = \mu_0 I(r) / 2\pi\rho(r), \quad (3)$$

$$\rho(r) = r \sin(\theta)$$

#### Inductance

$$L(r) = L_0 + L_f (1 - r/r_0) \quad (4)$$

Where

$$L_f = (\mu_0 r_0 / 2\pi) \ln( \tan(\theta_2/2) / \tan(\theta_1/2) )$$

$$\theta_1 = \pi - \theta - \Delta\theta$$

$$\theta_2 = \pi - \theta + \Delta\theta$$

#### Capacitor voltage

$$V(r) = d\Phi^m/dt = d/dt ( L(r) I(r) ) \quad (5)$$

#### QSC / Blowby condition

$$B^p(r) = \alpha B^{ct}(r), \quad 0 < \alpha \text{ constant} < 1 \quad (6)$$

We define  $x(r) = r_0/r$  so that by equation (2), the CT magnetic self-field scales as

$r^{-2}$ ,

$$B^{ct}(r) = B_o^{ct} (r_o / r)^2 = B_o^{ct} x^2 \quad (7)$$

and thus the magnetic self-field energy scales as  $x$ :

$$U^{ct}(r) = U_o^{ct} (r_o / r) = U_o^{ct} x \quad (8)$$

The driver current may be determined by combining equations (3) and (6):

$$B^p(r) = \mu_o I(r) / 2\pi r = \alpha B^{ct}$$

so that

$$I(r) = 2\pi r_o \alpha B_o^{ct} \sin(\theta) x / \mu_o \quad (9)$$

By defining an initial current  $I_o$ , we see that

$$I(x) = I_o (r_o / r) = I_o x \quad (10)$$

$$I_o = 2\pi r_o \alpha B_o^{ct} \sin(\theta) / \mu_o \quad (11)$$

By combining equations (4), (5), (8), (9), and (11), eliminating  $V(t)$  in equation (1) and solving for the time rate of change of  $x$ , we get

$$dx/dt = +A (a + bx + cx^2)^{1/2} \quad (12a)$$

where

$$a + b + c = 1 \quad (12b)$$

$$a = 1 + (L_o I_o^2 + 2U_o^{ct}) / CV_o^2 \quad (12c)$$

$$b = (L_f I_o^2 - 2U_o^{ct}) / CV_o^2 \quad (12d)$$

$$c = (-L_f I_o^2 g) / CV_o^2, \quad c < 0 \quad (12e)$$

$$g = 1 + L_o / L_f$$

The solution of equation (12a) is easily found<sup>9</sup> to be

$$x(t) = (1 + b/(2c)) \cos(\omega t) + (-c)^{-1/2} \sin(\omega t) - b/(2c) \quad (13)$$

where the circular frequency is

$$\omega = (C g L_f)^{-1/2} \quad (14)$$

Deformation information is transmitted across the CT on the order of the Alfven transit time.

Thus, the Alfven speed gives an indication as to CT stiffness. Let a characteristic length and time

for the system be 1m and 10 $\mu$ s, respectively. Then the characteristic speed is  $v_c = 10^5$  m/s. With

the Alfven speed defined as



$$v_a = B_0^{ct} / (2 \mu_0 \rho_f)^{1/2}$$

where  $\rho_f$  is the hydro-fluid density, let the "relative stiffness",  $\sigma$ , be defined as:

$$\sigma = B_0^{ct} / (2 \mu_0 m v_c^2)^{1/2} \quad (15)$$

Now, with the expression for  $x(t)$ , the QSC driver current (10) compatible with the blowby condition (6) is uniquely determined.

$$\alpha = \alpha(t)$$

If one considers  $\alpha$  a function only of time, then the analysis presented above must be modified somewhat. Since  $\alpha$  is no longer a specified parameter, then an additional relationship along with an initial condition is needed to uniquely determine its temporal history. The seventh relationship was chosen as Newton's second law of motion, despite valid arguments that it is the same statement as conservation of energy<sup>2</sup>:

$$F^{total} = ma = m d^2 r / dt^2 = F^{ct}(t) - F^p(t) \quad (16)$$

The QSC current becomes, with  $\alpha(t=0) = \alpha_0$  and  $I_0 = 2 \pi \sin \theta B_0^{ct} r_0 \alpha_0 / \mu_0$

$$I(t) = (I_0 r_0 / \alpha_0) (\alpha(t) / r(t)) \quad (17)$$

With a time dependant alpha and  $x(t) = r_0 / r(t)$ , equation 5 becomes

$$V(t) = L_f I_0 g \{ (x - g^{-1}) d\alpha/dt - x^{-2} r_0^{-1} \alpha(t) dr/dt \} / \alpha_0 \quad (18)$$

Since  $L(t) I(t)^2 = I_0^2 L_f (\alpha(t) / \alpha_0)^2 (g x^2 - x)$ , then using this in equation 1, solving for  $V(t)$  and equating to 18, we get

$$p(r) d\alpha/dt - h(r, dr/dt) \alpha - s(r, dr/dt, \alpha) = 0$$

Solving for the derivative of alpha,

$$d\alpha/dt = p(r)^{-1} \{ s(r, dr/dt, \alpha) - h(r, dr/dt) \alpha \} \quad (19a)$$

$$\text{where } p(r) = x - g^{-1} \quad (19b)$$

$$h(r, dr/dt) = x r_0^{-1} dr/dt \quad (19c)$$

$$s(r, dr/dt, \alpha) = \alpha_0 V_0 C \{ 1 + (L_0 I_0^2 - L(t) I(t)^2 + 2 U_0^{ct} (1 - x)) \}^{1/2} / (I_0 \omega^2) \quad (19d)$$

From equations 2, 3, and 6, the piston field is

$$B^p(t) = (\mu_0 I_0 x^2 \alpha(t)) / (2 \pi \alpha_0 r_0 \sin \theta) \quad (20)$$

Using equation 20, the piston force is the area integral of the piston magnetic pressure,

$B^2(t) / (2 \mu_0)$ , over the trailing edge of the CT, which is found to be<sup>6</sup>

$$F^P(t) = (\mu_0 I(t)^2 / 2\pi) \ln(\tan(\theta_2/2) / \tan(\theta_1/2)) \quad (21)$$

Upon substitution of equation 17 into equation 21, the piston force is

$$F^P(t) = L_f x(t)^2 \alpha(t)^2 I_0^2 / (2 r_0 \alpha_0^2) \quad (22)$$

The scalar repulsive CT force is, by equation 8,

$$F^{ct}(t) = -r \text{ Grad} (U^{ct}(t)) = U_0^{ct} x(t)^2 / r_0 \quad (23)$$

The force ratio is then

$$F^P(t) / F^{ct}(t) = (\alpha(t) / \alpha_c)^2 \quad (24a)$$

where alpha critical is found to be a purely geometric parameter using  $U_0^{ct} = n B_0^{ct} / (2 \mu_0)$

$$\alpha_c = n^{1/2} [2\pi\mu_0 \ln(\tan(\theta_2/2) / \tan(\theta_1/2))]^{-1/2} \quad (24b)$$

and from MACH2,

$$n = 0.0718634$$

This results in  $\alpha_c = 0.3493$ . To drive the CT into the bicone one must require that  $\alpha > \alpha_c$ . This critical value also holds for the constant alpha case derived above. Using this force ratio expression in equation 16 we get

$$F^{total} = m d^2 r / dt^2 = F^{ct}(t) - F^{ct}(t) (\alpha(t) / \alpha_c)^2 \quad (25)$$

Substitution of equation 23 into 25 gives

$$d^2 r / dt^2 = \{1 - (\alpha(t) / \alpha_c)^2\} b / r(t) \quad (26)$$

where  $b = U_0^{ct} r_0 / m$ , and  $m$  is the CT mass. Finally, we note that the velocity must be calculated at each point in time since it is present explicitly in equation 19c and 19d, thus,

$$v(t) = dr/dt \quad (27)$$

Now, given an initial velocity,  $v_0 = dr/dt|_{t=0}$ , and  $\alpha_0$ , we solve the set of three coupled differential equations 26, 27, and 19 a,b,c, and d simultaneously using a fourth-order Runge-Kutta method.

## **RESULTS**

### **$\alpha = \text{constant}$**

Two families of CT's were investigated; those with a "low" and "high" relative stiffness as derived in equation 15. Figures 3 and 4 shows the normalized trajectory solution  $x(t)^{-1}$  and associated QSC waveform for

$B_0^{ct}$ , mass, and  $\alpha$  taking on typical experimental values of 0.58T, 0.122mg, and 0.80, respectively. Note that the 1D theory yields a sinusoidal current waveform that is easily matched by Shiva Star in future QSC experiments. For a given self-field of 0.60T, Figure 5 displays the current as a function of time and  $\alpha$ . Note from equations 9 and 17 that QSC current scales linearly with both  $B_0^{ct}$  and  $\alpha$ . As shown in Table 1, there are 11 2D simulations broken into the two cases mentioned above. In this table,  $R_b$  is defined to be the normalized radius at which the CT CM first begins to "bounce" back towards the initial position.

### 2D CT QSC SIMULATION CASES

#### Low Relative Stiffness ( $\sigma < 10$ )

CASE	$B_0$ (T)	mass (m)	$\alpha$	$\sigma$	$R_b$	Blowby (Y/N)
31	0.58	1.50	0.80	3.0	< 0.10	Y
32	0.58	1.50	0.70	3.0	< 0.10	Y
35	0.58	1.22	0.80	3.3	0.97	N
1	0.50	1.50	0.80	2.6	0.91	Y
2	0.50	0.50	0.80	4.5	0.19	Y
8	1.58	1.50	0.80	8.1	0.77	Y

#### High Relative Stiffness ( $\sigma > 10$ )

29	0.75	0.12	0.80	13.5	0.42	N
30	0.75	0.12	0.62	13.5	0.46	N
33	0.58	0.12	0.70	10.5	0.31	N
6	3.00	1.50	0.80	15.5	0.87	Y
7	5.00	1.50	0.80	25.2	0.91	Y

**TABLE 1**

Figure 6 shows 2D center of mass trajectories as a function of time, corresponding to the cases listed in Table 1. In this plot, the stagnation region is that area lying below  $x^{-1} = 0.10$ . The solutions show that the 1D and 2D trajectories do not exhibit similar characteristics. Notice that the 1D calculation has a non-zero initial velocity whereas the CM location for all 2D calculations, from definition of initial conditions, has no initial velocity. By solving  $x(t)$  for  $r(t)$ , taking the derivative to find  $v(t)$ , it can be shown that the CT 1D theory velocity can never vanish initially. Also, in general, the trajectory curvatures (acceleration) are of opposite sign.

From Figure 6, one would think that CT's with low relative stiffness tend to blowby rather easily. However, comparing cases 32 and 35 from Table 1, we see that although both have about the same relative stiffness, and nearly the same driving waveform ( $\alpha_{32} = 0.7$ ,  $\alpha_{35} = 0.8$ ), case 32 exhibits blowby but case 35 does not. Recall that the driving current waveform is independent of mass in the 1D theory. This is illustrated in Figures 7a and 7b for cases 32 and 35, respectively. These snapshots are taken at  $2.5 \mu s$  just as blowby occurs. Rayleigh-Taylor instability may be a possible explanation.

Figures 8 and 9 compare cases 33 and 32, identical in every respect except for an order of magnitude difference in mass (an order of magnitude in  $\sigma$ ). The QSC current input into MACH2 is also the same, and so from the 1D theory we expect the same trajectory (the massless limit for non-relativistic kinetic energy is still valid)<sup>9</sup>. These 2D time histories document the magnetic flux isocontours and residual inductive store fluid for cases 32 and 33 listed in Table 1, respectively.

It was hypothesized<sup>6</sup> that as  $\sigma$  increased, the 2D CT trajectory would approach the 1D theory massless limit. Figure 6 shows this to be true for early times except after a severe blowby has occurred. As the current rises, the CT CM will accelerate more or less, depending on  $\sigma$  (equation 15). Again, Figures 8 and 9 (cases 33 and 32 with high and low  $\sigma$ , respectively) show the trailing edge of the low  $\sigma$  CT is highly compressed at early times, just before blowby occurs. Interestingly, cases 6 and 7 are given the highest  $\sigma$  yet they both bounce back from blowby at radius  $R_b = 0.87$  and  $0.91$ , respectively. In cases 2, 31, and 32 where  $\sigma$  is low and blowby occurs, and the initial self-field is low ( $B_0^{ct} < 1$ ), note that the CT CM still reaches the stagnation region. In cases 6, 7, and 8, the initial self-field is high, blowby occurs, and  $\sigma$  is high, the CT CM never reaches the stagnation region. This occurs because enough inductively stored energy has leaked so that the piston cannot overcome the repulsive self-field force (see equation 23).

#### $\alpha = \alpha(t)$

Figure 10a shows a family of 1D model solutions for  $B_0^{ct}$ ,  $m$ , and  $\alpha_0$  values of 0.581, 0.122 mg, and 0.10 to 0.80, respectively ( $\sigma = 10.5$ ). Note that as  $\alpha_0$  increases from 0.10 to 0.80, the 1D CT reaches the stagnation point in less time, as expected. Also, the 1D CT trajectory curves have no initial velocity and in addition have a negative acceleration. However, notice that the velocity near the stagnation region is as large as  $10^6$  m/s, not in accordance with the idea of QSC. As with the constant  $\alpha$  cases, the set of ODE's were solved within MACH2 to produce a driver current

waveform for  $\alpha_0 = 0.35$ . For this value of  $\alpha_0$  close to the critical equilibrium value, one might expect the 1D trajectory to exhibit a small initial acceleration. The current waveform is displayed with a dark line in Figure 10b. At  $1.5 \mu s$  this waveform appears to increase without bound. The associated 2D CT trajectory is the dark line in Figure 10a. Initially, the CT CM begins with zero velocity but then accelerates until  $2 \mu s$  where it begins to deaccelerate. At  $3 \mu s$  the CT CM again accelerates, moving into the stagnation region. Notice that this trajectory never resembles the case 33 counterpart listed in Table 1. Figure 11 shows that blowby did not occur, despite the large accelerations. The fact that blowby did not occur is probably accredited to slowly growing Rayleigh-Taylor instabilities rather than the piston blowby condition.

## CONCLUSIONS

### $\alpha = \text{constant}$

Since the 1D model does not account for 2D effects such as CT stiffness and Rayleigh-Taylor instability development, the position at a given instant in time may not be predicted correctly. In such a situation where the 1D theory waveform is input into the 2D system (as opposed to solving the RLC circuit equations within the 2D system), a mismatch develops between the required 1D and actual 2D inductance. This may partly explain why cases that do not exhibit blowby tend to bounce at about  $2/3$  the initial distance from the bicone vertex. To determine whether blowby can be prevented with the 1D waveform despite the apparent shortcomings, additional simulations with lower  $\alpha$  values and various other circuit parameters for the blowby cases is in order.

Also, the initial 1D model velocity cannot be made to vanish under any condition. The reason for this seems to stem from the requirement of non-zero initial capacitor voltage. Note that equation 5 gives the capacitor voltage as

$$V(t) = -L_f g I_0 x(t) (r_0 / r^2) v(t)$$

so that imposition of initial conditions requiring that the velocity vanish at  $t=0$  gives, with  $x(0) = 1$ ,

$$V(0) = V_0 = -L_f g I_0 v(0) = 0,$$

which contradicts<sup>6</sup> the assumption that  $V_0 \neq 0$ . Thus the 1D model is ill-posed in the sense that the CT can never be in an initial equilibrium state, as assumed within the 2D model and observed in MACH2 numerical experiments. Despite these problems, the 1D theory does provide a slow rise time, sinusoidal current for QSC experiments that can be matched by manipulation of the Shiva Star capacitor bank external inductances.

$$\alpha = \alpha(t)$$

Unfortunately, only a single 2D case was explored using this model. However, the initial results show that the current rise is incompatible with the idea of QSC. Recalling equation 18, we see that if the initial velocity is defined to vanish, then the initial voltage across the capacitor will not vanish if  $d\alpha/dt|_{t=0} = 0$ . This allows the alleviation of the problems mentioned above, but it is unclear at this time what contradictions may arise, and how this theory responds to blowby prevention.

### **ACKNOWLEDGEMENTS**

Sincere gratitude goes out towards Dr. Robert E. Peterkin, Jr. for his saintly patience and understanding. He has certainly *landscaped* my perception of the universe. I wish to thank Dr. Thomas Hussey for granting me the opportunity to participate within the PL/WSP Theory Group, and for use of their computational resources in order to complete an M.S. degree in a timely manner. I appreciate the enlightening discussions with Dr. Norm Roderick, Dr. Peter J. Turchi, Dr. David Bell, Dr. Uri Shumlak, Jim Havranek, and Melissa Douglas. Talks with Dr. Edward L. Ruden are *always* an interesting cultural experience.

### **REFERENCES**

- [1] R.E. Peterkin, Jr. *et al.*, "A Compact Torus Plasma Flow Switch", *Digest of Technical Paper: Eighth IEEE International Pulsed Power Conference*, 17-19 June 1991, San Diego, CA, R. White and K. Prestwich eds., p. 277 (IEEE, New York, NY, 1991.).
- [2] R. E. Peterkin, Jr., *et al.*, "A Long Conduction Time Compact Torus Plasma Opening Switch", *Proceedings of the XVth International Symposium on Discharges and Electrical Insulation in Vacuum*, 6-10 September 1992, Darmstadt, Germany.
- [3] R. J. Leiweke, "Compact Toroid Mass Entrainment Sensitivity To Initial Density Distributions Using Numerical Simulation", *Final Report for AFOSR Summer Research Program*, September, 1992.
- [4] R. E. Peterkin, Jr. and R. J. Leiweke, "Analytic and Numerical Studies of Quasi-Static Compression of a Compact Toroid", *Abstract Submitted for the Thirty-Fifth Annual*

*Meeting of the Division of Plasma Physics of the American Physical Society, 1-5 November 1993, St. Louis, Mo.*

- [5] Uri Shumlak, private communications, 1993.
- [6] R. E. Peterkin, private communications, 1993.
- [7] R. E. Peterkin, Jr., A. J. Giancola, and J. E. Sturtevant, "MACH2: A Reference Manual--  
Fifth Edition", MRC/ABQ-R-1490, updated 1992.
- [8] R. E. Peterkin, Jr., development of the one-dimensional QSC theory to prevent blowby,  
January, 1993.
- [9] "Handbook of Mathematical, Scientific, and Engineering Formulas, Tables, Functions,  
Graphs, and Transforms", Research and Education Association, 1991.

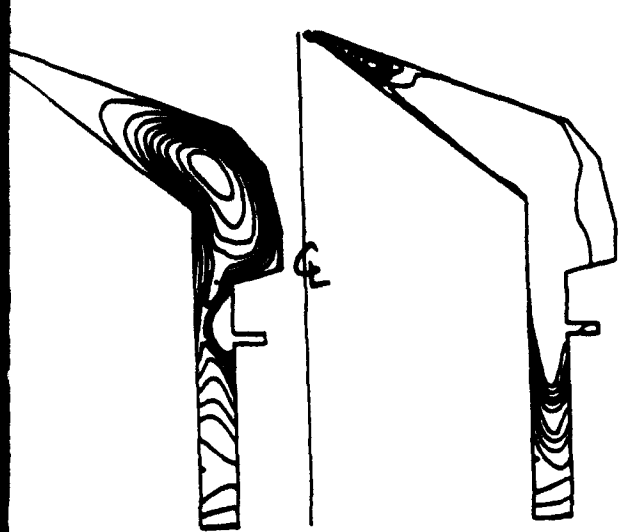


Figure 1

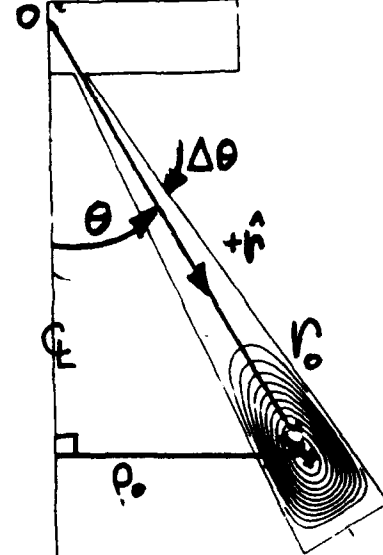
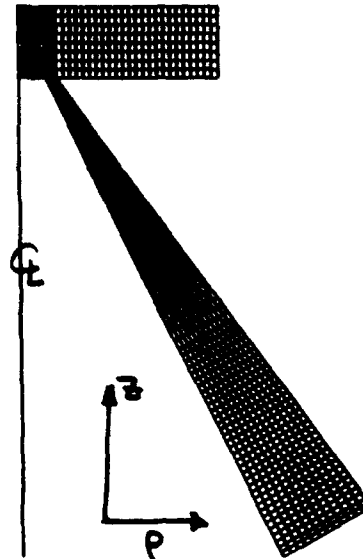


Figure 2a,b

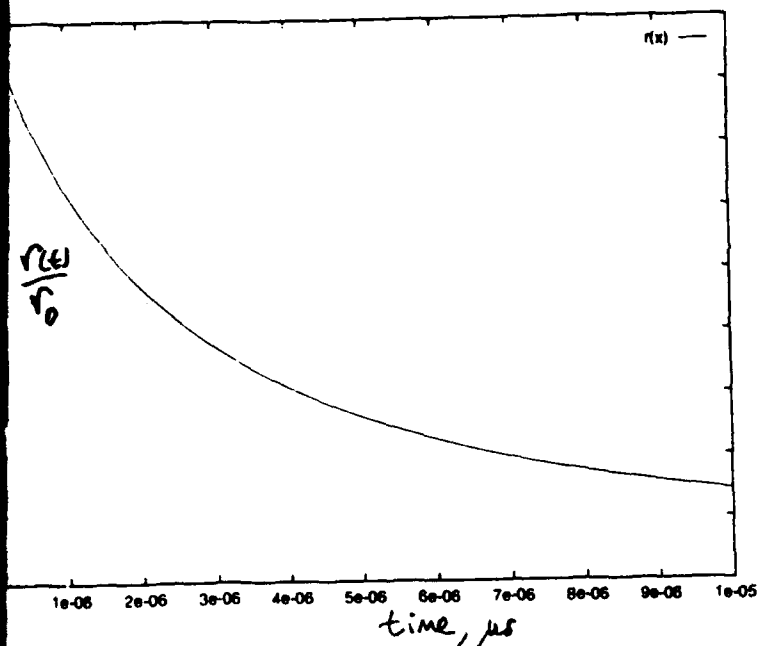


Figure 3

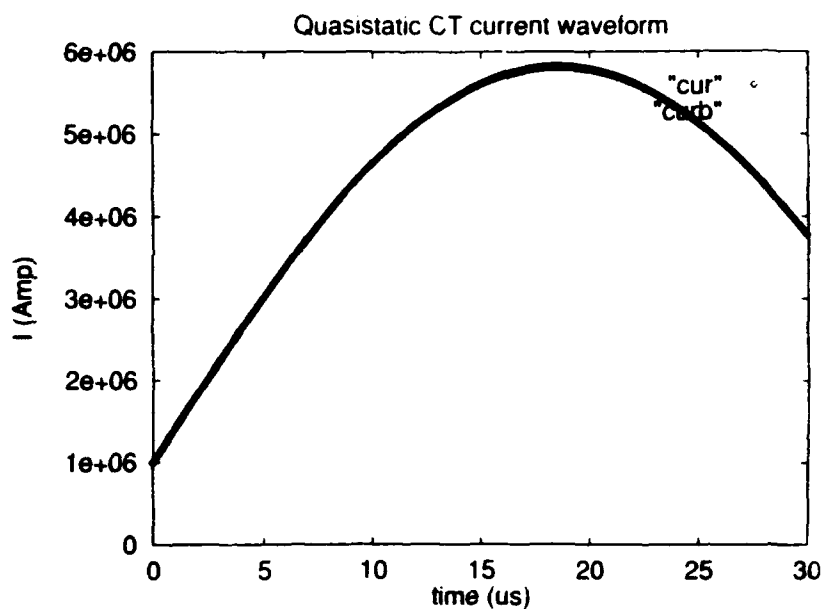


Figure 4

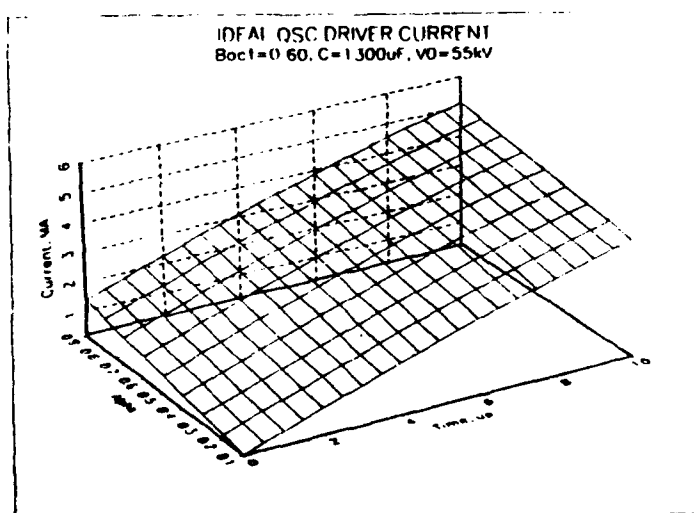


FIGURE 5

20-15



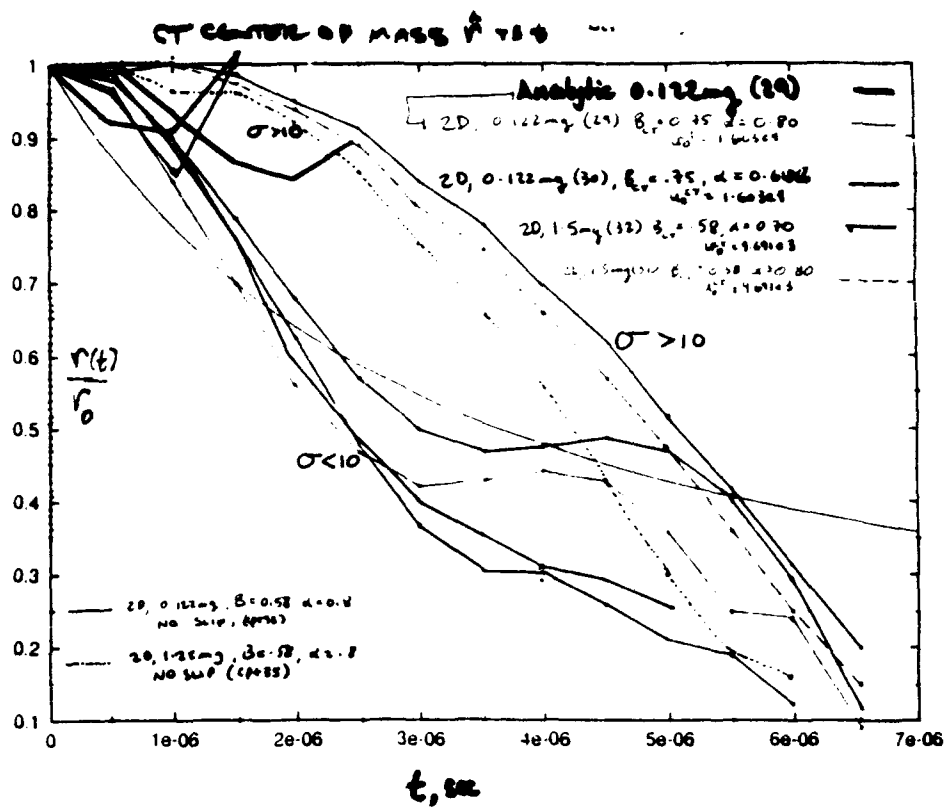


FIGURE 6

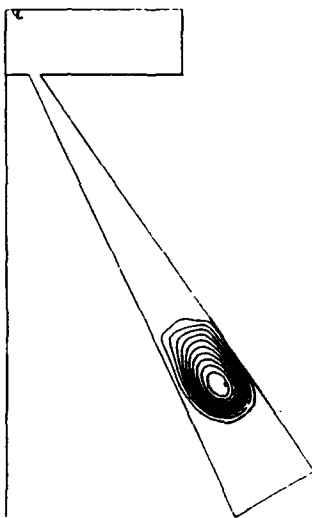


FIGURE 7a

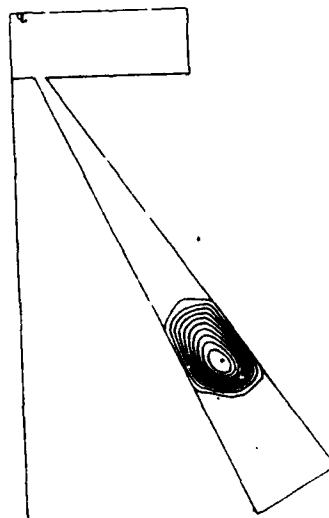
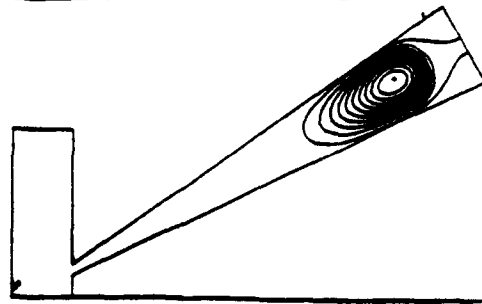
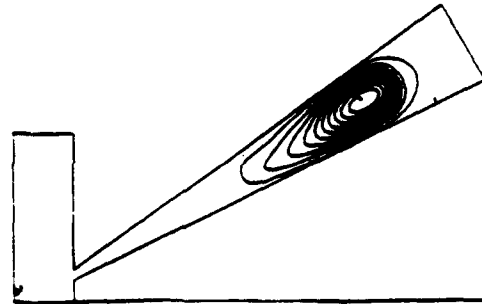


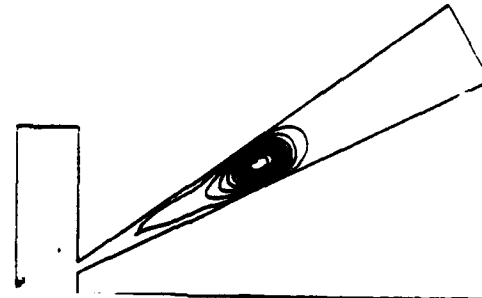
FIGURE 7b



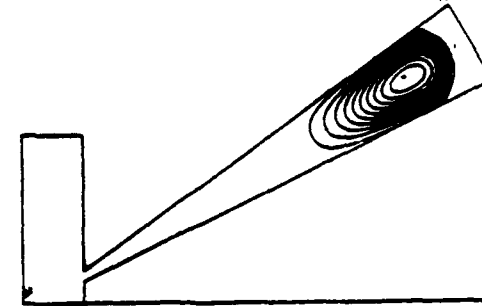
$\frac{1}{2} \mu$   
1/2 μs



1 μs

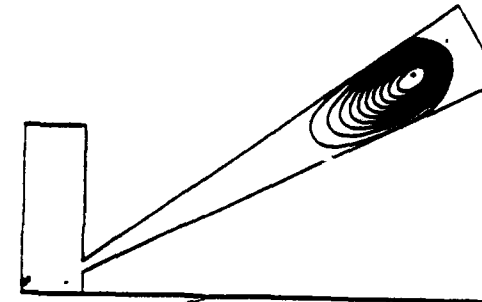


2 μs

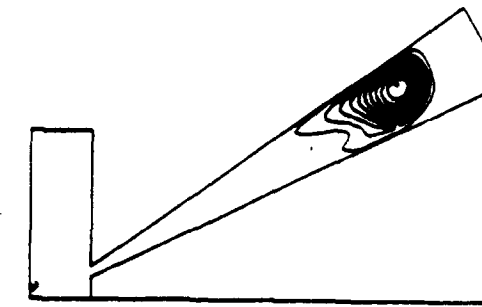


$\frac{1}{2} \mu$   
1/2 μs

MAGNETIC FLUX



1 μs



2 μs

20-17

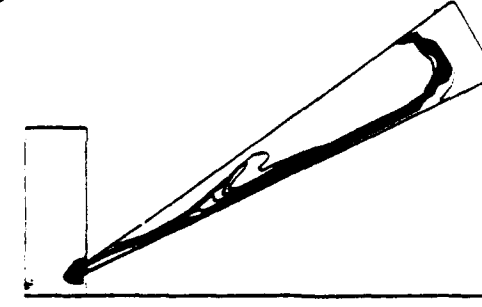
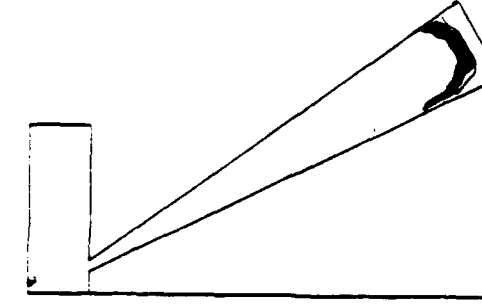
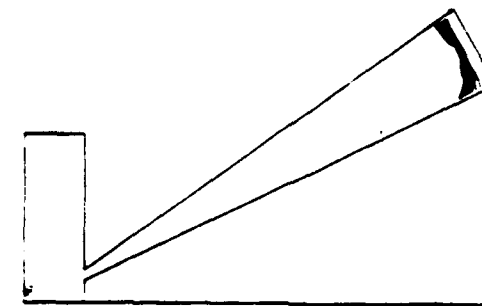
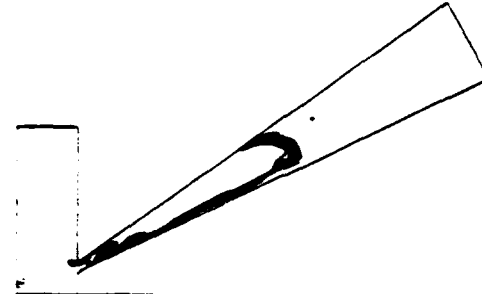
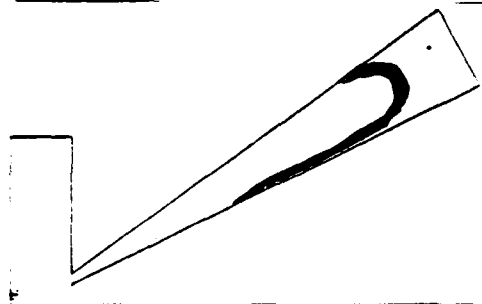
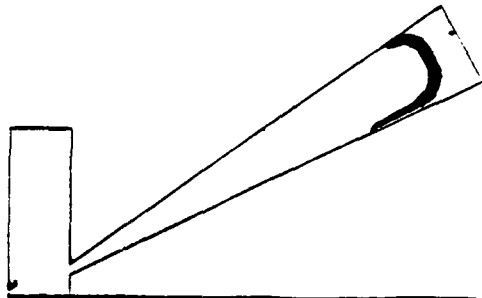


FIGURE 8

FLUID BEHIND CT

FIGURE 9

# CT TRAJECTORIES, $\alpha = \alpha(t)$

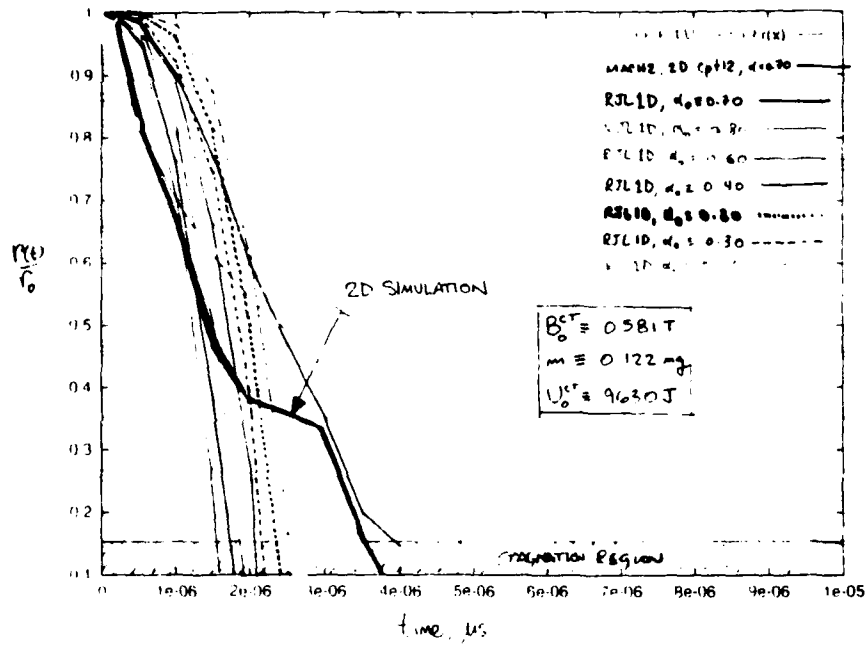


FIGURE 10a

# CURRENT WAVEFORM, $\alpha = \alpha(t)$

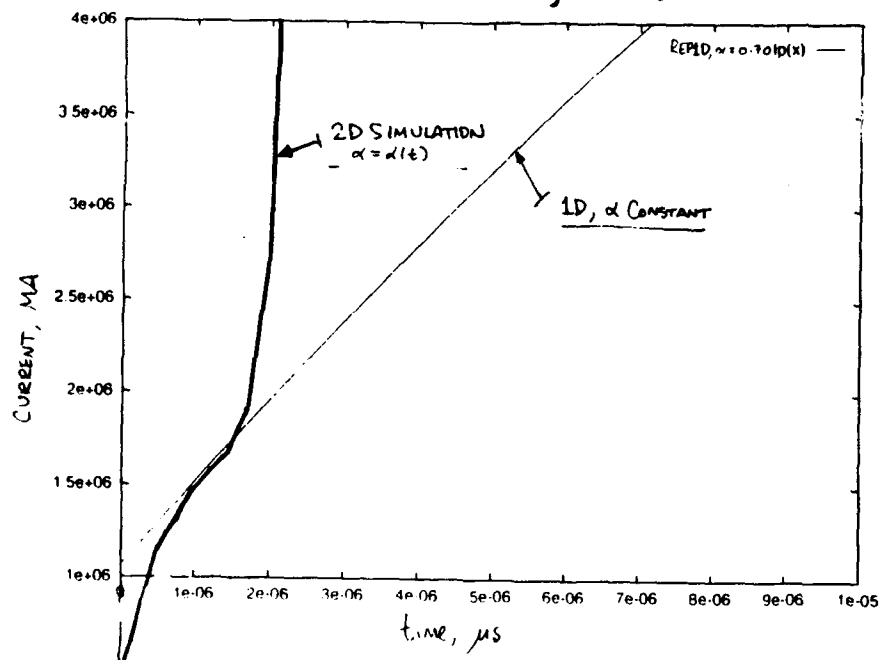
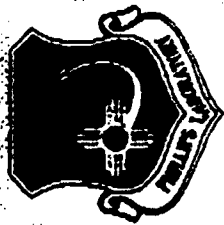
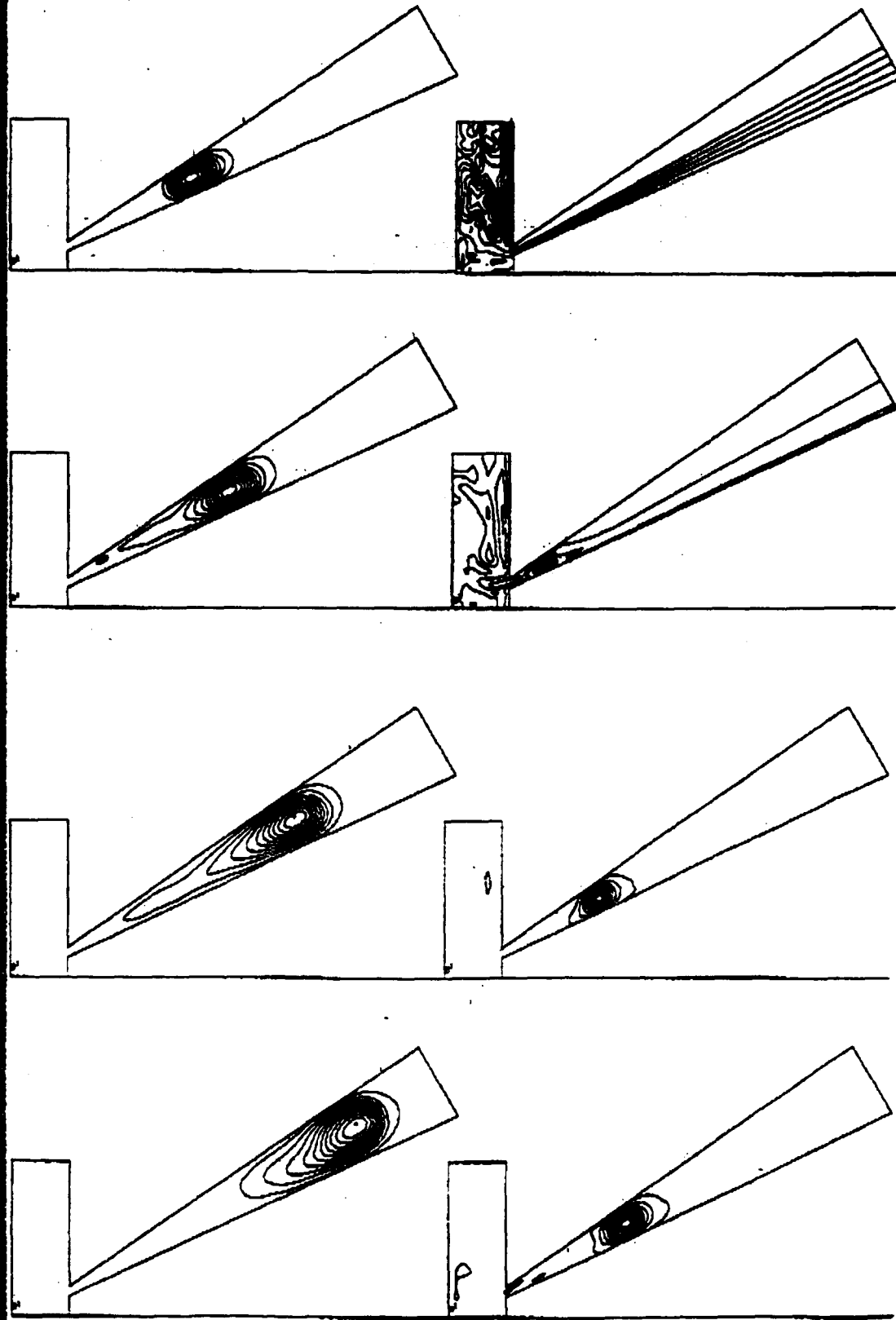


FIGURE 10b



MACH2, computes the compression of CT by a radial factor of 9  
between a pair of conical electrodes.  
Snapshots of poloidal magnetic flux lines are shown at  
0.5  $\mu$ s time intervals between 1 and 4.5  $\mu$ s.



Jane Messerschmitt's report unavailable at time of publication.

SCATTERING OF DIELECTRIC SPHERES IN  
DRY TO LOW MOISTURE CONTENT SOILS

Mark C. Worthy  
Graduate Student  
Department of Electrical Engineering

University of Alabama in Huntsville  
Huntsville, AL 35899

Final Report for:  
Graduate Student Research Program  
Phillips Laboratory

Sponsored by:  
Air Force Office of Scientific Research  
Bolling Air Force Base, Washington, D.C.

September 1993

SCATTERING OF DIELECTRIC SPHERES IN  
DRY TO LOW MOISTURE CONTENT SOILS

Mark C. Worthy  
Graduate Student  
Department of Electrical Engineering  
University of Alabama in Huntsville

Abstract

The problem of test range cleanup is introduced. A brief discussion of subsurface radar is supplied. Using Stratton's original scattering equations a model is compiled for generating the back-scattering cross section for dielectric spheres (in any media). The backscattering cross section for dielectric spheres of various sizes and dielectrics are shown (in various media). Finally, the system is checked by comparing H.C. Hulst's 1957 tabulated values for a perfect dielectric in free space.

# SCATTERING OF DIELECTRIC SPHERES IN DRY TO LOW MOISTURE CONTENT SOILS

Mark C. Worthy

## 1. INTRODUCTION

The problem of removing unexploded ordnance on (and under) government land is proving to be a technical and financial nightmare. "As a result of decades of neglect, the American taxpayer will be saddled with billions of dollars in cleanup costs," said Rep. George Miller, D-Calif. [Associated Press, 1993]. Potentially 1,200 Department of Defense sites across the country could have unexploded ordnance buried "in" the sites [Temple, 1993]. This unexploded ordnance is not only limited to military test ranges; there are at least 15 federal wildlife refuges that are known to have ordnance on them (ranging from rifle ammunition to several hundred pound bombs) [Beamish, 1993]. The composition of the unexploded ordnance ranges from plastics to various metals and ores (for instance: the unexploded ordnance at Aberdeen Proving Ground in Maryland includes 82,000 kilograms of depleted uranium rounds) [Beamish, 1993].

Solutions for finding these uxo's (unexploded ordnance) ranges from airborne sensors to IR imaging. One of the more promising solutions might lie in the use of subsurface radar.

Subsurface radars have been in development for at least the last 30 years [Oswald, 1988]. In soils these short-pulsed radars typically transmit between 100 and 1000MHz, and have ranges of up to 5 km (where the range and frequency is dependent on the soil type) [Daniels et al., 1988].

As you might guess, these radars have many physical limiting factors which worsen their performance, including: attenuation (from the dielectric losses), air-to-ground clutter, and filtering from the inhomogeneous ground (rocks, roots, water tables, bedrock, moisture content, and soil variations degrade the back-scattered



signal significantly) [Oswald, 1988]. {For more on subsurface radars see IEE PROCEEDINGS-F: Special issue on Subsurface radar, August, 1988.}

Another factor that is detouring the success of these radars is that there is a lack of published results on the scattering of geometrical objects in lossy media. It is the purpose of this paper to supply such results for the case of the dielectric sphere.

In the pages that follow I will discuss the dielectric characteristics of soils with respect to water content, I will set up the classical mathematical model for scattering waves from a sphere, and I will illustrate the back scatter from these spheres in various lossy medias (for various sphere sizes and dielectrics). I will also check the system by imputing some idealistic parameters.

## 2. DIELECTRIC PROPERTIES OF SOILS

Scattering of electromagnetic waves occur when there is a difference between the dielectric properties of the target and the media [McCann et al., 1988]. Targets of interest for subsurface radars are typically nonmetallic. This means that the scattering cross section will be highly dependent on the properties of the surrounding medium [Daniels et al., 1988].

Since dry materials transmit electromagnetic energy better than saturated materials [McCann et al., 1998], we would obviously want to only operate these radars in desert regions. Unfortunately, we do not have this luxury.

The natural presence of water in the soil leads to the introduction of an imaginary dielectric term in our modeling.

The size of this imaginary term (as well as the size of the real term) will depend on the frequency of operation, the water content, and the soil type [Wang, 1979]. As the water content rises the real dielectric term,  $\epsilon'$ , rises quickly (for a water content rise from 0 to 40%  $\epsilon'$  rises from 3 to  $\approx 20$  for clays and from 3 to  $\approx 30$  for sandy soils), where as the imaginary dielectric term,  $\epsilon''$ , rises very slowly (from zero to  $\approx 5$ ) [Wang, 1978].

For the results found in the following pages I will assume that the water content of the soil is between 0 and 15%, and that the frequency of the signal is between 500Mhz and 2.5GHz (where: the lower the frequency, the greater the penetration, and the higher the frequency, the better the resolution). These parameters will mean that  $\epsilon'$  ranges between 3 and 15, and  $\epsilon''$  ranges between 0 and 1.5 [Wang, 1978].

### 3. THE DREADED CLASSICAL APPROACH

When I first approached the problem of a dielectric sphere in a lossy media I assumed that I would have no problem finding published results. I was mistaken. After extensively researching the topic I was only able to find papers which made large assumptions or approximations (free space media, perfect dielectric target, perfect dielectric media, very large sphere, very small sphere, etc.). Not only could I not find any exact solutions for this problem, but the papers that were somewhat related were quick to note that finding the exact solution would be too cumbersome of a task: "Serious difficulties may arise in the computational programs for the scattering from dielectric spheres which are only a few wavelengths in radius" [Kouyoumjian, 1963], "It (the classical theory) does not readily allow construction of a physical model of the phenomena which would be useful for studying the scattering from spheres with parameters for which rigorous calculations have not been carried out" [Rheinstein, 1968]. One paper pointed out what probably is the culprit for the lack of work on this topic: "waves existing inside the sphere which could contribute significantly" [Inada et al., 1970].

It seems that this very point is why any accurate approach to this problem must come via the classical theory.

The series solution for a plane wave falling upon a sphere was first introduced by Mie in 1908. In 1941 Julius Adams Stratton provided a more extensive and complete model of the problem in his infamous book entitled Electromagnetic Theory.

It is this model which I will follow for a solution to the dielectric sphere in a lossy media problem. Where  $r$  is the radius of the sphere,  $k_1$  is the propagation constant of the sphere, and  $k_2$  is the propagation constant for the media, we have the following expressions [Stratton, 1941]:

$$\mathbf{E} = \mathbf{E}_o e^{-i\omega t} \sum_{n=1}^{\infty} i^n \left[ \frac{2n+1}{n(n+1)} \right] (a_n^v \mathbf{m}_{o,n}^{(v)} - i b_n^v \mathbf{n}_{e,n}^{(v)}) ,$$

and

$$\mathbf{H} = \frac{-k_2 E_o}{\mu_2 \omega} e^{-i\omega t} \sum_{n=1}^{\infty} i^n \left[ \frac{2n+1}{n(n+1)} \right] (b_n^v \mathbf{m}_{e,n}^{(v)} + i a_n^v \mathbf{n}_{o,n}^{(v)}) .$$

Here  $v$  represents the wave's characteristic form (i.e. incident wave,  $i$ , transmitted wave,  $t$ , or scattered wave,  $s$ ) [Stratton, 1941]. The terms  $m$  and  $n$  are also dependent upon this characteristic wave form; where:

$$\mathbf{m}_{o,n}^{(v)} = \frac{1}{\sin \theta} z_n(k_2 r) P_n^1(\cos \theta) \frac{\cos \varphi}{\sin \varphi} \hat{\theta} - z_n(k_2 r) P_n^1(\cos \theta) \frac{\sin \varphi}{\cos \varphi} \hat{\varphi}$$

and

$$\mathbf{n}_{o,n}^{(v)} = \frac{n(n+1)}{k_2 r} z_n(k_2 r) P_n^1(\cos \theta) \frac{\sin \varphi}{\cos \varphi} \hat{r} + \frac{1}{k_2 r} [k_2 r z_n(k_2 r)]' P_n^1(\cos \theta) \frac{\sin \varphi}{\cos \varphi} \hat{\theta}$$

$$P_n^1(\cos \theta) \frac{\sin \varphi}{\cos \varphi} \hat{\theta} + \frac{1}{k_2 r \sin \theta} [k_2 r z_n(k_2 r)]' P_n^1(\cos \theta) \frac{\cos \varphi}{\sin \varphi} \hat{\varphi} .$$

Where  $'$  represents the derivative of the function, and  $\hat{r}$ ,  $\hat{\theta}$ , and  $\hat{\varphi}$  represent the spherical-directional unit vectors. It is important to note that I am assuming that the incoming wave is on the  $z$  axis; hence, in spherical coordinates this corresponds to the angles  $\theta$  and  $\varphi$  equal to zero. Therefore, the vectors  $m$  and  $n$  will be in the  $\theta$  direction only. The dependence that  $m$  and  $n$  have on the characteristic wave form is embedded in the  $z(k_2 r)$  term. For the incident wave  $z(k_2 r)$  is the spherical Bessel function,  $j(k_2 r)$  [Stratton, 1941]. For the transmitted wave  $z(k_2 r)$  is the spherical

Bessel function in terms of the targets propagation constant,  $j(k_1 r)$  [Stratton, 1941]. Finally, for the scattered wave  $z(k_2 r)$  is the spherical Hankel function,  $h(k_2 r)$  [Stratton, 1941].

The next step in the classical approach is to derive the coefficients  $a$  and  $b$  for the scattered wave. This is accomplished by using the boundary conditions of the problem. The boundary conditions for this problem are that at the surface of the sphere (call this distance  $a$ , the radius of the sphere; in bold type), the transmitted wave ( $E_t$ ,  $H_t$ ) is equal to the incident wave ( $E_i$ ,  $H_i$ ) plus the scattered wave ( $E_s$ ,  $H_s$ ); such that:

$$\hat{r} \times (E_i + E_s) = \hat{r} \times E_t, \quad \text{and}$$

$$\hat{r} \times (H_i + H_s) = \hat{r} \times H_t.$$

These conditions will lead to the solutions for the scattered coefficients,  $a$  and  $b$  (note that I am assuming  $\mu_1 = \mu_2$ ):

$$a_n^s = \frac{[k_2 a j_n(k_2 a)]' j_n(k_1 a) - [k_1 a j_n(k_1 a)]' j_n(k_2 a)}{[k_1 a j_n(k_1 a)]' h_n(k_2 a) - [k_2 a h_n(k_2 a)]' j_n(k_1 a)}$$

$$b_n^s = \frac{(k_1/k_2)^2 [k_2 a j_n(k_2 a)]' j_n(k_1 a) - [k_1 a j_n(k_1 a)]' j_n(k_2 a)}{[k_1 a j_n(k_1 a)]' h_n(k_2 a) - (k_1/k_2)^2 [k_2 a h_n(k_2 a)]' j_n(k_1 a)}$$

Finally, after obtaining an expression for the scattered coefficients, the scattering cross section for the sphere can be defined. It is:

$$Q_s = \sigma = \frac{2\pi}{k^2} \sum_{n=1}^{\infty} (2n+1) (|a_n^s|^2 + |b_n^s|^2) \quad \text{meters}^2$$

[Stratton, 1941].

#### 4. METHODOLOGY

Obtaining results for  $E_s$  and  $\sigma$  meant generating many modes. I first thought that generating the first 2 or 3 modes would be sufficient for accurate results. Unfortunately, I was mistaken. It seems that the number of modes needed for accurate results depends heavily on the parameters  $k_1$ ,  $k_2$ , and  $a$ . Many papers that I came across held the view that the first mode would be by far the largest mode, and therefore, it would be sufficient to only study the first mode ( $n=1$ ). However, I found that seldom ever is this the case. Usually the first mode was one of the smallest modes of investigation (in terms of the size of  $a$ ,  $b$ , and  $E_s$ ). The results demonstrated in this paper are all cases where the terms ( $a$ ,  $b$ , or  $E_s$ ) have fallen off enough by the tenth mode to give accurate results (note: in some cases these terms fell off sufficiently by the fifth or sixth mode).

To obtain results for  $E_s$  and  $\sigma$  I analytically generated the expressions for the first 6 modes of  $a$ ,  $b$ , and  $E_s$ . I then translated these expressions into a computer.

After discovering that some of these expressions were still diverging after 6 modes, I realized that I would have to generate more modes. This was somewhat dis-heartening since generating just one more mode meant that I would have to generate another spherical Bessel function, spherical Hankel function, and an associated Legendre polynomial, and their derivatives. By the sixth mode expressing just one coefficient equation (for one mode) took over one page (in its most reduced form). Therefore, instead of analytically generating the extra modes sufficient for accurate results I devised a computer program which required imputing tabulated values of spherical Bessel and Hankel functions (the tables were from: Abramowitz, M., and I.A. Stegun, Handbook of Mathematical Functions, National Bureau of Standards, Washington D.C., 1964).

For the derivatives of the Bessel and Hankel functions I mathematically derived the following expression:

$$[xf_n(x)]' = xf_{n-1}(x) - nf_n(x).$$

From this expression I could use the Bessel and Hankel tables to calculate the  $[xf(x)]'$  term.

The program also required imputing the corresponding Legendre value. I analytically produced these functions (and tabulated their values) myself (since I was unable to find any tabulated results past the tenth mode).

Upon computing the coefficients I observed that the absolute magnitude of both a and b oscillate between the limits of zero and one; just as the theory dictates [Stratton, 1941].

In the following pages I will demonstrate my graphical results of the backscattering cross section for a given  $k_2$  and radius, a (for varying values of  $k_1$ ). Where:

$$k_2 = \omega\{\epsilon_0\mu(\epsilon' - i\epsilon'')\}^{1/2}, \text{ and}$$

$$k_1 = \omega\{\epsilon_0\mu\epsilon'\}^{1/2}.$$

Obtaining these graphical results proved to be a very time consuming task (even with the aid of the computer). As I previously stated, finding just one point would mean the calculation of 10 modes (in most cases). This means that one point on any of the following graphs meant running 10 different computer programs (six programs one time for the first six modes, and one program four times for modes 7-10). Therefore, the realization of just one graph might take an entire day.

In the last graph, figure 12, I fixed the value of  $k_1$  (the target), and varied the value of  $k_2$  (the media). This is a reversal of figure 2. My reasoning for doing this was to provide a preliminary check on my system by demonstrating the "focusing effect" that occurs when  $k_1$  is greater than  $k_2$  (for a much more extensive check see Appendix A).

## Backscattering for $a=.05\text{m}, k_2=40\text{m}^{-1}$

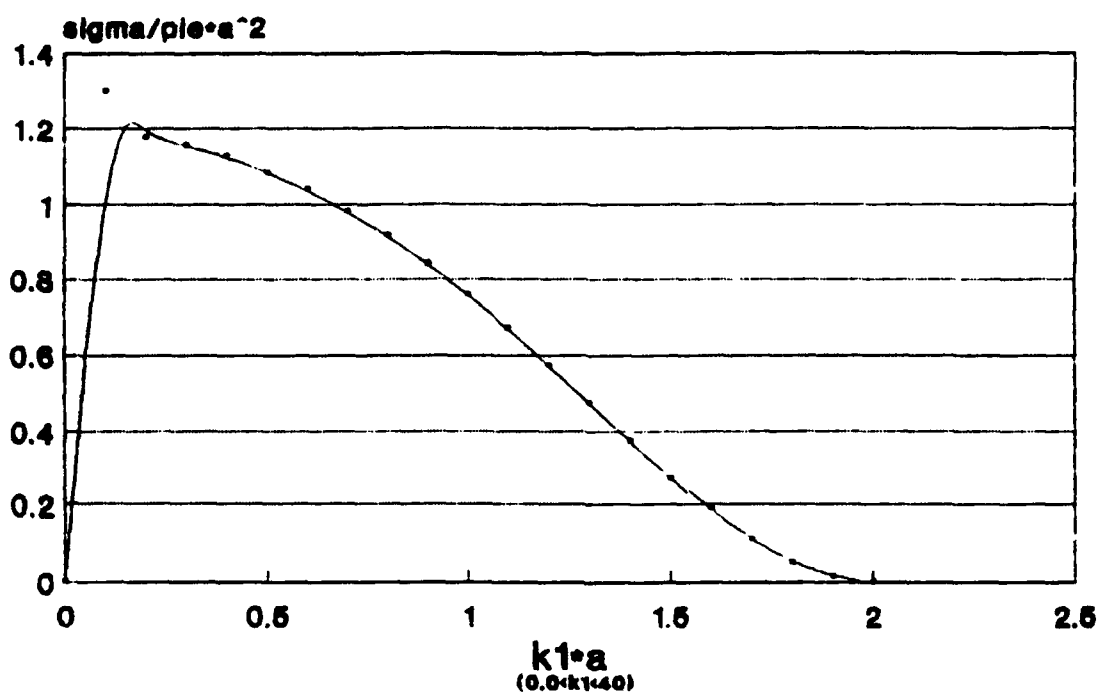


FIGURE 1

## Backscattering for $a=.05\text{m}, k_2=100\text{m}^{-1}$

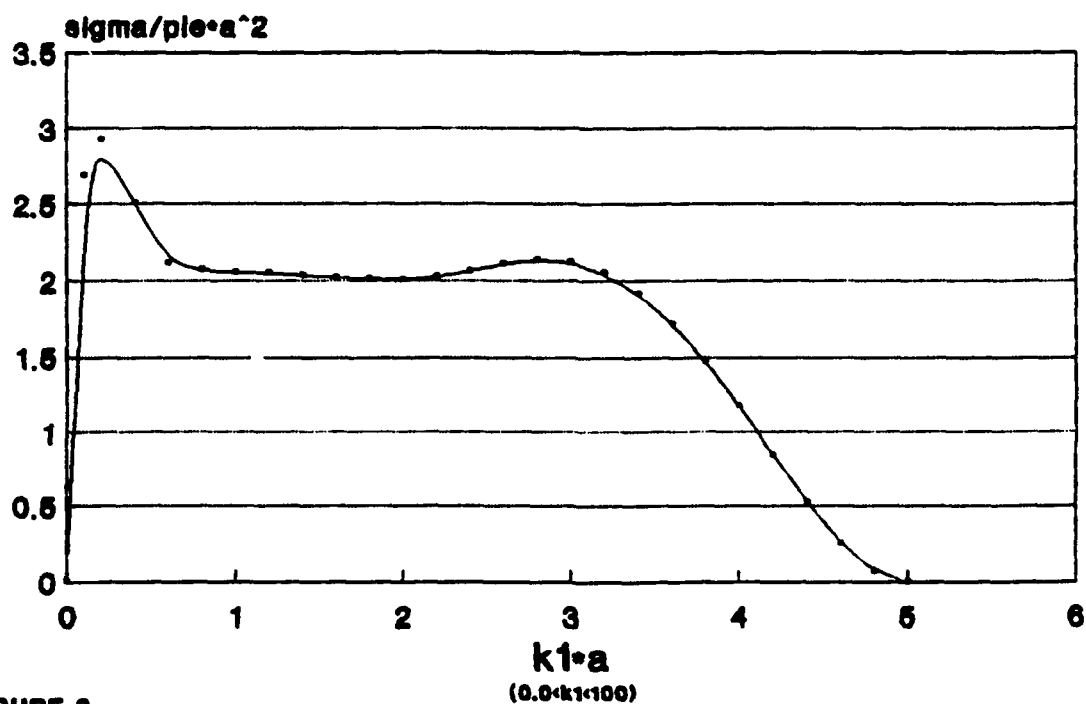


FIGURE 2

## Backscattering for $a=.05m, k_2=200m^{-1}$

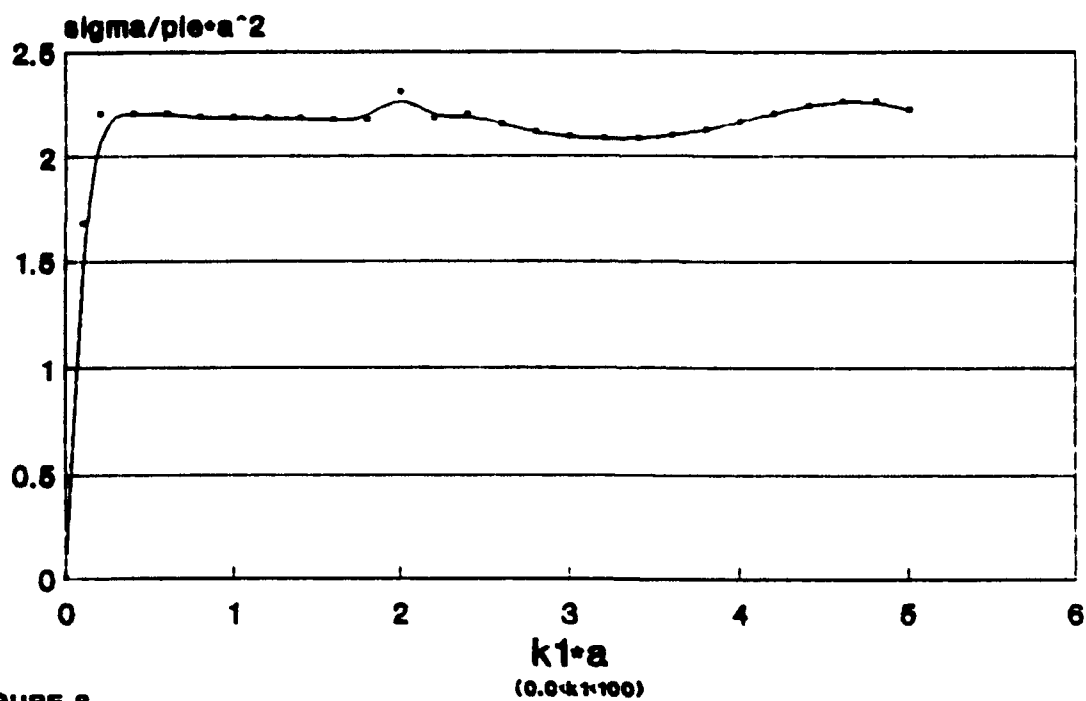


FIGURE 3

## Backscattering for $a=.1m, k_2=25m^{-1}$

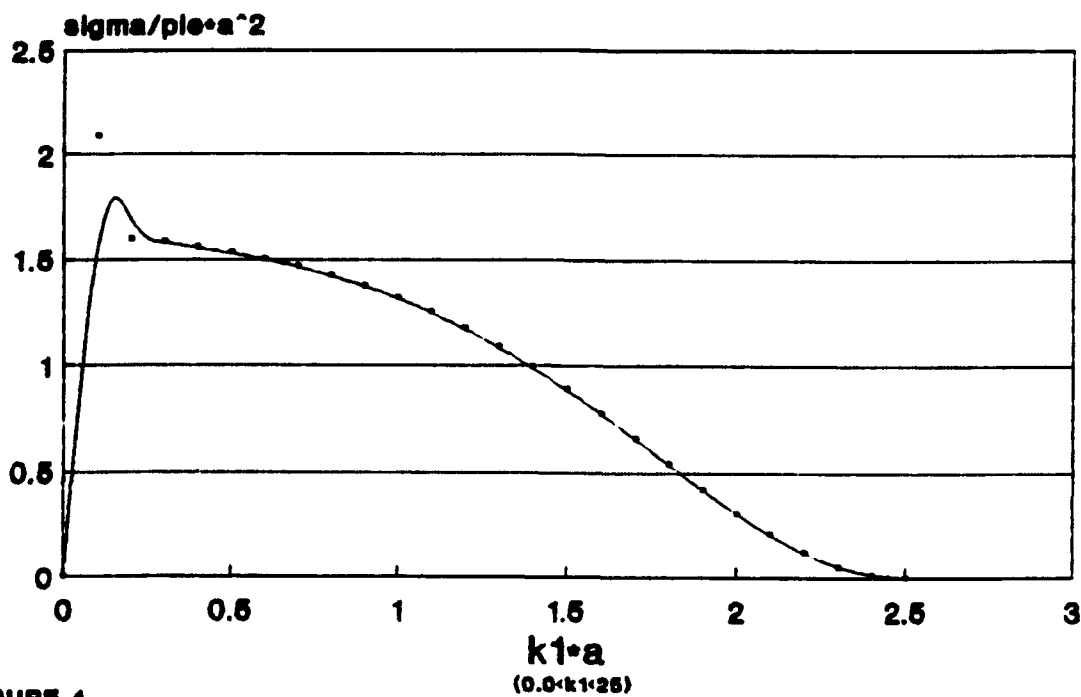


FIGURE 4



## Backscattering for $a=.1m, k_2=50m^{-1}$

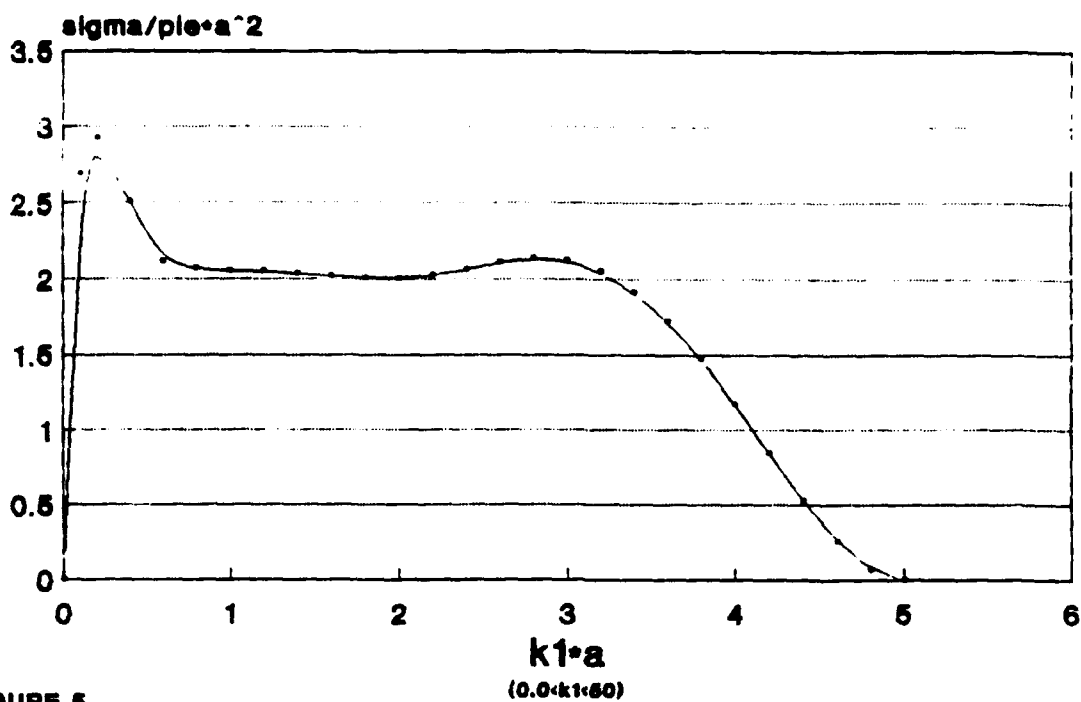


FIGURE 5

## Backscattering for $a=.1m, k_2=100m^{-1}$

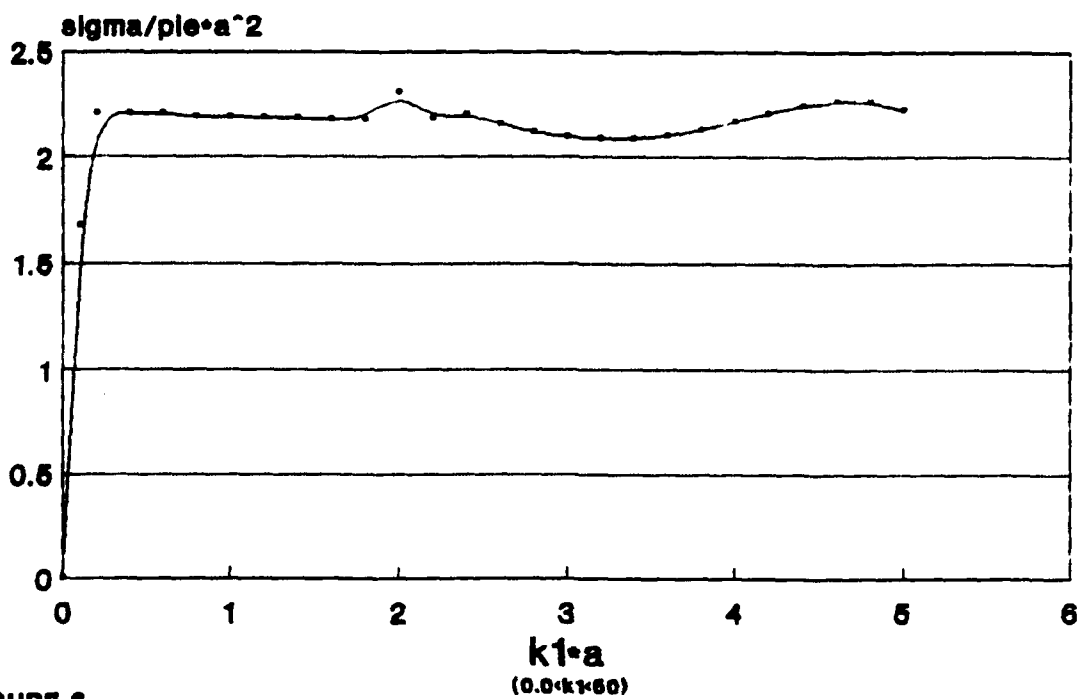


FIGURE 6

## Backscattering for $a=.2m, k_2=25m^{-1}$

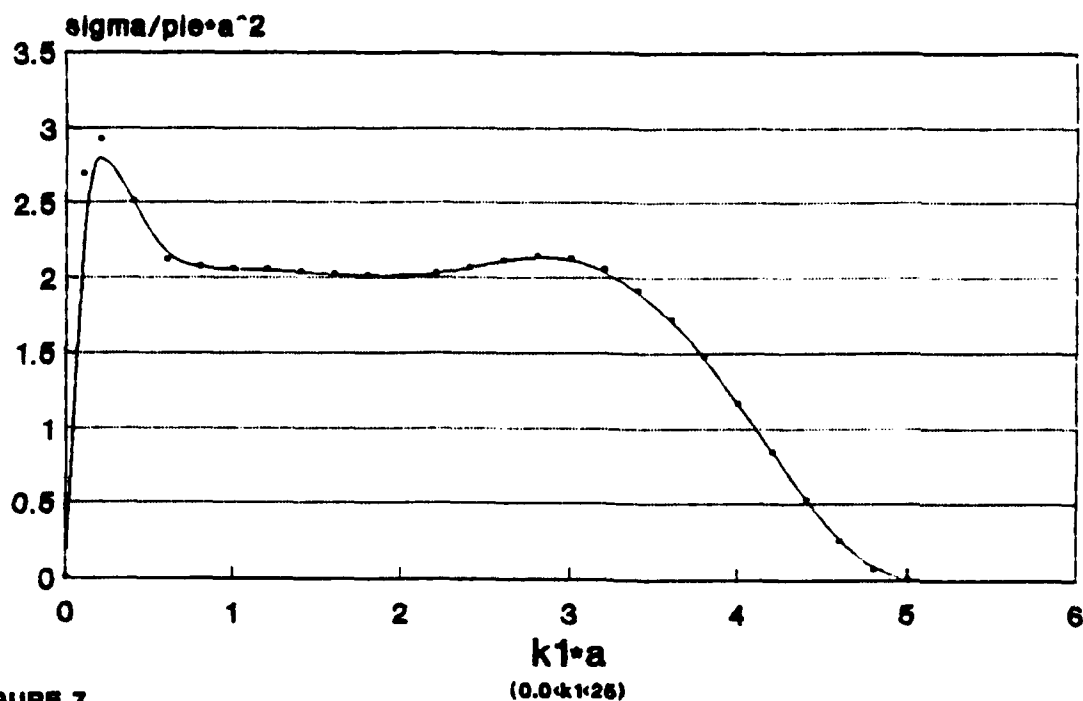


FIGURE 7

## Backscattering for $a=.2m, k_2=50m^{-1}$

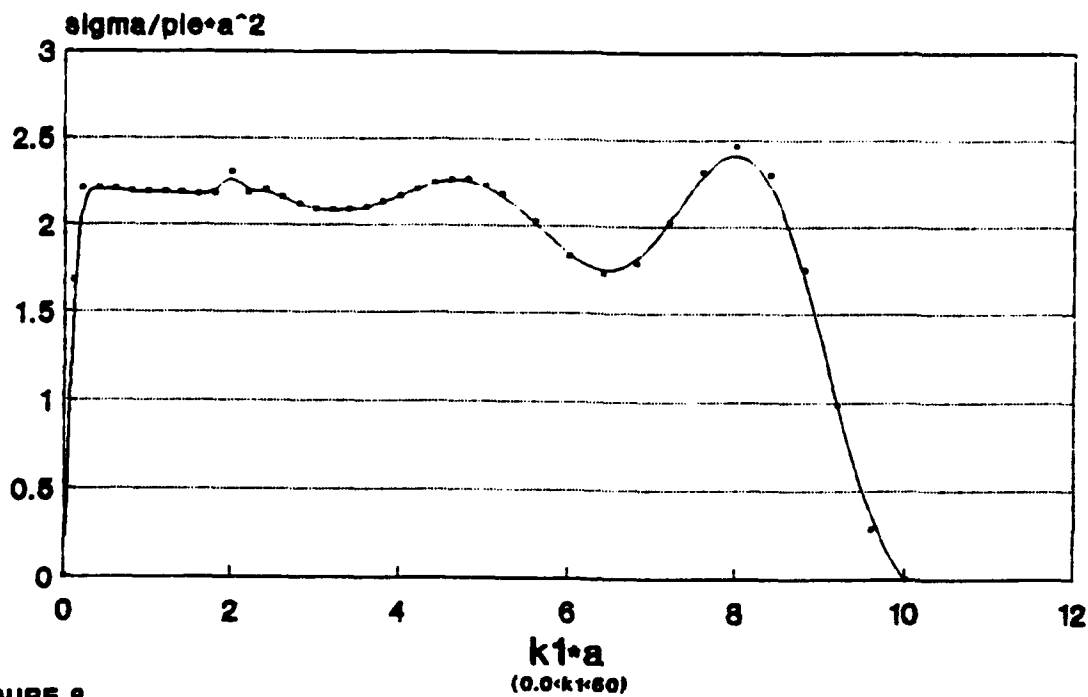


FIGURE 8

## Backscattering for $a=.05m, k_2=40, 100, 200$

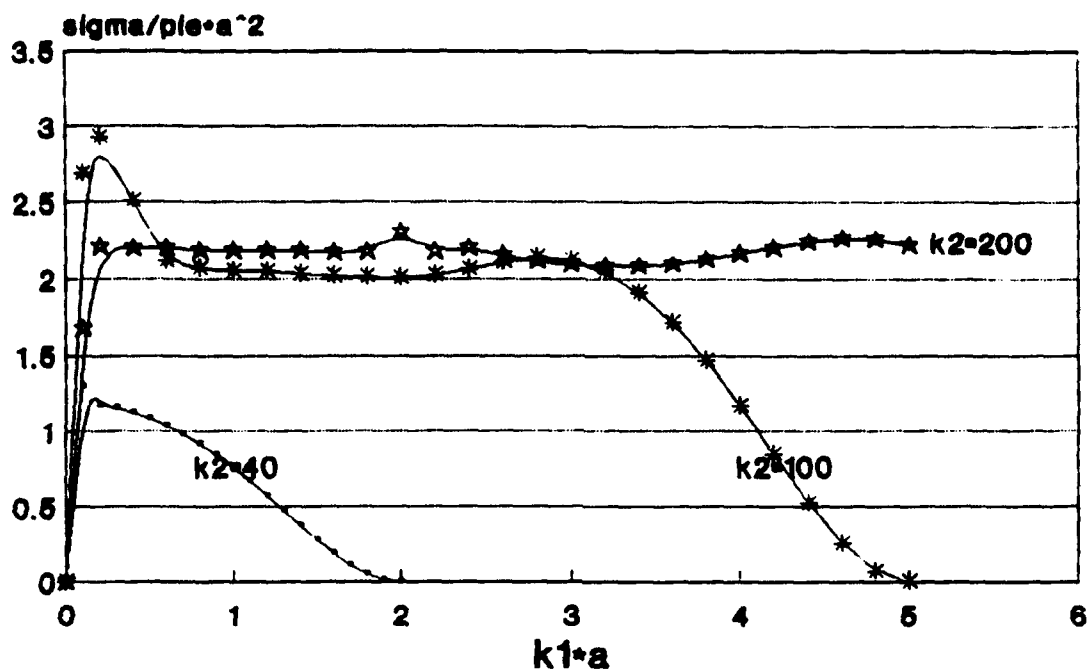


FIGURE 9

## Backscattering for $a=.1m, k_2=25, 50, 100$

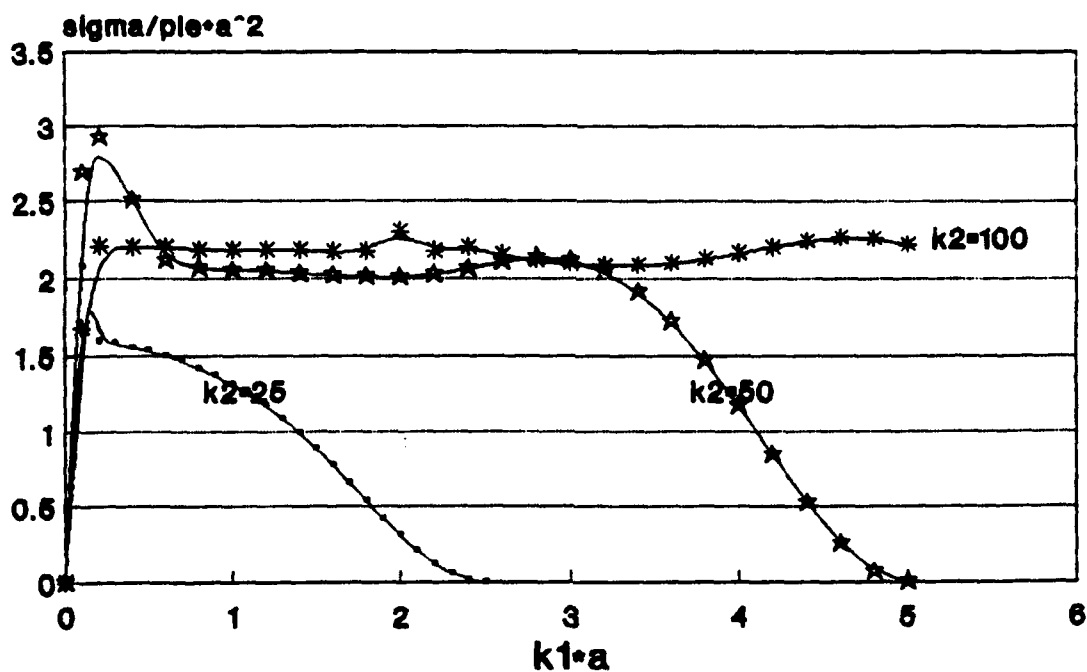


FIGURE 10

## Backscattering for $a=.2m, k_2=25,50$

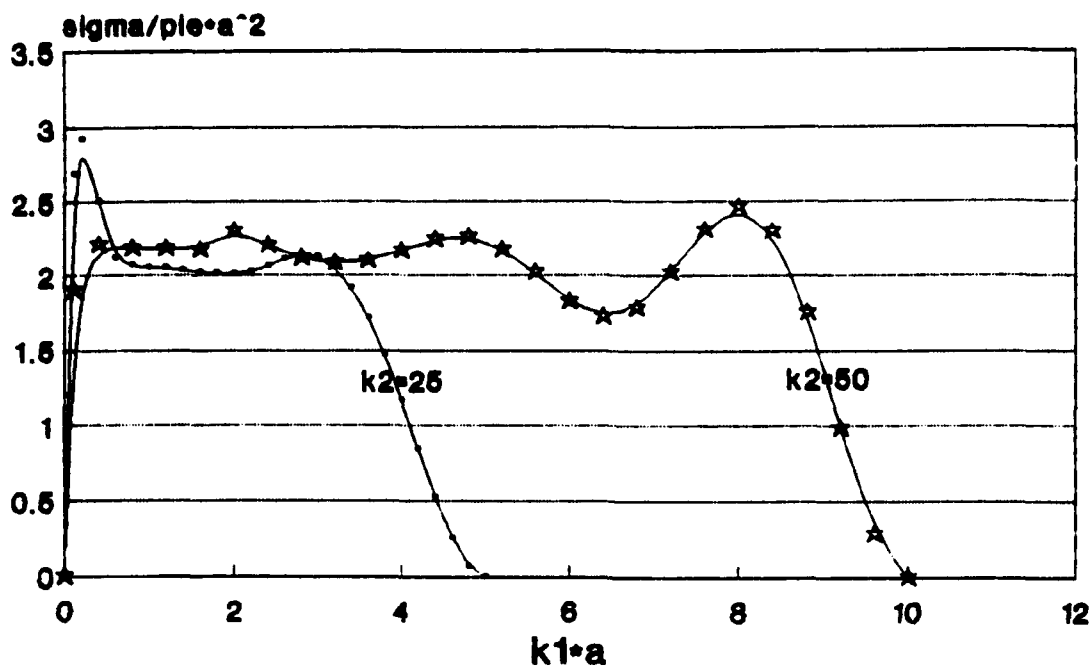


FIGURE 11

## Backscattering for $a=.05m, k_1=100m^{-1}$

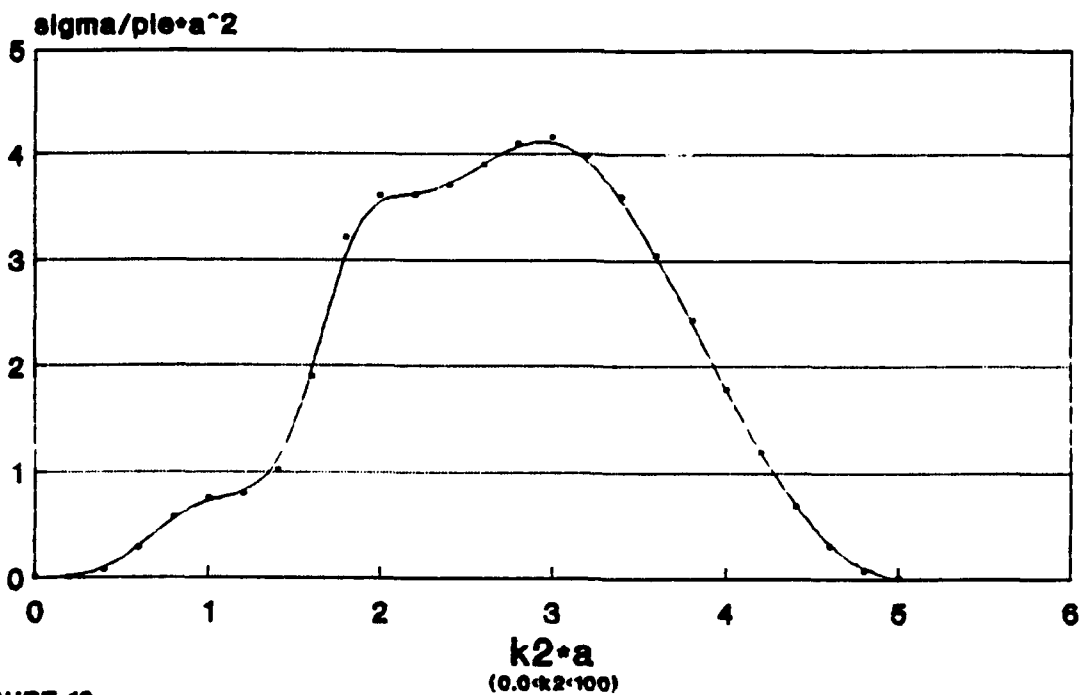


FIGURE 12

## 5. RESULTS

The first point worth noting about the results regards the nature of backscatter-theory. This theory holds that for the case of  $k_1 = 0$ , or  $k_1 = k_2$  there will be no scattered wave present (as was the case in the results). This is why the graphs fall-off as  $k_1$  approaches  $k_2$ .

Another important note here is the significance of  $\sigma/\pi a^2 = 2$ . The cross-sectional value found here is representative of the total scattered energy. It is not to be confused with the monostatic cross section (commonly called the radar cross section). In the case of the monostatic cross section the backscatter wave forms would be hovering around  $\sigma/\pi a^2 = 1$  (not 2). This value of two was noted by Bladel (and others) in his 1964 book on electromagnetic fields. According to Bladel "the asymptotic value of  $\sigma$  is twice the geometric cross section  $\pi a^2$ " [Bladel, 1964].

Another important point (unrelated to the previous discussion) has to do with the relatively large size of these cross sections. This phenomena seems to be due to the very nature of the problem at hand. Where, for the case of a dielectric sphere in soil, the internal (transmitted) waves of the sphere will have a larger wavelength than in the external waves found in the soil. This means that these internal waves will play a large role in the scattered waves, natural frequencies, etc.. This point was emphasized in experiments carried out by Atlas in 1963. Atlas notes that except for the interval  $30 < k_1 a < 40$ , the cross sections for plexiglass spheres is larger than that of metal spheres for the interval  $6 < k_1 a < 60$  [Atlas et al., 1963].

There is an interesting and mysterious observation taken from the graphs that might be worth mentioning as well. Note that for the cases when  $k_2 a$  is small the backscatter peaks early (around  $k_1 a = 0.2$ ). However, when  $k_2 a$  is large this peaking occurs much later in the cross section (just before it begins to fall off; not at the beginning).

Finally, as was stated earlier, the purpose of this paper is to

provide results on the backscattering cross section for dielectric spheres in dry to low moisture content soils. However, all of the graphs that I have presented here are for the case when the soil is perfectly dry ( $k_2 = \text{real}$ ). Some of the reasoning why graphs were not presented for moist soils was due to my graphics program. Results were found, however, for low moisture content soils (water content  $<15\%$ ). Recall that for low moisture content soils the imaginary term of the dielectric is very small compared to the real term ( $\epsilon' \approx 12$  when  $\epsilon'' \approx 1$ ). What this meant in terms of the backscatter cross section was that assuming  $\epsilon'' = 0$  only made for very small percent errors ( $\leq 5\%$ ). Therefore, I am confident that the graphs I have presented here will be sufficient for low moisture soils as well.

## 6. FURTHER POSSIBILITIES

As you may already know, EMF radars don't work very well in saturated media (this is one of the reasons why I chose low moisture content soils). A solution to this problem, for the organizations that will be involved with range clean up, may come from the application of acoustical imaging.

The benefits of acoustical imaging in medicine cannot be overstated; I refer you to the ultrasound equipment used on pregnant females. The hope is that one day we will be able to get such imaging for the earth (either by EMF or acoustical equipment). The problem with the acoustical equipment presently available is that they depend on a very saturated media and have a very small penetration ( $\approx 1$  ft.).

However, the wave theory for acoustical applications is analogous to that of the EMF applications. Where, for acoustical applications, the wavelength,  $\lambda$ , is dependent upon the bulk modulus of elasticity of the media,  $Y$ , and the density of the media,  $\rho$ , for a dry media, and the compressibility of the media,  $K$ , and the density of the media,  $\rho$ , for a completely saturated media [Moore, 1960]. Such that for a dry media [Moore, 1960]:

$$\lambda = (1/f) [(Y/\rho)^{1/2}],$$

and for a completely saturated media [Moore, 1960]:

$$\lambda = (1/f) [(\rho K)^{-1/2}].$$

These would be the only two adjustments necessary if one wanted to translate an acoustical theory into the general form of the classical EMF theory presented earlier.

## 7. CONCLUSIONS

The backscattering cross sections for dielectric spheres in lossy media were demonstrated for the frequency range  $500\text{MHz} < f < 2.5\text{GHz}$ , and the media dielectric range  $3 < \epsilon' < 15$  and  $0 < \epsilon'' < 1.5$ . These results were obtained by following the rigorous classical approach first introduced by Mie in 1908 (and later covered more extensively by Stratton, Panofsky, Phillips, and others).

The results found here seem to follow along with the theory in that  $\sigma/\pi a^2 = 0$  for  $k_1 = 0$  and  $k_1 = k_2$ , and  $\sigma$  is typically twice the size of the cross-sectional area.

The classical approach used in this paper could be translated into an acoustical theory for further application. The use of such acoustical knowledge might be applied in the area of subsurface "radar" where better imaging is needed for non-desert regions.

I am confident that the numerical results found in this paper will be a useful contribution for the study of dielectric spheres in lossy media because of the highly limited amount of work dealing with this topic.

## APPENDIX A: A FURTHER CHECK

As a further check on my system I will compare my results with those tabulated by Hulst in 1957 for a perfectly dielectric sphere. Since I cannot input infinite dielectric values into my computer

models there will be some errors noticeable in this check. The parameters that I will input into my models will be  $k_1 = 100,000m^{-1}$ , and  $a = 1m$ . Note that even with this approximation the errors are still very small. I am confident that if I could input large enough values my results would agree with those of Hulst. The following table demonstrates these results. (The infinite values are from Hulst's book; see [Hulst, 1957].)

$k_2a$	$k_1 = 100,000$	Hulst $k_1 = \infty$
0.2	0.00538	0.0054
0.4	0.088	0.086
0.6	0.45	0.466
0.8	1.24	1.257
1.0	2.036	2.036
1.2	2.2289	2.2280
1.4	2.206	2.204
1.6	2.125	2.115
1.8	2.15	2.136
2.0	2.21	2.209
3.0	2.171	2.172
4.0	2.138	2.140
5.0	2.117	2.116

TABLE 1: A comparison of the backscattering for a perfectly dielectric sphere in free space.

*Acknowledgments.* It is with pleasure that I acknowledge the comments and suggestions from Dr. Albert Biggs. I would also like to acknowledge AFOSR for their sponsorship in this work.

#### REFERENCES

- Associated Press release (unauthored), Dozens of former U.S. military sites may be sitting on ordinance, The Huntsville Times; Huntsville, Alabama; April, 1993.
- Atlas, D., L.J. Batton, W.G. Harper, B.M. Herman, M. Kerker, and E. Matijevic, Back-scatter by dielectric spheres, IEEE Trans. Antennas Propag., AP-13, 68, 1963.
- Beamish, R., Taxpayer-owned land full of hazards, report finds,



- Albuquerque Journal; Albuquerque, NM; pg. A7, July 9, 1993.
- Bladel, J.V., Electromagnetic Fields, McGraw-Hill Book Company, New York, San Francisco, Toronto, London, 1964.
- Daniels, D.J., D.J. Gunton, and H.F. Scott, Introduction to subsurface radar, Proc. IEE 135(F-4), 280-287, 1988.
- Hulst, H.C., Light Scattering by Small Particles, John Wiley and Sons, Inc., New York, 1957.
- Inada, H., and M.A. Plonus, The geometric optics contribution to the scattering from a large dense dielectric sphere, IEEE Trans. Antennas Propag., AP-18(1), 89, 1970.
- Kouyoumjian, R.G., L. Peters, Jr., and D.T. Thomas, A modified geometrical optics method for scattering by dielectric bodies, IEEE Trans. Antennas Propag., AP-13, 690, 1963.
- McCann, D.M., P.D. Jackson, and P.J. Fenning, Comparison of the seismic and ground probing radar methods in geological surveying, Proc. IEE, 135(F-4), 380-389, 1988.
- Moore, R.K., Traveling-Wave Engineering, McGraw-Hill Book Company, New York, Toronto, London, 1960.
- Oswald, G.K.A., Geophysical radar design, Proc. IEE, 135(F-4), 371-372, 1988.
- Rheinstein, J., Backscatter from spheres: a short pulse view, IEEE Trans. Antennas Propag., AP-16, 89, 1968.
- Stratton, J.A., Electromagnetic Theory, McGraw-Hill Book Company, New York, London, 1941.
- Temple, C., MTA cleansing old military ranges, The Huntsville Times; Huntsville, Alabama; April, 1993.
- Wang, J., T. Schmugge, and D. Williams, Dielectric constants of soils at microwave frequencies-II, NASA Technical Paper 1238; Goddard Space Flight Center; Greenbelt, Maryland; 1978.
- Wang, J.R., The dielectric properties of soil-water mixtures at microwave frequencies, NASA-TM80597; Goddard Space Flight Center; Greenbelt, Maryland; 1979.